

2008

A STUDY OF DENSE WATER FORMATION OVER ROCKALL BANK

O'NEILL, CLARE KATHERINE

<http://hdl.handle.net/10026.1/1754>

<http://dx.doi.org/10.24382/3692>

University of Plymouth

All content in PEARL is protected by copyright law. Author manuscripts are made available in accordance with publisher policies. Please cite only the published version using the details provided on the item record or document. In the absence of an open licence (e.g. Creative Commons), permissions for further reuse of content should be sought from the publisher or author.

**A STUDY OF DENSE WATER FORMATION OVER ROCKALL
BANK**

by

CLARE KATHERINE O'NEILL

A thesis submitted to the University of Plymouth in partial fulfilment for
the degree of

DOCTOR OF PHILOSOPHY

School of Earth, Ocean, and Environmental Sciences
Faculty of Science

November 2008

University of Plymouth Library
Item No. 9007938001
Shelfmark THESIS 551.4613 ONE

A study of dense water formation over Rockall Bank

by Clare Katherine O'Neill

Abstract

Rockall Bank is a large undersea bank situated in the north-east Atlantic. The region features steep bathymetry with the depth of Rockall Trough reaching 3000 m, rising to the surface at Rockall rock itself. Winter convective mixing in this area is strong and can reach 600 m or more. As this is deeper than a significant proportion of the bank, the water column above the bank becomes cooler than in the surrounding area, and a "cold water patch" forms. This water has been observed moving off the slope as a dense water cascade, a process that is important for shelf-ocean exchange and ventilation and which is also biologically important.

This research contributes to knowledge of the dense water formation over Rockall Bank by analysing remotely-sensed data as well as numerical model results. Within this study: i) satellite sea surface temperature data were obtained for a ten year time series and the presence and properties of the surface cold water patch were investigated, and ii) the POLCOMS numerical model was adapted to simulate the Rockall Bank under different climatological conditions.

It was demonstrated that a surface cold patch could be seen regularly in the satellite SST data, though more often there is a cold front associated with the Bank with no distinct cold patch. The duration of the cold patch and the duration of the front are inversely linked, and the cold patch is seen for longer in winters with a greater winter temperature difference across the Bank. The model successfully simulated the formation of the dense water in three test years, and the results show that the Bank greatly amplifies the effect of changing meteorological conditions. Dense water formation is very sensitive to changes in the winter air temperature, with a 2°C temperature decrease leading to a three-fold increase in the density difference between the water over the Bank and the surrounding area. The model results show a limited amount of cascading during the cooler years, but no cascading at all in the warmer year. Such large changes in the dense water formation caused by a relatively small change in air temperature suggests that climate change will have a significant impact on this system.

Contents

Abstract	iii
List of Figures	vii
List of Tables	xii
Acknowledgements	xiii
Author's Declaration	xiv
1 Introduction	1
1.1 Motivation and Objectives	1
1.2 Outline of the Thesis	3
2 Literature Review and Background	4
2.1 Rockall Bank Area	4
2.1.1 Topography	4
2.1.2 Water Masses	5
2.1.3 Circulation	6
2.1.4 Convection and Dense Water Formation	7
2.1.5 Biological Importance	8
2.2 Dense Water Cascades	8
2.3 Remote Sensing	12
2.4 Modelling	13
2.4.1 POLCOMS	13
2.4.2 Modelling of Rockall Bank	14
3 Methodology	16
3.1 Introduction	16
3.2 SST Satellite Data	16
3.3 Model Input Data Processing	18
3.3.1 Bathymetry	18
3.3.2 Initial Temperature and Salinity	21
3.3.3 Boundary Temperature and Salinity	24
3.3.4 Wind Speed	24
3.3.5 Tidal Constituents	27
3.3.6 Atmospheric Variables	28
3.3.7 Precipitation Rate	29
3.3.8 Summary Flow Charts for Data Preprocessing	29
3.4 Numerical Modelling	37
3.4.1 Model Description	37
3.4.2 Changes Made to the Model Code	51
3.5 Model Data Post-Processing	55

4	Satellite SST Data Analysis	58
4.1	Introduction	58
4.2	Typical Picture	58
4.3	Annual Variation	62
4.4	Summary	67
5	Sensitivity Study	68
5.1	Run T1	69
5.2	Run T2	70
5.3	Run T3	73
5.3.1	T3A	76
5.3.2	T3C	77
5.3.3	T3D	78
5.4	Run T4	79
5.5	Run T5	84
5.6	Run T6	87
5.7	Run T7	95
5.8	Run T8	98
5.9	Run T9	103
6	Full Model Runs	107
6.1	Introduction	107
6.2	F2001	111
6.3	F1950	116
6.4	F1978	120
6.5	Mixed Layer Depth and Stratification	124
7	Model Validation	137
7.1	Comparison of model to satellite SST	137
7.2	Geostrophic Currents	139
7.3	Time Averaged Currents	142
7.4	Summary	145
8	Discussion	147
8.1	Annual Variation in Dense Water Formation	147
8.2	Cascading	151
8.3	Summary	153
9	Conclusions	155
	References	159
	APPENDIX	
A	Matlab Routines used for data pre- and post-processing	163
B	List of All Changes Made to the Model Code	172
C	bostlong.for Code	182
D	Complete Set of AVHRR SST Images	Attached CD

List of Figures

2.1	Bathymetry of the Rockall Bank area	5
2.2	Location of reference points within dense water cascade. Adapted from Ivanov <i>et al.</i> (2004)	12
3.1	Diagram illustrating the calculation of size of the rotated domain.	21
3.2	Bathymetry after rotation	22
3.3	Location of the area which was smoothed and used as the model domain	22
3.4	The final bathymetry used for the model runs	23
3.5	Conversion of vector components from one coordinate system to another	26
3.6	Arrangement of tidal boundary points	28
3.7	Flow chart summarising the bathymetry data processing	30
3.8	Flow chart summarising the initial temperature and salinity data processing	31
3.9	Flow chart summarising the boundary temperature and salinity data processing	32
3.10	Flow chart summarising the surface wind data processing	33
3.11	Flow chart summarising the tidal data processing	34
3.12	Flow chart summarising the data processing for the meteorological data for the heat flux calculations	35
3.13	Flow chart summarising the precipitation data processing	36
3.14	Example arrangement of vertical s-levels	38
3.15	Arakawa B grid arrangement	39
3.16	Arrangement of points used to calculate the horizontal pressure gradient	45
3.17	Illustration of how the number of grid points in each 'ring' of the relaxation zone varies	53
3.18	Example of boundary zone indexing for relaxation zone width 3	53
4.1	AVHRR Sea Surface Temperature for December 1992, showing a temperature front between the Bank and Trough	60
4.2	AVHRR Sea Surface Temperature for February 1994, showing a temperature front between the Bank and Trough	60
4.3	AVHRR Sea Surface Temperature for January 1997, showing a distinct cold water patch	61
4.4	AVHRR Sea Surface Temperature for March 2002, showing a distinct cold water patch	61
4.5	Location of the two boxes in which the satellite SST data were analysed	62
4.6	Time series of SST in the Bank box O and the non-Bank box B	63
4.7	Time series of SST difference between the Bank box B and the non-Bank box O	63
4.8	Observed duration of the front and cold patch against mean temperature difference	65
4.9	Observed duration of the front against observed duration of the cold patch	66

5.1	T1: Surface velocity at 24 hours	69
5.2	T1: Surface velocity after 30 days	70
5.3	T2: Surface velocity at 24 hours	71
5.4	T2: Surface velocity after 30 days	72
5.5	T2: Velocity at 900m at 24 hours	72
5.6	T2: Velocity at 900m after 30 days	73
5.7	T3: Kinetic energy per unit volume	74
5.8	T3: Surface velocity at 60 days, during the kinetic energy peak	75
5.9	T3: Comparison of initial surface temperature and model output from 75 days	75
5.10	T3A: Comparison of initial temperature and model output from 92 days .	76
5.11	T3A: Kinetic energy per unit volume	77
5.12	T3C: Mean kinetic energy per unit volume for T3D compared to T3 . . .	79
5.13	T4: Location of the points for which data are plotted	80
5.14	T4: Sea surface elevation at point A	81
5.15	T4: Sea surface elevation at point B	81
5.16	T4: Surface v velocity at point A	82
5.17	T4: Surface v velocity at point B	82
5.18	T4: U velocity profiles at point (10,25) over a tidal cycle	83
5.19	T4: U velocity profiles at point B over a tidal cycle	83
5.20	T5: Location of the example point	85
5.21	T5: An example velocity profile illustrating the Ekman spiral	85
5.22	T5: Kinetic energy per unit volume compared to the mean wind speed. The thick black line is the wind speed, the thinner line is surface kinetic energy and the grey line is mean kinetic energy over the entire basin. . .	86
5.23	T6: Surface temperature at 8 November	88
5.24	T6: Surface temperature on 22 December	89
5.25	T6: Surface temperature on 31 January	89
5.26	T6: Location of the cross-sections	90
5.27	T6: Temperature along the section j=25 on 30 January	90
5.28	T6: Surface velocity on 31 January	91
5.29	T6: Velocity at 500m depth, on 31 January	91
5.30	T6: Potential density along the bottom s-level at 25 days	92
5.31	T6: Potential density along the bottom s-level at 48 days	93
5.32	T6: Location of the close up area used in Figure 5.33	93
5.33	T6: Potential density along the bottom s-level from days 47–50 showing plume moving downslope	94
5.34	T6: Potential density along the section i=130 on 30 January	94
5.35	T7: Surface salinity at 5 days	95
5.36	T7: Surface salinity at 12 days	96
5.37	T7: Surface salinity at 30 days	96
5.38	T7: Surface velocity at 30 days	97
5.39	T7: Velocity at 900m depth, at 30 days	98
5.40	T4: Sea surface elevation at point A	99
5.41	T4: Sea surface elevation at point B	99
5.42	T4: Surface v velocity at point A	100
5.43	T4: Surface v velocity at point B	100
5.44	T8: u velocity profiles at point A over a tidal cycle	101
5.45	T8: u velocity profiles at point B over a tidal cycle	102
5.46	T8: Temperature and u velocity profiles at point B	102

5.47	T9: Surface temperature at on 22 December	104
5.48	T9: Surface temperature on 1 March	104
5.49	T9: Cross section of potential density on 1 April, along the section i=130	105
5.50	T9: Potential density along the bottom s-level on 1 April	106
5.51	T9: Cross section of potential density at the end of the run, along the section i=130	106
6.1	Air temperature anomaly of winter 2001/2002	108
6.2	Wind speed anomaly of winter 2001/2002	108
6.3	Air temperature anomaly of winter 1950/1951	109
6.4	Air temperature anomaly of winter 1978/1979	110
6.5	Wind speed anomaly of winter 1950/1951	110
6.6	Wind speed anomaly of winter 1978/1979	111
6.7	Location of the Chapter 6 cross-sections	112
6.8	F2001: Cross section of potential density on 15 March 2002, along the section i=125	113
6.9	F2001: Potential density along the bottom s-level on 15 March 2002 . .	113
6.10	F2001: Potential density along the bottom s-level on 13 May 2002 . . .	114
6.11	F2001: Cross section of potential density on 13 May 2002, along the section i=125	115
6.12	F2001: Cross section of potential density at the end of the run, along the section i=125	115
6.13	F1950: Cross section of potential density on 15 March 1951, along the section i=125	116
6.14	F1950: Potential density along the bottom s-level on 15 March 1951 . .	117
6.15	F1950: Cross section of potential density on 13 May 1951, along the section i=125	118
6.16	F1950: Potential density along the bottom s-level on 13 May 1951 . . .	118
6.17	F1950: Potential density at the end of the run, on the bottom s-level . .	119
6.18	F1950: Cross section of potential density at the end of the run, along the section i=125	119
6.19	F1978: Cross section of potential density on 15 March 1979, along the section i=125	120
6.20	F1978: Potential density along the bottom s-level on 15 March 1979 . .	121
6.21	F1978: Cross section of potential density on 13 May 1979, along the section i=125	122
6.22	F1978: Potential density along the bottom s-level on 13 May 1979 . . .	122
6.23	F1978: Potential density at the end of the run, on the bottom s-level . .	123
6.24	F1978: Cross section of potential density at the end of the run, along the section i=125	123
6.25	Location of the areas sampled to analyse changes in stratification	124
6.26	Mean density profiles for the full model runs from the 'ocean box' on 1 November	127
6.27	Mean density profiles for the full model runs from the 'ocean box' on 15 November	127
6.28	Mean density profiles for the full model runs from the 'ocean box' on 1 December	128
6.29	Mean density profiles for the full model runs from the 'ocean box' on 8 February	128

6.30	Mean density profiles for the full model runs from the 'ocean box' on 6 March	129
6.31	Mean density profiles for the full model runs from the 'ocean box' on 27 March	129
6.32	Mean density profiles for the full model runs from the 'ocean box' on 9 April	130
6.33	Mean density profiles for the full model runs from the 'ocean box' on 1 May	130
6.34	Mean density profiles for the full model runs from the 'ocean box' on 6 May	131
6.35	Mean density profiles for the full model runs from the 'ocean box' on 30 June	131
6.36	Mean density profiles for the full model runs from the 'bank box' on 1 November	132
6.37	Mean density profiles for the full model runs from the 'bank box' on 30 November	132
6.38	Mean density profiles for the full model runs from the 'bank box' on 28 December	133
6.39	Mean density profiles for the full model runs from the 'bank box' on 20 April	133
6.40	Mean density profiles for the full model runs from the 'bank box' on 14 May	134
6.41	Mean density profiles for the full model runs from the 'bank box' on 24 May	134
6.42	Mean density profiles for the full model runs from the 'bank box' on 30 May	135
6.43	Mean density profiles for the full model runs from the 'bank box' on 30 June	135
6.44	Density profiles for all points within the 'Bank box' from 2 January 1979	136
7.1	F2001: January sea surface temperature from the model and from satellite data	138
7.2	F2001: February sea surface temperature from the model and from satellite data	138
7.3	F2001: March sea surface temperature from the model and from satellite data	138
7.4	March sea surface temperature from the WOA01 data set	139
7.5	Calculated geostrophic surface v component for run T3	140
7.6	Model output surface current from run T3	140
7.7	Location of the sections used in the calculation of geostrophic currents	141
7.8	Model output v velocity and calculated geostrophic v velocity from run T3 for the section j=30 on 30 June	141
7.9	Model output v velocity and calculated geostrophic v velocity from run T3 for the section j=5 on 30 June	142
7.10	Model output v velocity and calculated geostrophic v velocity from run T3 for the section i=30 on 30 June	142
7.11	Depth mean currents (top 500m) averaged over a two month period from run T3	143
7.12	Depth mean currents (top 500m) averaged over a 4 week period period for each of the full runs	144

7.13	Instantaneous surface currents from 9 April of run F2001	145
8.1	Maximum density over the Bank and offshore in F2001 and F1978	148
8.2	Mean SST from the AVHRR sample areas over the Bank and offshore areas in 1993/1994 (solid lines) and 1996/1997	150
8.3	Maximum density over the Bank and offshore in F1950 and F1978	151
8.4	Bottom density for selected days of F1978	153

List of Tables

3.1	Terms used in the heat flux equations	48
4.1	Characteristics of monthly AVHRR data over 10 years	64
5.1	Summary of the preliminary model runs	68

Acknowledgements

Thanks first of all must go to my supervisory team: to Grisha, my Director of Studies, thank you for all the guidance and support. To Sam, my second supervisor, thank you for your advice and for providing a different scientific perspective on this work.

I am grateful to Sarah Wakelin and Jason Holt who kindly agreed to host me on a visit to POL and shared their POLCOMS expertise with me; it was enormously helpful. Thanks also to Jason for providing the GOTM input parameters.

Thank you to Cecilia for helping me to get started and showing me how to compile and run POLCOMS, and for sharing your information and Matlab routines with me.

I want to thank all of my colleagues: to my office mates—Iain, Tim S, Tim P, Nigel—and our friends across the void thank you for the day to day advice, chats, and moral support. To Dima thank you for sharing your FORTRAN expertise which was vital to the success of this research.

To my friends in Plymouth both from the university and outside, thank you for the good times and for making my time here so enjoyable. I have had a fantastic time living in Plymouth and I will miss you all.

Thank you to James for your advice and support, for listening to my problems, for proof reading, but most of all thank you for persuading me to try \LaTeX ! I am sure this has saved a great deal of frustration and time.

Last but not least a huge thank you to my family for their continued support—my parents Patrick and Kathy, and my brother and sister PJ and Nicola. Thanks especially to my father for funding my studies over the years without which I would not have been able to take up this PhD opportunity.

This work was partly funded by EU-INTAS project 03-51-4620 *The Nordic Seas in the global climate system*.

Author's Declaration

At no time during the registration for the degree of Doctor of Philosophy has the author been registered for any other University award without prior agreement of the Graduate Committee.

A programme of advanced study was undertaken which included attending lectures in ocean modelling delivered and a course in teaching methods delivered by the University of Plymouth. The author participated in a research cruise and external institutions were visited for consultation purposes. Seminars were attended, work was presented at relevant scientific conferences, and several papers were prepared and submitted for publication.

The number of words in the main body of this thesis is **31,279**

Conferences Attended

- European Geosciences Union, Vienna Austria, April 2006, Poster Presentation
- Challenger Society for Marine Science, Oban Scotland, September 2006, Poster Presentation
- The Ninth Great British Research and R&D Show at the House of Commons, March 2007, Poster Presentation
- European Geosciences Union, Vienna Austria, April 2008, Poster Presentation

Publications

- O'Neill, C.K., Shapiro, G.I., Lavender, S.J., Variability in the winter cold water over Rockall Bank from remotely-sensed SST data, In Preparation for *Remote Sensing of Environment*
- O'Neill, C.K., Shapiro, G.I., Lavender, S.J., Annual variation in winter dense water formation and cascading over Rockall Bank, In Preparation for *Ocean Science*
- O'Neill, C.K., Shapiro, G.I., Lavender, S.J., 2008, Modelling dense water cascading at Rockall Bank, *Geophysical Research Abstracts, Proceedings of the EGU General Assembly, April 2008, Vienna, EGU2008-A-06612*

- O'Neill, C.K., Shapiro, G.I., Lavender, S.J., 2006, Cold water formation over Rockall Bank: A view from space, *Proceedings of the Challenger Conference for Marine Science, September 2006, Oban*
- O'Neill, C.K., Shapiro, G.I., Lavender, S.J., 2006, Cold water formation over Rockall Bank: A view from space, *Geophysical Research Abstracts, Proceedings of the EGU General Assembly, April 2006, Vienna, EGU06-A-00977*

Individual Contribution and Collaboration

The **individual contribution** of the author includes:

- Obtaining (from publicly available sources), processing and analysing remotely-sensed SST data
- Obtaining (from publicly available sources) and processing data for model input files
- Producing routines to automate pre- and post-processing of data
- Altering the POLCOMS code as necessary
- Conducting the model runs
- Processing model output and analysis of the results

The **contribution from collaborators** was:

- Director of Studies G. Shapiro¹ provided the initial rationale for the study, suggested the methodologies to use, and participated in scientific discussions regarding the interpretation of the results.
- The second supervisor, S. Lavender¹ also participated in scientific discussions, and gave guidance.
- D. Aleynik¹ helped in setting up the model, and provided computer routines to read binary data files.
- C. Enriquez² provided some routines for creating the temperature and salinity input files, and for reading output data
- S. Wakelin³ gave advice and helped in setting up the model, and provided the tidal data for boundary conditions (with permission from R. Flather).

Signed: 

Date: 04/11/08

¹University of Plymouth, UK

²formerly University of Plymouth, now CINVESTAV Unidad Mérida, Mexico

³Proudman Oceanographic Laboratory, UK

Chapter 1

Introduction

1.1 Motivation and Objectives

Rockall Bank is a large undersea bank situated in the north-east Atlantic. Along with Hatton Bank (located to the immediate north west of Rockall Bank) it separates the Rockall Trough from the Iceland Basin. The region features steep bathymetry with the depth of Rockall Trough reaching 3000m, rising to the surface at Rockall rock itself.

Winter convective mixing in this area is strong due to relatively weak stratification (Holliday *et al.*, 2000), and the mixed layer can reach 600m depth or more (Meincke, 1986). As this is deeper than a significant proportion of the bank, the water column above the bank becomes cooler than in the surrounding area, and a “cold water patch” forms (Shapiro *et al.*, 2003; Ivanov *et al.*, 2004; Mohn and White, 2007). This water has been observed moving off the slope as a dense water cascade (Huthnance, 1986; Shapiro *et al.*, 2003). Additionally, increased chlorophyll levels have been observed over the Bank (Mohn and White, 2007).

Dense water cascades are a type of buoyancy-driven current that occur when dense water formed over the continental shelf (by cooling, evaporation or freezing) descends down the continental slope (Huthnance, 1995). The first direct observation of cascading in the oceans was made by Nansen at the Rockall Bank in 1913 (Ivanov *et al.*, 2004). There are several different mechanisms for formation of the favourable horizontal density gra-

dients needed for a cascade; relevant to Rockall Bank are temperature driven cascades. Although the primary factor in temperature driven cascades is the surface response to meteorological conditions, advection of temperature and/or salinity may also play a role (either hindering or assisting the formation of cascade favourable conditions). In the case of the Rockall Bank, the cascades are driven by the response to surface cooling (Shapiro *et al.*, 2003). Dense water cascades are an important mechanism for the ventilation of intermediate waters as well as shelf-ocean exchange (e.g. Huthnance, 1995; Shapiro *et al.*, 2003).

Theoretical analysis based on heat balances (Symonds and Gardiner-Garden, 1994) and reduced-physics analytical models (Shapiro and Hill, 1997) indicate that shallow areas such as Rockall Bank can enhance dense water formation and subsequent cascading. Although there have been several observations of dense water over Rockall Bank, little is currently known about the extent to which it varies from year to year. The objective of this study was to contribute to current understanding of the formation and cascading of dense water over Rockall Bank by investigating the variability of these processes, and to test the sensitivity to meteorological conditions. We set out to achieve these goals by analysing a ten-year time series of remotely-sensed satellite sea surface temperature (SST) data, and by running various model simulations using the 3-D full-physics POLCOMS model. Modelling is useful here due to the sparse nature of in-situ measurements. Three-dimensional modelling is the natural next step to provide more detailed information following the reduced physics model developed by Shapiro and Hill (1997). The POLCOMS model was chosen as it has a number of features which make it particularly suitable for this study: the PPM advection scheme has been found to have good feature-preserving properties (James, 1996); the s-coordinate system of Song and Haidvogel (1994) allows high vertical resolution to be maintained near the bottom even with steep bathymetry; the horizontal grid used is the Arakawa (1972) B grid which is found to be more suitable than the C grid when modelling large horizontal density variations (Holt and James, 2001; James, 1986).

The questions and challenges posed during this study were:

- What is the annual variability of the cold water signal in satellite SST?

- Set up the POLCOMS model for the Rockall Bank area, and to simulate the cold water formation there
- Use the model to simulate different years with different conditions. How variable is the formation of cold water? Does cascading occur?

1.2 Outline of the Thesis

- This thesis continues in **Chapter 2** with a review of the relevant literature. This covers the properties of the Rockall Bank area, dense water cascading, a brief note on the main features of POLCOMS, and previous modelling studies involving Rockall Bank.
- **Chapter 3** describes the methodology used in this study, from initial data processing to the specifics of the model (including major changes made to the code), to the post-processing of the model output.
- **Chapter 4** outlines the results of the observational data analysis.
- **Chapter 5** contains the details and results of preliminary model runs which tested each aspect of the model.
- **Chapter 6** describes the full runs that were conducted and their results.
- **Chapter 7** compares the model output with observations and theory in order to validate the results.
- **Chapter 8** further analyses, compares, and discusses the results, linking the observational satellite data to the model results.
- **Chapter 9** provides an overall summary of the project and the results, and draws the conclusions of this thesis.
- The **Appendix** contains: full details of every change made to the model code; a list of the data processing routines that were written and used; the re-written temperature and salinity boundary routine used in the model; the complete set of AVHRR SST monthly figures (on CD).

Chapter 2

Literature Review and Background

2.1 Rockall Bank Area

2.1.1 Topography

Rockall Bank is situated off the West coast of Scotland and, along with Hatton Bank, separates the Rockall Trough (to the east of the Bank) from the Iceland Basin. The topography in this area is relatively steep with depths descending from 100 m or less over Rockall Bank to more than 2500 m in Rockall Trough. Figure 2.1 shows the bathymetry of the Rockall Bank, using ETOPO2 data downloaded from NOAA (National Geophysical Data Center; NOAA, 2005), along with the names of the main features in the area. There is in fact a small islet where the Bank reaches the surface, but at less than 30 m across this is too small to be represented by the 2 minute bathymetry data used to produce Figure 2.1 and subsequently is also too small to be included in the model domain in this study.

Various banks at the northern end of Rockall Trough restrict the flow between the channel and the surrounding ocean to depths of around 600 m in the north-east and 1200 m in the north-west (Ellett *et al.*, 1986). By contrast the southern entrance to the channel is over 3000 m deep.

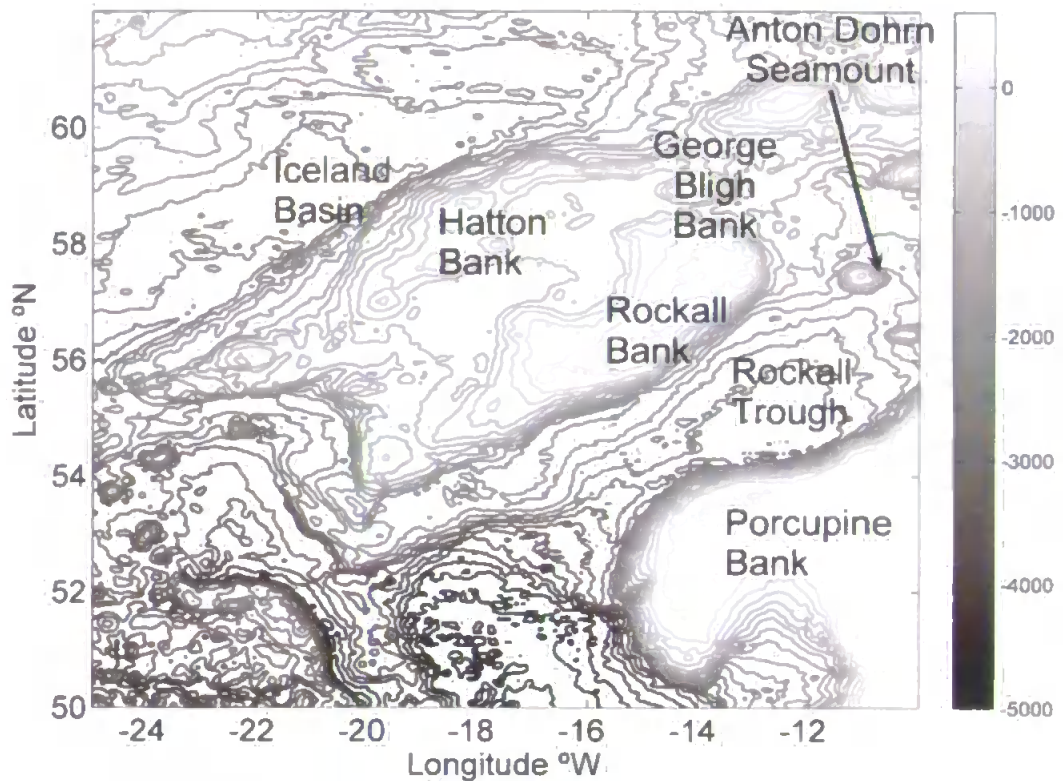


Figure 2.1 Bathymetry of the Rockall Bank area depth contours are shown every 200 m. This figure was produced from data from National Geophysical Data Center; NOAA (2005).

2.1.2 Water Masses

Rockall Trough

The predominant water masses present in the Rockall Trough (or Rockall Channel) are Eastern North Atlantic Central Water (ENAW) from the surface to around 1200 m, and Labrador Sea Water (LSW) below (Ellett *et al.*, 1986; Holliday *et al.*, 2000). ENAW is significantly more saline than the subpolar mode waters (SPMW) found in the nearby Iceland Basin. LSW may be seen in the deep waters as a salinity and vorticity minimum (Holliday *et al.*, 2000) and oxygen maximum at 1600–1900 m (Ellett *et al.*, 1986). Due to the topography of the Trough, which shallows towards the north, the LSW is prevented from escaping to the north and recirculates within the trench. Ellett *et al.* (1986) note that LSW retains its characteristic salinity minimum and oxygen maximum, suggesting regular renewal of this water; therefore a large proportion must circulate out of the Trough to the South.

To the north, Arctic Intermediate Water (AIW) and Norwegian Sea Deep Water (NSDW) are able to flow into the Trough (Ellett *et al.*, 1986). NSDW is denser than all the water masses mentioned so far, and it therefore lies below the LSW where it can be seen as a salinity maximum just below the salinity minimum associated with LSW. Dickson *et al.* (1986) note that the overflow of this water is at its maximum in summer/autumn.

North East Atlantic

Wade *et al.* (1997) found that the presence of Subarctic Intermediate Water (SAIW), which is comparatively fresh and is highly stratified, can restrict the depth of winter mixing by up to 150 m. In the North Atlantic, SAIW is predominantly found in the subpolar gyre and west of 20°W (Wade *et al.*, 1997) and is not found within Rockall Trough, leading to a weaker density gradient in the Trough (Holliday *et al.*, 2000).

2.1.3 Circulation

The Rockall Trough provides a route through which warm saline water is supplied to the Norwegian Sea (Ellett and Martin, 1973; Ellett *et al.*, 1986; Holliday *et al.*, 2000). However, as mentioned above this is limited to the upper waters since the Trough shallows to the north to a depth of 1200 m on the western side and 500-600 m to the northeast. The direction of currents in the deep water areas is extremely variable, but (Ellett *et al.*, 1986) describe some features of the mean circulation below the wind-driven surface layer: water enters the Rockall Trough from the south, to the west of Porcupine Bank, and then diverges from the slope current and flows to the northeast. Within the Rockall Trough, the mean current is anticyclonic with northward flow on the western side and southward flow in the east. In contrast, New and Smythe-Wright (2001) deduce that the circulation in the intermediate and lower waters is cyclonic in nature.

The eastern edge of the Rockall Trough features a slope-edge current (Huthnance, 1986; White and Bowyer, 1997; Gyory *et al.*, 2003). This is a northward current that is found throughout the year. The current generally increases to the north, is typically 50 km wide,

and has a mean speed which varies between 3 and 30 cms^{-1} (Huthnance, 1986). Estimates of the inshore transport range from 1.2–3.0 Sv (New and Smythe-Wright, 2001). The length and breadth of the slope current is maximum in autumn/winter (Dickson *et al.*, 1986).

The flow around Rockall Bank itself is anticyclonic (Ellett *et al.*, 1986; Huthnance, 1986) due to a combination of factors: first a Taylor column process is commonly seen at sea mounts. As the water column is forced over a Bank or sea mount, the depth of the water column is reduced. In order to conserve potential vorticity the relative vorticity must therefore also be reduced. This means the water must acquire negative, i.e. anticyclonic, rotation. Second is due to tidal resonance, which appears to be the dominant cause at Rockall Bank in particular (Mohn and White, 2007). Huthnance (1974) found that the diurnal tide at Rockall Bank is close in frequency to the natural frequency of a clockwise (anti-cyclonic) trapped wave around the Bank.

The anti-cyclonic circulation around Rockall Bank displays a seasonal signal in strength, with minimum mean flow at the north of the Bank in October/November (Dickson *et al.*, 1986). Dickson *et al.* (1986) also note that the weakening of this circulation is associated with an increase in the open ocean flow towards Rockall Bank.

2.1.4 Convection and Dense Water Formation

The weak density gradient due to the absence of SAIW in the Rockall Trough allows unusually deep winter convective mixing, with the mixed layer typically reaching depths of 600 m or more (Meincke, 1986) which leads to a strong seasonal temperature signal (Holliday *et al.*, 2000).

Meincke (1986) presents results from a cruise between Porcupine Bank, Rockall Bank, Hatton Bank, and the Hebrides shelf which took place in March 1984, and was repeated in June 1984. The observations include:

- In some areas, vertically homogeneous layers were observed to 630 m depth. These had a horizontal scale of less than 40 nm.

- At some stations the upper 600 m consisted of a sequence of homogeneous layers.
- Except for the summer heated surface layer, the weak vertical gradient (characteristic of the region) was preserved into the summer.

Meincke (1986) concluded that although the number of areas with deep convection is small and with a spatial extent of less than 40nm, over a long time period such deep convection occurs across the region. In addition, the similarity of the upper water column in the winter and summer cruises suggests that advection is low and so the water is not replaced between the seasons.

This deep convection results in differential cooling between the Bank and the deeper areas, leading to the formation of a dense "cold water patch" over the summit of the Bank which has been subsequently observed cascading downslope (Shapiro *et al.*, 2003; Ivanov *et al.*, 2004). Mohn and White (2007) used remotely-sensed sea surface temperature data to produce monthly climatologies for the Rockall Bank area. They conclude that the cold water is most clearly seen between December and March, although it is present in some form almost all year round.

2.1.5 Biological Importance

The area of cold water over Rockall Bank is coincident with higher levels of chlorophyll than in the surrounding areas (Mohn and White, 2007) indicating that the Bank has a significant impact on the local ecosystem. Submarine banks in general are recognised as important biological habitats (Mohn and White, 2007) and cold-water corals have been found at Rockall Bank (e.g. Kenyon *et al.*, 2003; Roberts *et al.*, 2003). The area is also an important fishery for the United Kingdom and Ireland (Mohn and White, 2007).

2.2 Dense Water Cascades

Dense water cascades are a type of buoyancy-driven current which occur when dense water formed over the continental shelf (by cooling, evaporation or freezing) descends down

the continental slope (Shapiro *et al.*, 2003). The first direct observation of cascading was made by Nansen at Rockall Bank in 1913.

There are numerous sites around the world where cascading is known to occur, and there are several different mechanisms for the formation of the favourable horizontal density gradients. Temperature-driven cascades occur due to surface cooling of the ocean, which has a differential effect between the shelf and ocean areas, or by advection of cold water. Salinization may facilitate cascading by several means: by advection of more saline water, by surface evaporation in hot climates, or by ice formation (leading to fresh water removal). Relevant to this study are temperature-driven cascades. Although the primary factor in temperature driven cascades is the surface response to meteorological conditions, advection of temperature and/or salinity may also play a role (either hindering or assisting the formation of cascade favourable conditions) (Shapiro *et al.*, 2003). In the case of the Rockall Bank, the cascades are driven purely by the response to surface cooling.

Cascading is a mesoscale process and generally friction is important. This means that the constraint of conservation of potential vorticity does not apply and geostrophy is broken, allowing the flow to cross isobaths (Shapiro and Hill, 1997). In addition, this moderate spatial scale means that the f -plane approximation is sufficient when analysing cascading (Shapiro and Hill, 1997).

Shapiro and Hill (1997) used a '1.5 layer' model to investigate the dynamics of cascading for some simplified cases. The model uses a homogenous layer of dense water, with an overlying upper layer (also homogeneous). Their first case was on a flat surface with no entrainment between the two layers, and no current in the upper layer; they found that the resulting propagation of dense water was a slow diffusive-like spreading. When entrainment between the upper and lower layers was included, the propagation was significantly enhanced because the entrainment enables water from the main body of the plume to steepen the dense water interface. When a current in the upper layer was added (and entrainment set to zero again), the bottom front of the dense water layer advanced twice as quickly as it did without the upper current.

The second case considered by Shapiro and Hill (1997) was that of a uniformly sloping bottom. As with the flat bottom case, without an upper layer current there is diffusive-like spreading, and the propagation is enhanced when entrainment is considered. Unlike the flat bottom case however, there is now a downslope component of reduced gravity g' which could create downslope motion within the Ekman layer (where the gravity is only partially opposed by the Coriolis force).

With the addition of the current in the upper layer (and no entrainment), the result was dependent upon the direction of the current. When the current was flowing in the same direction as the Coriolis force, a downslope (ie to the left) Ekman flow is induced which enhances the propagation of the density interface. When the upper layer current was flowing in the opposite direction, the Ekman flow that is induced is in the upslope direction which opposes, and blocks, the downslope propagation of the dense water (Shapiro and Hill, 1997).

Laboratory experiments were carried out by Condie (1995) which simulated cascading using a circular source of dense (saline) water at the centre of a rotating tank. When the tank was rotated rapidly, the isopotentials are distorted so that the gradient in fluid depth increases linearly with the radius of the tank and the system represents dense water at the top of a slope. With a continuous supply of dense water at the source area, Condie (1995) observed that the front between the two layers spread radially. The induced flows were more stable than the surface currents produced in earlier studies with similar conditions, suggesting the Ekman layer has a stabilising effect (Condie, 1995). Condie (1995) also found that when the supply of dense water was stopped, before it separates from the source region the dense fluid continues to be removed (by Ekman transport) until the entire volume is distributed across a viscous flow, which flows down slope.

Shapiro *et al.* (2003) obtain the following equations for use in analysing conditions for temperature-driven cascades:

$$\Delta T = T_c - T_s = \frac{1}{2} \frac{dT}{dz} \frac{(H_c - H_s)^2}{H_s} - \frac{\beta}{2\alpha} \frac{dS}{dZ} \frac{(H_c - H_s)^2 (H_c + H_s)}{H_c H_s} \quad (2.1)$$

$$\Delta\rho = \rho_c - \rho_s = \left(\beta \frac{dS}{dz} - \alpha \frac{dT}{dz} \right) \frac{(H_c - H_s)^2}{2H_s} \quad (2.2)$$

where subscripts s and c refer to shelf and offshore regions respectively, H_s is the depth of the shelf, H_c is the final depth of the offshore mixed layer, α and β/ρ are the thermal expansion and salinity contraction coefficients respectively.

The use of these equations assumes

- The heat fluxes are the same across the shelf/offshore regions
- There is initially a uniform mixed layer of depth H_s , the depth of the shelf
- The temperature gradient below the mixed depth is constant
- There is no horizontal advection

Shapiro *et al.* (2003) find good agreement between observed values of ΔT and $\Delta\rho$ in Rockall Trough and values calculated using Equations 2.1, and 2.2, supporting their use when studying dense water cascading in this region as well as giving further support to the idea that temperature is the driver of cascading here.

Ivanov *et al.* (2004) define a parameter r (Equation 2.3), which increases over the life-cycle of the cascade. In the early stages a cascade has large r , which reduces in value as the cascade matures.

$$r = \frac{\rho_A - \rho_C}{\rho_A - \rho_D} \quad (2.3)$$

where the subscripts A, C, and D refer to different parts of the cascade: A is the point of maximum density on the sloping bottom. C is the location on the bottom of the local density minimum between A and B (where B is the depth level with the same density as the cascading water). D is at the same depth as A but in the ambient water. This arrangement is illustrated in Figure 2.2 (adapted from Ivanov *et al.* (2004)).

Ivanov *et al.* (2004) also define a parameter h , the dimensionless thickness of the cascade, as

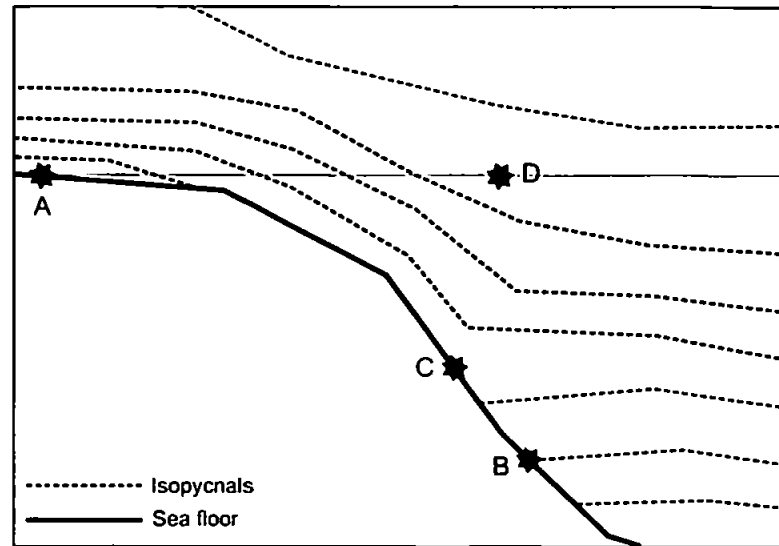


Figure 2.2 Location of reference points within dense water cascade. Adapted from Ivanov *et al.* (2004)

$$h = \frac{H_c}{|Z_A|} \quad (2.4)$$

where H_c is the thickness of the layer of dense water at the point A (depth $|Z_A|$).

Analysing data from a cascade off Rockall Bank in January 1967, Ivanov *et al.* (2004) found that $h = 1$, showing that production of dense water had started. In addition, a relatively large value of r indicates the cascade, initiated by surface cooling, is in its early stages.

2.3 Remote Sensing

One of the aims of this study was to examine remotely-sensed Sea Surface Temperature (SST) data in order to investigate how variable the surface cold water patch is. Previous work has established that the cold water over Rockall Bank can be seen in satellite data (Mohn and White, 2007) but the annual variability has not yet been studied. Satellite data are useful as they are available over a wide spatial area and temporally on timescales from monthly to daily composite pictures. This allows a more direct comparison between different dates than is often the case with in situ data, which are typically patchy in both time and space. The limitations of using satellite data include the limited date range,

as the technology is relatively recent. It is also only possible to measure the surface temperature.

The data analysed by Mohn and White (2007) were Advanced Very High Resolution Radiometer (AVHRR) data. The AVHRR sensor measures infrared radiation in the range 10–12 μm which correlates well with ocean temperature (Robinson, 1997). The major disadvantage of AVHRR is that clouds are not transparent to infrared, so will cause gaps and errors in the data. The spatial resolution obtained is around 1 km, or 4 km in low resolution mode.

SST may also be estimated by microwave radiometry. Because the wavelengths used are relatively long (1.5–300 mm), microwaves are not scattered by clouds (Robinson, 1997) and therefore are able to provide greater coverage of the ocean than the AVHRR method. However, it should be noted that raindrops are large enough to scatter microwaves (Maul, 1985). Due to the weaker signal in this wavelength range the sensor needs a wider field of view, and therefore the spatial resolution is not as high as that of AVHRR (Robinson, 1997).

For both data types, the raw satellite data must be calibrated and corrected using estimates of parameters such as atmospheric absorption (Maul, 1985) and assumptions for the link between temperature and the level of infrared or microwave radiation emitted.

2.4 Modelling

2.4.1 POLCOMS

The main focus of this study is numerical modelling of the Rockall Bank. The model used here is the Proudman Oceanographic Laboratory Coastal Ocean Modelling System (POLCOMS). POLCOMS is a three-dimensional model which has been developed over many years (e.g. James, 1986, 1996; Holt and James, 1999). It has been validated for various parts of the world ocean such as the Black Sea (Enriquez, 2005), the Persian

Gulf (National Centre for Ocean Forecasting, 2008), and the European continental shelf (Holt and James, 2001, 2006). It is also used operationally by the UK Met Office for the European Shelf area, with a nested high resolution North Sea grid. It has not yet been applied to the Rockall Bank area. POLCOMS is designed to be able to cope with regions of steep bathymetry, combining shelf areas with deeper ocean. This is clearly a useful feature when modelling the Rockall Bank area—the depth of the model domain used in this study ranged from just over 100 m depth to almost 2800 m. Notable features of POLCOMS, which will be explained in more detail in Chapter 3, include:

- The advection scheme used is the Piecewise Parabolic Method (PPM). This method has good feature-preserving properties, making it an ideal choice for modelling baroclinic features such as fronts (Holt and James, 2001, and references therein).
- Unlike many shelf-sea models such as POM and NEMO Shelf, which use the Arakawa (1972) C grid, POLCOMS uses the B grid. This grid is more commonly used in deep water models, but is useful here as it does not require the Coriolis term to be averaged. This makes it suitable for the study of horizontal density gradients, and it prevents the dispersion of fronts which may otherwise occur. The minor disadvantage of using the B grid is that it does require the averaging of velocity components for the continuity and scalar equations.
- POLCOMS uses the modified σ -coordinate system of Song and Haidvogel (1994). This system allows high vertical resolution to be maintained at the surface and at the bottom, even in regions of steep topography.

2.4.2 Modelling of Rockall Bank

An area focussing on Rockall Bank and Porcupine Bank has been previously modelled (Mohn and White, 2007) using the S-coordinate Primitive Equation Model (SPEM). Mohn and White (2007) modelled a highly idealised case, initialised from late spring/early summer hydrographic conditions and featuring no wind or seasonal forcing, in order to model the distribution of Chlorophyll over the two Banks. Tracers were released to map

the retention of particles over the Banks. The results included a residual anti-cyclonic circulation around Rockall Bank centred on the 500 m isobath and with a speed up to 20 cm s^{-1} . The tracer results showed that a large proportion of particles were retained by Rockall Bank, with 60% of the initial concentration over the Bank remaining after 90 days.

New and Smythe-Wright (2001) used a model based on the Miami Isopycnic Coordinate Ocean Model (MICOM) to model the Atlantic ocean, including Rockall Bank, with a grid resolution of $1/3^\circ$. They use an isopycnic model, where the vertical layers are situated on levels of constant density, in order to track movement of different water masses. Unlike the simulations of Mohn and White (2007), New and Smythe-Wright (2001) include both wind and heat flux forcing within their model. The data used are climatological means. New and Smythe-Wright (2001) find that, due to the discretisation of the isopycnal levels, the model significantly overestimates the depth of the mixed layer in the Rockall Trough. Whereas observations typically put the depth of the mixed layer at 600 m or similar (e.g. Meincke, 1986), the New and Smythe-Wright (2001) model predicts a mixed layer of 1200–1300 m depth. In contrast to previous observations and modelling, the results of New and Smythe-Wright (2001) (which represent spring conditions) show a cyclonic circulation in the upper water around Rockall Bank. However, they conclude that overall the model results are consistent with observations. New *et al.* (2001) use the same model as well as a z -coordinate model based on GFDL-MOM (Geophysical Fluid Dynamics Laboratory Modular Ocean Model) and a σ -coordinate model based on SPEM and model the same Atlantic grid. The z and σ models provide a more realistic mixing depth, and New *et al.* (2001) conclude that overall the results from the three different models are in broad agreement with observations.

Chapter 3

Methodology

3.1 Introduction

The methodology used in this study can be divided into four main areas:

- Processing and analysing remotely-sensed sea surface temperature data
- Producing data input files for the model runs
- The POLCOMS model
- Processing the model output

This chapter describes fully the methods and materials used in each of these areas in turn.

3.2 SST Satellite Data

There were two main publicly available sources of remotely sensed SST which were considered for this work: microwave data from REMSS (Remote Sensing Systems, 2003) and infra-red data from NASA (NASA Physical Oceanography Distributed Active Archive, 2003). Infra-red data were available as AVHRR data which have a high spatial resolution of approximately 4 km. The disadvantage of these data is that AVHRR is affected by cloud cover, which is prevalent in this region especially during winter. Microwave data

have the advantage of being unaffected by cloud cover, but were available at a significantly lower resolution of around 25 km. It was decided that the AVHRR data were most suitable for this study. This was due to the higher resolution, and also the microwave data displayed more short timescale variation from diurnal surface warming which would mask changes in the dense water formation.

Version 5 AVHRR data were obtained from NASA (NASA Physical Oceanography Distributed Active Archive, 2003). Matlab was used in the processing of the satellite data, and details of the routines that were written and used for this work are found in Appendix A.

AVHRR monthly composites were downloaded for the period October 1992 to December 2003, providing a long time series of data covering 10 winters. The data are provided as integers which need to be converted to temperature °C. The conversion used was provided by an information file from the same source as the data and is performed as

$$\text{SST} = 0.075D - 3.0 \quad (3.1)$$

where SST is the new value in °C and D is the original integer value. Bad data (i.e. those affected by clouds) were then masked by ignoring all values less than 7 °C. This value was chosen, after inspecting images of the unmasked data, as a value which would not remove real data points from the Bank area but would remove a large amount of the cloud-affected data. Both ascending (day-time) and descending (night-time) data were processed, and then combined together by taking the average of the two data sets so as to fill in some of the gaps that were caused by the clouds. This averaging was performed after the conversion to °C mentioned above. It is these combined data that are used in this study. When using day time data it is necessary to be careful that diurnal warming of the sea surface is not adversely affecting the results. From inspecting the two different data sets here it was felt that this was not a problem in this case, and both day and night data were suitable to be combined in this way.

Images were produced for each month, and the data analysed using visual inspection of

the plots as well as Matlab routines to quantify temperature differences. The results will be presented in Chapter 4 with some representative images. The full set of images produced can be found in Appendix ?? on the attached CD.

Weekly (8-day) composite AVHRR data were also initially downloaded and processed in the same way. However, it was decided not to use these data in the final analysis as the cloud cover was so extensive in these shorter composites that not enough useful data could be gathered.

3.3 Model Input Data Processing

In order to run in its simplest form, POLCOMS requires bathymetry, complete initial temperature and salinity fields and, with open boundaries as we have here, boundary temperature and salinity data to cover the length of the run. The initial density and boundary density are three-dimensional fields, and data are required for every grid point at every depth level in the model domain. Additional files needed for a full run are tidal constituent data, wind speeds, and meteorological data to calculate the heat fluxes (these are atmospheric pressure, relative humidity, air temperature, and cloud cover). As discussed in §3.4.2 below, the heat flux routines also require the latitude and longitude coordinates of each point. Full runs are conducted from a warm start, using the output of a 'geostrophic adjustment' spin-up run (where the only forcing comes from the initial density field) as the input; this provides initial currents that are compatible with the initial density structure.

The majority of the data processing was conducted using Matlab, and various routines were written (Appendix A) to automate the steps described here. Visual summaries of the data processing methods are outlined in the flow charts of Figures 3.7 to 3.13.

3.3.1 Bathymetry

The bathymetry of the Rockall Bank area was obtained from the National Oceanic and Atmospheric Administration (NOAA) National Geophysical Data Center (NGDC) Geo-

physical Data System (GEODAS) "Design-a-grid" website (National Geophysical Data Center; NOAA, 2005). The bathymetry is from the ETOPO2 2 minute database and has a resolution of 2 minutes in both longitude and latitude which corresponds to a latitudinal resolution of around 4 km and a longitudinal resolution of around 2 km.

The bathymetry in this area (see Figure 2.1 in the literature review) is very steep in places and is also very rough. Steep bathymetry can be problematical in numerical modelling due to two main causes of error in the calculation of the horizontal pressure gradient: First, truncation errors can arise due to the subtraction of terms that are similar in magnitude. This is especially important in topography-following coordinate models and may be alleviated by careful choice in the method of calculation. §3.4.1 on page 44 provides more details. The second source of error is the "hydrostatic inconsistency". This arises if the following condition is not met (Haney, 1991), leading to a non-convergent solution:

$$\left| \frac{\sigma}{D} \frac{\delta D}{\delta x} \right| \delta x < \delta \sigma \quad (3.2)$$

where D is the ocean depth and δD the variation in depth across the grid box, and δx is the horizontal grid size. σ is the terrain-following vertical coordinate and is related to the standard z coordinate by the relation $\sigma = \frac{z}{D}$ and varies between 0 at the surface and -1 at the sea bed. When Equation 3.2 is satisfied it guarantees that a given sigma level that is above another will remain above it within the space of a horizontal grid point (Haney, 1991). This second source of error can be reduced by reducing the topography gradient, generally by smoothing the data (Computational Science Education Project, 1995).

In addition to smoothing the bathymetry, it was decided to rotate the grid so that it is aligned with the main axis of the Bank. This also allows the domain to be cropped closer to the bank without including a large area of the Rockall Trough, thus decreasing the grid size and therefore the computing power needed. The equations of motion remain the same.

The rotation of the grid was achieved by multiplying each pair of latitude/longitude

coordinates by the rotation matrix L , giving a new pair of coordinates in the new rotated system:

$$L = \begin{vmatrix} \cos(\theta) & \sin(\theta) \\ -\sin(\theta) & \cos(\theta) \end{vmatrix} \quad (3.3)$$

where θ is the angle of rotation, in this case 26° . The transformation was performed as follows:

1. The coordinate of the south western point of the domain (25°W , 50°N) was first subtracted from the coordinates of each point (meaning the origin is now the centre of rotation), and the position vector then multiplied by L to give the position in the new coordinate system. These new coordinates X and Y are related to the longitude x and latitude y by $X = (x + 25) \cos(26^\circ) + (y - 50) \sin(26^\circ)$ and $Y = -(x + 25) \sin(26^\circ) + (y - 50) \cos(26^\circ)$ (note that here longitude x is negative as all points are west of 0°).
2. Using the Matlab function *griddata* the bathymetry was linearly interpolated from the previous points onto a uniform grid in the new coordinate system. The grid size used was chosen such that the resolution of the domain (in terms of grid points) would remain approximately at its original size, as shown in Figure 3.1. Figure 3.2 shows the bathymetry after being rotated. We can see that the southern edge of the Bank is now aligned in the X direction.
3. The rotated bathymetry was then smoothed, using a moving average, and cropped in Surfer. This smoothing method filters the data by taking the average of all the points within a specified ellipse radius of a grid point. In this case the value 0.2 was used for both the semi-major and semi-minor axis. The grid was at the same time cropped closer to the bank, and the new grid size changed to 150×55 points, corresponding to a grid resolution of approximately 4km in the X direction and 6km in the Y direction. The limits used were: X 6–15, Y 0.25–3.5

The resulting bathymetry file was then used both as the input for the model runs and for calculating the position of the s -coordinate levels in creating the temperature and salinity files. POLCOMS also requires a mask file, which in this case is simply an array

of ones, as there is no land in the final cropped domain. The position of the cropped region that was used is shown by the box in Figure 3.3; the final grid after rotation and smoothing is shown in Figure 3.4.

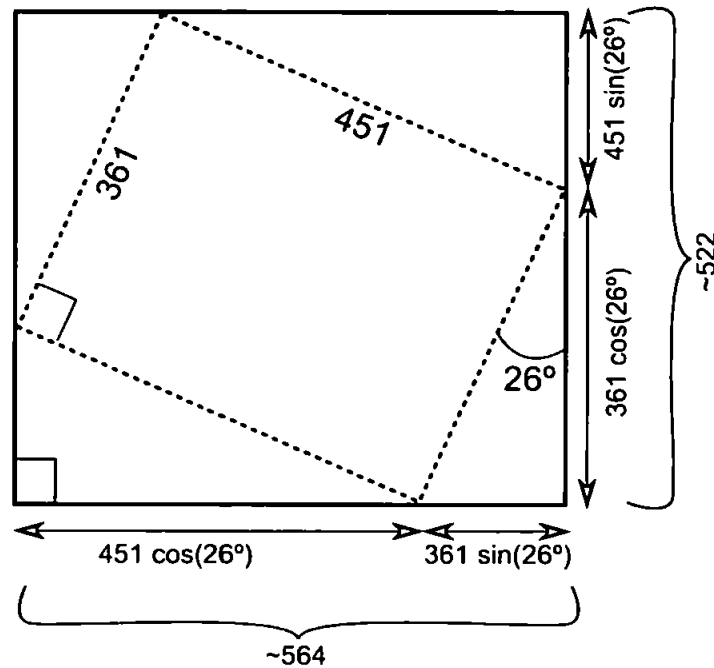


Figure 3.1 Diagram illustrating the calculation of size of the rotated domain. The dashed box represents the original coordinate system, and the solid box the new coordinate system, with the dashed domain rotated into it. The numbers represent the number of grid points.

3.3.2 Initial Temperature and Salinity

POLCOMS requires a complete initial temperature and salinity field, with data for every grid point at every depth level (in s-coordinates). The World Ocean Atlas 2001 (Boyer *et al.*, 2005) WOA2001 was chosen as the source as it has good spatial coverage and the model requires data for every point in the domain. Unfortunately WOA2001 monthly climatology data are available only to a depth of 1500 m whereas the deepest part of the model domain is 2780 m. The data were therefore supplemented with the WOA2001 seasonal climatology, downloaded from the same source, which are available to 5500 m depth. The data were allocated by taking December, January, and February as Winter; March, April, and May as Spring; June, July, and August as Summer; September, October, and November as Autumn.

The input data for the model were created with the following method, modelled on the

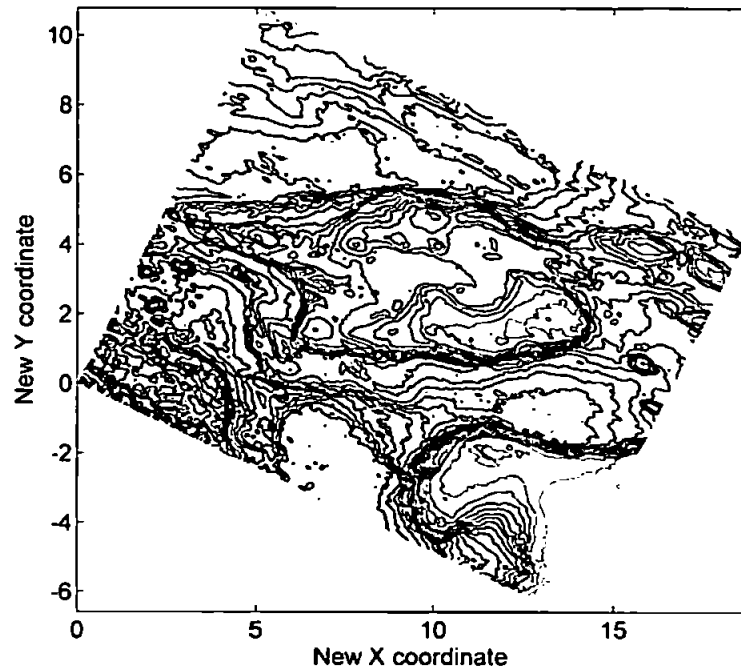


Figure 3.2 Bathymetry after rotation; contours every 200 m. Note that the origin of the new coordinate system is at the SW corner of the data. Recall that the new X and Y coordinates are related to longitude x and latitude y by $X = (x + 25) \cos(26^\circ) + (y - 50) \sin(26^\circ)$ and $Y = -(x + 25) \sin(26^\circ) + (y - 50) \cos(26^\circ)$.

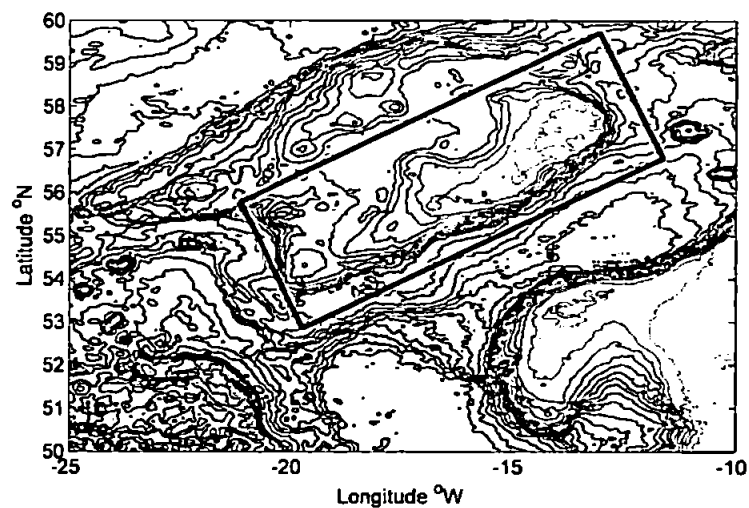


Figure 3.3 Location of the area which was smoothed and used as the model domain; contours every 200 m. Although the domain that was extracted is rectangular in the new coordinates, it does not appear exactly square when plotted against latitude and longitude.

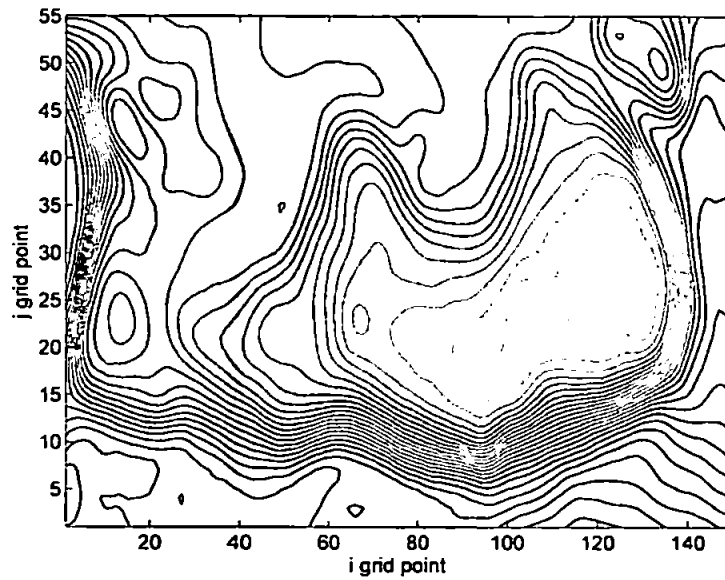


Figure 3.4 *The final bathymetry used for the model runs; contours every 100 m. The model grid is not shown for clarity, but there are 150 i points and 55 j points.*

procedure used in previous work using POLCOMS (Enriquez, 2005):

1. The temperature and salinity data for the relevant month(s) are fitted to the rotated domain using the same method as described for the bathymetry above.
2. The rotated data are interpolated in Surfer using a point kriging method (Cressie, 1993) to fill in any gaps. This method of interpolation is part of the least squares family, and gives good results here.
3. This process is repeated for the seasonal data files, though with only the necessary depth levels extracted (1750 m, 2000 m, 2500 m, and 3000 m). Because data at these depths are sparse, these files are interpolated first and then fitted to the rotated grid.
4. The interpolated, gridded files are combined to provide data down to 3000 m depth over the entire domain.
5. The z depth is calculated for each point in the model's XYs-coordinate domain as follows: the location of the s-levels are calculated and then these values (always between 0 and 1) are multiplied by the total depth at the grid point to find the depth of that s-level in the z coordinate space.

6. The temperature and salinity are linearly interpolated from their original z levels onto the new range of points which correspond to the s -coordinate levels.
7. The monthly files are designed to represent the 15th of the month. The model runs in this study all begin on 1 November, so the initial temperature and salinity is created by linearly interpolating between the October and November data.

3.3.3 Boundary Temperature and Salinity

In order for the sponge relaxation scheme (see §3.4.1) to be used at the open boundaries it is necessary to provide the model with temperature and salinity data for the boundary zone (4 points wide) over the entire length of the run. The boundary zone data were extracted from the final monthly data files created in the initial temperature and salinity processing (ie the stage just before the data were interpolated to the model start time). These data were rearranged to follow the order of the boundary points, in a clockwise spiral, and were written to the file for the model. In order for the model to be able to correctly interpolate in time between the monthly data, an additional file was created which contains the time in days since the start of the run of each of the monthly data sets. The first data set must be from before the start of the run, in order to be able to interpolate to the model start time, and therefore the first time label is negative.

3.3.4 Wind Speed

NCEP/NCAR reanalysis wind data were downloaded from the Climatic Research Unit (CRU) at the University of East Anglia (UEA) (Harris, 2003) [2001/2002 data] and the NOAA Climate Diagnostics Center (CDC) (Kalnay *et al.*, 1996; Physical Sciences Division NOAA/ESRL, 2007) [1950/1951, 1978/1979 data]. The resolution is approximately 2° and data are available 4 times daily. The data from NOAA took the form of NetCDF files and the CSIRO NetCDF Matlab interface (Mansbridge *et al.*, 1997) was used to open these.

As discussed in the bathymetry section above, it was necessary to fit the data to the new

domain. However, this was slightly more complicated than with the scalar bathymetry and temperature/salinity data because wind is a vector. The original data take the form of meridional and zonal components, but for the rotated domain the components must instead be parallel and perpendicular to the new XY coordinate system. This is achieved in two stages: first fitting the data to the new grid points and then rotating each pair of components to the new orientation. The methodology is as follows:

1. First, as with the bathymetry data, the original coordinates of the wind data are multiplied by the rotation matrix described above.
2. The data are then linearly interpolated (each component separately) onto the same grid points as the final smoothed bathymetry domain.
3. This results in a data field in which the grid points are in the correct positions, but in which the components' directions are not those of the coordinate system. To calculate the components in the directions parallel to the new X and Y coordinates the wind vector for each point was multiplied by the rotation matrix L . Figure 3.5 below and the following text demonstrates that this method does correctly give the new components of the same vector.

Considering Figure 3.5 we see that the components of the wind vector \mathbf{W} may be expressed in the old and new coordinate systems as follows:

$$\begin{aligned} u &= |\mathbf{W}| \cos \phi \\ v &= |\mathbf{W}| \sin \phi \end{aligned} \tag{3.4}$$

$$\begin{aligned} x &= |\mathbf{W}| \cos(\phi - \theta) \\ y &= |\mathbf{W}| \sin(\phi - \theta) \end{aligned} \tag{3.5}$$

Now, multiplying the original vector components u and v by the rotation matrix L (Equation 3.3) we get

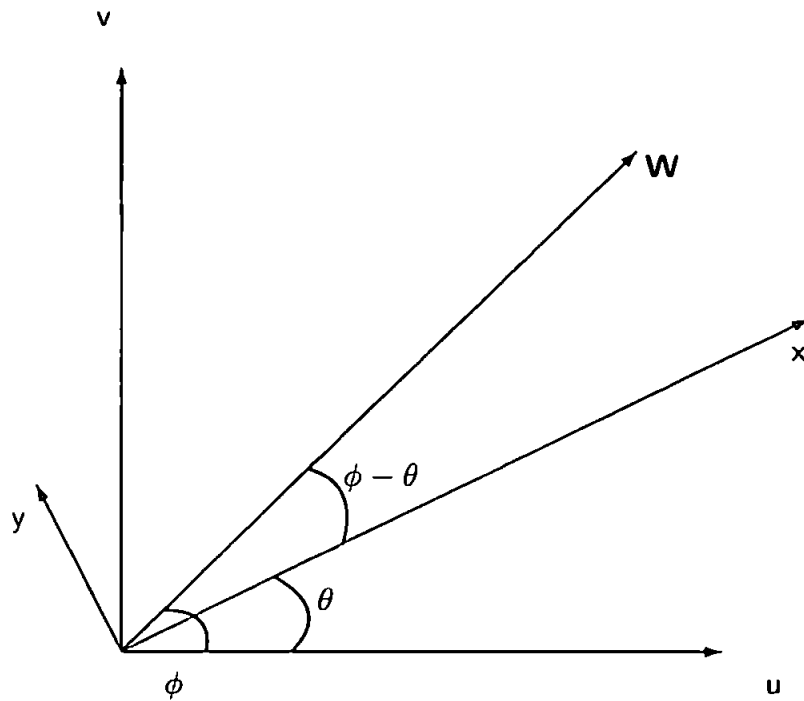


Figure 3.5 Conversion of vector components from one coordinate system to another. u and v are the original components of vector \mathbf{W} ; x and y are the components in the new directions

$$\begin{aligned}
 \begin{vmatrix} x' \\ y' \end{vmatrix} &= \begin{vmatrix} \cos \theta & \sin \theta \\ -\sin \theta & \cos \theta \end{vmatrix} \times \begin{vmatrix} u \\ v \end{vmatrix} \\
 &= \begin{vmatrix} u \cos \theta + v \sin \theta \\ -u \sin \theta + v \cos \theta \end{vmatrix}
 \end{aligned} \tag{3.6}$$

which gives (using Equation 3.4)

$$x' = |\mathbf{W}| \cos \phi \cos \theta + |\mathbf{W}| \sin \phi \sin \theta$$

$$y' = -|\mathbf{W}| \cos \phi \sin \theta + |\mathbf{W}| \sin \phi \cos \theta$$

and thus

$$x' = |\mathbf{W}| \cos(\phi - \theta)$$

$$y' = |\mathbf{W}| \sin(\phi - \theta)$$

We see then that x' and y' are identical to the expressions for x and y in Equation 3.5 and therefore the multiplication by the rotation matrix has correctly given the new component

pair.

3.3.5 Tidal Constituents

The tidal elevation and currents in the model are proscribed at the boundary points, and are calculated within POLCOMS from constituent data. These constituents must be given for every boundary point. In harmonic analysis the total tide is approximated by a finite (in this case there are 15) series of trigonometric curves. The data required to represent these 15 harmonic constituents are the amplitude and phase speed (i.e frequency), and these are required for elevation, u velocity, and v velocity in turn. POLCOMS requires these constituent parameters for each boundary grid point.

The necessary tidal data (Flather, 1981) were obtained, with the permission of Roger Flather, from Proudman Oceanography Laboratory. Because the velocity components are meridional/zonal components it was necessary to rotate them so that they are instead the parallel and perpendicular components of the new rotated grid system. This was done in the same way as the wind data treatment described above (though note that in the case of the tidal data it is not necessary to fit the data to the grid first as the data were provided already on the correct boundary points). The elevation boundary points are b (scalar variable) points, as with the temperature and salinity points. Because the four sides of the border are treated separately rather than as a continuous circle, the four corner points are each included in two boundaries and so the total number of boundary points is four greater than it was for the outer temperature points. The number of elevation boundary points is therefore simply $2(l + m)$ where l and m are the number of horizontal points in the model grid. The velocity boundary points must be proscribed on u (vector) points, which are displaced half a grid square to the south west of the b points. In addition, there is an extra row and column of points to the north and west respectively (meaning that the u boundary points are all outside the b points), giving a total of $2(l + 1 + m + 1)$ points. The order of the boundaries is the same as for the elevation points. This arrangement is shown in Figure 3.6.

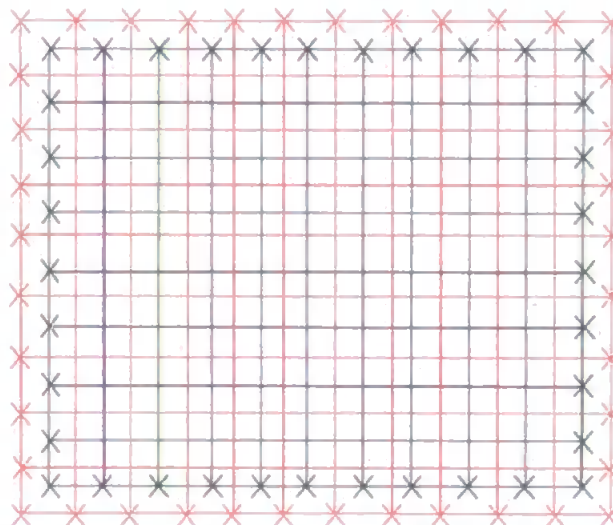


Figure 3.6 Arrangement of tidal boundary points. Black crosses are elevation boundary points, grey crosses are velocity boundary points. Note that there are 11 elevation points and 12 velocity points on each side.

3.3.6 Atmospheric Variables

There are four additional variables required for POLCOMS to calculate the incoming solar radiation and outgoing longwave radiation which in turn are used in the calculation of heat flux. These are: atmospheric pressure, air temperature, relative humidity, and percentage cloud cover. Six hourly data for all these variables were downloaded from NOAA CDC (Kalnay *et al.*, 1996; Physical Sciences Division NOAA/ESRL, 2007). These were available as NetCDF files and the CSIRO NetCDF Matlab interface (Mansbridge *et al.*, 1997) was used to read the data.

The data were fitted to the rotated grid in the same manner as the other scalar variables. The air temperature data were originally in K and were converted to $^{\circ}\text{C}$ before being written to the model input files. The air pressure data units were Pa, and this was converted to mb within the model code by dividing by 100 after the data were read in.

The heat flux calculation also requires the latitude and longitude of each grid point in order to estimate the position of the sun. For reasons described later in the modelling section (§3.4.2) these values are also provided by external files. To calculate these values, the new XY coordinate of each point was multiplied by the rotation matrix as described above, but with the angle set to -26° , and the coordinates of the SW-point were added;

this has the effect of performing a 'backwards' rotation and provides the latitude and longitude of each point.

3.3.7 Precipitation Rate

6-hourly precipitation data were downloaded from NOAA CDC (Kalnay *et al.*, 1996; Physical Sciences Division NOAA/ESRL, 2007) and were fitted to the rotated grid in the same way as the other input data. Again the CSIRO interface (Mansbridge *et al.*, 1997) was used to open the NetCDF files. Before being written to the file for the model, the data were divided by 1000 to convert the units from mms^{-1} to ms^{-1} .

3.3.8 Summary Flow Charts for Data Preprocessing

Figures 3.7 to 3.13 are flow charts summarising the data preprocessing procedures that were described in this Chapter. Initial data and the subsequent manipulated data are shown as rectangular boxes, and processes are shown in diamond boxes. Each chart ends with the model files being written and then sent to the model. More details of the particular Matlab routines that were used for each step are found in Appendix A.

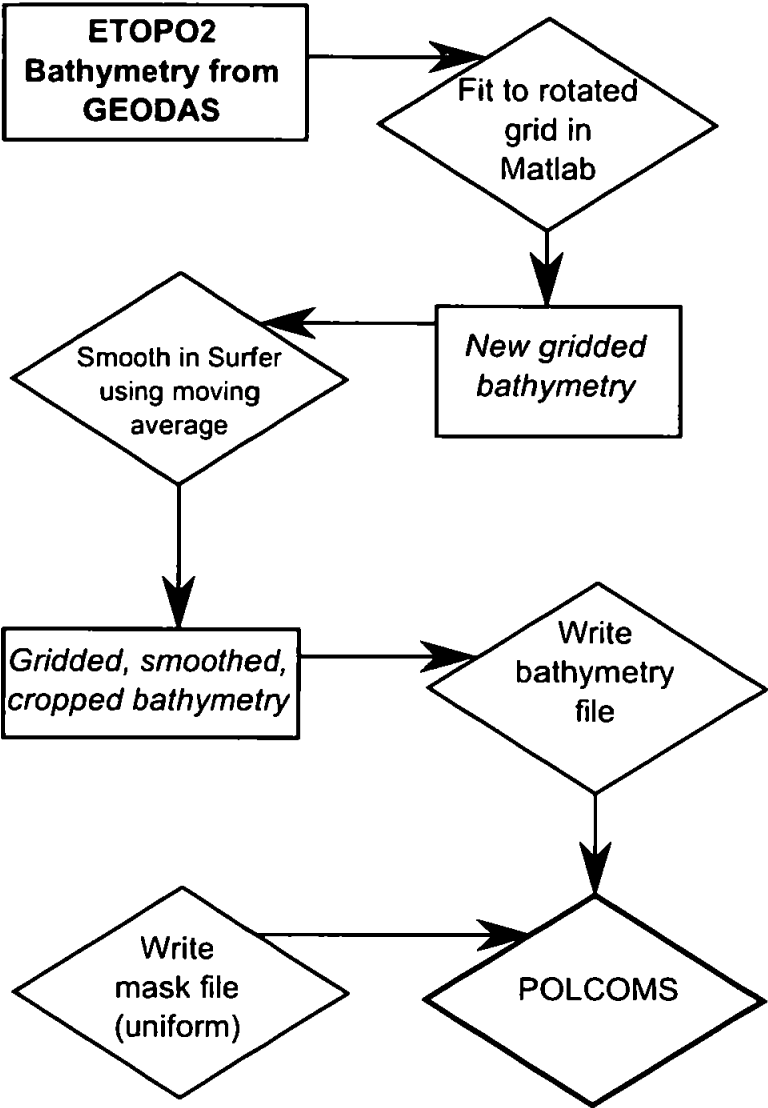


Figure 3.7 Flow chart summarising the bathymetry data processing.

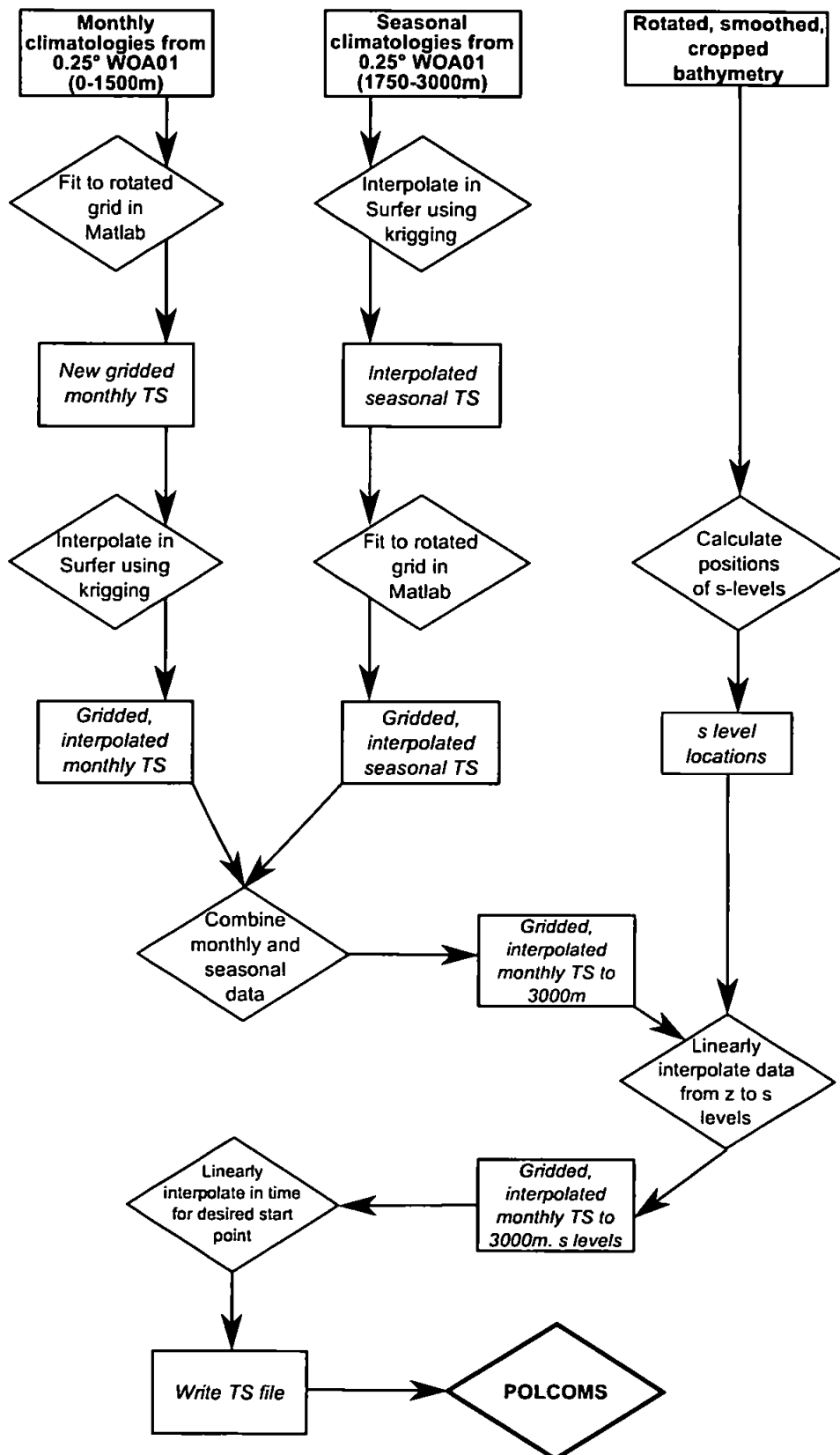


Figure 3.8 Flow chart summarising the initial temperature and salinity data processing.

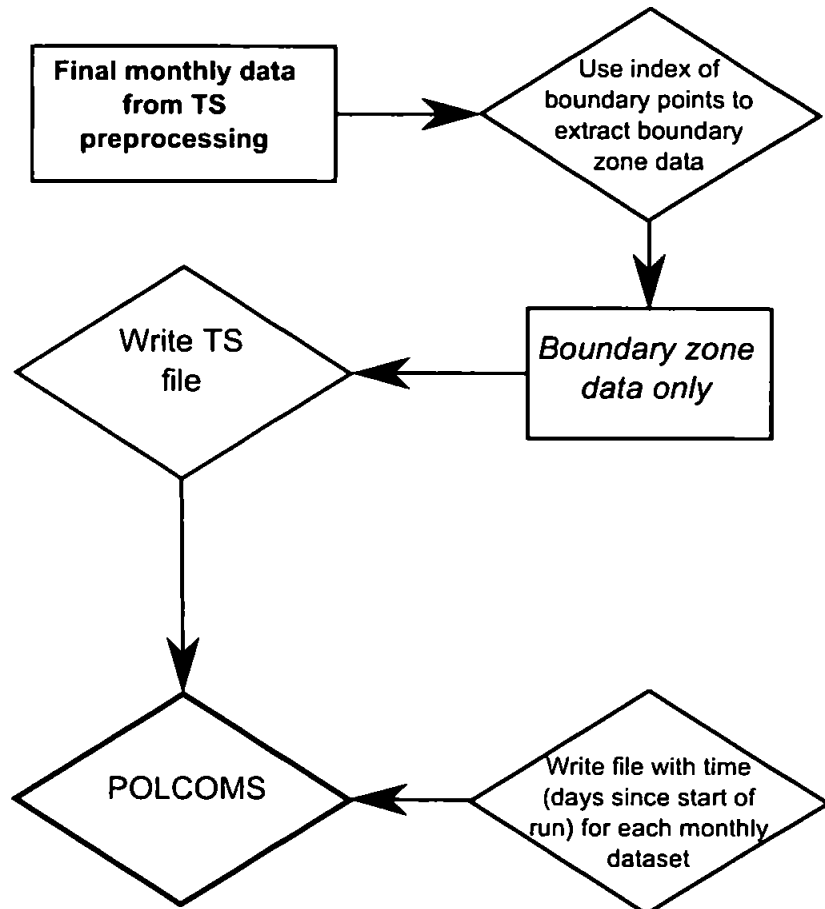


Figure 3.9 Flow chart summarising the boundary temperature and salinity data processing.

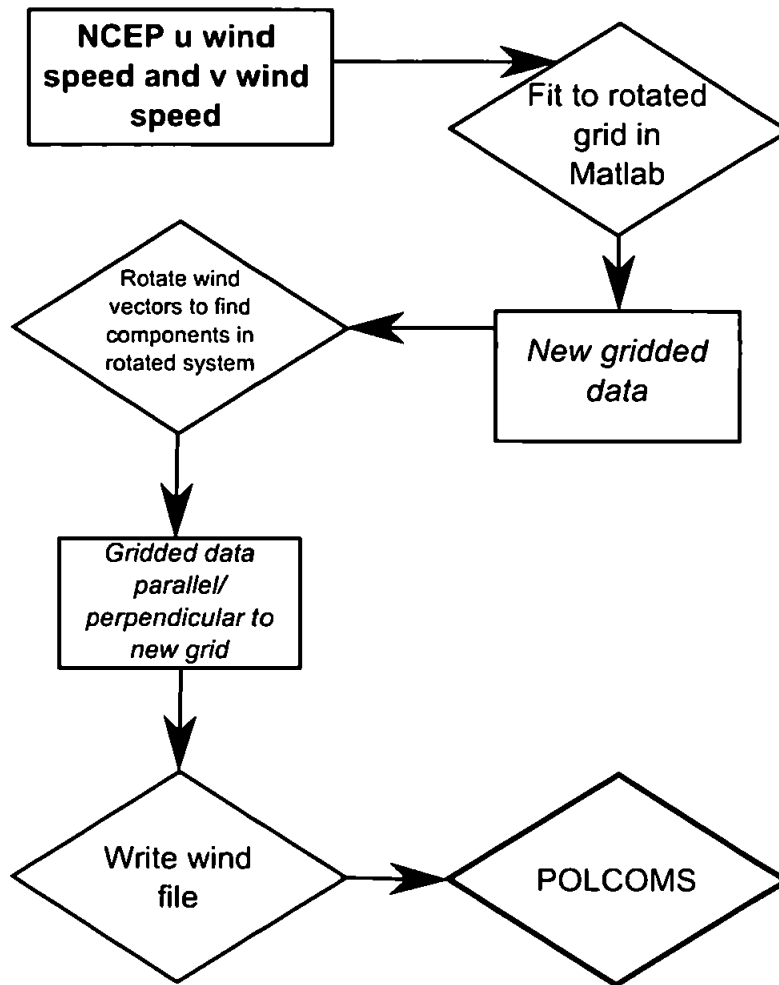


Figure 3.10 Flow chart summarising the surface wind data processing.

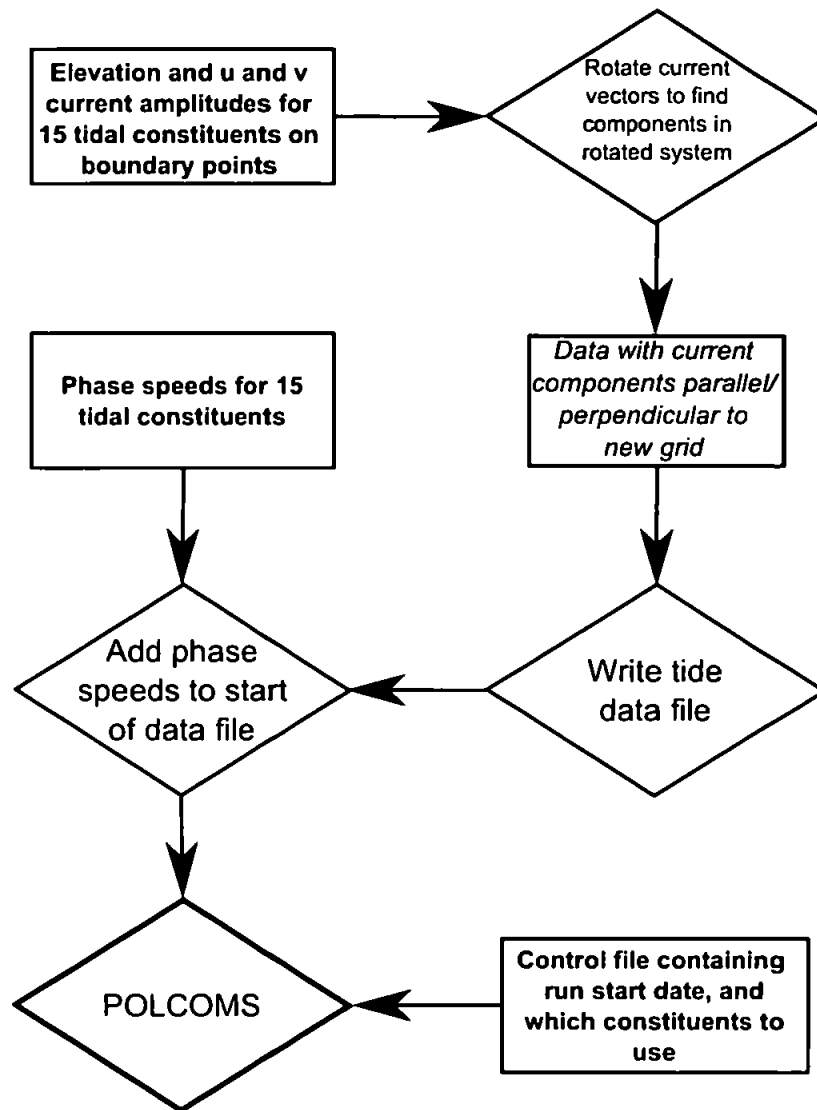


Figure 3.11 Flow chart summarising the tidal data processing.

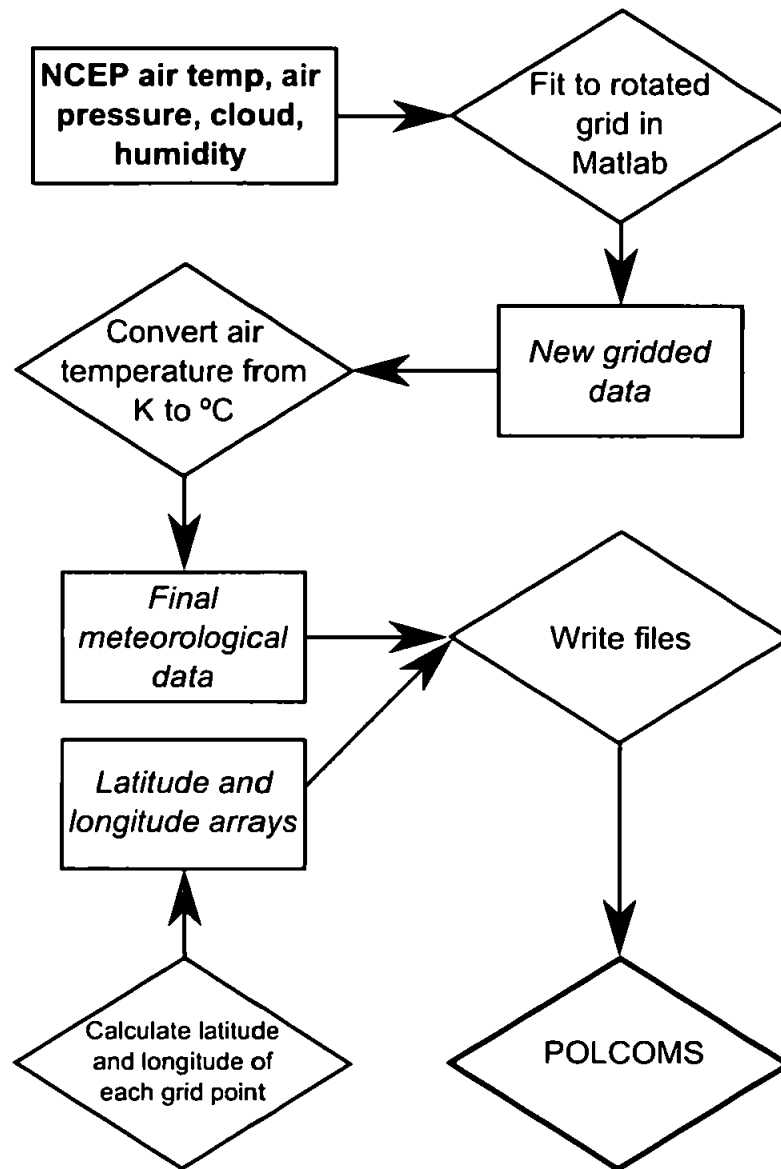


Figure 3.12 Flow chart summarising the data processing for the meteorological data for the heat flux calculations.

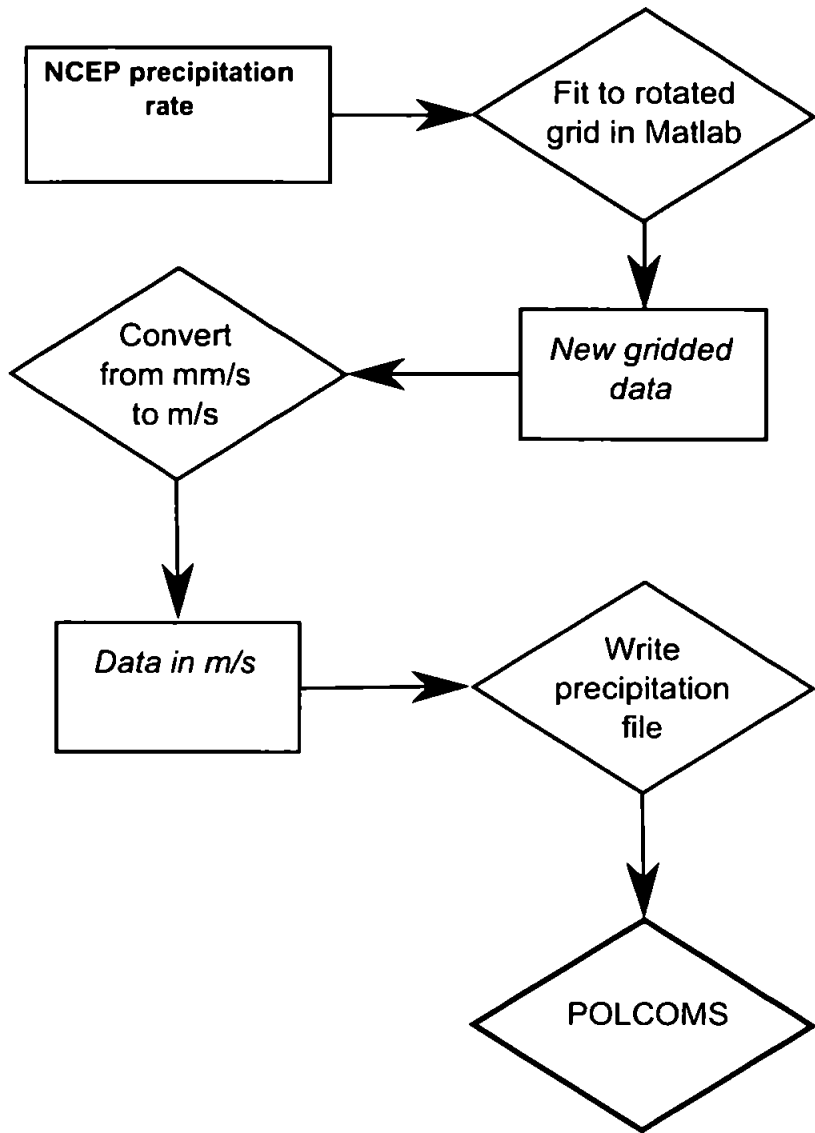


Figure 3.13 Flow chart summarising the precipitation data processing.

3.4 Numerical Modelling

3.4.1 Model Description

Introduction

The model chosen for this work was the Proudman Oceanographic Laboratory Coastal Ocean Modelling System, POLCOMS (Holt and James, 2001; POL, 2005). It was chosen due to key features such as the choice of coordinates, advection scheme, and horizontal pressure gradient which make it particularly suitable for modelling areas with steep bathymetry or large horizontal density gradients. This section will fully describe the equations and methods used by each physical aspect of the model.

Coordinate System and grid

POLCOMS uses a spherical polar coordinate system comprising χ (x direction) and ϕ (y direction) in the horizontal and σ in the vertical. The spacing of the σ levels is allowed to vary in the horizontal in a way based on the general coordinate system used by Song and Haidvogel (1994). The transformation used is as follows:

$$\begin{aligned}\sigma &= S_k + \frac{h - h_c}{h} [C(S_k) - S_k] & h > h_c \\ &= S_k & h \leq h_c\end{aligned}\tag{3.7}$$

where S_k are evenly spaced levels between -1 and 0 , h is the total depth at the point, and h_c is a critical water depth. In this study 300 m was used as the critical depth, so at points where the total water depth was less than this evenly spaced vertical levels were used. $C(S_k)$ is a set of curves which give the deviation from standard σ levels and is defined as:

$$C(S_k) = (1 - B) \frac{\sinh(\theta S_k)}{\sinh(\theta)} + B \frac{\tanh[\theta(S_k + 0.5)] - \tanh(0.5\theta)}{2 \tanh(0.5\theta)} \quad (3.8)$$

B is a bottom control parameter, which takes a value between 0 and 1; θ is a surface control parameter which has the range 0–20. As θ approaches 0 the coordinate system becomes the standard σ system (Song and Haidvogel, 1994). In this case we are using values $B = 1$ and $\theta = 8$ with 24 levels which gives good resolution at both the surface and bottom. Figure 3.14 shows an example from the domain used in this study, illustrating the arrangement of s-levels. We can see from this Figure that the vertical levels are closest together at the surface and near the bottom, and that they follow the terrain.

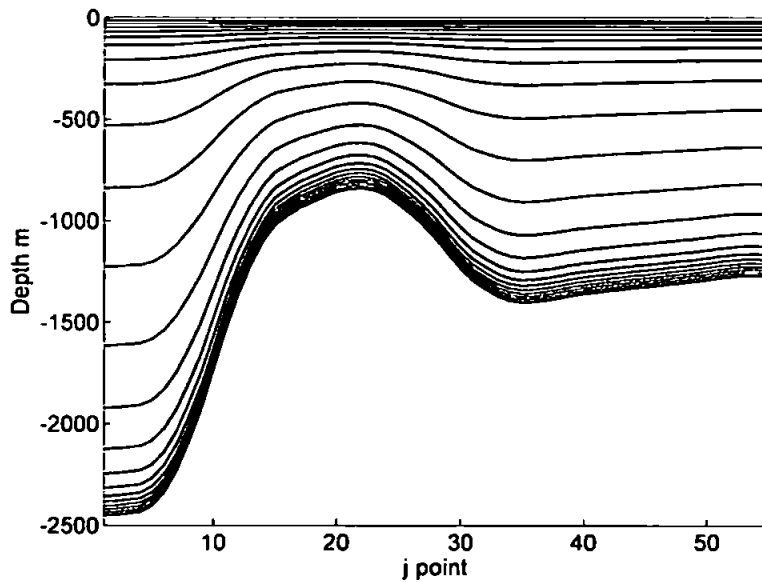


Figure 3.14 Example arrangement of vertical s-levels

In the horizontal the model grid is arranged as an Arakawa (1972) B grid and therefore both velocity components are calculated on points (*u-points*) located to the southwest of the elevation points (*b-points*). This arrangement is illustrated in Figure 3.15. Because the *u-points* are shifted in the horizontal, they also require slightly different vertical level positions. These are calculated from the s-levels at the surrounding *b-points*. The B grid was chosen during the development of the model as it was found to give superior results (compared to the C grid) when modelling large horizontal density variations such as fronts (James, 1986). This is because the C grid requires the Coriolis terms to be averaged over four velocity points. The density feature preserving property of the B grid

is clearly an advantage when seeking to model dense water over Rockall Bank.

Model Equations

Equation of State

The density is calculated using an approximation to the full UNESCO equation of state:

$$\rho(T, S, p) = \rho(T, S, 0) + \rho'(T, S, p) \quad (3.9)$$

where $\rho(T, S, 0)$ is taken from the UNESCO equation and $\rho'(T, S, p)$ is calculated using the following equation (following Mellor (1991)):

$$\rho'(T, S, p) = 10^4 \frac{p}{c^2} \left(1 - 0.2 \frac{p}{c^2} \right) \quad (3.10)$$

where

$$c = 1449.2 + 1.34(S - 35) + 4.55T - 0.045T^2 + 0.00821p + 15 \times 10^{-9}p^2 \quad (3.11)$$

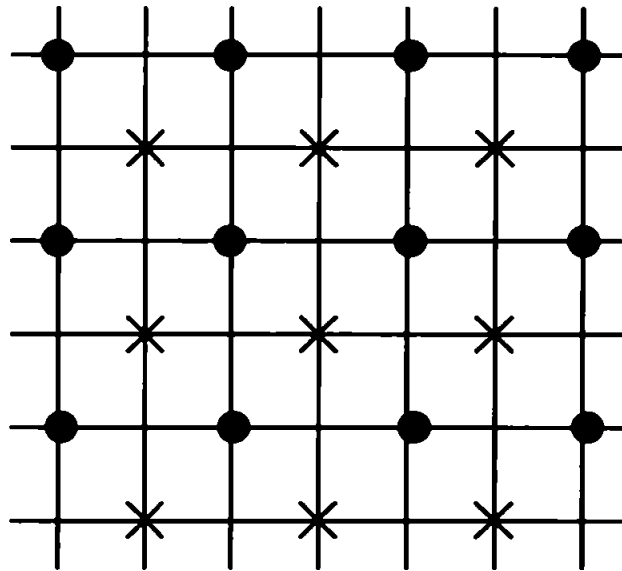


Figure 3.15 *The Arakawa B grid arrangement. Circles are elevation points ('b-points') and crosses are velocity points ('u-points').*

The buoyancy is defined similarly as $b = b_0 + b'$ where b_0 is the 'potential' buoyancy, given by Equation 3.12, and b' represents the variation of compressibility due to temperature and salinity, and is given by Equation 3.13.

$$b_0 = \frac{g}{\rho_0} (\rho_0 - \rho(T, S, 0)) \quad (3.12)$$

$$b' = \frac{g}{\rho_0} (\bar{\rho}(Z) - \rho') \quad (3.13)$$

ρ_0 is a reference density, here 1027 kgm^{-3} , Z is the depth of the water column excluding sea surface elevation (equal to σH) and $\bar{\rho}$ is defined as $-0.004564Z$.

Finally, the hydrostatic pressure is

$$P = P_a + \rho_0 (\psi + g\zeta - gz) + 0.002282gZ^2 \quad (3.14)$$

where P_a is atmospheric pressure, $\psi = H \int_0^\sigma b d\sigma$, and ζ is the sea surface elevation.

Equations of Motion

POLCOMS solves the equations of motion with the incompressible, hydrostatic, and Boussinesq approximations. These approximations are defined as follows (e.g. Griffies, 2004; Pond and Pickard, 1983; Dyke, 2001):

Incompressibility The volume of a water packet does not change. This is a good approximation for most circumstances as changes in density with time are small compared to the magnitude of the density.

Hydrostatic The water column is in hydrostatic balance, i.e. the vertical pressure gradient is calculated from the buoyancy alone. This approximation is valid when the horizontal scale is larger than the vertical scale, which is the case in this research.

Boussinesq The Boussinesq approximation is also dependent on density differences in time being small. The effect of this approximation is that a water parcel's mass, and therefore the momentum, is not affected by changes in the density.

The equations are also time split into baroclinic and barotropic modes by splitting the u and v velocity components into depth varying and depth independent parts. So u becomes $\bar{u}(\chi, \phi, t) + u_r(\chi, \phi, \sigma, t)$; similarly, v becomes $\bar{v} + v_r$.

The depth mean equations of motion are:

$$\frac{\partial \bar{u}}{\partial t} = f\bar{v} - (R \cos \phi)^{-1} \left[g \frac{\partial \zeta}{\partial \chi} + \rho_0^{-1} \frac{\partial P_a}{\partial \chi} \right] + H^{-1} [F_S - F_B] + NLB_\chi \quad (3.15)$$

$$\frac{\partial \bar{v}}{\partial t} = -f\bar{u} - R^{-1} \left[g \frac{\partial \zeta}{\partial \phi} + \rho_0^{-1} \frac{\partial P_a}{\partial \phi} \right] + H^{-1} [G_S - G_B] + NLB_\phi \quad (3.16)$$

where R is the radius of the Earth, F_S and G_S are surface stress components and F_B and G_B are bottom stress components. NLB_χ and NLB_ϕ are the depth mean non linear and buoyancy terms, defined by

$$NLB_\chi = \int_{-1}^0 \left[-L(u) + \frac{uv \tan \phi}{R} - \Pi_\chi \right] d\sigma \quad (3.17)$$

$$NLB_\phi = \int_{-1}^0 \left[-L(v) + \frac{u^2 \tan \phi}{R} - \Pi_\phi \right] d\sigma \quad (3.18)$$

where $\Pi_\chi = (R \cos \phi)^{-1} \frac{\partial \psi}{\partial \chi} \Big|_z$ and $\Pi_\phi = R^{-1} \frac{\partial \psi}{\partial \phi} \Big|_z$.

The depth-varying equations are:

$$\frac{\partial u_r}{\partial t} = -L(u) + f v_r + \frac{uv \tan \phi}{R} - \Pi_\chi + D(u) - H^{-1} [F_S - F_B] - NLB_\chi \quad (3.19)$$

$$\frac{\partial v_r}{\partial t} = -L(v) - f u_r - \frac{u^2 \tan \phi}{R} - \Pi_\phi + D(v) - H^{-1} [G_S - G_B] - NLB_\phi \quad (3.20)$$

The advection terms $L(u)$ and $L(v)$ are

$$L(a) = \frac{u}{R \cos \phi} \frac{\partial a}{\partial \chi} + \frac{v}{R} \frac{\partial a}{\partial \phi} + \Omega \frac{\partial a}{\partial \sigma} \quad (3.21)$$

where

$$\Omega = -\frac{\sigma}{H} \frac{\partial \zeta}{\partial t} - (HR \cos \phi)^{-1} \times \left[\frac{\partial}{\partial \chi} \left(H \int_0^\sigma u d\sigma \right) + \frac{\partial}{\partial \phi} \left(H \cos \phi \int_0^\sigma v d\sigma \right) \right] \quad (3.22)$$

Turbulence Closure

The version of POLCOMS initially used in this study implemented a Mellor-Yamada-Galperin (Mellor and Yamada, 1974; Galperin *et al.*, 1988) turbulence scheme, and this was replaced with GOTM (General Ocean Turbulence Model) which POLCOMS has recently been made compatible with. GOTM (2006) is a one-dimensional water column model which can be coupled to 3D models and allows one of several types of turbulence schemes to be chosen; this study has used the k - ϵ type scheme with a dynamic dissipation rate equation for the length scale. These options have previously been found to work well with POLCOMS (Jason Holt, personal communication).

The fundamental difference between the two types of turbulence closure scheme is in the calculation of the mixing length L (Burchard *et al.*, 1998). This is a length scale that relates to the largest turbulent eddies in the system. Both Mellor-Yamada and k - ϵ schemes use the relation $L = (c_\mu^0)^{1/2} \frac{k^{3/2}}{\epsilon}$. k is the turbulent kinetic energy, and ϵ is its dissipation rate. L is the mixing length, a length scale that describes the largest turbulent

eddies (Burchard *et al.*, 1998).

Mellor-Yamada type schemes use an algebraic equation for L and use this to calculate ϵ whereas conversely $k-\epsilon$ models use a transport equation to calculate ϵ and use this to calculate L . (Burchard *et al.*, 1998; Burchard, 2001). c_μ^0 is a constant which acts as a stability function. Stability functions correct for the effects of stratification and tend to damp or enhance turbulent mixing in stratified or unstratified conditions respectively (Burchard *et al.*, 1998).

Advection

The advection scheme used in POLCOMS is the Piecewise Parabolic Method or PPM (Colella and Woodward, 1984). PPM works by assuming that the value of the variable a at the beginning of the time step is the grid box average value \bar{a} , and that this variable is distributed parabolically across the grid box. The parabolas are then defined according to Equation 3.23.

$$a(\eta) = a_L + \eta[a_R - a_L + a_6(1 - \eta)] \quad (3.23)$$

$$a_6 = 6\bar{a} - 3(a_L + a_R)$$

where η is a coordinate across the width of the grid box, which varies from 0 to 1. a_L and a_R are the values at the left and right edge of the box respectively and are estimated from a polynomial fit. The parabolas are integrated in an upwind sense to calculate the advective flux, and this is split into separate calculations in the u and v directions. The advection order is alternated on successive timesteps, so that on odd timesteps u advection is performed first and on even timesteps v advection is performed first.

Points near boundaries are treated slightly differently as there are not enough neighbouring points to calculate the parameters of the parabola. Instead, the variable is reduced

to a constant value across the box at or next to boundaries, and to a linear slope in the next boxes away from the boundary.

James (1996) found that the PPM performs well in simulations of features such as fronts, which makes it particularly suitable in this study.

Horizontal Pressure Gradient

One of the main limitations of using a σ -coordinate model is that the horizontal pressure gradient is not easily represented accurately, particularly in regions of steep topography (Haney, 1991; Mellor *et al.*, 1994; Griffies, 2004). The problem arises because the horizontal pressure gradient is by definition perpendicular to the z direction, whereas the σ surfaces are generally not. The traditional approach is to consider the horizontal pressure gradient as the sum of two terms (Griffies, 2004):

$$\nabla_z p \approx \nabla_\sigma p + \rho g \nabla_\sigma z \quad (3.24)$$

where $\nabla_z p$ is the true horizontal pressure gradient, and $\nabla_\sigma p$ is the pressure gradient along the σ surfaces. The second term on the right hand side is the so called “correction term” and includes the slope of the σ levels with respect to z , $\nabla_\sigma z$. Where the topography is steep the two terms are of equal magnitude but have opposite signs, so should cancel each other out; in reality this often leads to large truncation errors which in turn can drive spurious currents (Haney, 1991; Holt and James, 2001).

In order to reduce this error, POLCOMS takes a different approach where the pressure is estimated at the four corners of the horizontal plane which has a u grid point as the centre (and the corners on the surrounding b columns). This was found to give improved results when the thermocline is flat, or sloping in the opposite direction to the σ levels (Holt and James, 2001). The pressure gradients on these edges are calculated as follows. Figure 3.16 illustrates the arrangement of points.

A horizontal plane around the current u grid point is used, which meets the surrounding b columns at points q (where q is $1 \dots 4$). The nearest σ level above each of these b

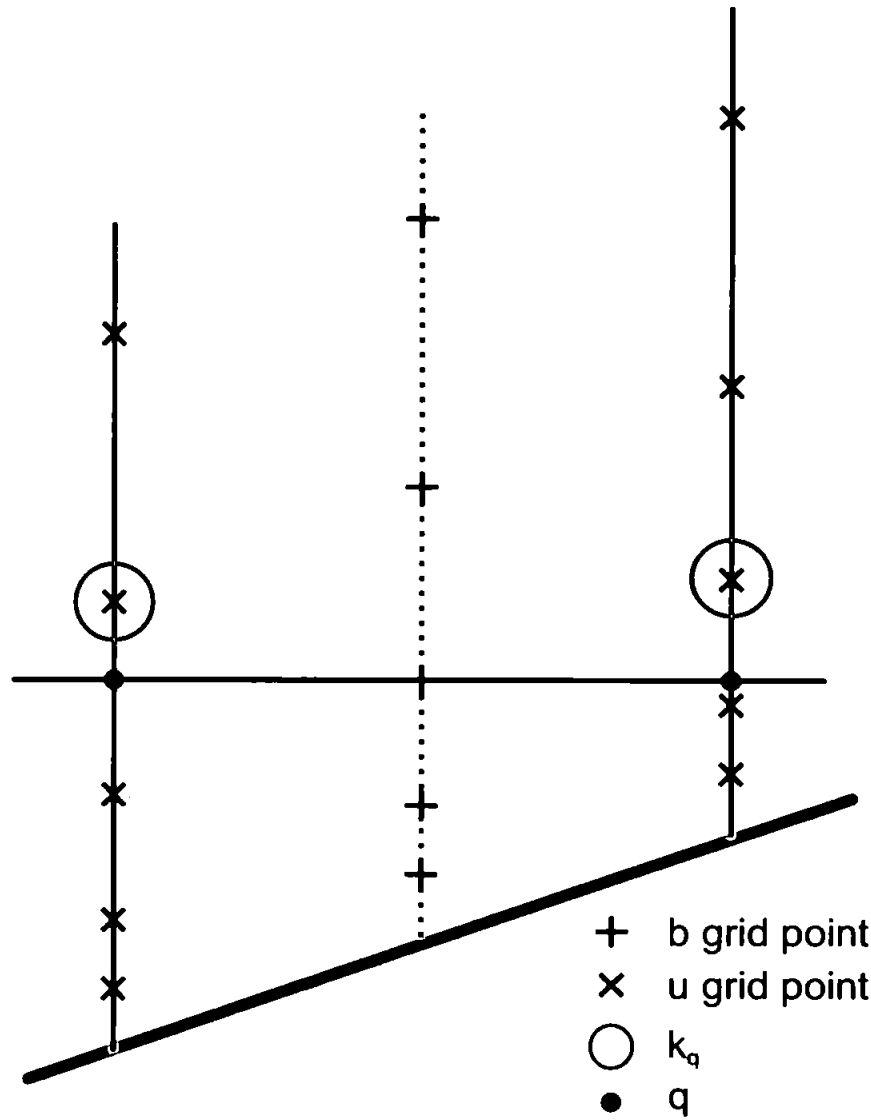


Figure 3.16 Arrangement of points used to calculate the horizontal pressure gradient. The solid vertical lines are b columns and the dashed vertical line is the u column. Note that the diagram is shown from the side for clarity, and the u column is in fact centred between four b columns (as illustrated by Figure 3.15). The horizontal line is the surface on which the pressure gradient is calculated and it passes through the u point and meets the b columns at points q , marked by solid circles. Open circles show the nearest b points above this horizontal surface.

column points is identified and labelled k_q). The fractional distance between the points q and k_q is then

$$r = \frac{\sigma_{k_q} - \sigma_q}{\sigma_{k_q} - \sigma_{k_q-1}} \quad (3.25)$$

The pressure at points k_q and $k_q - 1$ is known and the buoyancy b is assumed to vary linearly between σ levels; therefore the pressure ϕ at q can be estimated using the following Equation (Holt and James, 2001):

$$\phi_q = -\frac{1}{2}\delta\sigma \left[b_{q,N-2} + \sum_{k=k_q}^{N-2} (b_{q,k} + b_{q,k+1}) + (2r - r^2) b_{q,k_q} + r^2 b_{q,k_q-1} \right] \quad (3.26)$$

However, at the surface level ($k = N - 1$) there is no point $k + 1$ and the following equation must be used instead.

$$\phi_q = -\frac{1}{2}\delta\sigma [(2r - r^2)b_{q,k_q} + r^2 b_{q,k_q-1}] \quad (3.27)$$

The pressure gradients along the four edges of the plane are then

$$\begin{aligned} \Delta\phi_1 &= \phi_1 - \phi_2 & \Delta\phi_2 &= \phi_2 - \phi_3 \\ \Delta\phi_3 &= \phi_4 - \phi_3 & \Delta\phi_4 &= \phi_1 - \phi_4 \end{aligned} \quad (3.28)$$

and the resultant velocity changes are

$$\Delta u = -\frac{1}{2} \frac{\Delta t}{R \cos \phi \Delta \chi} (\Delta\phi_1 + \Delta\phi_3) \quad (3.29)$$

$$\Delta v = -\frac{1}{2} \frac{\Delta t}{R \Delta \phi} (\Delta\phi_2 + \Delta\phi_4) \quad (3.30)$$

Temperature and Salinity Boundary Condition

The temperature and salinity at the open boundaries (which in this case is the entire boundary) are relaxed to climatological data using a sponge relaxation layer. This is a region around the boundary, 4 grid points wide in this case, in which the model temperature and salinity are adjusted using climatological values as shown in Equation 3.31. This has the effect that across the relaxation layer, from the outside to the inside, the

temperature/salinity value becomes progressively closer to the model solution.

$$T = r \times T_b + (1 - r)T \quad (3.31)$$

where r is the relaxation parameter which varies linearly from 1 on the outermost points to 0 on the interior points which are not part of the relaxation zone. T is the temperature (or salinity) from the model solution and T_b is the boundary climatological value.

Tides

The tidal elevation and depth mean velocity are proscribed on the border points, where a flux/radiation condition is used to allow waves to escape. Up to 15 tidal harmonic constituents may be used, in any combination. The constituents that may be used are Q1, O1, P1, S1, K1, 2N2, MU2, N2, NU2, M2, L2, T2, S2, K2, M4. The change in elevation (z_C) and the change in velocity in the u (u_C) and v (v_C) directions are calculated using the following equation:

$$X_C = \sum_{n=1}^{15} (X_{1n} \cos(\sigma_n t) + X_{2n} \sin(\sigma_n t)) \quad (3.32)$$

where X here stands for the elevation (z_C) or velocity component (u_C or v_C) as the case may be. n is the constituent number, σ_n is the angular speed of the constituent, and t is the time (GMT). X_{1n} and X_{2n} are the amplitudes of the constituents which have been adjusted for nodal corrections. These corrections to the lunar constituents are necessary to take account of the changes in the moon's orbital plane inclination which has a cycle of 18.6 years and therefore cannot be represented by harmonic analysis of a year's data (Pugh, 1987).

Heat Flux

Heat fluxes are forced at the surface from meteorological data using the bulk formulae of Elliott and Clarke (1991), following Gill (1982). The total heat loss from the surface,

q_l , is the sum of the outgoing longwave radiation h_l , the sensible heat flux s_k , and the evaporative heat flux s_{ke} . These are calculated using Equations 3.33 to 3.40. The heat flux into the sea surface due to solar radiation, q_{in} , is calculated using Equations 3.41 to 3.44. The variables and constants used in all these equations are listed in Table 3.1. The heat budget is also influenced by the temperature boundary condition.

Table 3.1 *Terms used in the heat flux equations*

SYMBOL	NAME	VALUE
b_l	transmission coefficient	0.76
c	cloud cover	from data
c_c	cloud cover coefficient	0.4
c_h	Stanton number	1.45×10^{-3}
c_p	specific heat of air	$1004 J kg^{-1} K^{-1}$
d	declination of sun	Equation 3.44
e_a	vapour pressure of water	Equation 3.38
e_m	saturated vapour pressure of water	Equation 3.37
e_w	emissivity of sea surface	0.985
h_l	outgoing longwave radiation	Equation 3.34
l_t	latent heat of water	$2.5 \times 10^6 - 2.3 \times 10^3 t_s$
p	atmospheric pressure	from data
q_a	specific humidity of air at air T	Equation 3.40
q_{in}	heat flux into surface	Equation 3.41
q_l	heat loss from surface	Equation 3.33
q_s	radiation available to the surface (if no clouds)	Equation 3.42
q_w	specific humidity of air at sea surface T	Equation 3.39
r_h	relative humidity of air	from data
S_c	solar constant	$1368 W m^2$
s_k	sensible heat flux	Equation 3.35
s_{ke}	evaporative heat flux	Equation 3.36
snh	sine of sun's altitude angle	Equation 3.43
t	time since 00:00 1st January	from model time
t_a	air temperature	from data
t_s	sea surface temperature	from within model
w	wind speed	from data
α	sea surface albedo	0.4
ρ	reference seawater density	$1027 kg m^{-3}$
ρ_a	air density	$1.25 kg m^{-3}$
σ	Stephan's constant	$5.67 \times 10^{-8} W m^{-2} K^{-4}$
ϕ	latitude	from grid

$$q_l = h_l + s_k + s_k e \quad (3.33)$$

$$h_l = e_m \sigma \left((t_s + 273.15)^4 \right) (0.39 - 0.05 \sqrt{e_a}) (1 - 0.6c^2) \quad (3.34)$$

$$s_k = c_h \rho c_p w (t_s - t_a) \quad (3.35)$$

$$s_{ke} = c_e \rho w (q_w - q_a) t_l \quad (3.36)$$

$$\log_{10} e_w = \frac{0.7859 + 0.03477t_s}{1 + 0.00412t_s} \quad (3.37)$$

$$e_a = r_h e_w \quad (3.38)$$

$$q_w = \frac{0.62e_w}{p - 0.38e_w} \quad (3.39)$$

$$q_a = \frac{0.62e_a}{p - 0.38e_a} \quad (3.40)$$

$$q_{in} = q_s (1 - c \times c_c - 0.38c^2) \times (1 - \alpha) \quad (3.41)$$

$$q_s = S_c b_1 \times snh \quad (3.42)$$

$$snh = -\cos \phi \cos d \cos \left(\frac{2\pi t}{24} \right) + \sin \phi \sin d \quad (3.43)$$

$$d = \cos \left(\frac{2\pi(t - 171.5) \times 24}{365.24 \times 24} \right) \times 23.5^\circ \quad (3.44)$$

These inward and outward heat fluxes are kept separate within the model and their effects on the ocean surface are calculated separately. The cooling at the surface from the outward heat flux is applied to the top box only, using Equation 3.45.

$$T^{p+1} = T^p + \frac{q_l}{c_p \rho} \times \frac{\Delta t}{\Delta z} \quad (3.45)$$

where T^{p+1} is the new temperature and T^p the old one; q_l is the heat flux leaving the surface as calculated in Equation 3.33; c_p is the specific heat of water ($3986 \text{ J kg}^{-1} \text{ K}^{-1}$); ρ is a reference density of seawater (1027 kg m^{-3}); Δt is the timestep length; Δz is the depth of the surface grid box. Note that q_l here is negative, so the effect is a decrease in temperature.

The incoming solar radiation is allowed to penetrate down the water column and heat it according to Equation 3.46.

$$T_k^{p+1} = T_k^p + \frac{q_{in}}{c_p \rho} \times \frac{\Delta t}{\Delta z} \times (e^{\lambda z_k} - e^{\lambda z_{k-1}}) \quad (3.46)$$

where again T_k^{p+1} is the new temperature and T_k^p the old one for a given depth level; q_{in} is the incoming heat flux from Equation 3.41; c_p and ρ are the specific heat and density as above; Δt is again the timestep length; Δz is the distance between the depth levels k and $k-1$; λ is the transmissivity; z_k and z_{k-1} are the depths of levels k and $k-1$ respectively. POLCOMS allows the water column transmissivity to be set either as a constant or as a function of water depth. In this work the constant value of 0.154 is used.

Wind Stress

The data input into the model is in the form of wind speed components. The wind stress is then calculated inside POLCOMS using (following Smith and Banke (1975)):

$$\tau_i = \frac{\rho_a}{\rho} (0.63 + 0.066W) \times 10^{-3} W u_i \quad (3.47)$$

where u_i is the u or v wind speed component, τ_i is the corresponding stress component, W is the scalar wind speed, ρ_a is the air density (taken to be 1.25 kgm^{-3}), and ρ is the water density.

Salt Input

There are no rivers in the domain used in this study, so the only freshwater input is from the precipitation/evaporation balance. The precipitation rate is read in from external data, and, the evaporation rate is calculated within POLCOMS using

$$E = \frac{c_e \rho_a w}{\rho} (q_w - q_a) \quad (3.48)$$

where E is the evaporation rate, c_e is the Dalton number (1.5×10^{-3}), and all other terms are as defined in Table 3.1.

The salinity is then adjusted on the surface level only, using

$$S^{p+1} = \frac{S^p}{1 - ep \times \frac{\Delta t}{\Delta z}} \quad (3.49)$$

where S^{p+1} is the new adjusted salinity, S^p the old salinity value, ep is the net salt flux (evaporation – precipitation), and Δt and Δz are the time and vertical space step lengths respectively.

3.4.2 Changes Made to the Model Code

Before any of the model runs could be conducted it was first necessary to alter the model code so that it could run on a Windows desktop computer, and also so that it was compatible with the Rockall Bank domain and set up. This section describes the major changes made to the model. With such a large, sophisticated model there were a large number of minor amendments and not every change can be listed here: a complete list may be found in Appendix B. There were also some changes that were only necessary for particular model runs, and these are outlined in Chapters 5 and 6 where the individual

runs are described.

- The modelling studies in this thesis were conducted with the most up to date version of the model available at the time, version 6.2. This was obtained from POL direct in its original form, which was designed for use on parallel UNIX machines. Previous work using an older version of the model (Enriquez, 2005) had required lengthy work to convert to code to a form that could be used in Windows. However in this study the use of a more powerful compiler significantly simplified this process as it allowed the C preprocessing commands to be used.
- As described fully in §3.3.1, the model domain used was a rotated box which was not therefore congruent with latitude and longitude lines. In order to ensure that this compatible with the POLCOMS code it was advised that the f-plane approximation be used rather than the β -plane (Jason Holt, personal communication). As noted by Shapiro and Hill (1997) the f-plane is sufficient when analysing dense water cascading. This simplification was enabled by defining the parameter FLAT in the preprocessor.
- The existing routine for dealing with the temperature and salinity at the open boundaries (`bost.for`) had been written for a specific domain. This therefore needed to be changed so that it worked for the Rockall Bank domain where the boundary is completely open, with no coastline. The existing indexing method did not work correctly as it had been written such that each "ring" within the boundary relaxation zone contains the same number of points. In reality the inner rings are smaller as illustrated by Figure 3.17.

This discrepancy led to the indices in the corners being overwritten and the indexing was therefore not continuous. The routine was rewritten such that that the indices of the boundary zone points go around correctly in a spiral; every point then has a unique index and the indices increased in a series with no gaps. This arrangement is shown in Figure 3.18 where the arrows indicate the clockwise spiral. The value of the index is also shown for selected points.

Additionally, the original routine could only be used for short runs as it read in

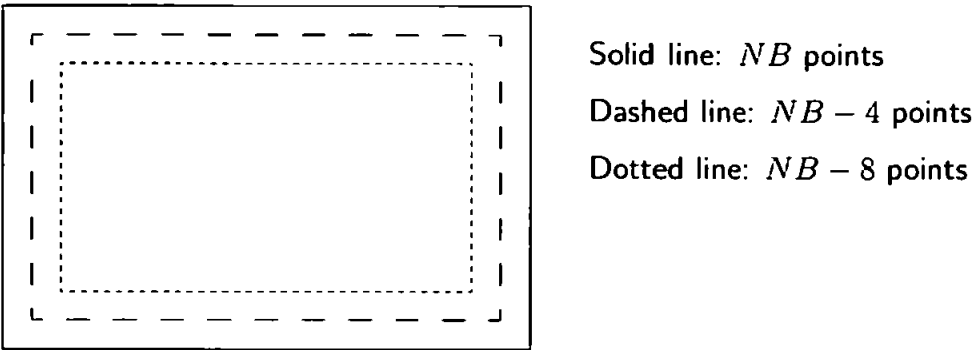


Figure 3.17 Illustration of how the number of grid points in each 'ring' of the relaxation zone varies. Note that the number of points on the outer edge $NB = 2(L + M) - 4$ where L and M are the grid dimensions

→	L+M	→	→	→	→	→	→	→	→	→	↓
↑	→	→	→	→	→	→	→	→	→	↓	↓
↑	↑	→	→	→	→	→	→	→	↓	↓	↓
↑	↑	↑	All indices zero in inner domain						↓	↓	↓
↑	↑	↑							↓	↓	↓
↑	↑	↑							↓	↓	↓
↑	↑	↑							↓	↓	↓
↑	↑	↑							↓	↓	↓
↑	↑	↑							END	↓	↓
L+2	↑	↑	←	←	←	←	←	←	←	←	↓
L+1	↑	←	←	←	←	←	←	←	←	NB +1	←
L	←	←	←	←	←	←	←	←	3	2	1

Figure 3.18 Example of boundary zone indexing for relaxation zone width 3. L and M are the horizontal dimensions of the grid; NB is the number of points on in the outer edge [ie $2(L+M) - 4$].

boundary data for 'last month', 'this month' and 'next month' only, and then interpolated to the current time. Therefore once the model reached the latter half of 'next month' there were no data to perform an accurate interpolation. This was rewritten so that new data are read in each month as necessary for as long as the run continues. For clarity this was saved in a new routine `bostlong`. The new version of this routine may be found in Appendix C.

- As discussed in §3.4.1 Version 6.2 of POLCOMS contains the facility to introduce a new turbulence scheme, from the General Ocean Turbulence Model GOTM, instead of the original Mellor-Yamada-Galperin level 2.5 scheme. This was enabled by downloading the GOTM code (GOTM, 2006), incorporating the relevant files into POLCOMS, and selecting the GOTM preprocessor setting.

- A new version of the routine to read in meteorological data (`metset_cko.for`) was written so that it was fully compatible with the type and format of data available for this study. Modelled on the existing routine (`metset.for`) it reads in variables every six hours, and linearly interpolates them to find the appropriate values for the current time.
- As briefly mentioned previously, it was necessary for the model to read in the latitude and longitude of each grid point. The latitude is needed by the heat flux routine `heatin` to calculate the declination of the sun; due to the use of the rotated domain the latitude was not calculated correctly by the model because the calculation assumed that the grid lies on lines of constant latitude and longitude. Therefore to ensure that accurate values were used, the code was altered so that the latitude at each point is taken from an external data file.
- The solar radiation calculation also needs the time in order to estimate the position of the sun. In the original code the same time (GMT) was used for every point in the grid. This was rewritten to use the local apparent time at each individual grid point instead, allowing a higher accuracy in the heat flux calculation. The correction used was to add 4 minutes of time per degree of longitude. In this case the domain is west of 0° so the effect is a subtraction of 4 minutes per degree. An approximation to the equation of time was then applied. The equation of time is the difference between local solar time and clock time (i.e. mean solar time) which is caused principally due to the non-circular nature of the Earth's orbit and the tilt of the Earth's rotation axis. The approximation to the equation of time was obtained from Wikipedia (2008). This is a simple approximation which nevertheless reproduces well the shape and magnitude of the real curve. The total adjustment made to the time is given by

$$\begin{aligned}
 T_l &= T_m + \frac{1}{60} [4 \times lon + 9.87 \sin(2B) - 7.53 \cos(B) - 1.5 \sin(B)] \\
 B &= \frac{2\pi(N - 81)}{384}
 \end{aligned}
 \tag{3.50}$$

where T_l is the local apparent time in hours, T_m is the global model time, lon is the longitude of the point, and N is the Julian day number. As with the latitude mentioned above, a file of longitude values needs to read in to this modified subroutine.

- A bug in the code meant that it was not possible to reset the model time to zero when starting from a warm start (which we wished to do here). This was because the option `-resettm` (which should reset the time) was triggering the response to option `-reset` which resets the whole system. This was solved by changing the code so that it looks for `-tmreset` instead of `-resettm` to reset the time.
- New preprocessor commands were added so that the full meteorological forcing is enabled by simply including `ROCKALLFULL` in the preprocessor options. Setting this option automatically selects the flat Earth setting and turns on the tides, heat flux, salt flux, and wind. The corresponding option `ROCKALLGA` was added for the 'spin-up' runs which do not include forcing other than the density distribution. Both options also enable the `ROCKALLBC` setting which was written in to include the settings for the open boundary.
- The outputs from the model were all handled by subroutine `data_out` rather than `tidemeanout`. The code in this routine was changed regularly depending on which outputs were needed for the particular run. A previous study introduced a routine to estimate the mean kinetic energy of the basin (Enriquez, 2005) which used a basin volume specific to the Black Sea; this was updated so that it estimated the volume from the topography.

3.5 Model Data Post-Processing

Because the output from the model is in binary files (with the exception of the kinetic energy output) it needed to be processed into a more easily useable form before it could be analysed. Matlab routines were written to automate this process (see the list in Appendix A) and the main steps common to all the model runs are as follows:

1. Read the data (temperature, salinity, u , v) from binary files into Matlab
2. Linearly interpolate from s -levels back to z -levels
3. Save both s and z level data as Matlab files so they can be used later
4. The *CSIRO SEAWATER Toolkit* (Morgan, 1993) function `sw_pden` was used to calculate the potential density σ_θ from the temperature and salinity data (on both s - and z -levels)

The kinetic energy output is more simple to deal with as the model output are plain text ASCII files, so these need no processing other than being read and plotted.

Some additional processing was necessary for some of the runs. The 'geostrophic' runs were validated by comparing the model currents to those calculated from the density distribution. These were calculated using

$$V = \frac{(\Delta\Phi_{i+1} - \Delta\Phi_i)}{fL_i} \quad (3.51)$$

where $\Delta\Phi_i$ and $\Delta\Phi_{i+1}$ are the geopotential anomalies at the sea surface at two points, f is the coriolis parameter, and L_i is the distance between the points i and $i + 1$. The geopotential anomaly is calculated using the following equation, which is integrated up the water column from the reference level to the surface.

$$\Delta\Phi = \rho_0 g \bar{\delta}(z_2 - z_1) \quad (3.52)$$

where ρ_0 is a reference density, taken as 1000 kgm^{-3} ; $\bar{\delta}$ is the specific volume anomaly averaged between the two depths z_1 and z_2 .

As this method gives only the component of velocity that is perpendicular to the transect of points, transects in both the x and y directions were used. The reference level in each case was the deepest level common to all points in the transect. As the geostrophic method can calculate only relative velocities (relative to the assumed zero-motion level), the velocity from the model at the reference level depth was subtracted from the surface velocity to provide a relative velocity that can be compared to the geostrophic

calculations. Again Matlab routines were written to automate the process.

With all the data extracted into more readable forms, routines were then written to generate maps and cross-sections automatically.

Chapter 4

Satellite SST Data Analysis

4.1 Introduction

In order to complement and validate the model results, satellite sea surface temperature (SST) data from the Pathfinder AVHRR dataset were analysed. Monthly composite data were used and the study period was October 1992 to December 2003, providing a long time series for analysis. This builds upon the work of Mohn and White (2007) who used similar data over the period 1998–2004 and showed that the cold water over Rockall Bank can be seen in AVHRR satellite data. Where Mohn and White (2007) used the data to produce monthly average climatologies, this study looks instead at the annual variation. This chapter first describes the typical results that are seen each year, before looking more deeply into the variation between different winters.

4.2 Typical Picture

Upon examination images of the sea surface temperature (note that the full set can be found in Appendix D), a regular front could be seen during the winter and spring months. The front is aligned with the southern slope of Rockall Bank, typically lying along the 400m contour. This front breaks down during the summer, reforming the following winter. This feature is typically present from November or December to April or May, but during the sample period it started as early as October and finished as

late as June on some occasions. The typical temperature difference reached was around 1.0–1.5 °C.

Figures 4.1 and 4.2 show two illustrative examples of a cold front that appears to be aligned with Rockall Bank. We can see the edge of the front (indicated by the arrows) aligned with the contours of the Bank. Away from this edge the cold water extends North and there is no further link with the bathymetry of the Bank apparent. We can also see in these, and the following, Figures that in general the clouds have been successfully minimised. The white areas are those points which were identified as clouds and removed. There are still some cloudy patches evident as anomalous colours, but their effect on the data has been reduced.

A distinct cold 'patch' over just the Bank summit itself is seen less often, usually between January and March but sometimes in December or April. The smallest patches tended to lie within the 100 m contour, with the larger ones lying within the 400 m contour. Figures 4.3 and 4.4 show two examples of distinct cold patches (indicated by the arrows). We can see that these differ from the front images in that there is warmer water immediately to the North, and the colder water lies entirely within the Bank area.

These results compare well with those of Mohn and White (2007) who collated similar data for the period 1998–2003 and produced monthly SST climatologies. Mohn and White (2007) found that the cold core over the Bank was most pronounced between December and March and weakens in the summer before reforming in autumn. They also find that the cold water is typically found within the 300 m contour.

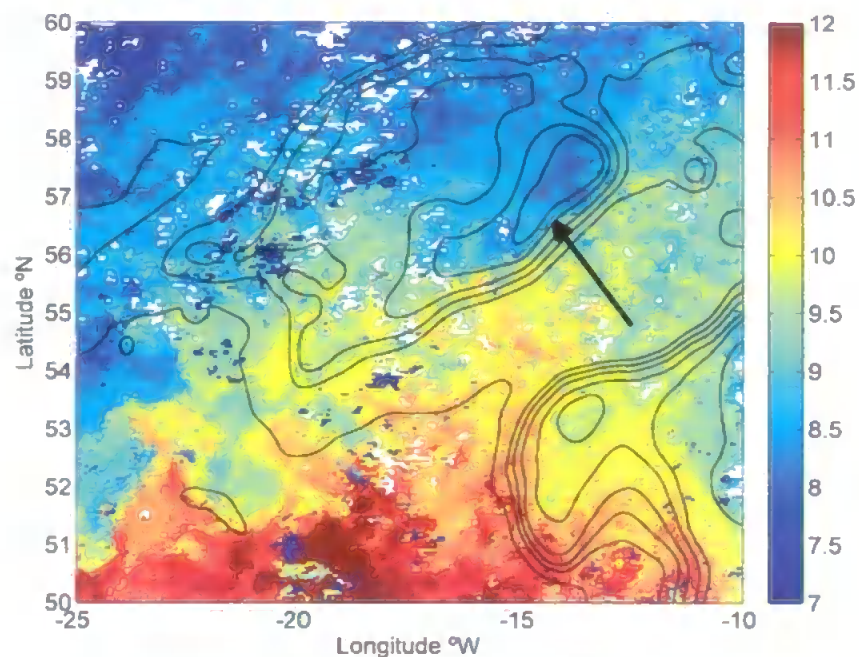


Figure 4.1 AVHRR Sea Surface Temperature for December 1992, showing a temperature front between the Bank and Trough (indicated by the arrow). Bathymetry contours for 100, 250, 500, 1000, 1500, 2000 and 3000m are shown.

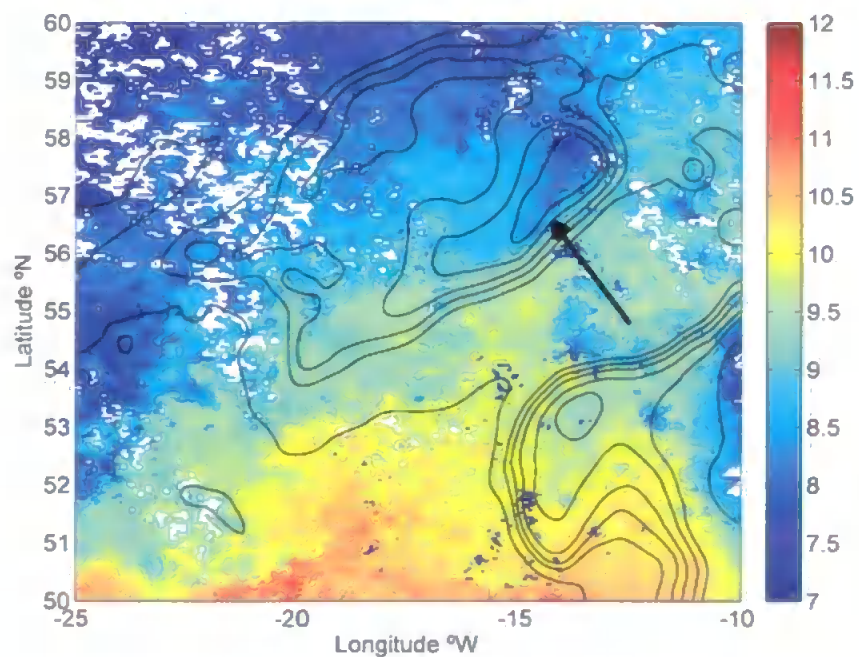


Figure 4.2 AVHRR Sea Surface Temperature for February 1994, showing a temperature front between the Bank and Trough (indicated by the arrow). Bathymetry contours for 100, 250, 500, 1000, 1500, 2000 and 3000m are shown.

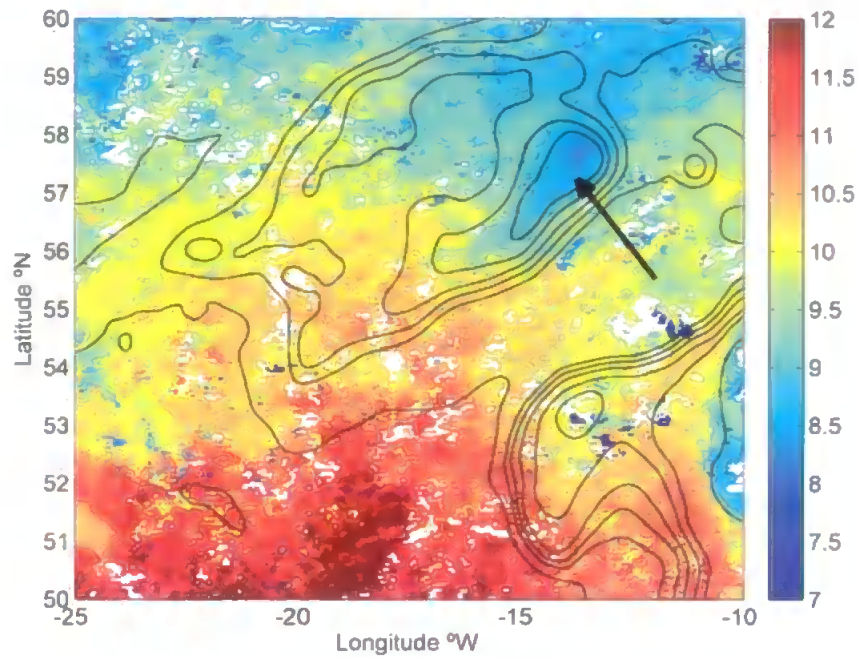


Figure 4.3 AVHRR Sea Surface Temperature for January 1997, showing a distinct cold water patch (indicated by the arrow). Bathymetry contours for 100, 250, 500, 1000, 1500, 2000 and 3000m are shown.

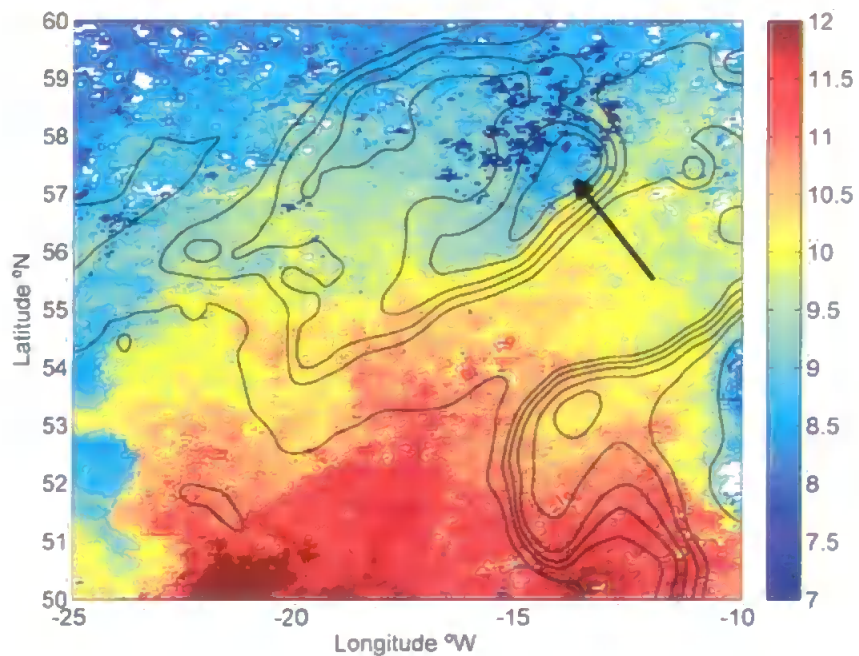


Figure 4.4 AVHRR Sea Surface Temperature for March 2002, showing a distinct cold water patch (indicated by the arrow). Bathymetry contours for 100, 250, 500, 1000, 1500, 2000 and 3000m are shown.

4.3 Annual Variation

This research expands on the findings of Mohn and White (2007) by looking at the inter-annual variation of the surface cold water. The temperature difference was analysed by extracting data from two small areas - a "box" over the top of the Bank (B), and an equal-sized box at the same latitude over a deeper area to the west of the Bank (O). The location of these boxes is shown in Figure 4.5.

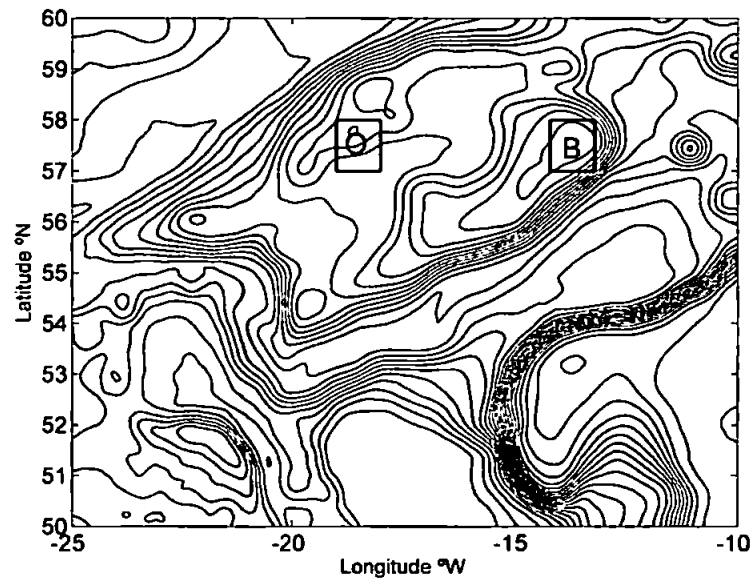


Figure 4.5 Location of the two boxes in which the satellite SST data were analysed: 'Bank box' B and 'non-Bank box' O. Bathymetry contours are every 200 m.

The median temperature of all points within each box was then calculated and labelled T_B and T_O for boxes B and O respectively. The median was used rather than the mean in order to reduce the effect of any remaining bad quality data points. Figure 4.6 shows T_B (black line) and T_O (grey line) over the 10 year period. We see that the temperature of both boxes displays a seasonal cycle as would be expected. We also see that the Bank temperature T_B is consistently cooler than T_O during the winter. During the summer, in contrast, the temperature of the box B is the around the same as, or warmer than, that of box O.

We also see from Figure 4.6 that the temperature difference between the two areas is not the same each year. This is illustrated more clearly by Figure 4.7 which displays the difference between T_B and T_O . We see the seasonal variation, with the values alternating

between positive and negative. We also see that the magnitude of the winter temperature difference varies between less than 0.5°C in the winter of 1993/1994, to almost 1.5°C in 1997. In most cases the largest temperature difference was seen in January, whereas the lowest temperatures were reached slightly later in February or March. In 1995/1996 and 2000/2001 the largest temperature difference was reached later in February or March. In 1993/1994, where there was only a small difference between T_B and T_O , the temperature difference is almost constant between October and April.

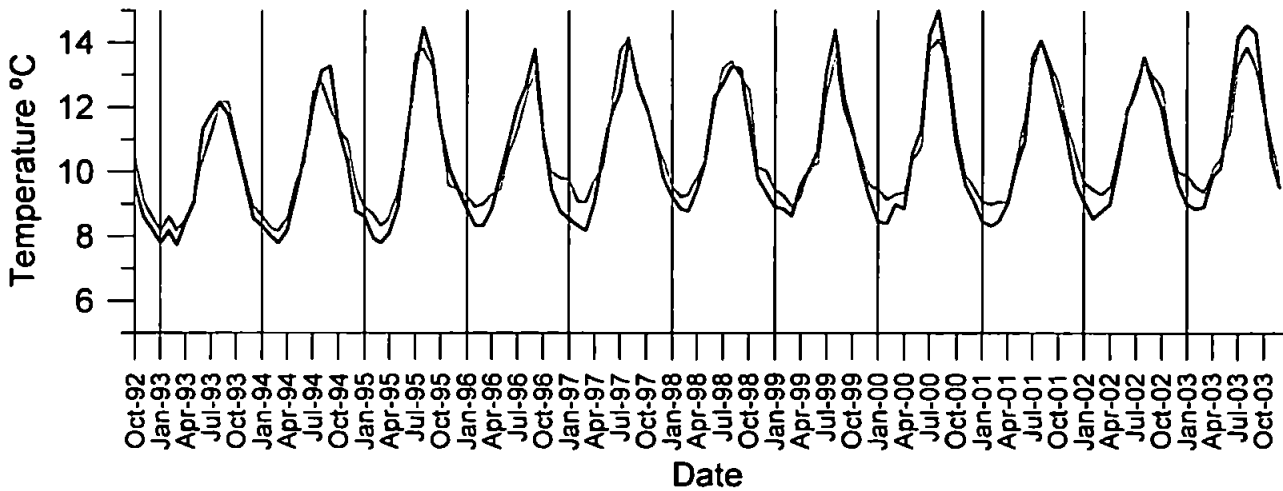


Figure 4.6 Time series of mean temperatures T_B (black line) and T_O (grey line)

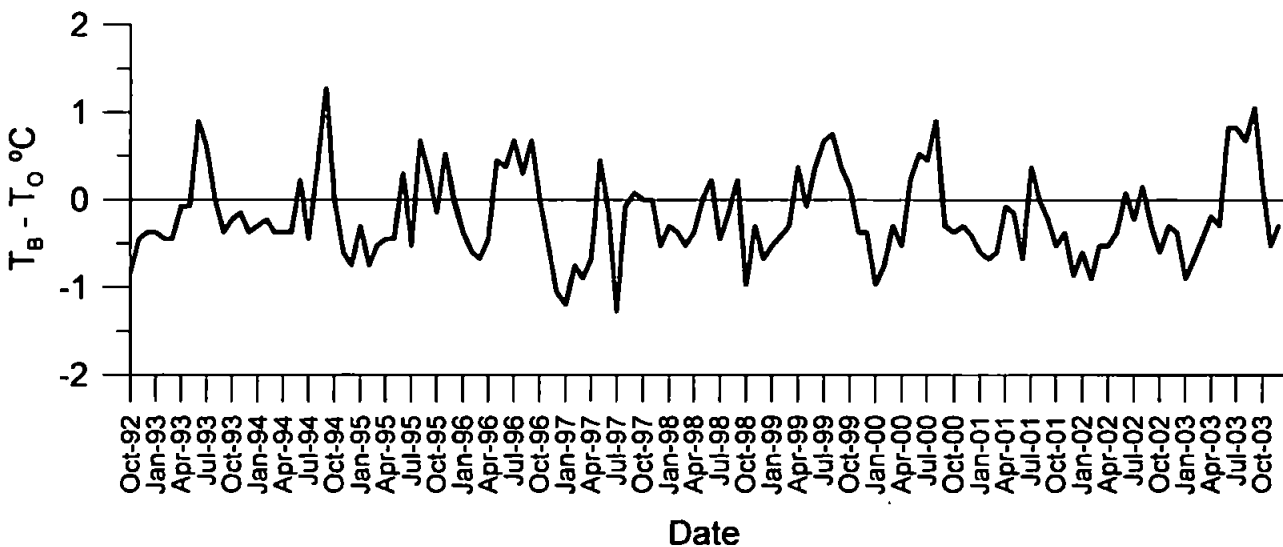


Figure 4.7 Time series of SST difference between the Bank box B and the non-Bank box O. Negative values indicate the Bank box is cooler than the non-Bank box.

The images for each month over the 10 year study period were inspected and identifying characteristics were tracked: the presence of a cold front between the Bank and Trough, and the presence of a distinct cold patch over the bank itself. These results of these

observations are summarised in Table 4.1. Although this is by its nature a subjective measurement, it does provide a useful and simple method of comparison.

Table 4.1 *Characteristics of monthly AVHRR data over 10 years. F indicates the front between the Bank and Trough is present, but there is no distinct cold patch; C indicates the cold patch is present; X indicates the data are too patchy to judge.*

Month	1992	1993	1994	1995	1996	1997	1998	1999	2000	2001	2002	2003
Jan		F	F	F	C	C	F	C	F	F	C	C
Feb		F	C	C	F	C	X	C	F	F	C	C
Mar		C	C	X	F	C	C	F	F	F	C	C
Apr		C	F	F	F	-	F	F	F	F	C	F
May		F	F	-	-	-	F	-	F	F	-	-
Jun		-	F	-	-	-	-	F	-	-	-	-
Jul		-	-	-	-	-	-	-	-	-	-	-
Aug		-	-	-	-	-	-	-	-	-	-	-
Sep		-	-	-	-	F	-	F	F	-	-	-
Oct	F	-	-	-	-	-	-	F	F	-	-	-
Nov	F	F	F	-	F	F	F	-	F	-	F	-
Dec	F	F	C	F	C	F	F	F	F	C	F	F

We can see from Table 4.1 that there is a lot of variation in the duration over which a front or cold patch could be seen, and in the month in which it starts. These observations were used with the temperature parameters T_B and T_O to produce more quantitative analysis of these differences in duration. Each year was considered to run from August to August such that any front/cold patch seen later in the autumn is considered to be part of the next year. Where a cold patch was identified, this was counted also as a continuation of the front, and only the first and last months observed were used meaning that gaps are ignored. For example the season 1998/1999 was considered to have a front duration of 8 months (November 1998–June 1999), and a cold patch duration of 2 months (January 1999–February 1999). The temperature difference between T_B and T_O for the months of October–April each year were then picked out and averaged (arithmetic mean) to provide a single parameter T_{IV} that can be compared between the different years. The estimated duration of the front and cold patch are compared to the season's mean temperature difference T_{IV} in Figure 4.8. The results for the total duration of the front and/or cold patch (Figure 4.8A) are counterintuitive and appear to suggest an inverse relationship with a larger magnitude T_{IV} generally being seen in years with a shorter duration of front/cold patch. However, there is one outlying point which does not fit this pattern

at all, corresponding to the 1995/1996 season. There is a more clear, and positive, correlation when we look at the duration of the cold patch alone (Figure 4.8B). A line has been fitted to Figure 4.8B which is given by $Y = -0.0614X - 0.315$, where X is duration of the front/cold patch in months, and Y is the mean temperature difference T_W . This gives an r^2 value of 0.47. If we look only at those years in which a cold patch was identified, removing 1999/2000 and 2000/2001, (Figure 4.8C) the r^2 value increases to 0.81 (line given by $Y = -0.107X - 0.170$). These results indicate a link between the degree of cooling and the duration of the cold patch (in years when it is present), with a larger temperature difference tending to occur when the cold patch was seen for longer. This does not, however, explain the presence of the two years which featured no cold patch but a relatively large temperature difference (1999/2000 and 2000/2001).

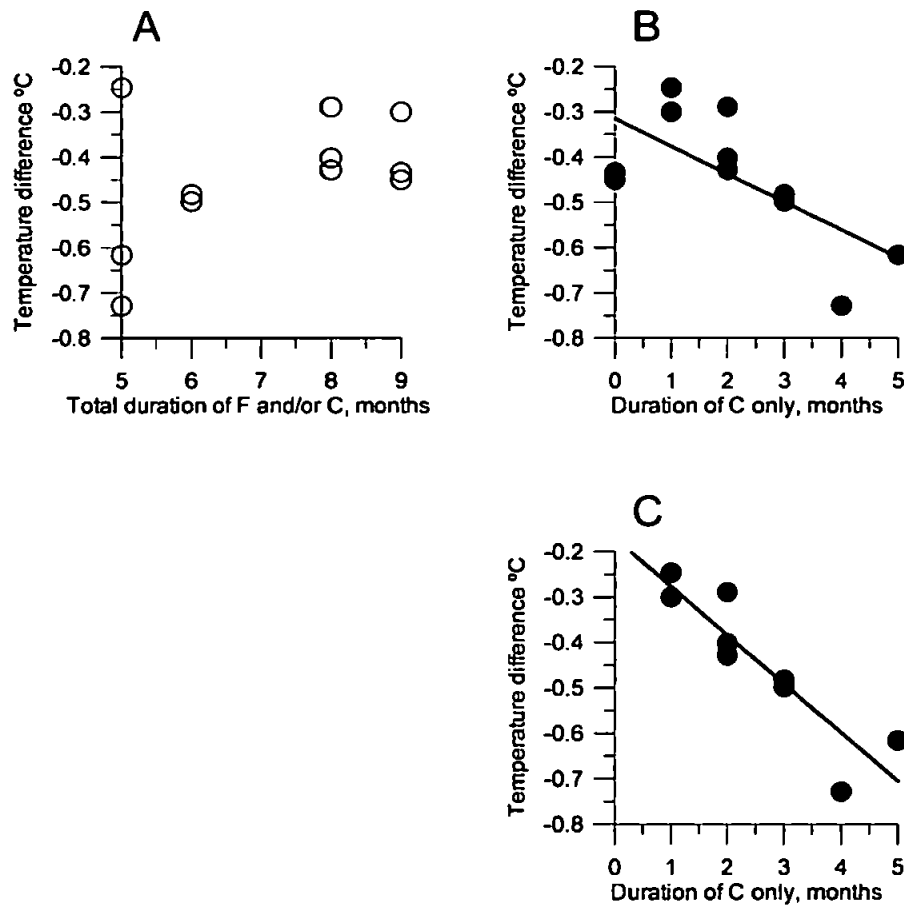


Figure 4.8 A: Observed total duration of the front and/or cold patch (both F and C in Table 4.1) against the Oct–Apr mean temperature difference between the Bank and non-Bank boxes
 B: Observed duration of the cold patch only (C in Table 4.1) against the Oct–Apr mean temperature difference between the Bank and non-Bank boxes
 C: Observed duration of the cold patch only (C in Table 4.1) against the Oct–Apr mean temperature difference between the Bank and non-Bank boxes, with the two years featuring no cold patch removed.

The observed durations of the front and cold patch are compared in Figure 4.9, that is the duration of the cold patch alone is compared to the total duration of any temperature feature aligned with the Bank. As suggested by the opposite trends of Figures 4.8A and 4.8B there appears to be an inverse relationship between the duration of the two states. The line fitted to Figure 4.9 is given by $Y = -0.695X + 7.02$ where X is the duration of the front and/or cold patch, and Y is the duration of only the cold patch. This gives an r^2 value of 0.56. The outlying point at (5,1) is the same year, 1995/1996, as the main outlying point from Figure 4.8A, and the r^2 value would be 0.9 without this year. The two years which did not fit well into the temperature difference/cold patch duration pattern (1999/2000 and 2000/2001) do appear to fit well with the correlation here. Care must be taken in interpreting this Figure as it is not clear whether the front and cold patch are truly linked, or whether the front is instead a separate underlying condition. If the two phenomena are related then these data suggest that the system can vary between two extreme conditions: from a long-lasting period featuring mainly a front but no distinct cold patch, to a shorter but more intense period featuring where the cold patch is seen over the whole period (and anything in between). The link with T_{IV} suggests that it is primarily the winter temperature difference that determines which state will occur.

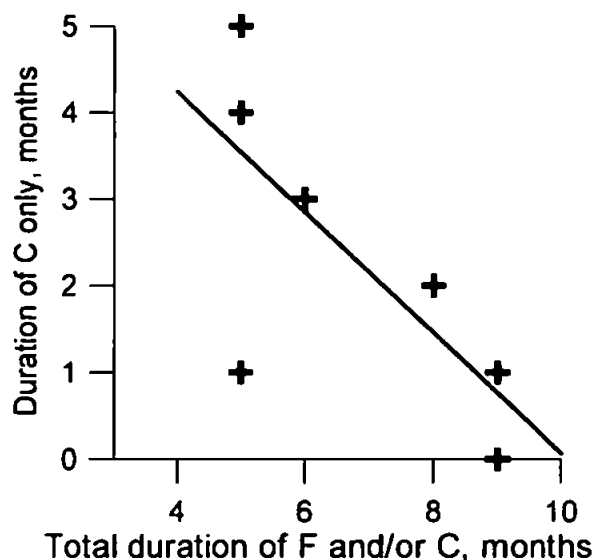


Figure 4.9 Observed total duration of the front and/or cold patch (F and C in Table 4.1) against observed duration of the cold patch alone (C in Table 4.1)

4.4 Summary

The AVHRR SST data show that the cold water patch over Rockall Bank can be seen regularly with either a distinct cold patch or a temperature front seen at the Bank every year over the studied period. This is in broad agreement with previous findings (Mohn and White, 2007). Although cold water is visible in some form every winter, its duration and the temperature difference vary significantly from year to year. A distinct cold patch was present from anything from 0 to 5 months, while the total duration of either a front or cold patch varied from 5 to 9 months.

The winter mean temperature difference between the two sample boxes, T_W , varied from 0.25°C to 0.75°C and the cold patch is generally seen for longer in winters where the mean temperature difference between the Bank and adjacent areas is largest. There were however two years, 1999/2000 and 2000/2001, in which there was a relatively large temperature difference, but no cold patch was identified.

Counterintuitively there appears to be an inverse link between the duration of the separate cold patch and the total duration of either a front or cold patch. The distinct cold patch is most likely to be seen in years where the overall timescale for the presence of a surface temperature signal is shorter. Although this is not conclusive it is nevertheless an interesting result, which warrants further investigation in order to determine the cause of this apparent link. One year in particular, 1995/1996, does not fit well into this pattern and at this stage there is no obvious reason for this.

Chapter 5

Sensitivity Study

Before the full modelling runs were begun, a number of simplified runs labelled T1–T9 were done in order to test the sensitivity to the different types of forcing and to check that each element was working correctly. This chapter describes each of these runs with brief descriptions of any necessary changes made to the model code. The complete details of all changes may be found in Appendix B. The results of each run will also be outlined in each section.

Each run was started at 1st November 2001, although they continue for different lengths of time. The main properties of the runs are summarised in Table 5.1 below.

Table 5.1 *Summary of the preliminary model runs*

RUN	BATHYMETRY	REAL TS	TIDES	WIND	HEAT	SALT	DURATION
T1	-	-	-	-	-	-	1 month
T2	✓	-	-	-	-	-	1 month
T3	✓	✓	-	-	-	-	3-8 months
<i>There are several variations of T3, using different settings not outlined in this table.</i>							
T4	✓	-	✓	-	-	-	1 month
T5	✓	-	-	✓	-	-	3 months
T6	✓	-	-	-	✓	-	3 months
T7	✓	-	-	-	-	✓	1 month
T8	✓	✓	✓	-	-	-	3 months
T9	✓	✓	-	-	✓	-	3 months

5.1 Run T1

The first experiment—T1—is the simplest and comprises a flat box with constant depth 1000m, a homogeneous initial temperature and salinity field with values 15°C and 35 respectively, and no meteorological forcing. This month long run is to check that no spurious currents are produced by the model. The model was run with all settings such as meteorological forcing switched off, though open boundaries are used.

As this run included no forcing at all there were no significant currents generated. Figures 5.1 and 5.2 show the surface velocity (which is representative of the results) after 24 hours and then the end at 720 hours respectively. At the first output time, 24 hours into the run, the maximum current speed is of the order $2 \times 10^{-13} \text{ ms}^{-1}$. By the end of the run, a month later, this has increased only to $2 \times 10^{-12} \text{ ms}^{-1}$. Although the correct solution would be zero currents, the velocities here are so extremely small that we can deduce that the model is not generating spurious currents. We can see from the structure of the velocity field in Figures 5.1 and 5.2 that there is no pattern to these tiny currents: they have the appearance of computer noise. Both the temperature and salinity remain unchanged from their original values (15°C and 35) at all points throughout this run.

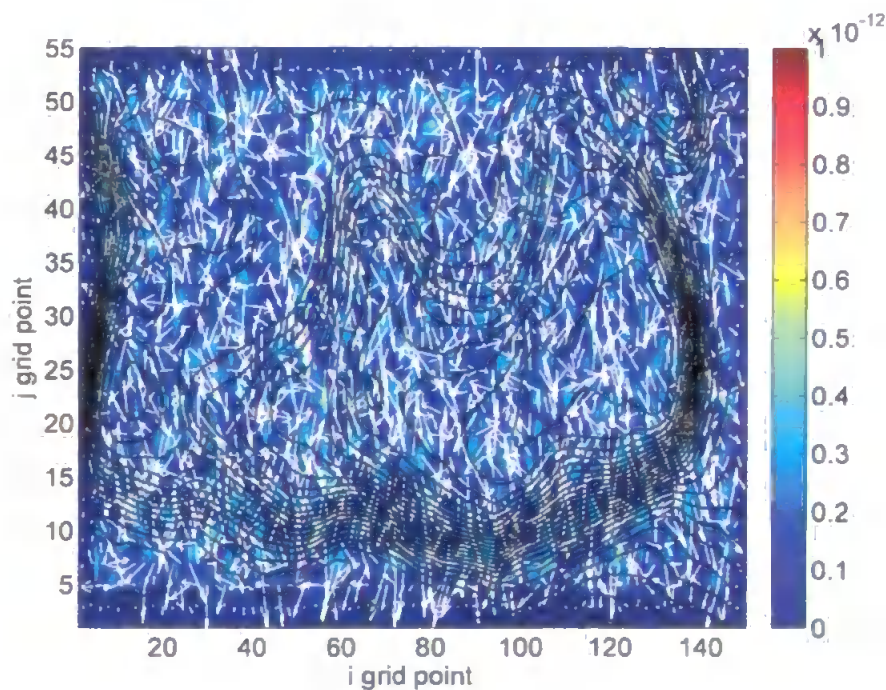


Figure 5.1 T1: Surface velocity ms^{-1} after 24 hours. Bathymetry contours are also shown.

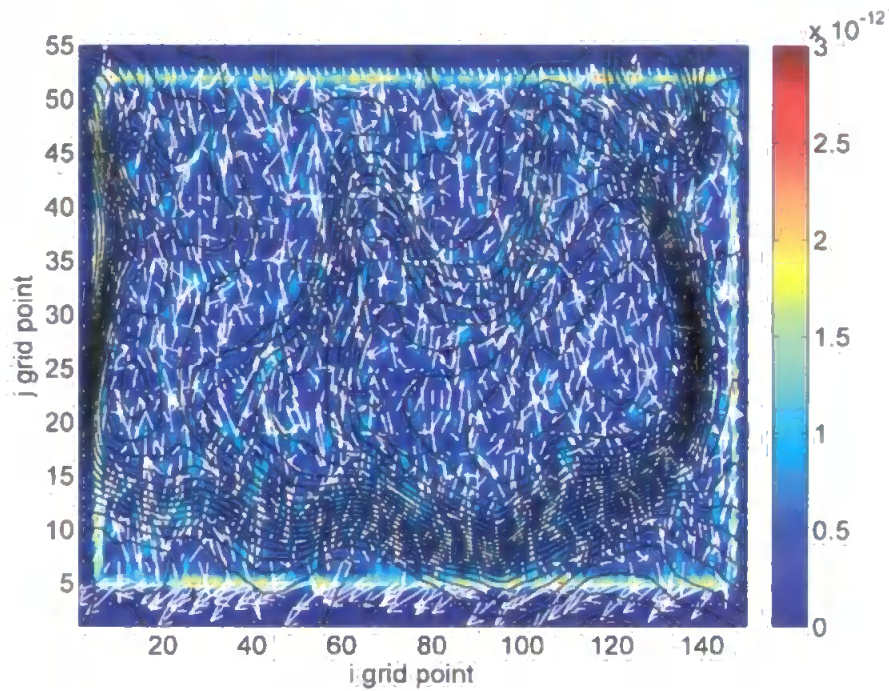


Figure 5.2 T1: Surface velocity ms^{-1} after 30 days. Bathymetry contours are also shown.

5.2 Run T2

Next, in run T2, the Rockall Bank bathymetry was introduced in order to see what effect this has on the model and to check that the grid does not cause the model to become unstable, especially in regions with steep slopes. As with T1 there is no other forcing and the initial temperature and salinity field is homogeneous. Therefore we would again expect to see no significant currents produced. The code used is exactly the same as in T1, as only the bathymetry input file needs to be changed.

As with T1 the temperature and salinity fields remained constant at all times. The introduction of the steep bathymetry did cause stronger currents to be generated than in T1, but these were still small at under 1 mm s^{-1} by the end of the month-long run. These currents are initially induced in areas where the bathymetry is steepest and over time they split into several eddies. Figure 5.3 shows the surface currents early in the run, after 24 hours, and we can see that the strongest currents are along the slope at the bottom of the image. In Figure 5.4, showing the surface currents after one month (the end of the run), we see that numerous eddies have formed from the original current although the magnitude has not changed over the course of the run. These currents

are also almost constant with depth as illustrated by Figures 5.5 and 5.6 which show the currents at 900 m. We can see that they are very similar to the surface currents in Figures 5.3 and 5.4. From these results we conclude that although the bathymetry does have some impact on the model, the currents that are generated are small enough to be ignored.

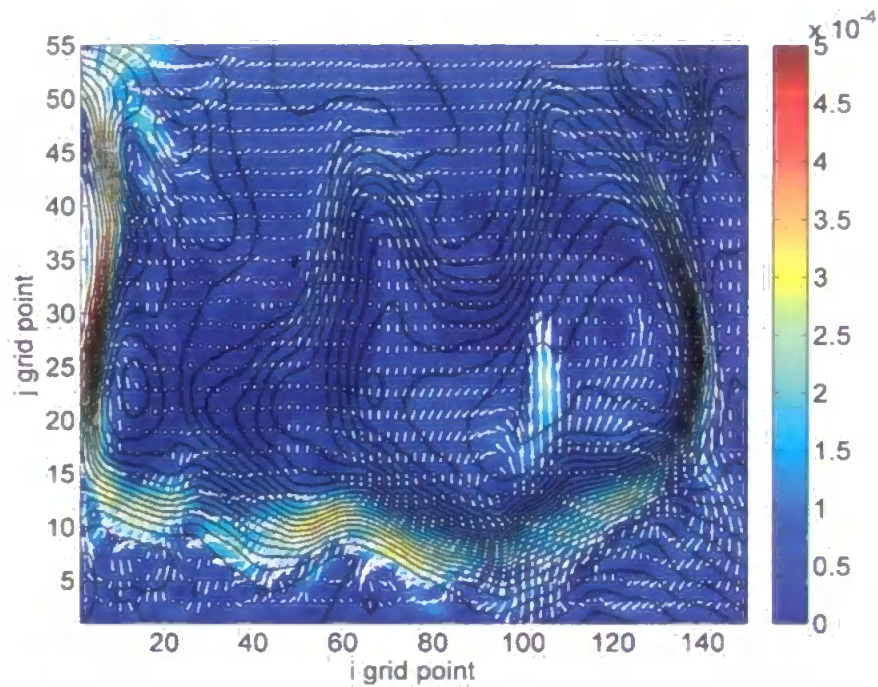


Figure 5.3 *T2: Surface velocity ms^{-1} after 24 hours. Note that the strongest currents occur where the bathymetry is steepest. Bathymetry contours are also shown.*

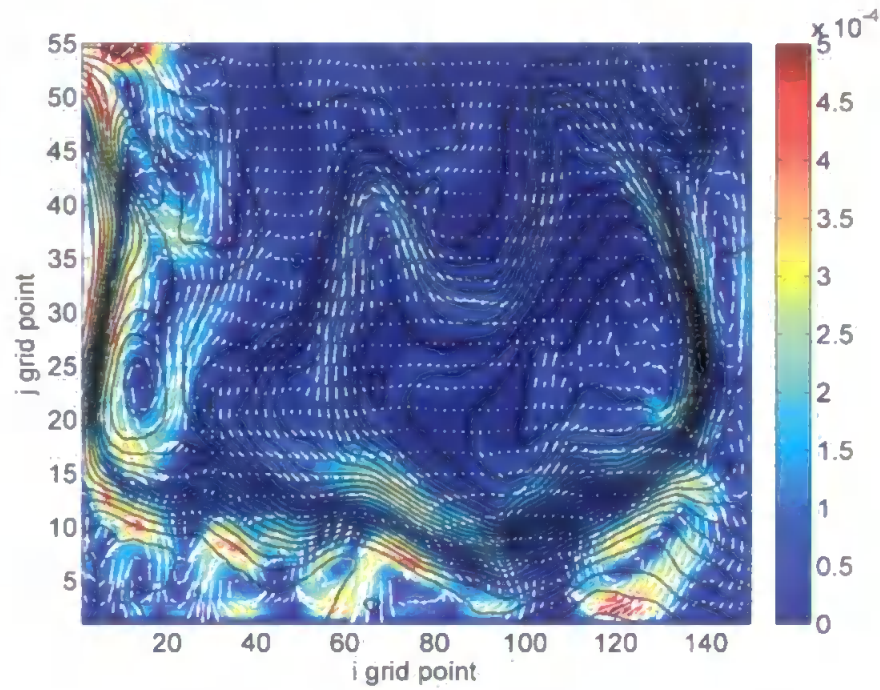


Figure 5.4 *T2: Surface velocity ms^{-1} after 30 days. The current along the South of the bank area has degenerated into different eddies. Bathymetry contours are also shown.*

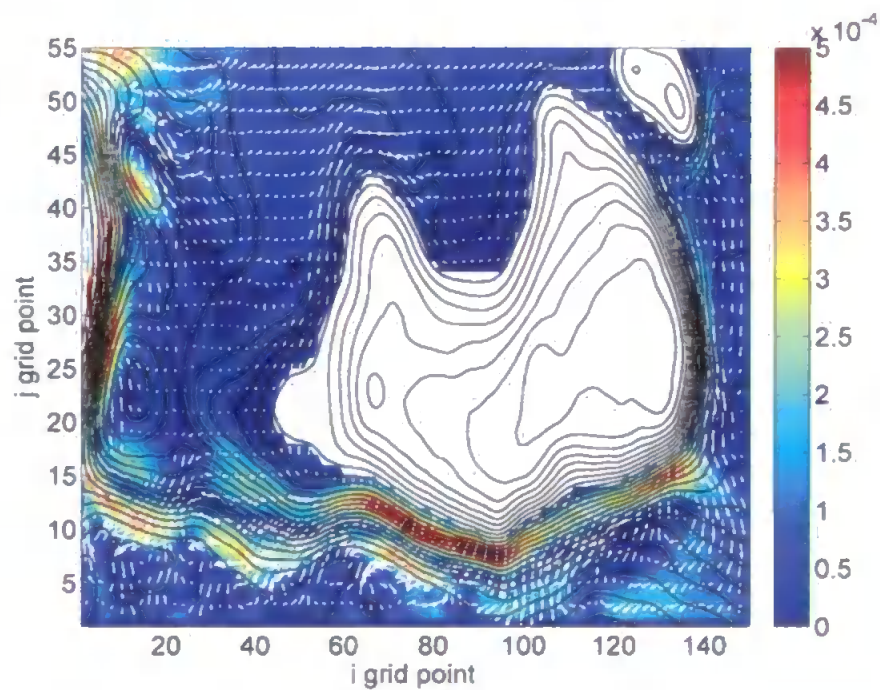


Figure 5.5 *T2: Velocity ms^{-1} at 900m after 24 hours. Bathymetry contours are also shown. The large white areas are where the water depth is less than 900m.*

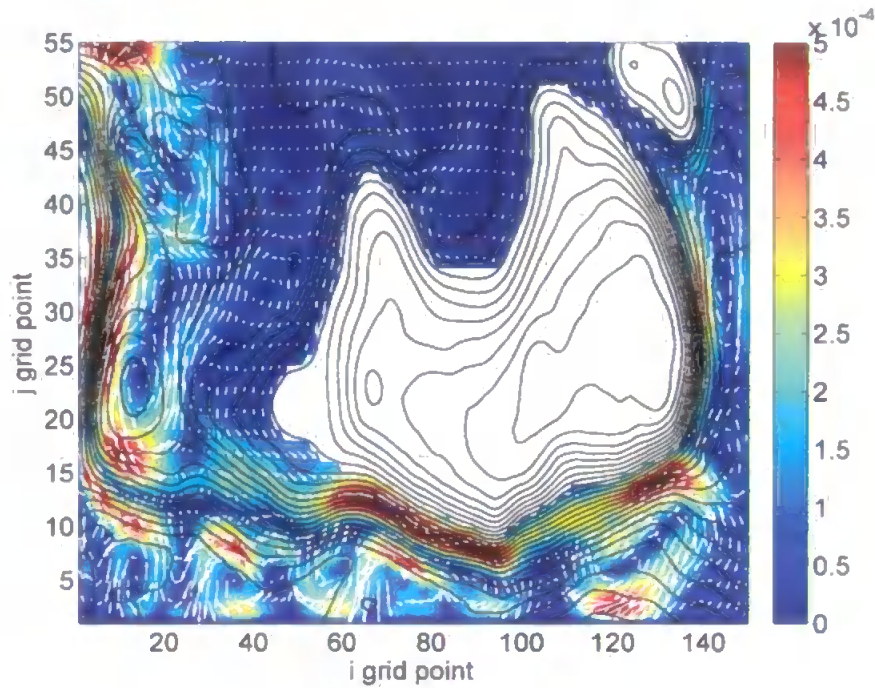


Figure 5.6 *T2: Velocity ms^{-1} at 900m after 30 days. Bathymetry contours are also shown. The large white areas are where the water depth is less than 900m.*

5.3 Run T3

The T3 series of runs all introduce forcing in the form of the initial density distribution by using the Rockall Bank bathymetry and temperature and salinity. They each use slightly different other settings. The first in this series, T3, is identical to T2 except that the climatological temperature and salinity initial input is used. The function of this run is to check that the model is stable with a realistic density distribution. T3 was run for the same length as the longest expected full runs (1st November–30th June) in order to ensure that the model would remain stable over the life of the full runs. These runs allow us to confirm that the steep bathymetry is not causing errors in the generation of the horizontal pressure gradient, as discussed in §3.4.1 earlier on page 44. The other reason for these runs is to provide initial currents for the full model runs later.

The kinetic energy per unit volume is shown in Figure 5.7. We see that it initially appears to stabilise at around 250 hours, but then rises further in a large peak between 500 and 1000 hours. This corresponds to an increasing current speed in a small area over the shallowest part of the bank. Figure 5.8 shows an example of the surface velocity during this time. There is a clear area of increased velocity over the Bank, on the right hand

side of the image.

The kinetic energy then begins to decrease again, returning to approximately the same value as before the peak at around 1800 hours (mid January). This increased current over the Bank also dissipates during this time. From this point there are no further extreme changes in kinetic energy, although it does not remain constant. In order to use T3 as a warm start condition for the full runs it is necessary to wait for the currents to 'spin up'. However, in the time that this takes the density distribution also would be significantly deformed; this makes it less than ideal for use as a warm start file because the resulting currents would not be compatible with the initial density. This is illustrated by Figure 5.9 which shows the how the surface temperature has changed after 75 days (after the peak in kinetic energy that we saw earlier). We see that the surface temperature has in general cooled down significantly. Run T3A was subsequently created to provide a more suitable run to provide initial currents to the full runs, as it allows the currents to spin up but without losing the initial density field. Therefore the currents generated by this run will be more suitable for starting the full runs, as they will be consistent with the full runs' initial density pattern.

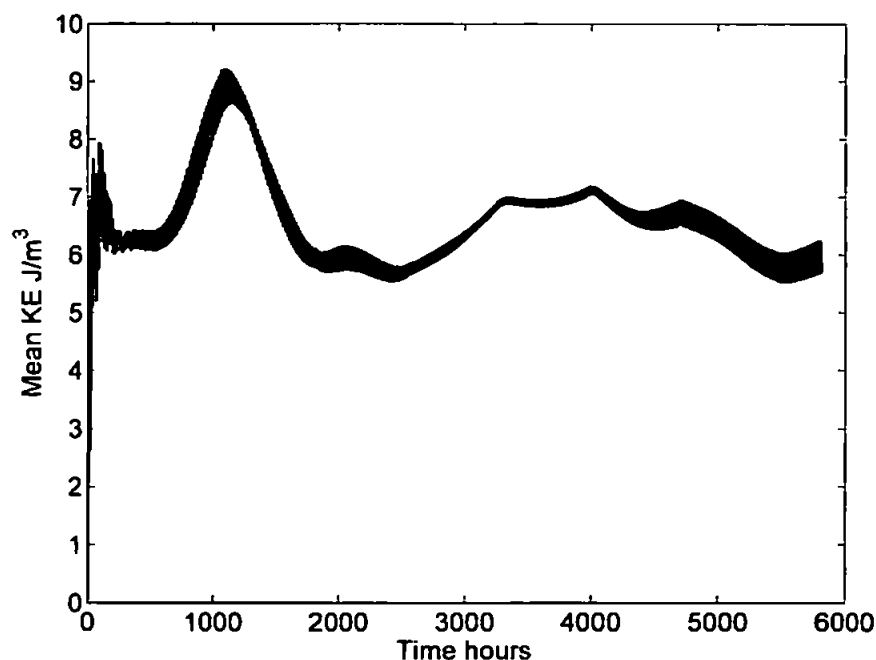


Figure 5.7 T3: Kinetic energy per unit volume

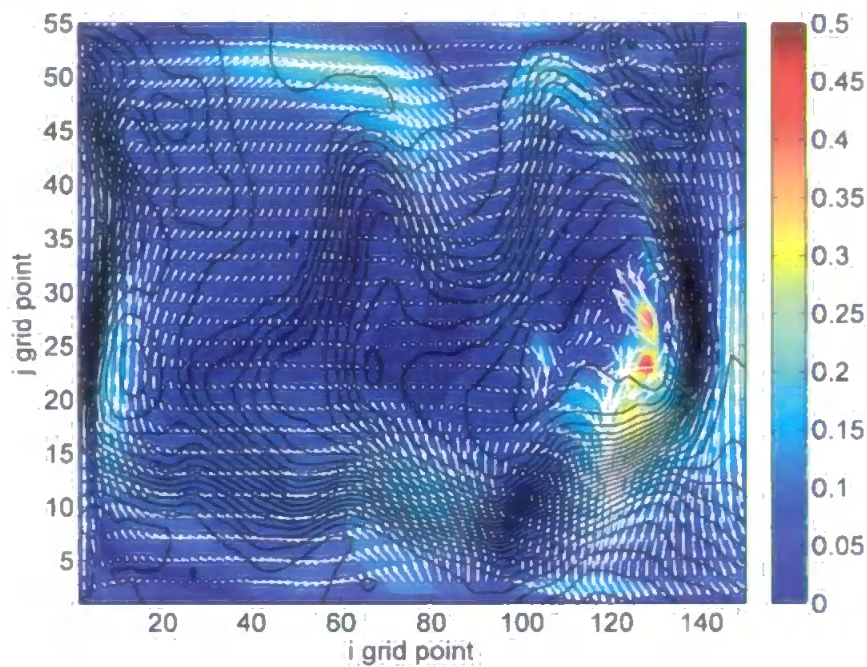


Figure 5.8 *T3: Surface velocity ms^{-1} at 60 days, during the kinetic energy peak. Bathymetry contours are also shown. Note the high velocity just over the shallowest part of the Bank.*

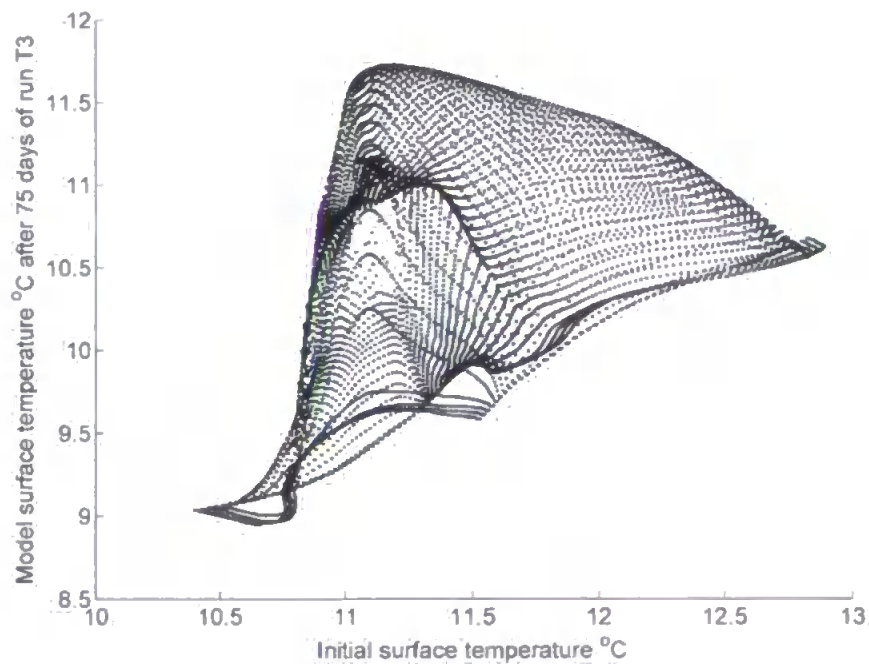


Figure 5.9 *T3: Comparison of initial surface temperature $^{\circ}\text{C}$ and model output from 75 days. There has clearly been significant alteration.*

5.3.1 T3A

T3A is similar to T3 in that the only forcing is provided by the density distribution, but with the added restriction that the temperature and salinity were forced to remain unaltered over the duration of the run by resetting them to their original values at the end of each baroclinic timestep. As the output data are written slightly before the temperature and salinity are reset, for simplicity, there are some small differences between the initial temperature and the outputs. These differences are extremely small however, and may be ignored. This is illustrated by Figure 5.10 which, similarly to Figure 5.9, shows the surface temperature at the end of run T3A compared to the temperature at the start. This is representative of the other depth levels. We see that the temperature is virtually unchanged.

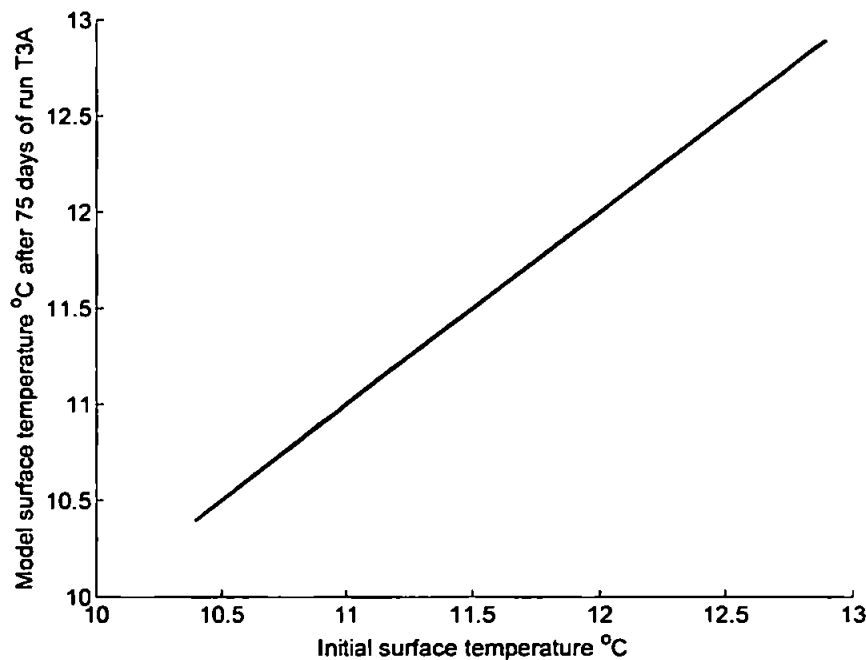


Figure 5.10 T3A: Comparison of initial temperature (at all points of the domain) °C and model output from 92 days. Although this plot only shows the surface temperature, this is representative of other levels.

The kinetic energy per unit volume in this run is significantly more settled than it was in T3. Figure 5.11 shows the kinetic energy from run T3A, and we see that after the initial 'spin up' it settles down relatively quickly and begins to converge around a constant value after around 250 hours. A checkpoint file after 500 hours of this run was used to provide initial currents to the full runs described in the next chapter.

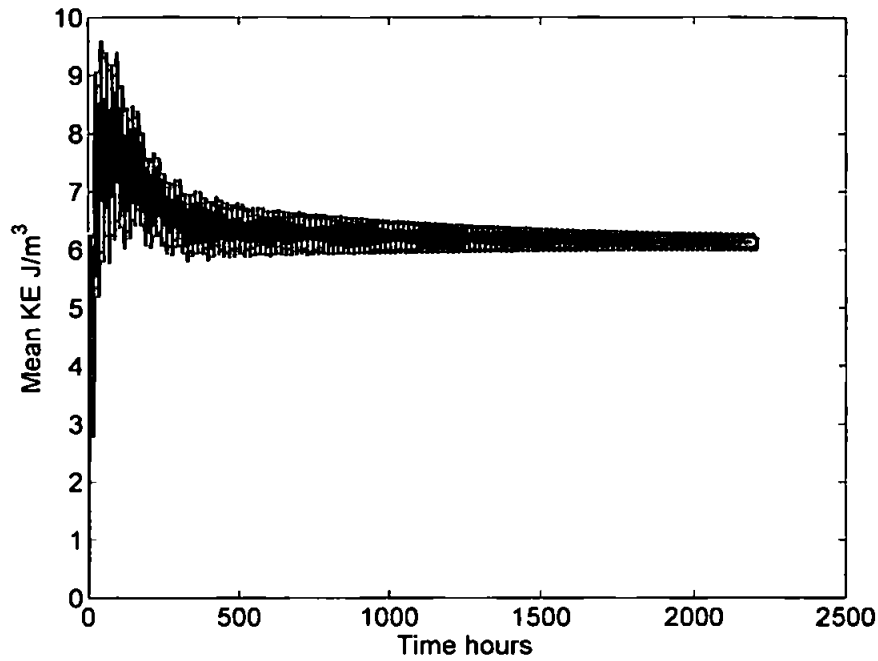


Figure 5.11 T3A: Kinetic energy per unit volume

5.3.2 T3C

Run T3C uses identical code and input files to T3, but the timesteps are changed from 200s and 20s to 100s and 10s in order to check that this does not have a significant effect on the model results. The ideal timestep to use is one that does not use too much computer power, but is in a range where the results are not dependent on the timestep used.

The kinetic energy results of T3C are almost identical to T3 such that when the two are plotted together the lines cannot be distinguished. This indicates that the 200s/20s timesteps are suitable, as it is quicker to run than 100s/10s but they are within a range where the results do not change when the timesteps are changed. These timesteps are also compatible with the Courant-Friedrichs-Lewy (CFL) condition. This is a necessary, but not sufficient, condition for model stability (Dyke, 2001) and is given by:

$$C = c \frac{\Delta t}{\Delta x} < 1 \quad (5.1)$$

where C is the Courant number, c is the fastest expected wave speed, and Δt and Δx are the time and space step lengths. In other words, this condition states that the grid

size must be sufficiently large (or the timestep sufficiently small) such that waves cannot pass across a grid square quicker than the timestep.

We have a barotropic timestep of 20s and the minimum horizontal grid spacing is approximately 4500 m. The fastest barotropic waves would be generated by the tide which behaves as a shallow water wave with speed $c = \sqrt{gh}$. With maximum depth approximately 2800 m this gives the maximum possible barotropic wave speed as 165 ms^{-1} . Using Equation 5.1 we therefore obtain a Courant number $C=0.7$ which satisfies the condition.

5.3.3 T3D

Similarly to T3C, run T3D also changes the timesteps, but this time they are increased to see if further computing power can be saved. Initially 250s and 25s were tried. Although this still satisfies the CFL condition, with Courant number 0.9, the increased timestep caused the model to crash after only a few minutes. 220s and 22s were then used instead and the model completed the 3 month run.

However, although the model ran without crashing with these larger timesteps, the results show that it is not behaving stably. Comparing the kinetic energy to that of T3 (with timesteps 200s and 20s) there is little difference for the first 500 hours, but after this point they diverge with the kinetic energy from T3D continually increasing (Figure 5.12). This shows that T3D is unstable and the timesteps used were too large.

From the results of T3C and T3D we deduce that the timesteps of 200s and 20s are around the maximum values that will produce stable results. In this regard they are ideal timesteps to use as they use the least computing time possible without sacrificing the stability of the model.

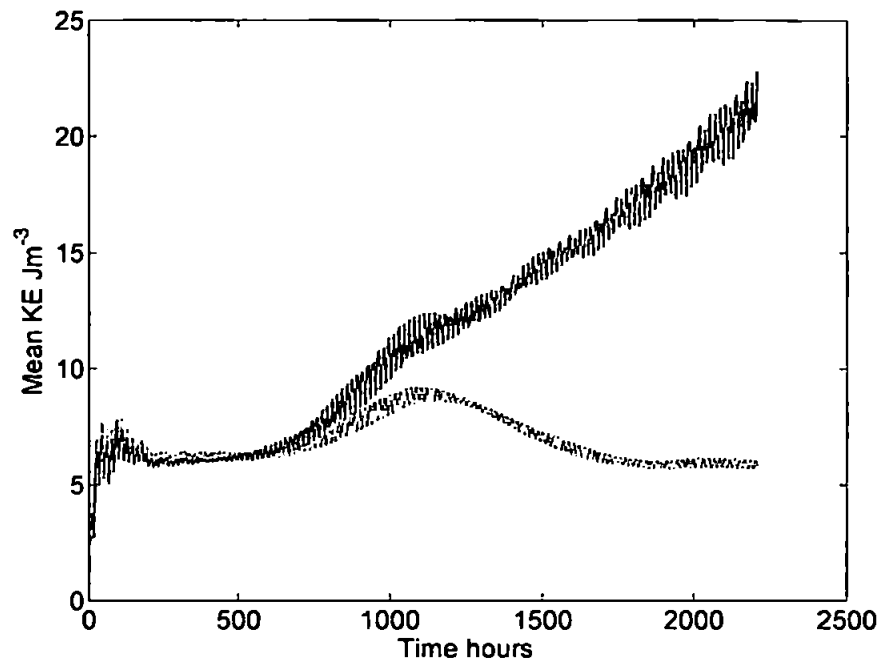


Figure 5.12 T3A: Mean kinetic energy per unit volume for T3D (solid) compared to T3 (dashed)

5.4 Run T4

Run T4 goes back to the homogeneous temperature and salinity field of run T2 (with the Rockall Bank bathymetry) and introduces tides. This run is to check that the barotropic tide is introduced correctly. The only changes made to the code from T1 were:

- Tides are switched on (using the preprocessor)
- The velocity and temperature/salinity data are outputted every hour rather than every 24 hours. Additionally, sea surface elevation is outputted.

As with previous runs starting from homogeneous initial temperature and salinity, they remained constant across the domain. The sea surface elevation at two points, one on the Bank and one away from it, is illustrated in Figures 5.14 and 5.15. The location of these points is shown by Figure 5.13. We see from these Figures that there is a clear semidiurnal tidal signal in both areas, with a frequency of 12 hours. We also see evidence of the diurnal tide in the differing amplitude of the two daily semi-diurnal peaks. This is especially prominent at point B. In Figure 5.15 we see a significant difference in the magnitude of the two daily semi-diurnal tides, especially the low tide. Figure 5.14 for

point A shows a similar pattern, but the difference is smaller and the high tide shows little diurnal variation during spring tides. This is at odds with previous results (Huthnance, 1974) which found that the diurnal tide was stronger on the western side of the Bank (close to point A) than at stations on top of the Bank (close to point B).

Similar patterns are seen in the velocity components as illustrated by Figures 5.16 and 5.17 which show the v component of surface velocity at the same points at the elevation Figures (plots of the u component are very similar in nature). We again see that both Figures show a semi-diurnal signal with a diurnal contribution, but the diurnal signal is even more marked at point B (Figure 5.17) than it was in the sea surface elevation (Figure 5.15).

Because this run uses a homogeneous temperature and salinity field only the barotropic tide is present. Therefore, the currents are almost constant with depth. Figure 5.18 shows an example velocity profile for point A over a 24 hour period. The velocity is always constant down to around 900–1000 m at which point it begins to deviate due to the influence of the sea bed. This contrasts with the example from the shallower point B shown in Figure 5.19 where the influence of the sea bed can be seen in much of the water column (although the currents are still relatively similar with depth).

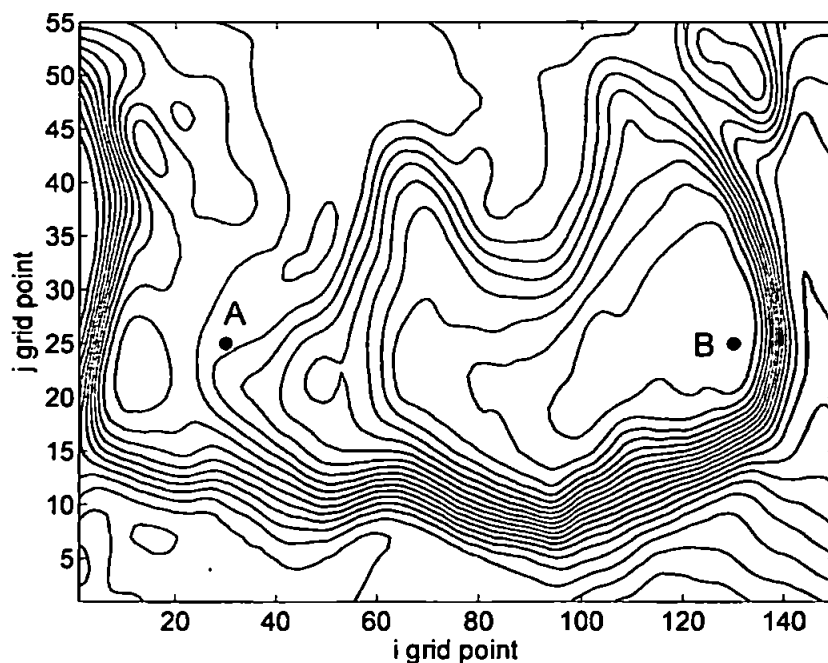


Figure 5.13 T4: Location of the points for which data are plotted

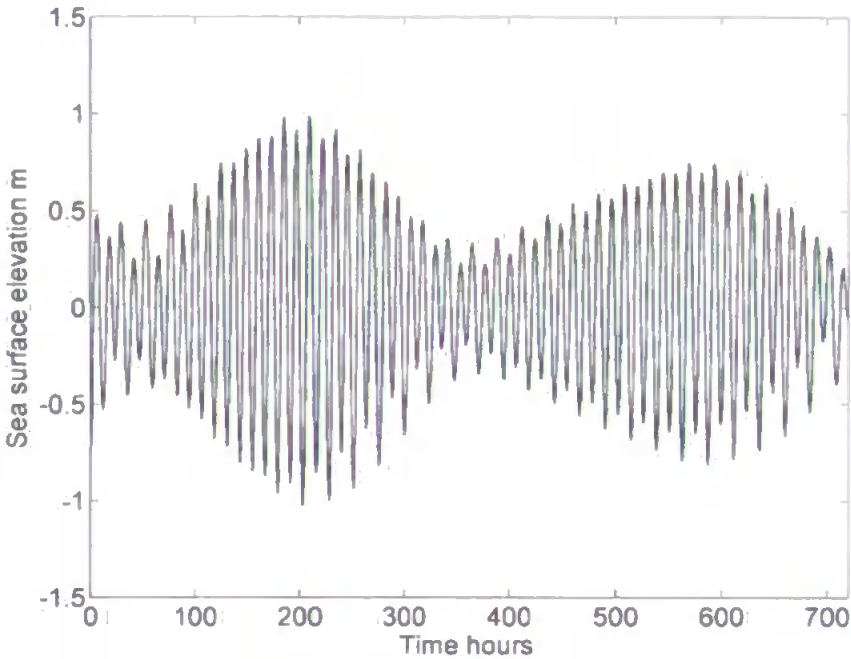


Figure 5.14 T4: Sea surface elevation m at point A.

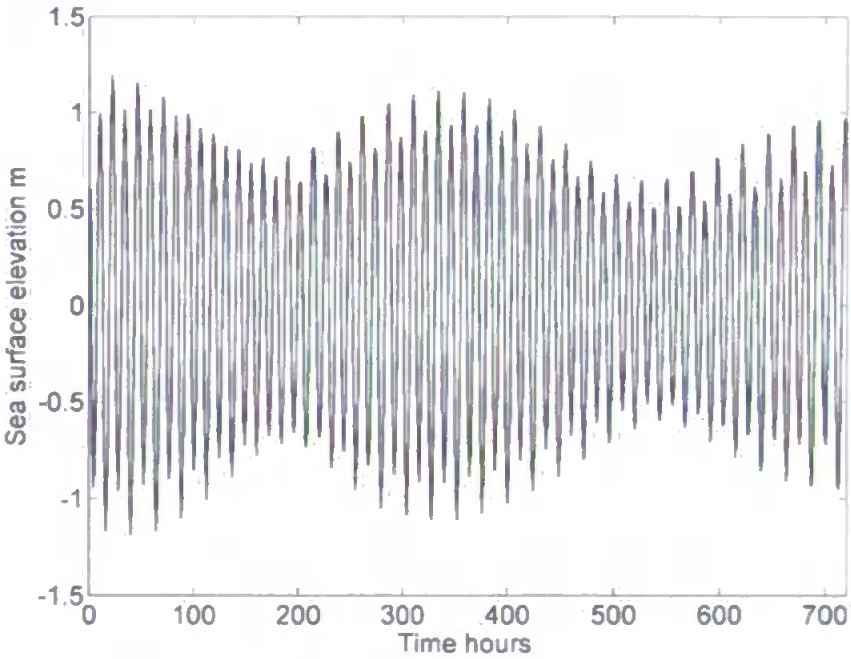


Figure 5.15 T4: Sea surface elevation m at point B.

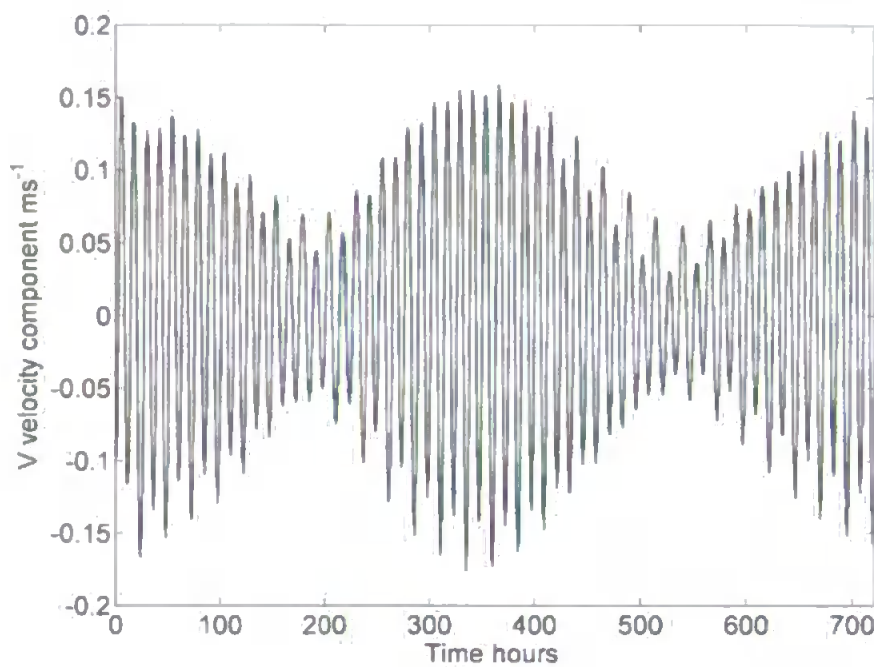


Figure 5.16 T4: Surface v velocity ms^{-1} at point A.

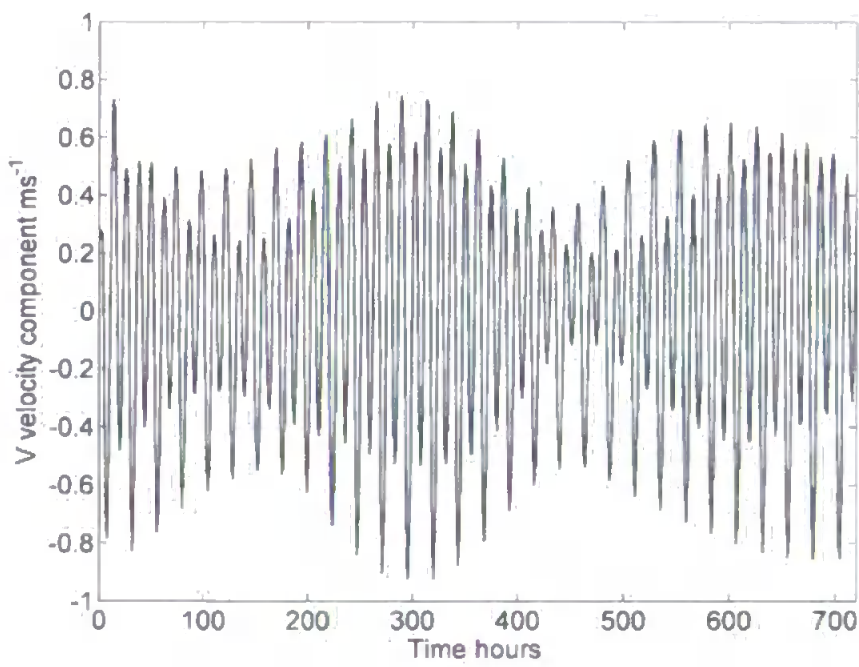


Figure 5.17 T4: Surface v velocity ms^{-1} at point B.

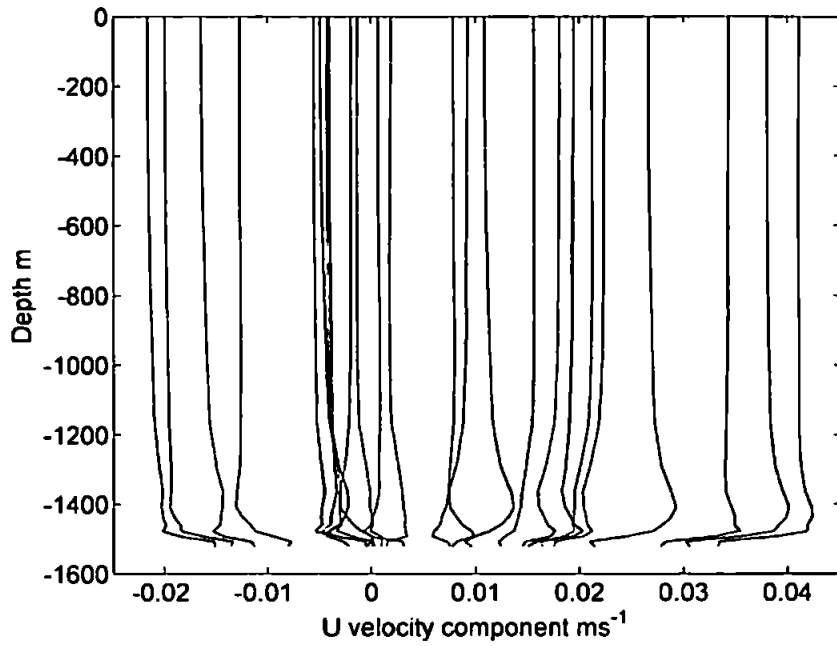


Figure 5.18 T4: Velocity ms^{-1} profiles at point A over a tidal cycle. Darker lines are earlier profiles; lighter lines are later.

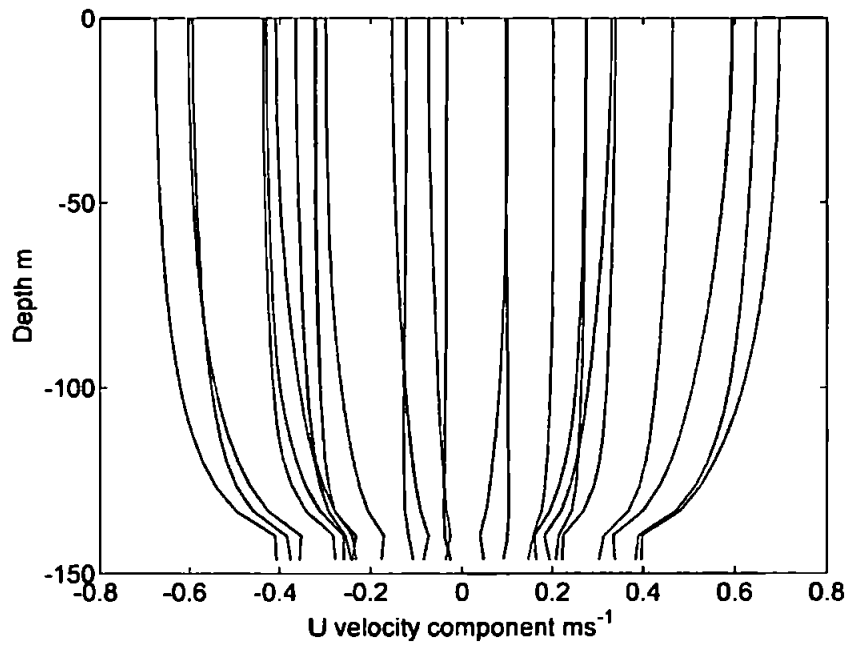


Figure 5.19 T4: Velocity ms^{-1} profiles at point B over a tidal cycle. Darker lines are earlier profiles; lighter lines are later.

5.5 Run T5

T5 includes wind forcing with the Rockall Bank bathymetry and homogeneous density distribution. The duration was 3 months. The changes made over the T1 code were:

- The wind forcing switched on, but heat fluxes remain off. The preprocessor is used for both of these tasks.
- Outputs every 6 hours

The temperature and salinity distribution remained constant for the entire run, and so the currents were generated by entirely the wind (excluding the very small bathymetry-induced currents we saw in run T2).

Figure 5.21 shows a representative example of the velocity distribution with depth. This example is from the end of the model run, 31 January, from the point located at the dot in Figure 5.20. We see in Figure 5.21 that the highest currents are found near the surface, and the current speed then decreases with depth. We can also see that the direction of the near surface current changes in a clockwise direction as the depth increases. This Ekman spiral pattern is what we would expect from currents that are generated by surface wind (Pond and Pickard, 1983).

The kinetic energy output indicates that the magnitude of the currents is related to the wind speed. This is more clearly seen in the kinetic energy of the surface level. Figure 5.22 shows the mean kinetic energy per unit volume of the basin, the kinetic energy per unit volume of just the surface layer, and the mean wind speed throughout the length of the run. We can see that when there are peaks in the wind speed there are also peaks in the kinetic energy, and that the kinetic energy of the surface layer is more sensitive than that of the basin as a whole. The correlation coefficient between the wind speed and surface kinetic energy is 0.45. This is lower than might be expected, primarily due to oscillations in the kinetic energy signal with frequency of around 16.5 hours. Nevertheless it is a positive correlation and the author believes it shows a link between the wind speed and surface kinetic energy.

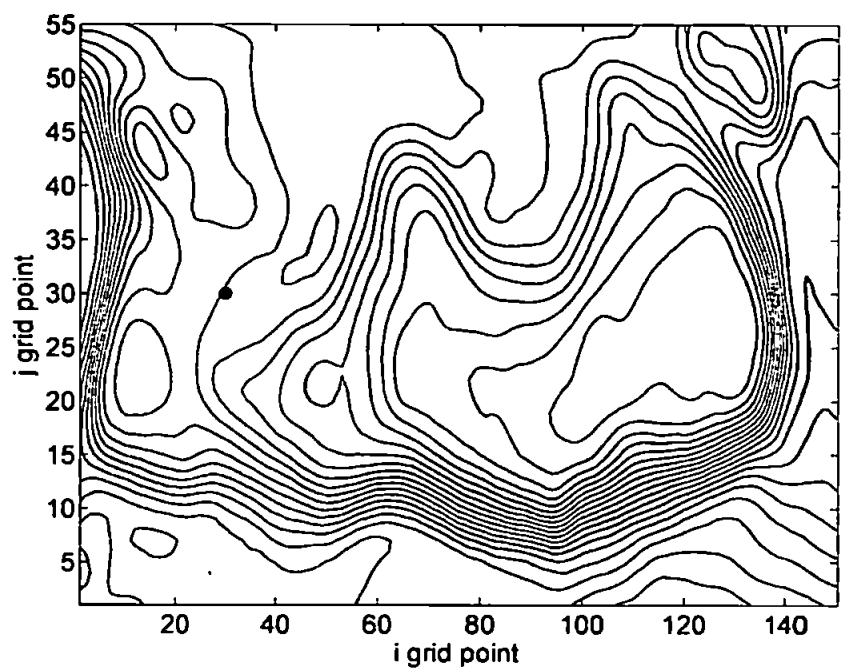


Figure 5.20 T5: Location of the example point used for Figure 5.21.

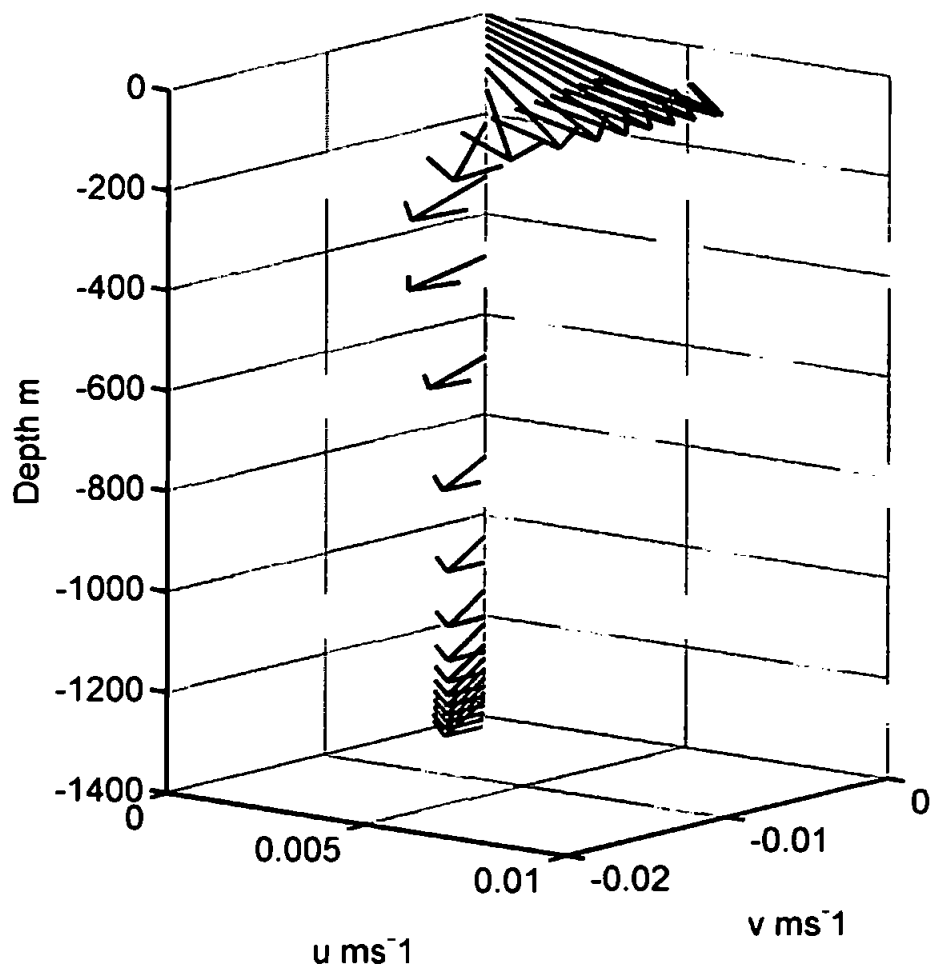


Figure 5.21 T5: An example velocity ms^{-1} profile illustrating the Ekman spiral.

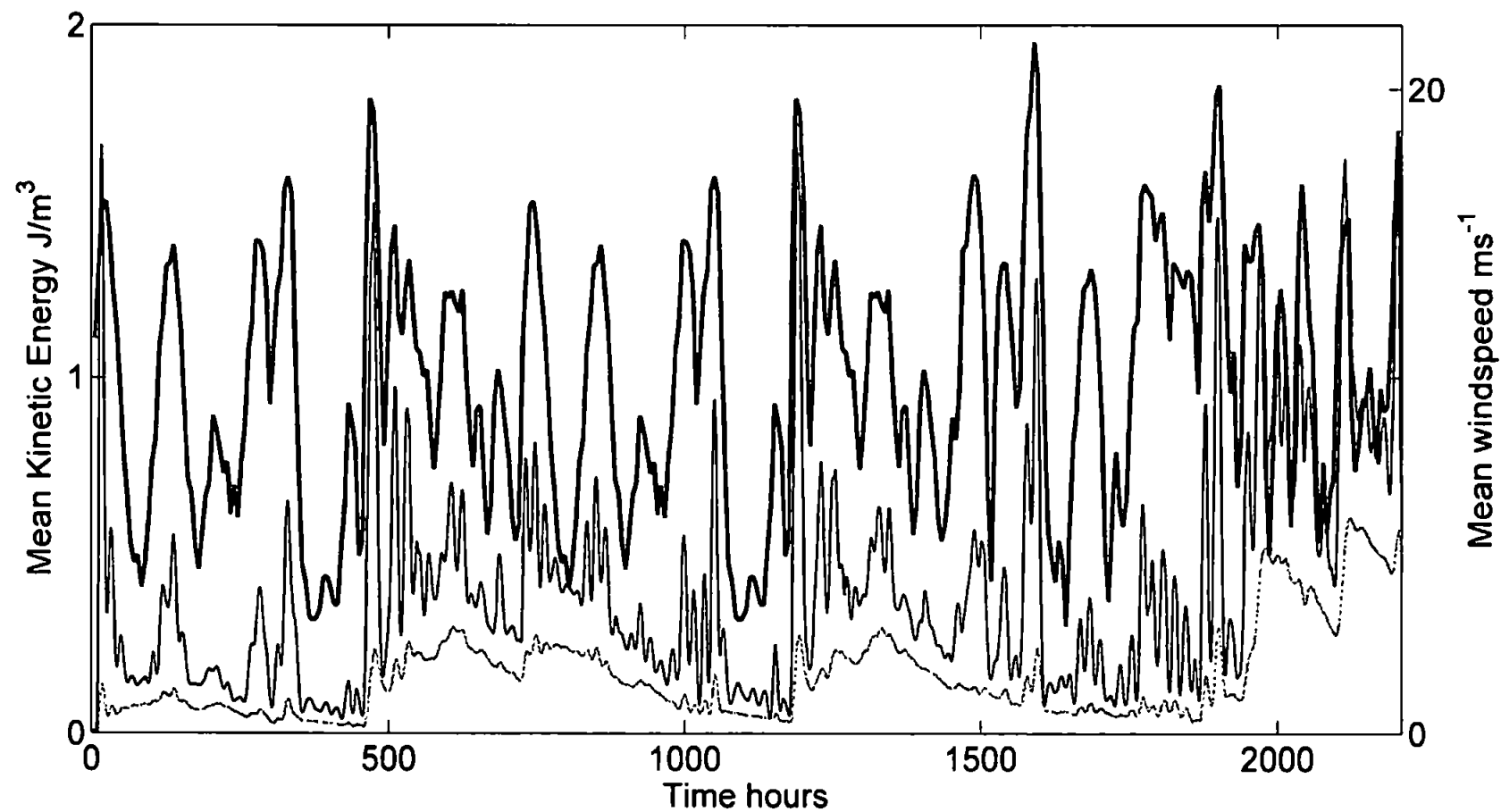


Figure 5.22 T5: Kinetic energy per unit volume compared to the mean wind speed. The thick black line is the wind speed, the thinner line is surface kinetic energy and the grey line is mean kinetic energy over the entire basin.

5.6 Run T6

This run incorporates the surface heat flux, still with homogeneous initial temperature. The changes to the code to achieve this were:

- Heat flux switched on, using the preprocessor.
- As the heat flux calculation requires wind speed, it was necessary to also select the wind forcing option in the preprocessor to ensure that the wind data are read in. The code was modified so that the wind data are used only in the heat flux calculation, and do not directly generate currents as it did in run T5.
- Similarly the air pressure is also read in but only used in the heat calculation.

The salinity remained constant throughout the entire run, whilst the temperature distribution was of course modified by the surface heat flux. The surface water begins to cool almost immediately. Figure 5.23 shows the surface temperature after only 8 days (i.e. 8 November). We can see that already the water over the Bank is starting to become cooler than the water in surrounding areas. This cold patch continues to grow and cool until the coldest part is approximately 13°C , compared to the initial 15°C . This state is reached after around 6 weeks, in mid-late December. Figure 5.24 shows an example from 22 December, by which time the cold water has reached 13°C , and we can see that the cold water is centred over the shallowest area of the Bank.

In the remainder of the run the water does not then get any colder than this, but it remains present for the whole duration. Figure 5.25 shows the surface temperature at the end of the run, 31 January, and by comparing it to Figure 5.24 we see that the general pattern is the same. The water has not cooled further. Although the cold patch remains present for the duration of the run it does of course move around. The water circulates anti-cyclonically around the top of the Bank, in accordance with observations and theory (e.g. Ellett *et al.*, 1986; Huthnance, 1986).

Of course, cooling and subsequent dense water formation at the surface ensures that the water column remains well mixed, in order to maintain stability. An example temperature cross-section is shown in Figure 5.27. We can see that the water column over Rockall

Bank is relatively cold, and is well mixed from surface to bottom. The location of this cross-section is indicated by the horizontal line on Figure 5.26.

The currents induced in the model have typical values of $0.1\text{--}0.4\text{ ms}^{-1}$, with isolated areas reaching 0.8 ms^{-1} , even in the deeper water. These values are reasonable, although larger than observations from Rockall Bank. We would not however expect realistic currents to be generated in this run as the density distribution is not realistic. Examples of the instantaneous currents are shown in Figures 5.28 and 5.29 which show the final velocity (i.e. on 31 January) at the surface and at 500 m respectively.

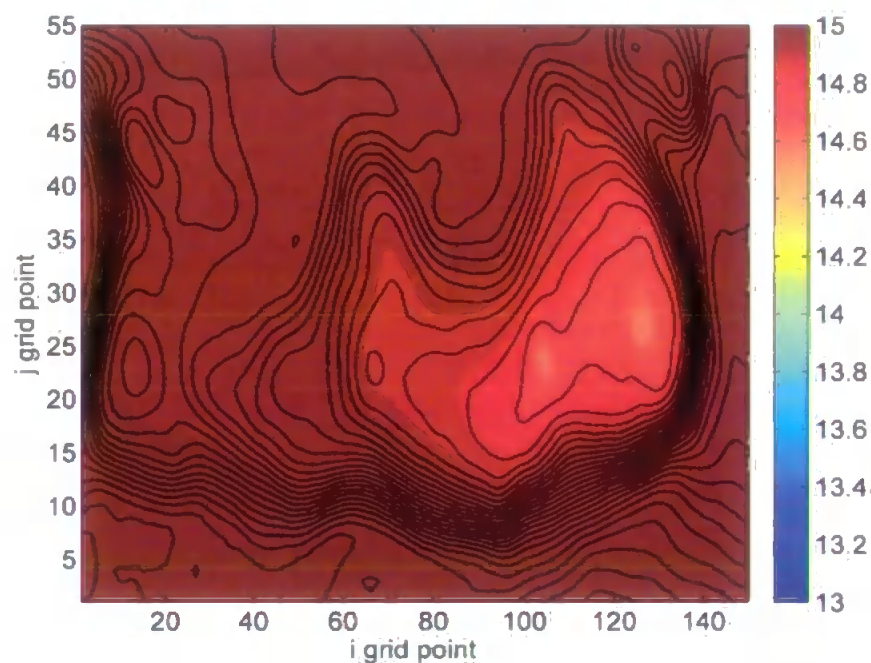


Figure 5.23 *T6: Surface temperature $^{\circ}\text{C}$ at 8 November. The cold patch is starting to form.*

Sections of potential density σ_{θ} show a clear area of denser water over the top of the bank corresponding to the colder temperature. The temperature difference was up to 2°C , which led to a density difference of up to 0.3 kgm^{-3} . The potential density of the bottom layer (which follows the topography) is the most relevant here as this gives an indication of whether the dense water can escape from the bank. Figure 5.30 shows the potential density along the bottom s-level early in the formation of the cold patch, 25 days into the run. Although the dense water is not yet fully formed it is already denser than the bottom water elsewhere in the domain. This is due to this run being initialised with a homogeneous density structure. As soon as the density over the Bank

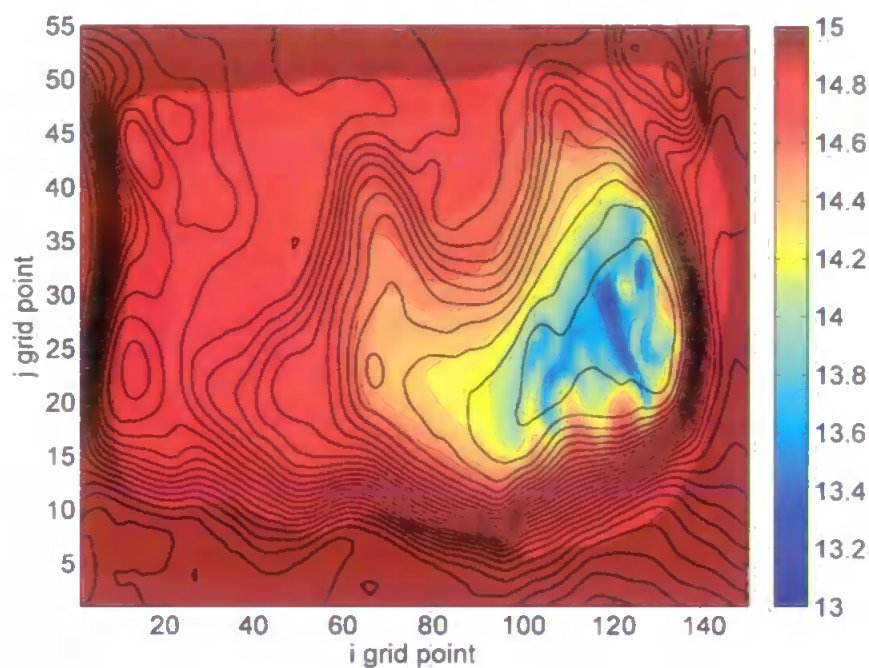


Figure 5.24 T6: Surface temperature $^{\circ}\text{C}$ on 22 December. The cold patch is fully developed.

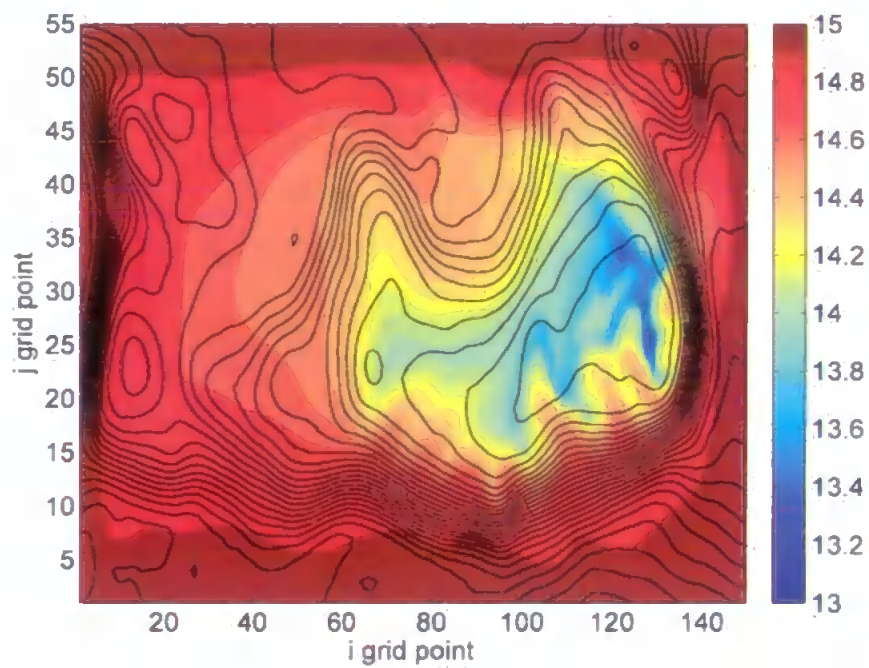


Figure 5.25 T6: Surface temperature $^{\circ}\text{C}$ on 31 January.

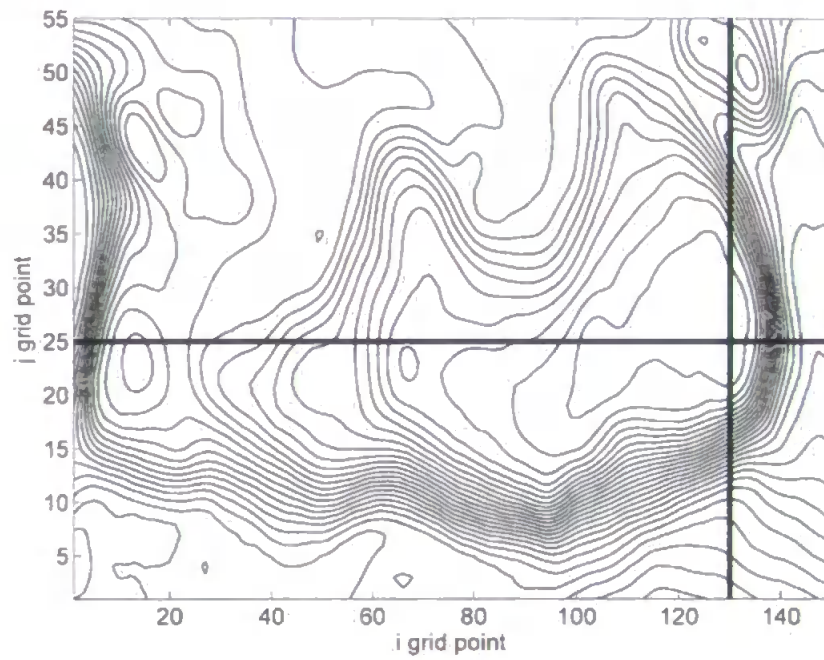


Figure 5.26 T6: Location of the cross-sections. The horizontal line is $j=25$ (used to produce Figure 5.27) and the vertical line is $i=130$ (used to produce Figure 5.34).

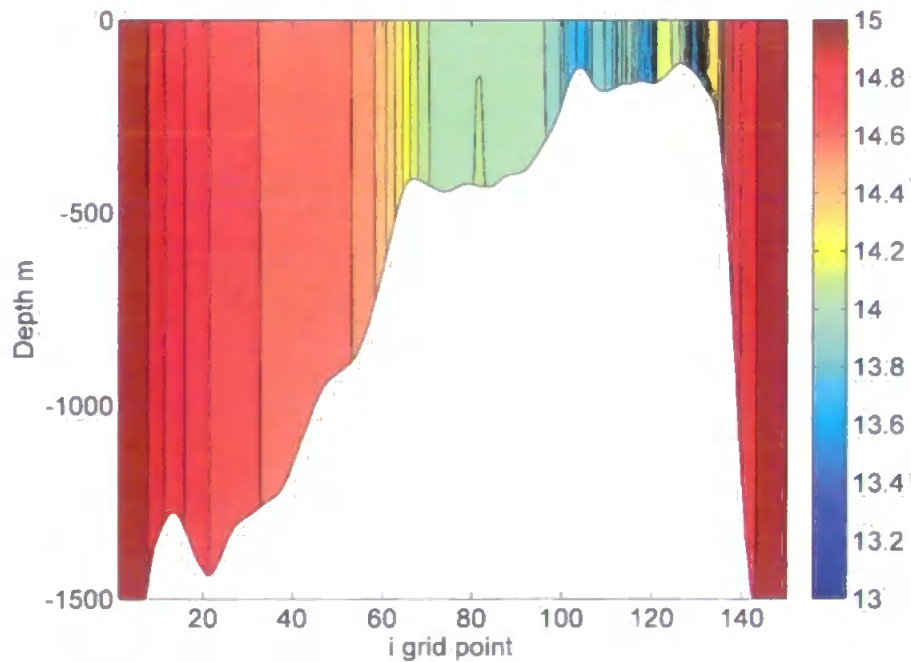


Figure 5.27 T6: Temperature $^{\circ}\text{C}$ along the section $j=25$ on 30 January.

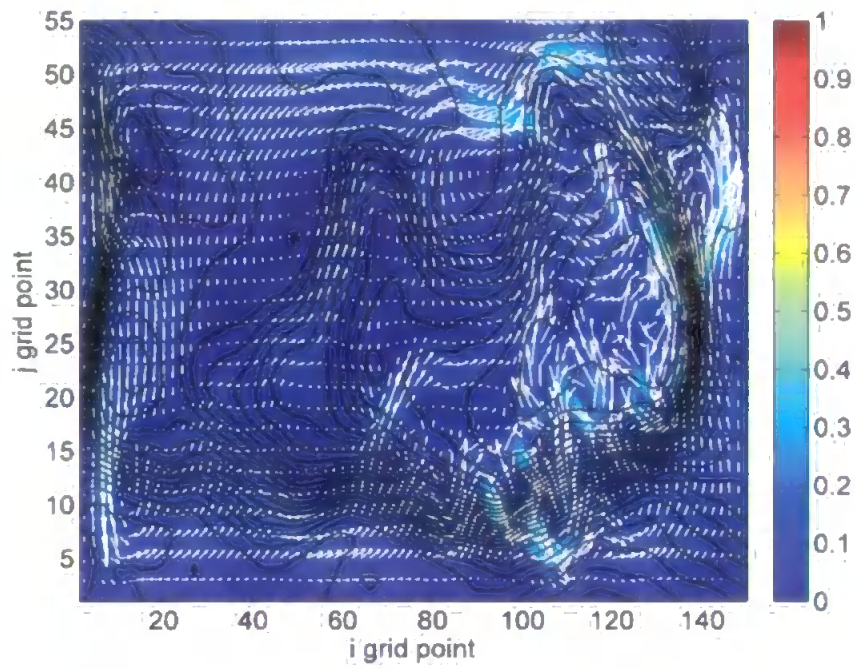


Figure 5.28 T6: Surface velocity ms^{-1} on 31 January.

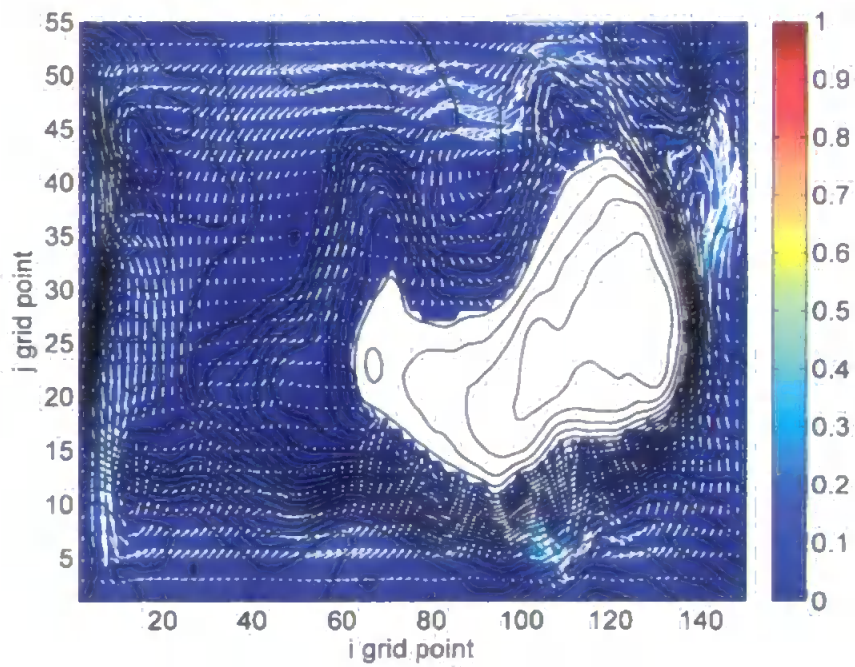


Figure 5.29 T6: Velocity ms^{-1} at 500m depth, on 31 January.

began to increase it was already denser than the deepest water that we started with. Therefore we would expect that this water will be able to sink if it reaches the slope. As time progresses the cold area grows larger, and numerous "arms" form as shown in Figure 5.31. On frequent occasions there is evidence of cascading as these arms protrude further down the slope. One such example is shown in figure 5.33. This is a close up of the bottom potential density for an area on the north east slope of the Bank over a series of 4 days (the location of the selected area is shown by the box in Figure 5.32). We can clearly see that an area of dense water crosses the bathymetry contours and protrudes down the slope. Another example is shown in the cross-section of Figure 5.34. We can clearly see an area of dense water extending down the slope. Note that the location of this section is shown by the vertical line in Figure 5.26.

These cascading events are commonly seen in this area as well as on the southern slope of the bank. These are the steepest slopes, and we do not see any cascading in this run on the shallower slope to the north/north west.

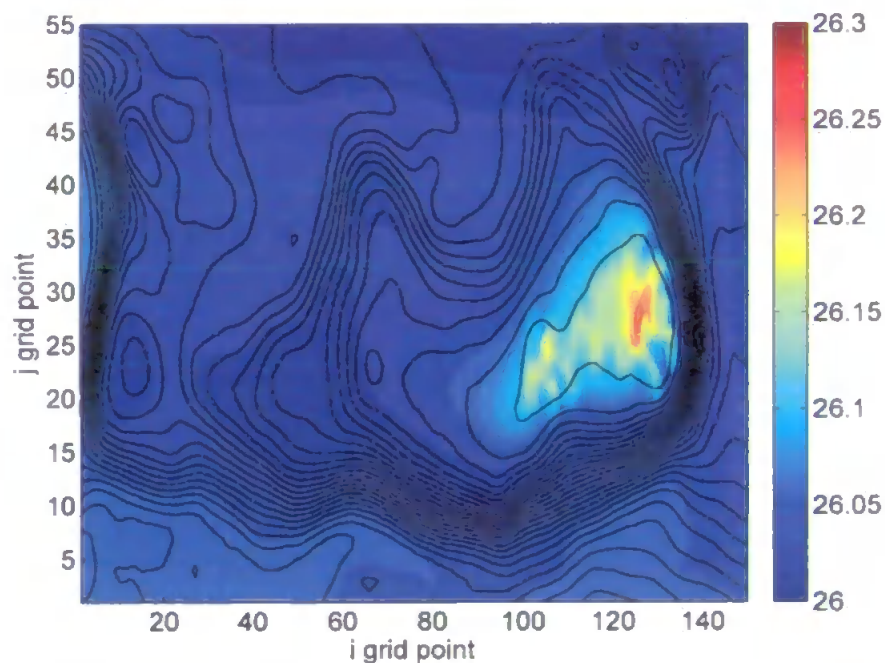


Figure 5.30 *T6: Potential density σ kgm^{-3} along the bottom s -level at 25 days.*

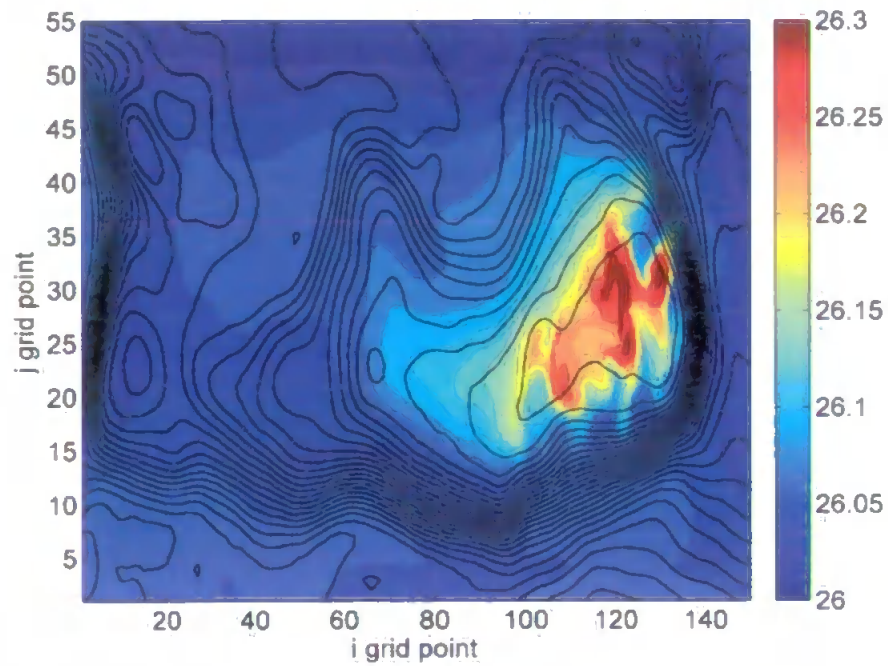


Figure 5.31 T6: Potential density σ kgm^{-3} along the bottom s -level at 48 days showing the protruding "arms".

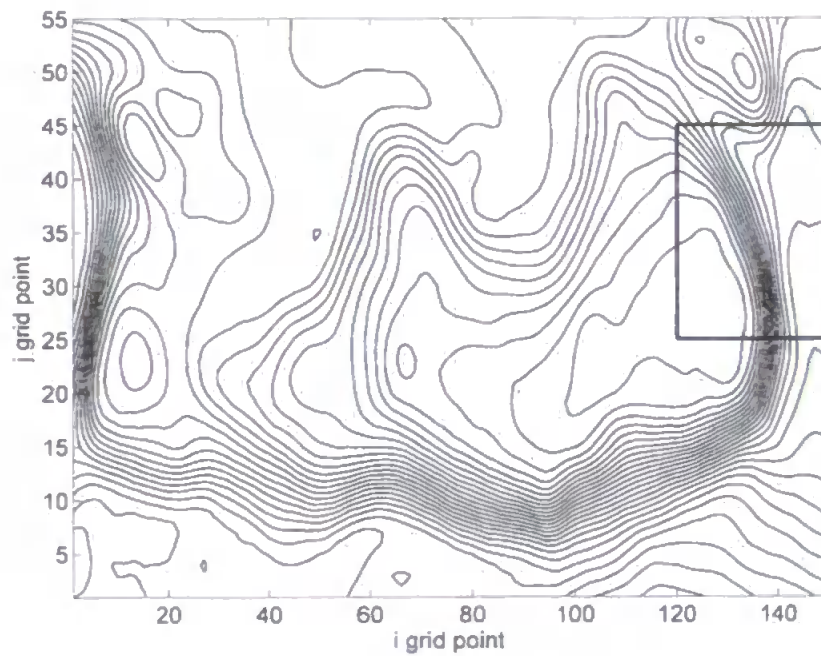


Figure 5.32 T6: Location of the close up area used in Figure 5.33.

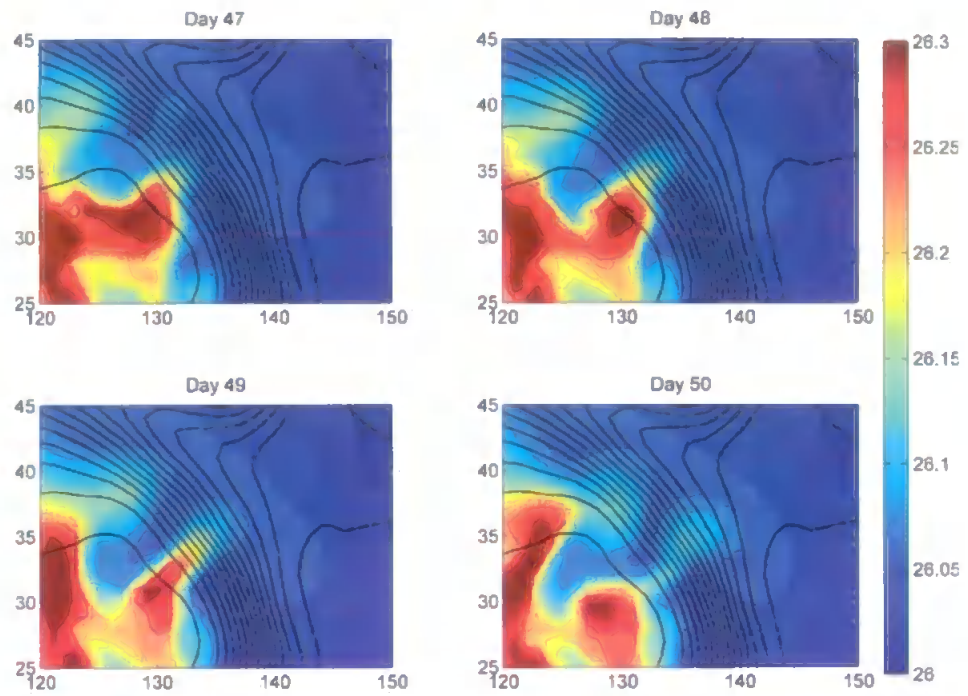


Figure 5.33 T6: Potential density $\sigma \text{ kg m}^{-3}$ along the bottom s-level from days 47–50 showing plume moving downslope. Note that the water is shallowest on the left hand side, and then deepens to the right as indicated by the contour lines.

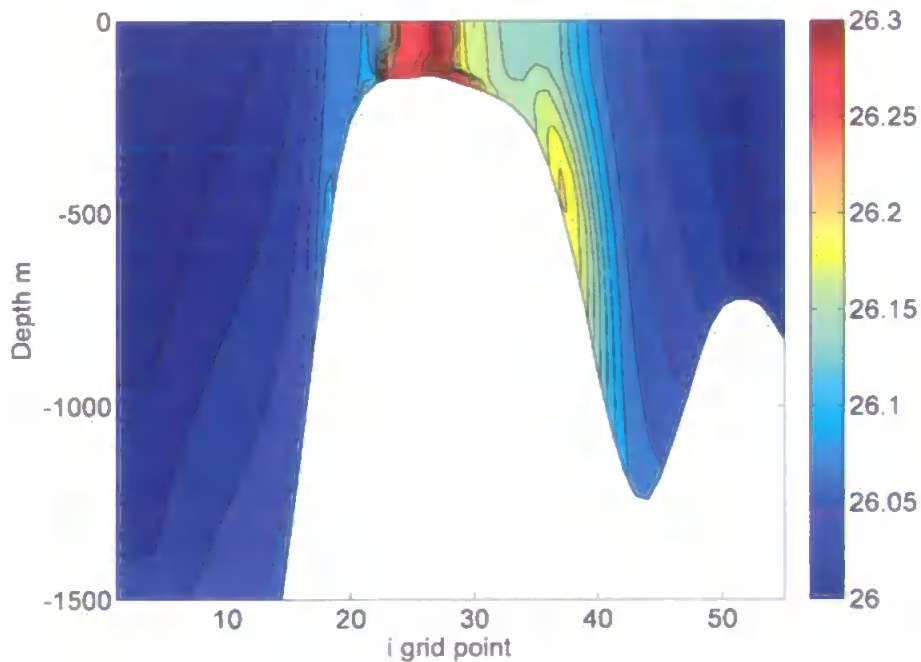


Figure 5.34 T6: Potential density kg m^{-3} along the section $i=130$ on 30 January. Note the cold water can be seen from the surface to the bank. There is an area of dense water extending down the slope of the bank.

5.7 Run T7

Run T7 is the final run with homogeneous initial temperature and salinity, and includes evaporation-precipitation balance as the only forcing. Similarly to T6, the wind speed and meteorological variables still need to be read in as they are needed to calculate the evaporation rate (the precipitation rate is provided separately). The code changes were:

- Both wind and meteorological variables are read in, but are used only in the calculation of the evaporation rate. The heat fluxes are set to zero.

Initially there is a general freshening over much of the domain (illustrated by Figure 5.35). As time progresses this changes. Figure 5.36 shows the surface salinity after 12 days. We see the salinity has returned near to its initial value 35 over a wide part of the domain, and in the shallowest area over the Bank it is slightly more saline. Later at the end of the run after 30 days, the water over the Bank has become more saline still and the rest of the domain is similar to the start value. The salinity changes involved are small however, with differences of up to 0.1 PSU only.

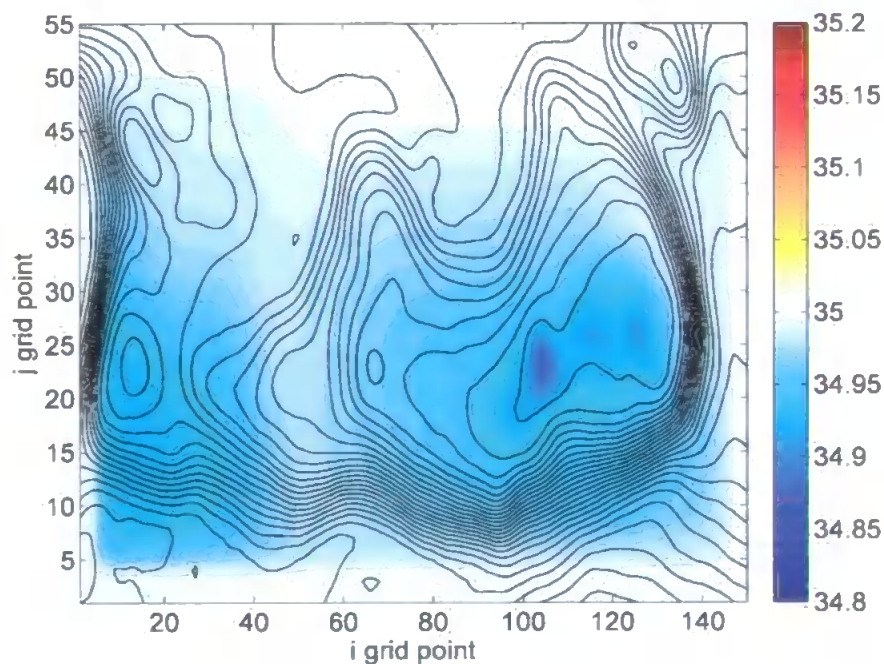


Figure 5.35 T7: Surface salinity at 5 days. General freshening can be seen.

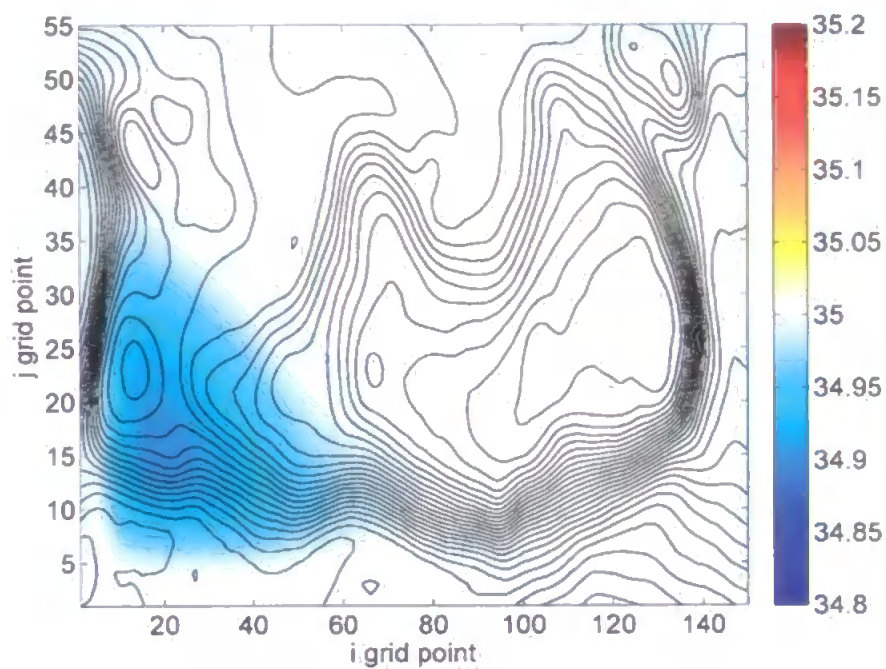


Figure 5.36 T7: Surface salinity at 12 days. Water over the bank is becoming more saline.

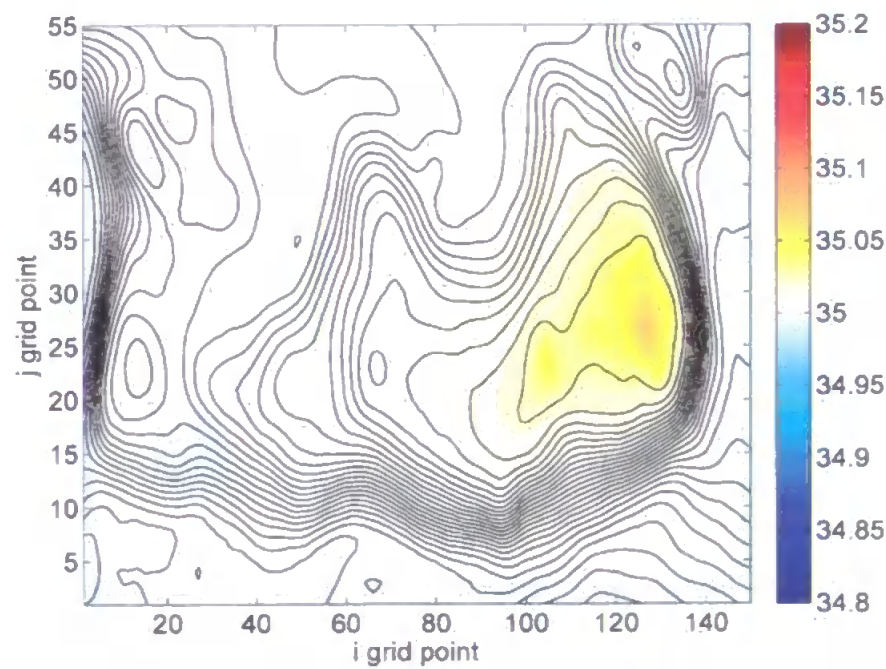


Figure 5.37 T7: Surface salinity at 30 days.

Because the salinity change is small the effect on density, and therefore circulation, is also small. The currents generated by the varying salinity reached a maximum of only $0.01\text{--}0.02\text{ ms}^{-1}$, and in most areas were even smaller than this. Figures 5.38 and 5.39 show the instantaneous velocity at the surface and at 900m respectively at the end of the run. We see that the largest currents are seen on the left hand side, adjacent to the slope and on top of the Bank.

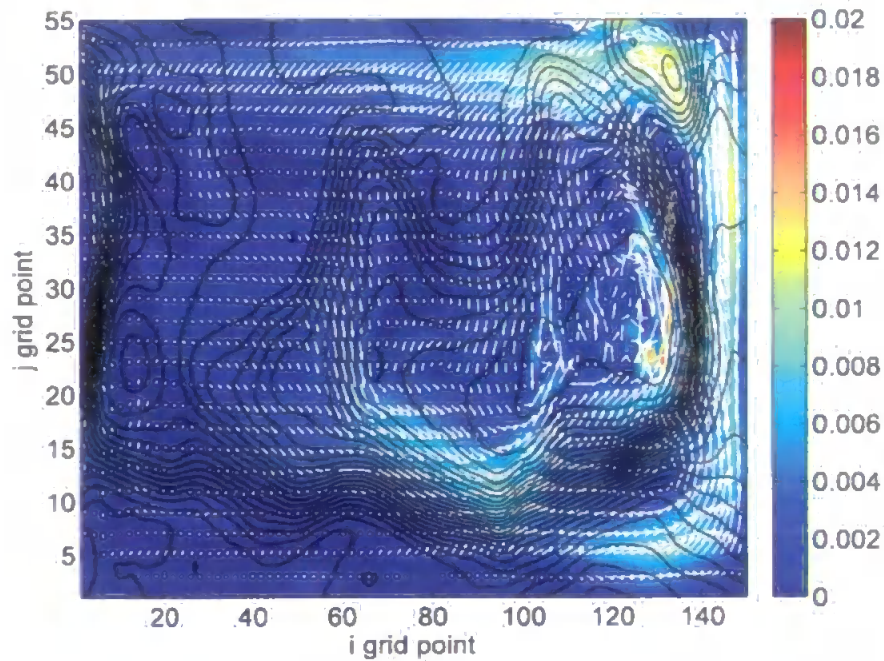


Figure 5.38 T7: Surface velocity ms^{-1} at 30 days.

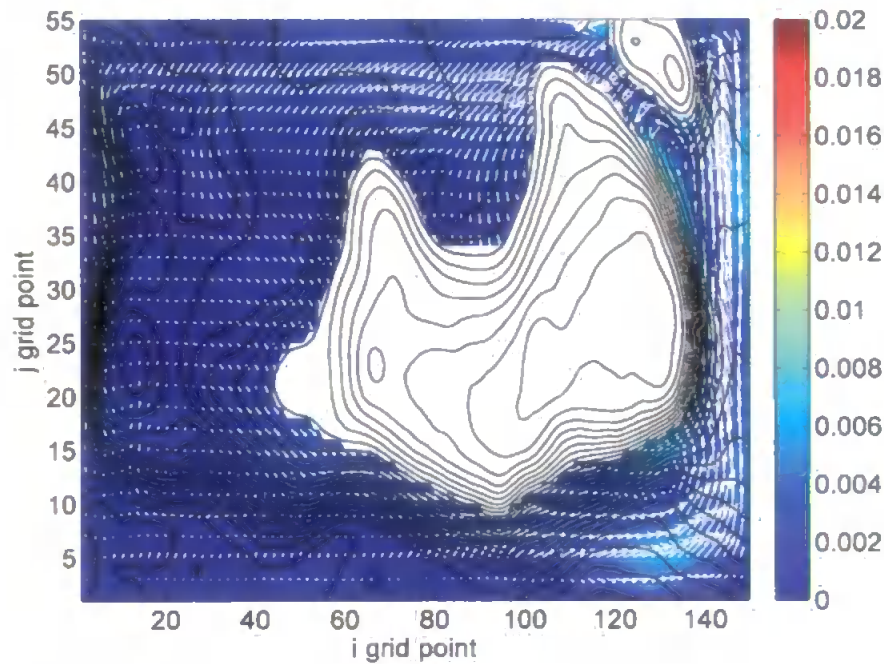


Figure 5.39 T7: Velocity ms^{-1} at 500m depth, at 30 days.

5.8 Run T8

This run is similar to T4 as it includes the tides, but it also adds the real initial density distribution which means that it includes the baroclinic tide. Therefore the code used is the same as T4, with just different temperature and salinity input files. As the baroclinic tide moves more slowly than the barotropic this run was longer than T4 and was run for 3 months.

We see a similar pattern to run T4, with a clear semi-diurnal signal present at both sample points, and a stronger diurnal modification on top of the Bank. Figures 5.40 and 5.41 show the sea surface elevation over the duration of the run for two example points. The location of these sample points are the same as the T4 plots above, and are shown in Figure 5.13. We see by comparing these to Figures 5.14 and 5.15 that the sea surface elevation is almost identical to that of run T4.

The velocity on the other hand does show some slight differences. Figures 5.42 and 5.43 show the v component of surface velocity at the same two points. These may be compared with Figures 5.16 and 5.17 for T4. We see that overall the behaviour is very similar. At both points A and B there is a strong semi-diurnal signal, with diurnal

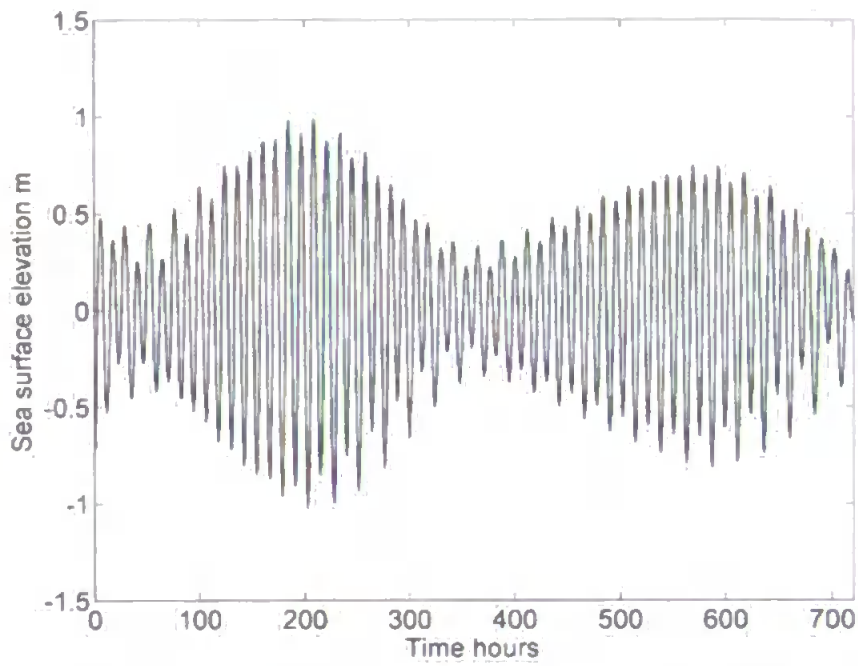


Figure 5.40 *T4: Sea surface elevation m at point A.*

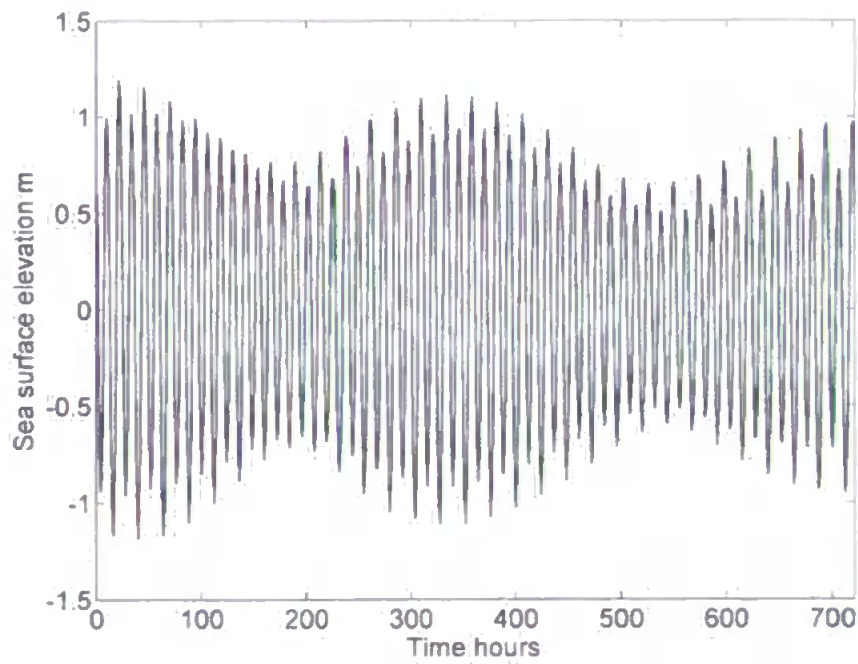


Figure 5.41 *T4: Sea surface elevation m at point B.*

modification. Again the diurnal signal is strongest at point B. The magnitude of the velocity is similar to T4 at point B, but at point A it is higher in this run with a maximum of around 0.25 ms^{-1} rather than 0.15 ms^{-1} . The magnitude during the neap periods is similar however, so we see a more extreme spring/neap difference at point A in this run T8 than we did in T4.

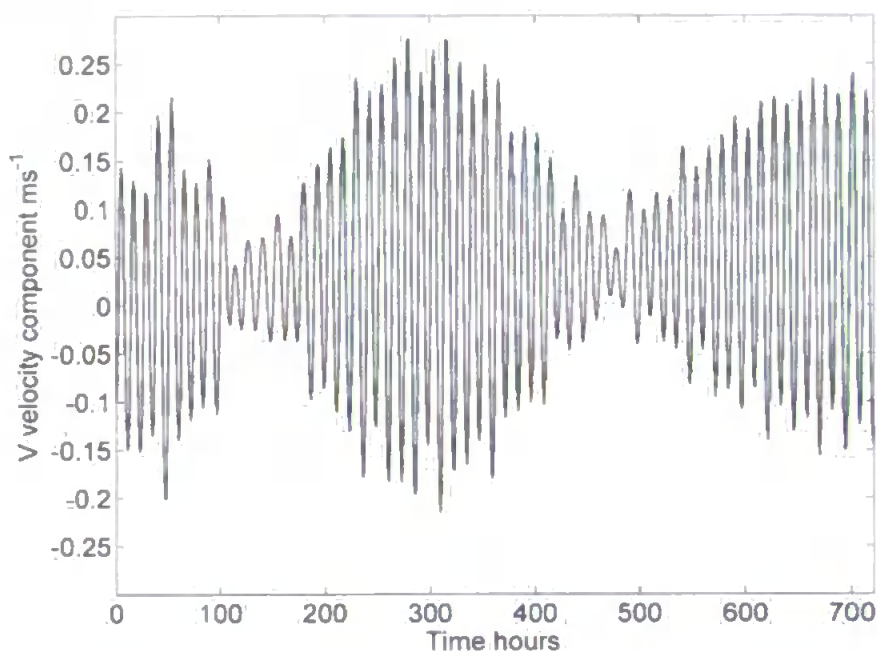


Figure 5.42 T8: Surface v velocity ms^{-1} at point A.

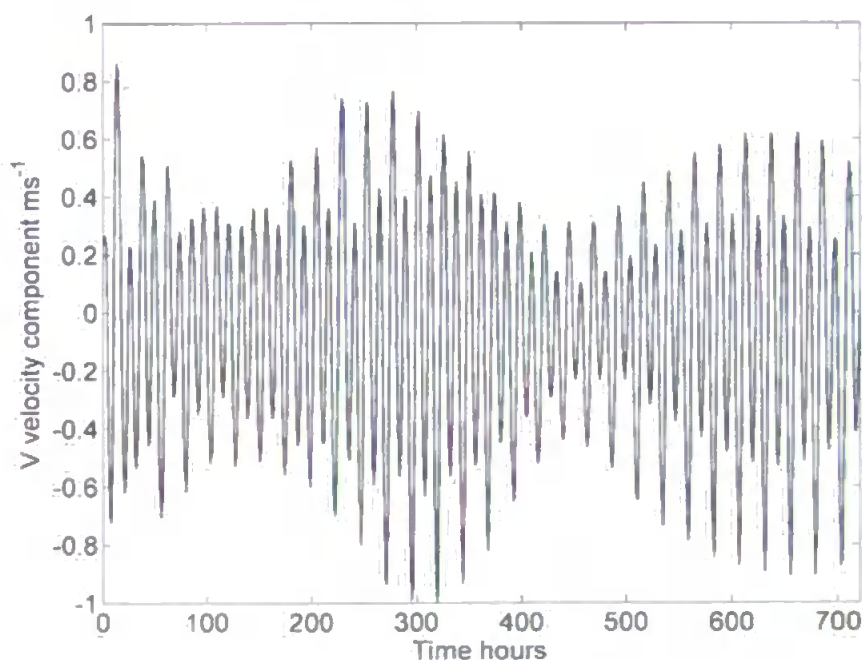


Figure 5.43 T8: Surface v velocity ms^{-1} at point B.

With the addition of the non-homogeneous density field, the currents are no longer constant with depth. Figures 5.44 and 5.45 show u velocity profiles at the same sample points as previous Figures. By comparing to Figures 5.18 and 5.19 we see that at both sample points the magnitude of the u velocity is very similar to that in T4.

In Figure 5.45, from the point over the Bank, shows that the velocity is always disrupted at around 50 m: this is the depth of the thermocline. This relationship is illustrated by Figure 5.46 which shows the u velocity and temperature profiles at this point for a single representative time. We clearly see that the change in velocity at around 50 m coincides with the change in temperature.

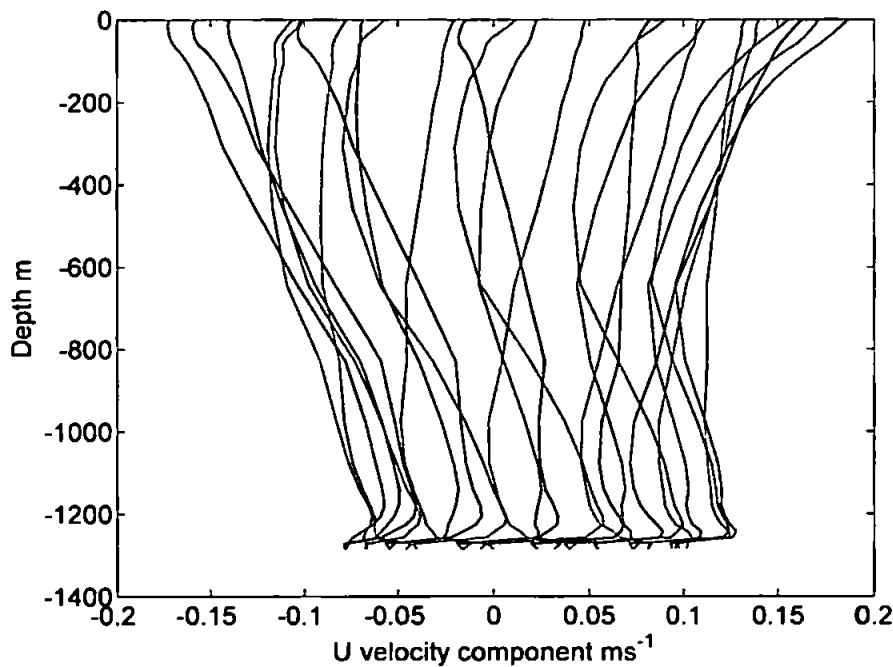


Figure 5.44 T8: u velocity ms^{-1} profiles at point A over a tidal cycle. Darker lines are earlier profiles; lighter lines are later.

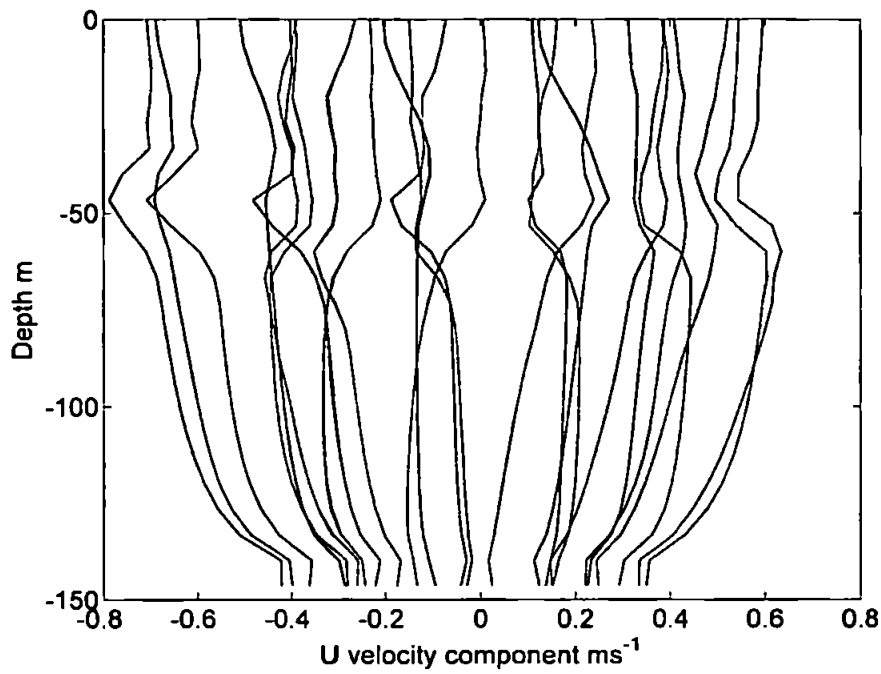


Figure 5.45 T8: u velocity ms^{-1} profiles at point B over a tidal cycle. Darker lines are earlier profiles; lighter lines are later.

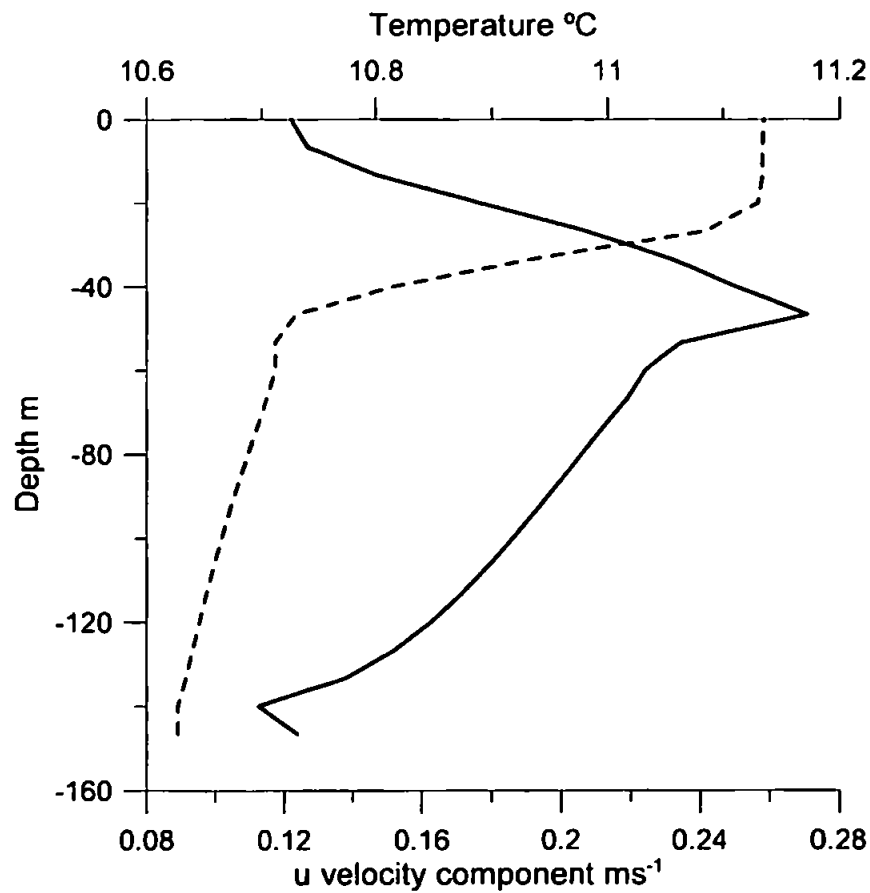


Figure 5.46 T8: Temperature and u velocity profiles at point B
T8: Temperature $^{\circ}\text{C}$ (dashed line) and u velocity ms^{-1} (solid line) profiles at point B

5.9 Run T9

The final run in this series, T9, includes both real initial temperature and salinity and the surface heat flux in order to check that the cold water patch could form successfully with the realistic initial density field. This run uses the same code as T6 but with different input files. Initially T9 was run for 3 months, as with T6, but the results suggested that a longer time was needed for the dense water to form. It was subsequently rerun for 8 months (1st November–30th June).

Similarly to run T6, the salinity remained unchanged and the temperature was altered due to the surface heat flux. However, in this case the difference between the water temperature and the air temperature is smaller. This has led to a less dramatic cooling of the water over the bank, although it does still become colder and therefore denser than the adjacent water. It also takes longer for the temperature difference to appear. This is illustrated by Figure 5.47 which shows the surface temperature on 22 December. This is the same time as Figure 5.24 for run T6 (note that different colour scales have been used). We can see that in T6 there is a fully formed surface cold patch over the Bank. In T9 however, there is no sign at all of the cold water patch until around ten days later. The water continues to cool until it reaches its minimum temperature in early March. This is significantly later than in T6, where the minimum temperature was reached in late December. Figure 5.48 shows an illustrative example from 1 March where the surface cold patch is now fully formed in T9. The maximum temperature difference between the surface water over the Bank and over the water on the left hand side of the image is again around 2°C , similar to T6. However, in this T9 the water to the top right is much more similar in temperature to the water over the Bank. The surface cold water in T9 begins to disappear around late April as spring arrives and surface warming takes place. By mid May the cold water is no longer visible from the surface.

The density structure is rather different to that of T6 due to the non-homogeneous initial temperature distribution. In run T6, the water at depth had the same potential density as the surface water, so only a small amount of cooling was necessary to make the water over the bank denser than the deep water. This meant that the cool water from the

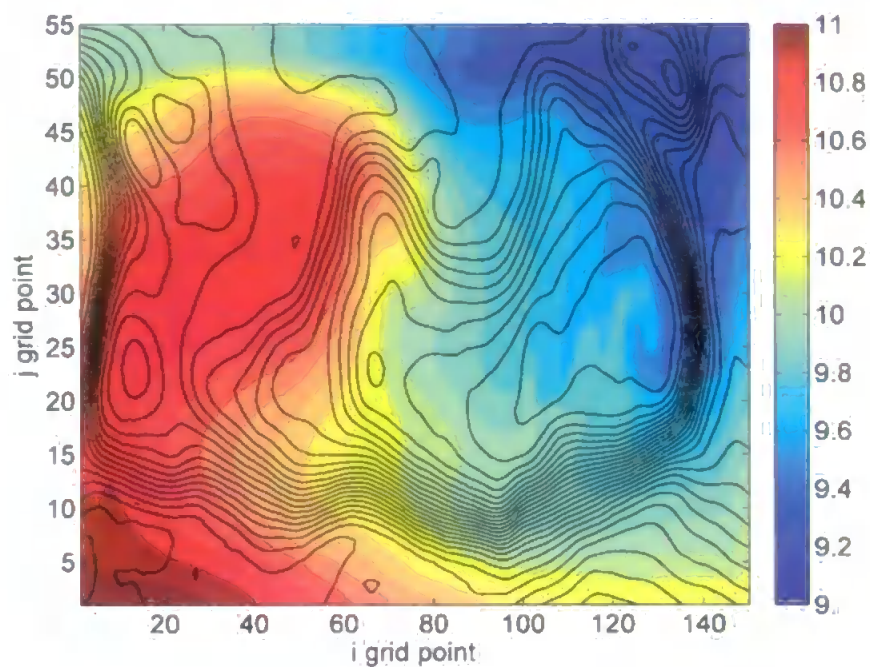


Figure 5.47 T_9 : Surface temperature $^{\circ}\text{C}$ on 22 December. The cold patch has not yet formed.

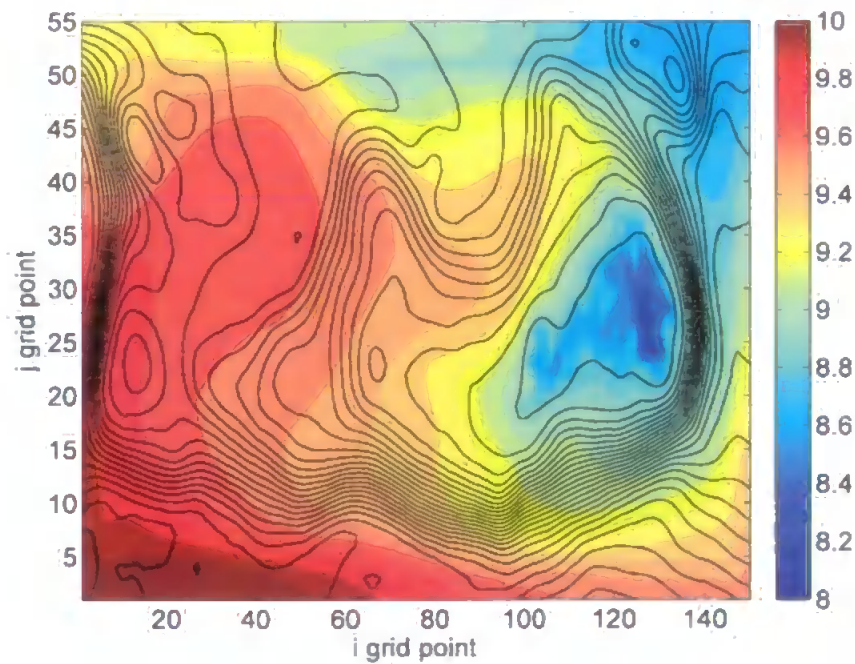


Figure 5.48 T_9 : Surface temperature $^{\circ}\text{C}$ on 1 March. The cold patch is now fully developed.

bank would be able to sink a significant distance. In T9 on the other hand, the cold water over Rockall Bank still becomes denser than the surrounding shallow waters but the cooling is not severe enough to make its density greater than the deep water. Where T6 had a maximum density difference of 0.3 kgm^{-3} , in T9 the colder water on top of the Bank is only 0.1 kgm^{-3} denser than the immediate surrounding water and is less dense than the very deep water. Therefore this water will not be able to sink as far. Figure 5.49 shows an example cross section of potential density on 1 April, at which time there is a marked cold water column. The location of this section is shown in by the vertical line on Figure 5.26. Figure 5.50 shows the potential density on the bottom s-level at the same time. We can see from these figures that although the potential density over the top of the bank is relatively high, it is not higher than that of the water over much of the slope. Consequently we do not see any evidence of dense water cascading in these results.

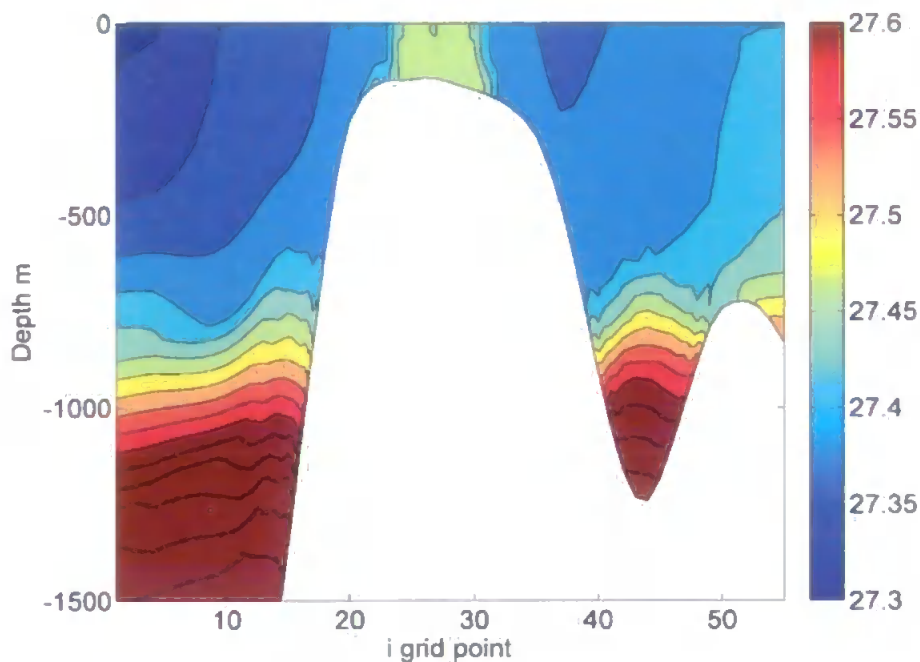


Figure 5.49 T9: Cross section of potential density $\sigma \text{ kgm}^{-3}$ on 1 April, along the section $i=130$.

Towards the end of the run the warming weather leads to the surface stratification returning, but the dense water remains under the surface warm water until the end. Figure 5.51 shows a cross-section of density at the end of the run. The location of this section is shown by the vertical line on Figure 5.26. We can see that there is a layer

of warm, low density, water within the upper 50–100 m. Below this there is a dome of water over the Bank with very slightly increased density compared to the surrounding water.

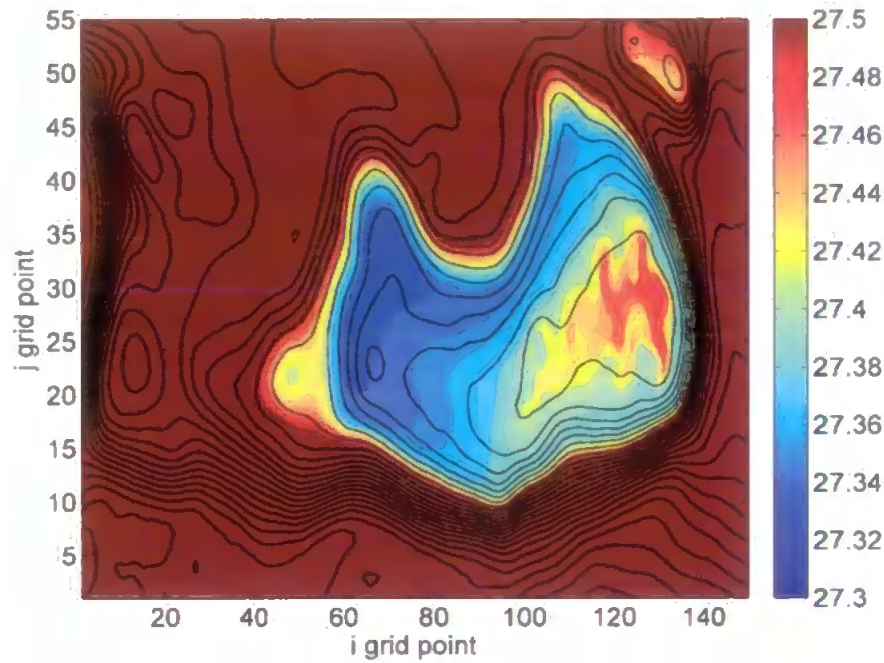


Figure 5.50 T9: Potential density σ kgm^{-3} along the bottom s -level on 1 April.

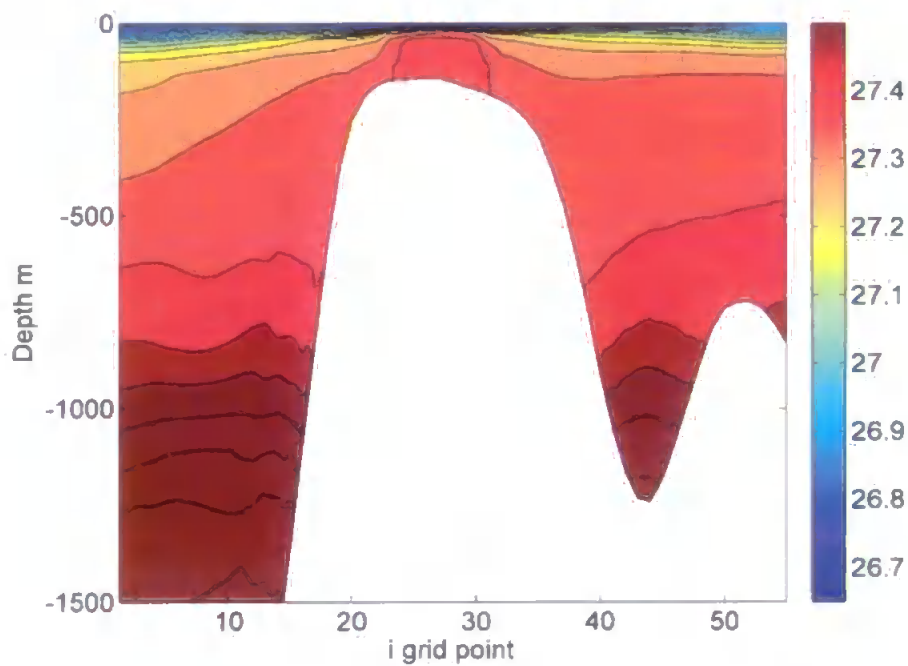


Figure 5.51 T9: Cross section of potential density σ kgm^{-3} on 30 June (the end of the run), along the section $i=130$.

Chapter 6

Full Model Runs

6.1 Introduction

Following satisfactory results from the simpler preliminary runs, the next stage was to conduct full simulations representing different climatological conditions in order to provide information about the sensitivity of the formation of dense water to atmospheric conditions.

Three years were chosen to be modelled: 1950/1951, 1978/1979, and 2001/2002, with model runs labelled F1950, F1978, and F2001 respectively. The preliminary runs (see Chapter 5) that required meteorological input used the data from 2001/2002.

The mean air temperature and wind speed for the winter period November–March were compared to long term mean values (calculated using data from 1968–1996) from NCEP/NCAR reanalysis data (Physical Sciences Division NOAA/ESRL, 2007). Figure 6.1 shows the deviation from the climatic mean of the winter air temperature of 2001/2002. We see that the air temperature over this period was around 1.0–1.5°C warmer compared to the 1968–1996 mean. Figure 6.2 shows the wind speed anomaly for the same period. Over a wider area there is a rather complex picture, with some parts having higher than average winds and other parts lower than average. However, over Rockall Bank itself (in the top right of the image) we see that the wind speed was not significantly different to the average.

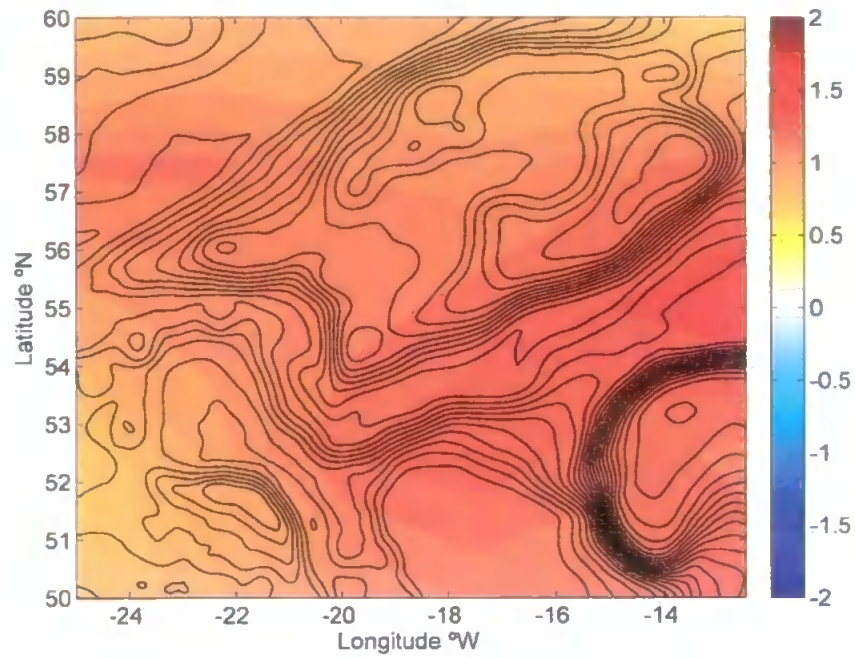


Figure 6.1 Air temperature anomaly $^{\circ}\text{C}$ of winter 2001/2002. Mean November–March values compared to climatological means from 1968–1996.

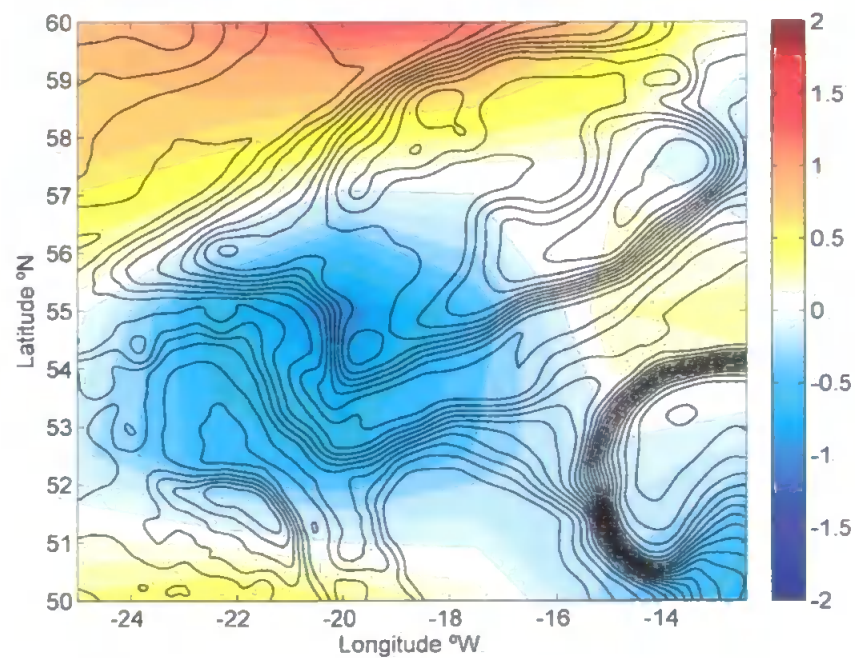


Figure 6.2 Wind speed anomaly ms^{-1} of winter 2001/2002. Mean November–March values compared to climatological means from 1968–1996.

The other two years that were modelled were selected due to their lower than average air temperature over the winter period. This provides a comparison to the warm winter case, allowing us to investigate the effect that variation in air temperature has upon the formation of dense water. The winters of 1950/1951 and 1978/1979 were chosen; these winters both have similar mean air temperatures, with values approximately 0.5 to 1 °C colder than the long term mean. Figures 6.3 and 6.4 show the air temperature anomalies for these two years, illustrating the similarity in temperature over Rockall Bank.

Although the air temperature was similar, these two winters featured different wind speed trends. Figure 6.5 shows the wind speed anomaly of the winter of 1950/1951. We see that the mean winter wind speed in this year was 1–2 ms^{-1} lower than the climatic mean. As a percentage of the mean speed this is around 10–15% lower. In 1978/1979 on the other hand, the wind speed was higher by around 1–1.5 ms^{-1} or 10%. This is illustrated by Figure 6.6.

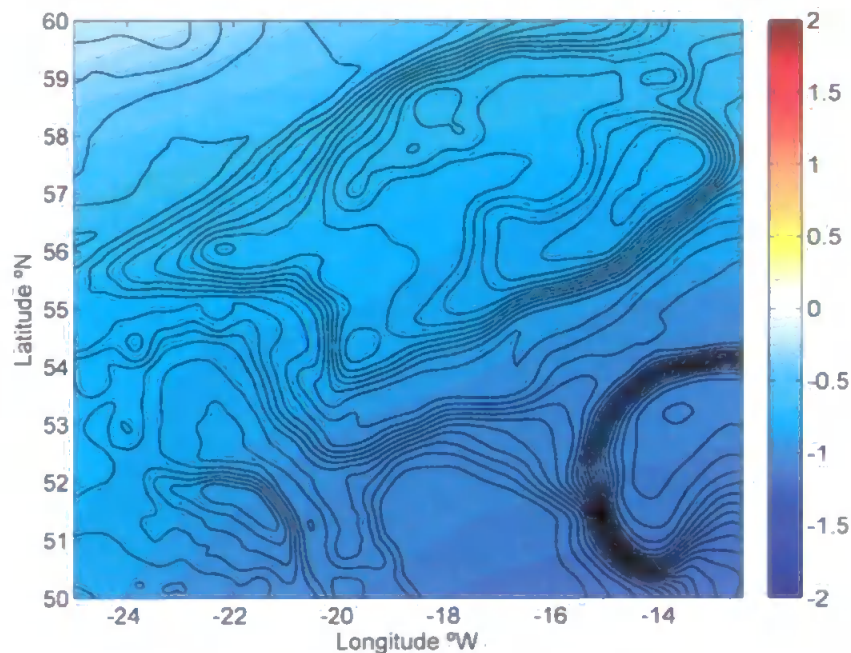


Figure 6.3 *Air temperature anomaly °C of winter 1950/1951. Mean November–March values compared to climatological means from 1968–1996.*

Together, these three different simulations will allow us to deduce the impact that changing air temperature and wind speed have on the formation and cascading of dense water at Rockall Bank.

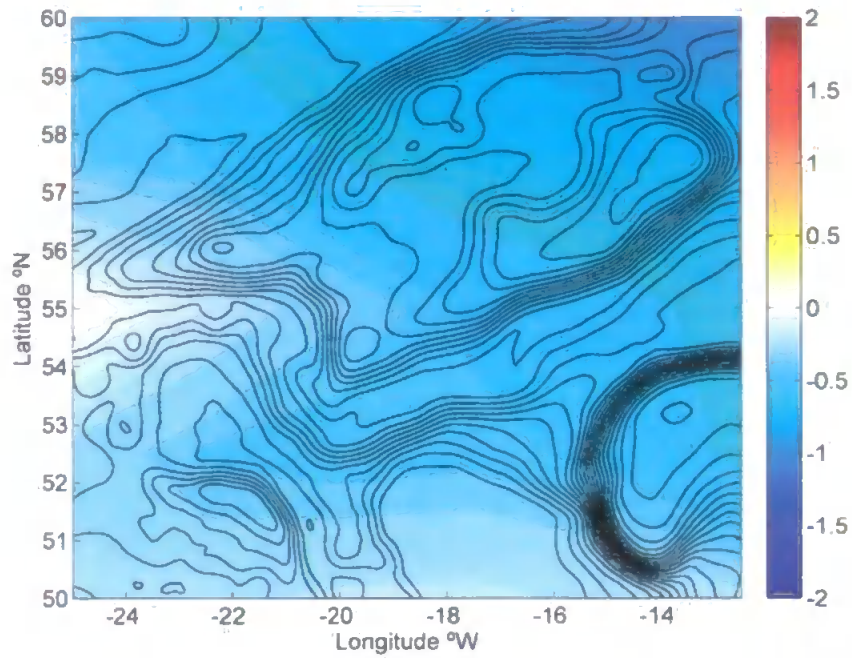


Figure 6.4 Air temperature anomaly $^{\circ}\text{C}$ of winter 1978/1979. Mean November–March values compared to climatological means from 1968–1996.

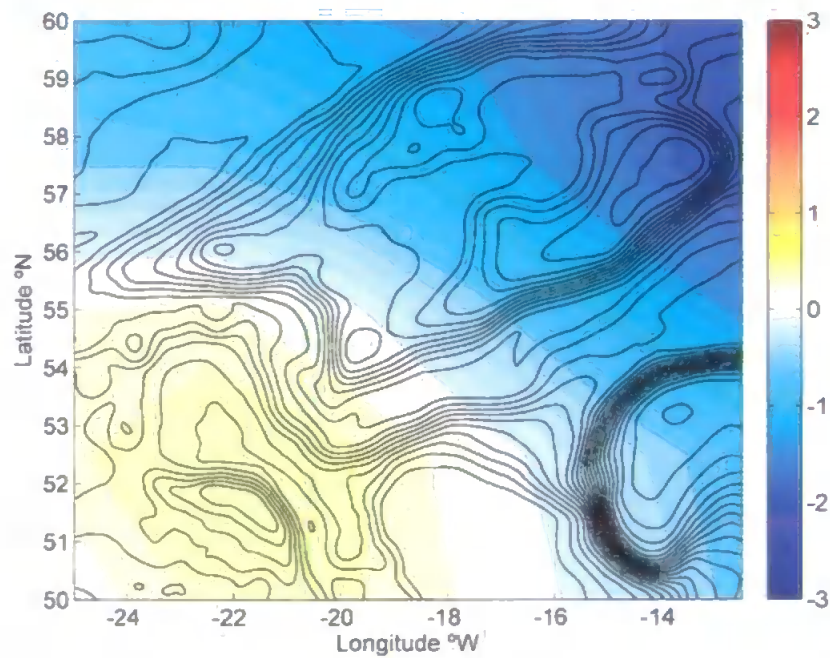


Figure 6.5 Wind speed anomaly ms^{-1} of winter 1950/1951. Mean November–March values compared to climatological means from 1968–1996.

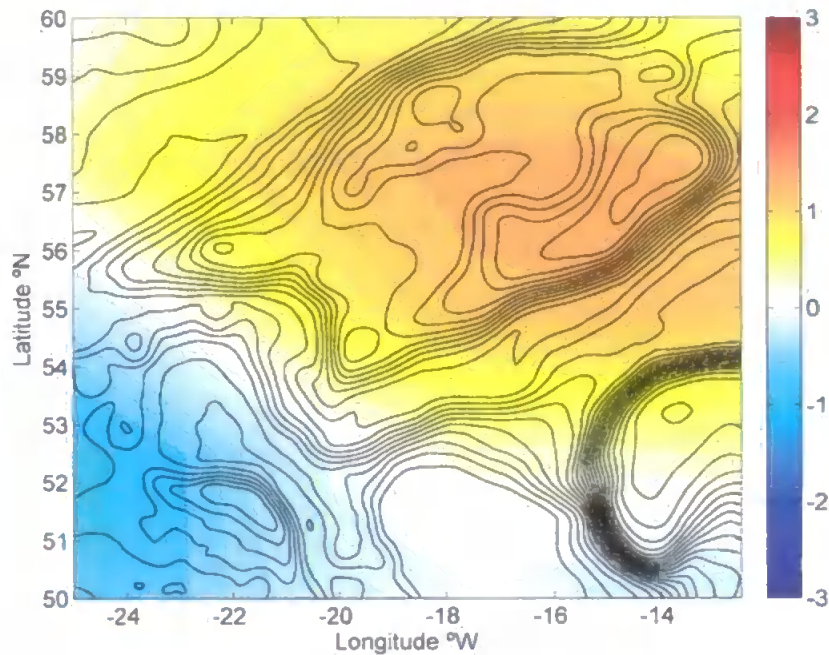


Figure 6.6 *Wind speed anomaly ms^{-1} of winter 1978/1979. Mean November–March values compared to climatological means from 1968–1996.*

The full runs were all initialised from a warm start file, which provides an initial current distribution that is compatible with the density. A checkpoint file from run T3A (§5.3.1) at 500 hours was used. T3A was the 'geostrophic spin-up' run that forced temperature and salinity to be kept constant, so that the resulting currents match the initial density distribution. The output from 500 hours was used as this was after the initial spin up peak and the model had stabilised by this point (see Figure 5.11 on page 77). Because the density field is taken from climatic data, each of the different years uses the same initial conditions but with the atmospheric forcing for that particular year. The duration of each run was from 1 November to 30 June. The rest of this chapter outlines brief results from the model runs. More in depth and quantitative analysis will be conducted in Chapter 8.

6.2 F2001

Because F2001 used the same meteorological data as the test run T9, in many respects the formation of the cold water here was similar. As with T9 there was a relatively small density difference between the water over the bank and the surrounding water. In

fact F2001 reached a slightly lower density than T9 and the density difference was less than 0.1 kgm^{-3} . The dense water can be seen forming over the Bank from around late January/early February and is at its densest during March. These timings are similar to the results of T9 where we saw the dense water forming in January, reaching its maximum in March. Figure 6.8 is a representative cross-section of the density distribution during the peak density time. The location of this section, and subsequent ones in this Chapter, is shown in Figure 6.7. We see in the cross-section that there is a well mixed column of dense water over the top of the Bank, and the density is the same as the density at around 700 m in the surrounding deep water. Figure 6.9 shows the density along the bottom level at the same time and clearly shows the dense water patch located over the shallowest part of the Bank.

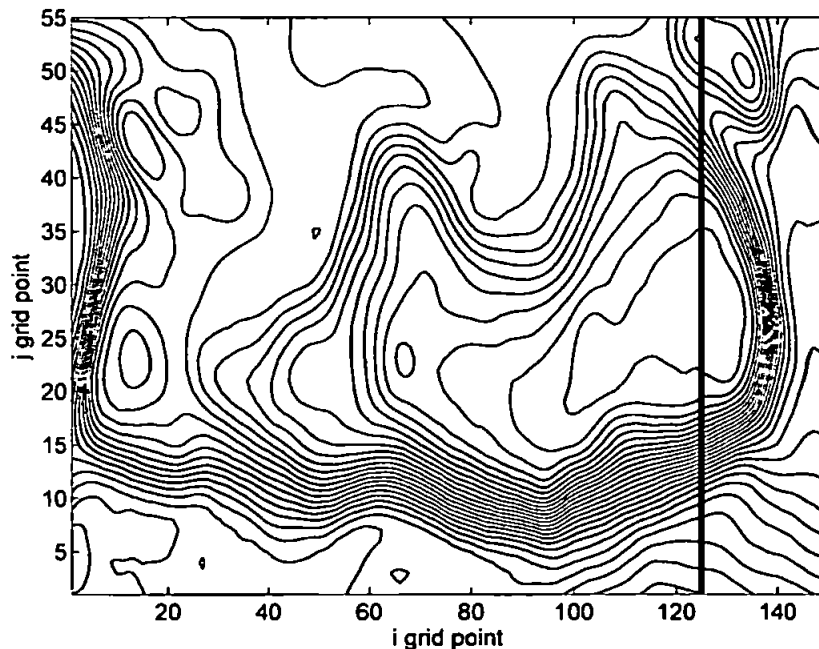


Figure 6.7 *Location of the Chapter 6 cross-sections*

F2001 differs significantly to T9 in its behaviour later in the spring as the weather is warming. In run T9 the dense water over the bank remained in place until the end of the run (although the density difference was greatly reduced). By contrast, in F2001 the dense water gradually disappears and becomes less dense, and by mid-May it has disappeared. Figure 6.10 shows the bottom density on 13 May and we can see that there is no cold water patch present any more. Although the water over the Bank is now closer in density to the surrounding water, we do still see a difference between the

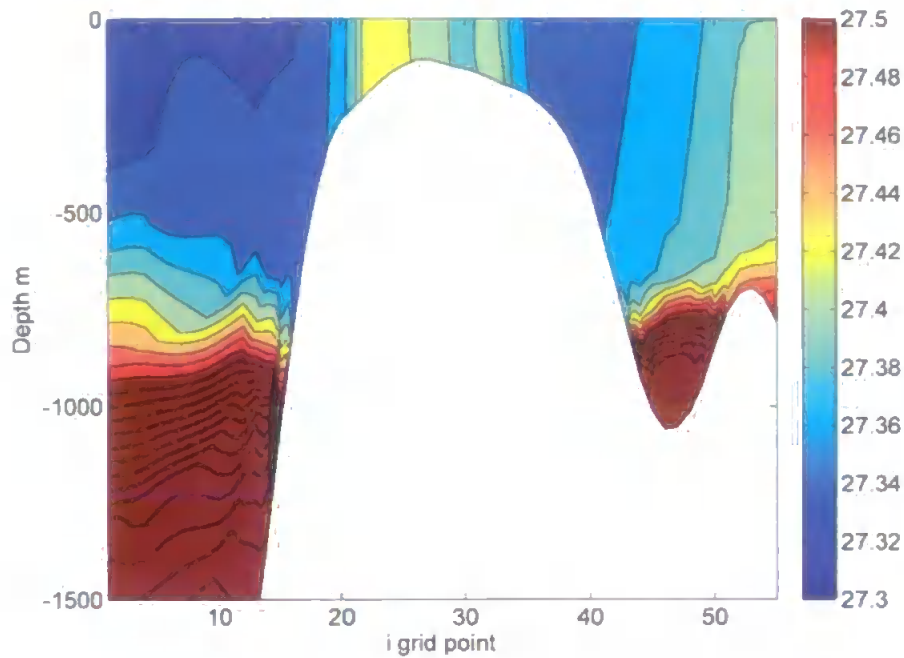


Figure 6.8 *F2001: Cross section of potential density σ_0 kgm^{-3} on 15 March 2002, along the section $i=125$. Density contour lines are every 0.02 kgm^{-3} from 27.1 to 27.9. The colours highlight the range $27.3\text{--}27.5 \text{ kgm}^{-3}$.*

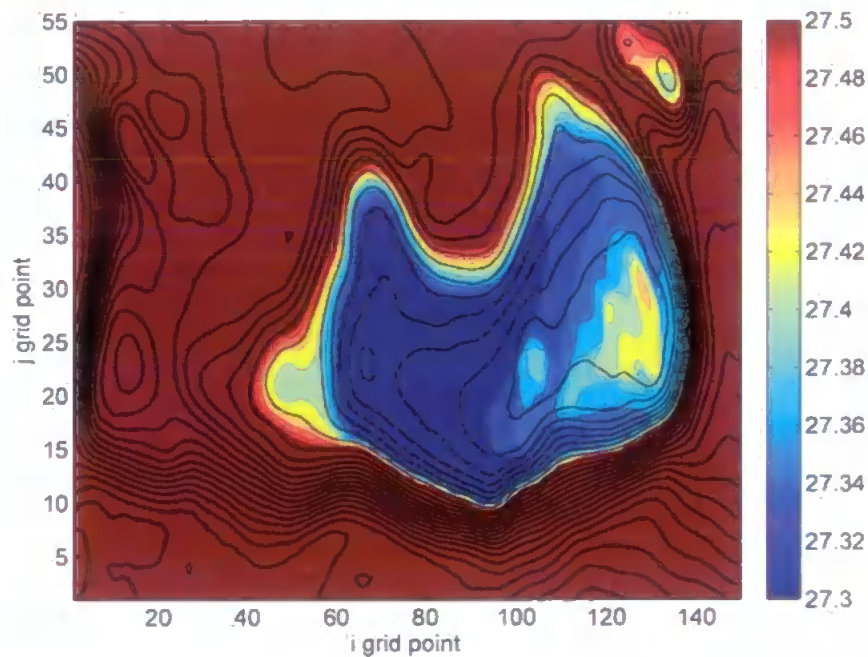


Figure 6.9 *F2001: Potential density σ_0 kgm^{-3} along the bottom s -level on 15 March 2002. Bathymetry contour lines are every 100 m. The colours highlight the range $27.3\text{--}27.5 \text{ kgm}^{-3}$.*

Bank and the deeper ocean: the summer surface stratification is present over the deeper water from late April, but the water column over the top of the Bank is still relatively well mixed in mid May. This is illustrated by Figure 6.11 which shows stratification over the deeper areas but not over the Bank.

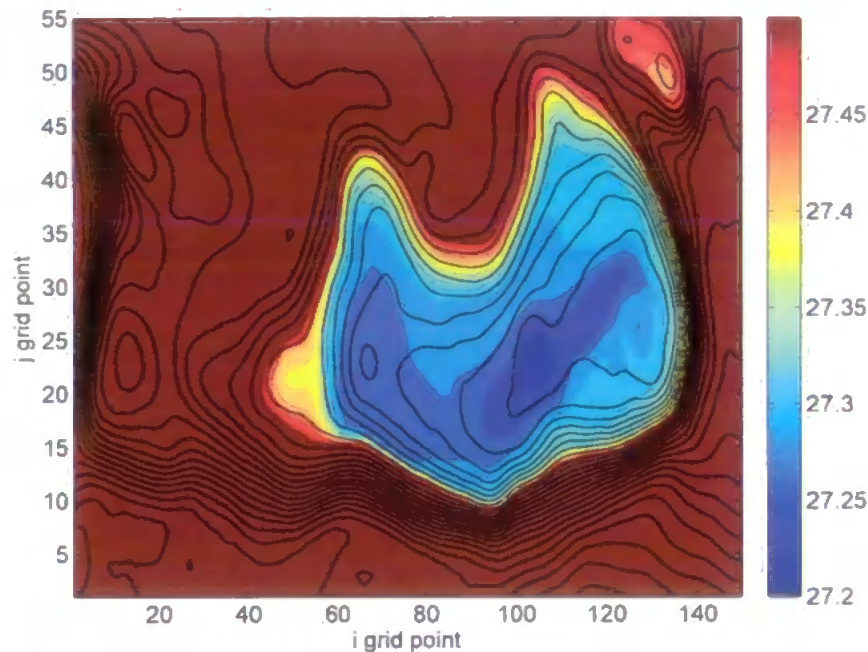


Figure 6.10 F2001: Potential density σ_θ kgm^{-3} along the bottom s -level on 13 May 2002, showing the cold patch is no longer present. Density contour lines are every 0.02 kgm^{-3} from 27.1 to 27.9. The colours highlight the range $27.3\text{--}27.5 \text{ kgm}^{-3}$.

The water over the top of the Bank then quickly becomes *less* dense than in the surrounding areas. The shallow surface stratification is formed over the Bank at the start of June, and the relatively low density water then remains on top of the Bank until the end of the run at the end of June. Although this water is less dense than the water at similar depths in the surrounding areas it is still heavier than the surface water above the stratification. Figure 6.12 is a cross section of the density at the end of the run which illustrates this reversal. Compare this to Figure 5.51 on page 106 showing the same cross-section from run T9, where the dense water remains underneath the surface stratification.

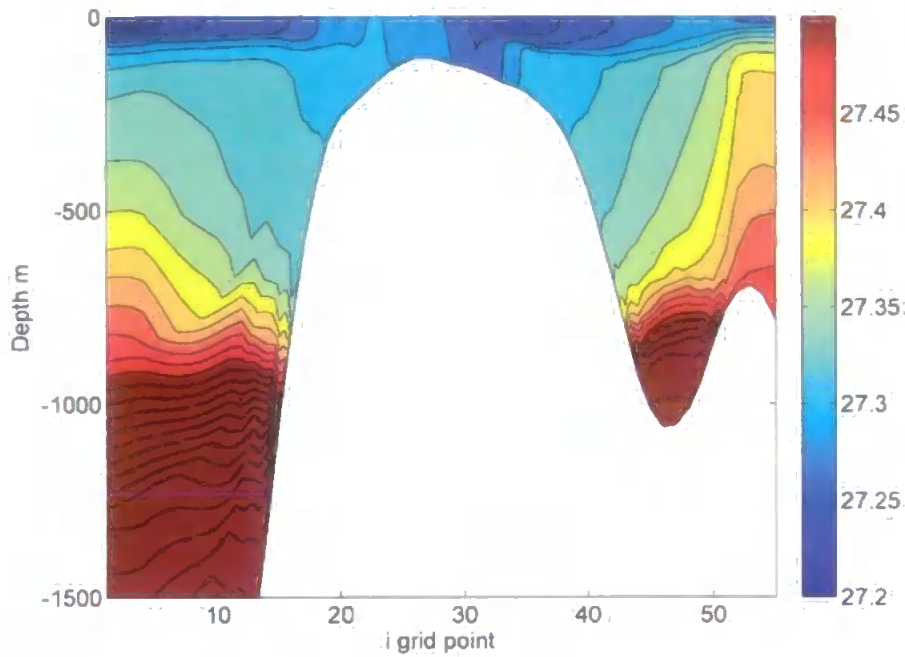


Figure 6.11 *F2001*: Cross section of potential density σ_0 kgm^{-3} on 13 May 2002, along the section $i=125$. Density contour lines are every 0.02 kgm^{-3} from 27.1 to 27.9. The colours highlight the range $27.2\text{--}27.5 \text{ kgm}^{-3}$.

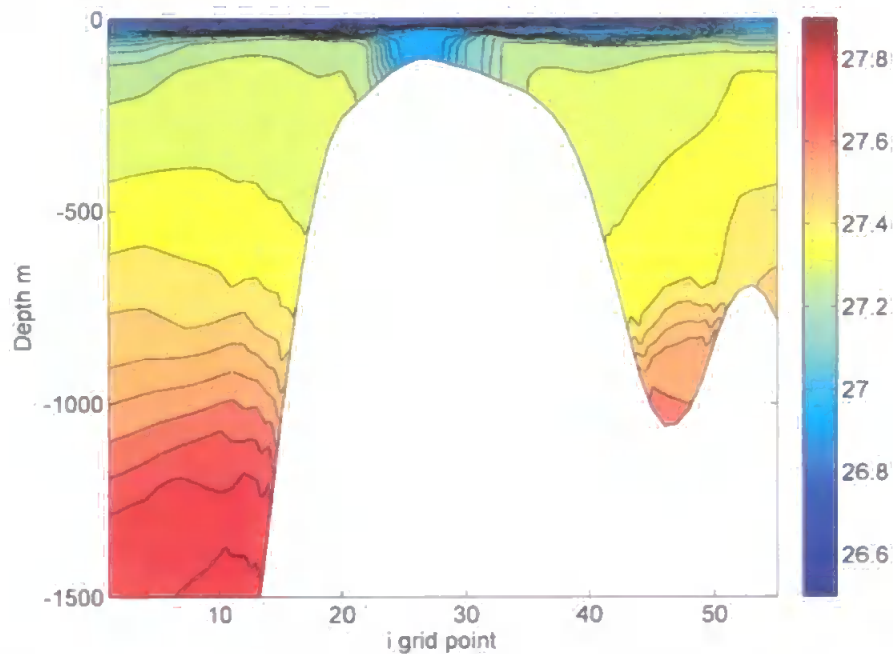


Figure 6.12 *F2001*: Cross section of potential density σ_0 kgm^{-3} at the end of the run (30 June 2001), along the section $i=125$. Density contour lines are every 0.05 kgm^{-3} from 26.5 to 27.9 and the colour scale has the same limits. (note that this is a different colour scale to the other *F2001* figures)

6.3 F1950

The dense water forms more quickly in run F1950 than in F2001 and is first visible from mid December. The peak period is during February and March through to the first half of April. The typical density difference between the Bank and deeper areas during this time is $0.2\text{--}0.3\text{ kgm}^{-3}$ compared to just 0.1 kgm^{-3} for F2001. Figure 6.13 is an example cross-section of the density. This is from 15 March and may be compared to Figure 6.8 for F2001 (note the difference colour scales). We see that the density over the Bank is higher in F1950, but the density over the rest of the ocean is similar. Therefore we see a greater density difference in F1950. Figure 6.14 is the bottom density from the same time period. Although we can see the density over the Bank is higher than it was in F2001 (shown in Figure 6.9), it is still lower than the water further down the slope.

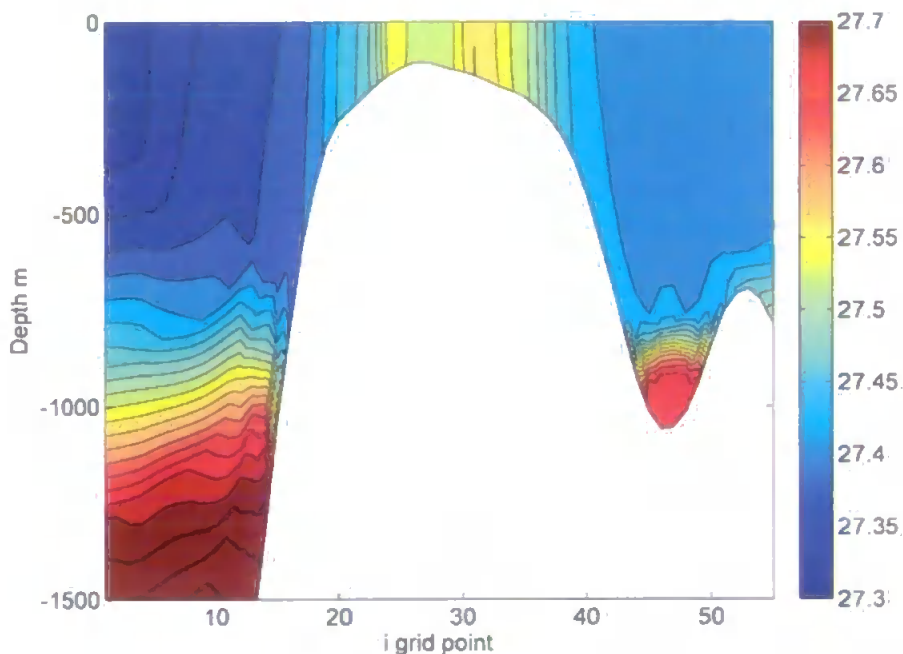


Figure 6.13 *F1950: Cross section of potential density σ_θ kgm^{-3} on 15 March 1951, along the section $i=125$.*

Density contour lines are every 0.02 kgm^{-3} from 27.1 to 27.9. The colours highlight the range $27.3\text{--}27.7\text{ kgm}^{-3}$.

This dense water is much more persistent in this run than it was in F2001. Figures 6.15 and 6.16 from mid-May show that there is still a relatively strong density difference. This is in contrast to F2001 where the dense water had already disappeared by this time (shown in Figures 6.11 and 6.10). We do see from Figures 6.15 and 6.16 that the water

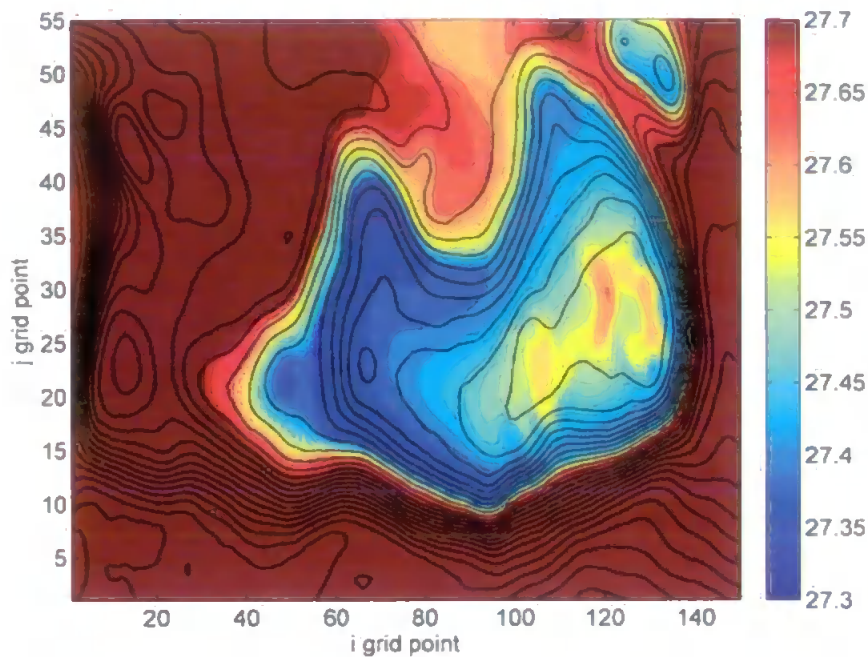


Figure 6.14 F1950: Potential density σ_0 kgm^{-3} along the bottom s-level on 15 March 1951. Bathymetry contour lines are every 100 m. The colours highlight the range 27.3–27.7 kgm^{-3} .

column over the top of the Bank is still relatively well mixed at this stage, which we also saw in F2001. The surface water surrounding the Bank has begun to become stratified, though this is weaker than it was at the same time in run F2001.

Whereas the dense water completely disappeared by mid-May in F2001, in F1950 there was still some trace of the dense water over the Bank even at the end of the run at the end of June. However, there were also areas where the water is less dense than in the open ocean. Figure 6.17 shows this complex density distribution on the bottom s-level at the end of the run on 30 June. The two least dense patches (the dark blue areas) correspond to the shallowest parts of the Bank and to the immediate north we see a denser patch. Figure 6.18 is an example cross-section from the same point in time which shows the vertical extent of these features. We see from Figure 6.18 that the surface stratification has now formed over the Bank, although the water beneath is still well mixed as it was in F2001.

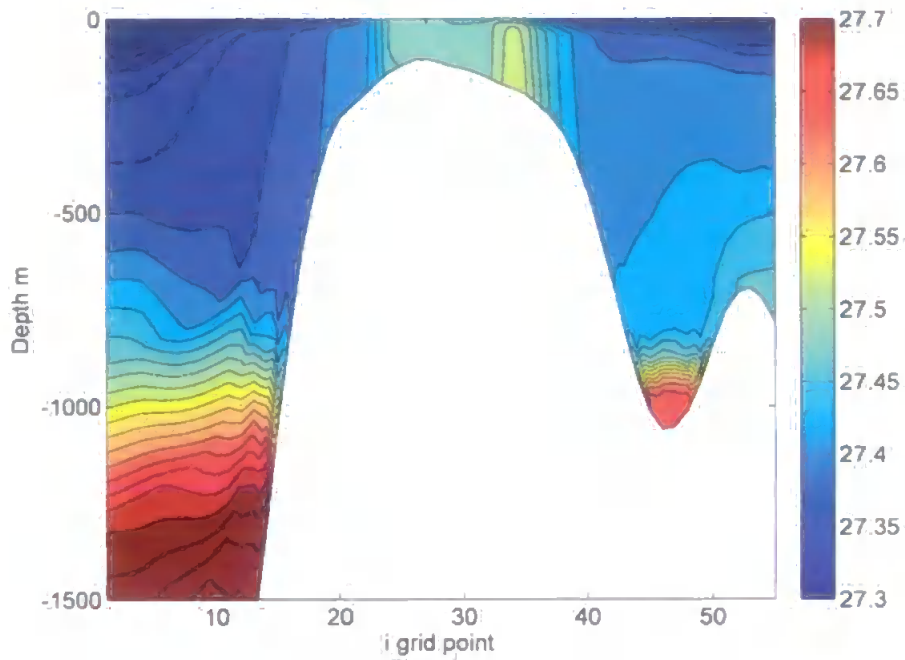


Figure 6.15 *F1950: Cross section of potential density σ_θ kgm^{-3} on 13 May 1951, along the section $i=125$. Density contour lines are every 0.02 kgm^{-3} from 27.1 to 27.9. The colours highlight the range $27.3\text{--}27.7 \text{ kgm}^{-3}$.*

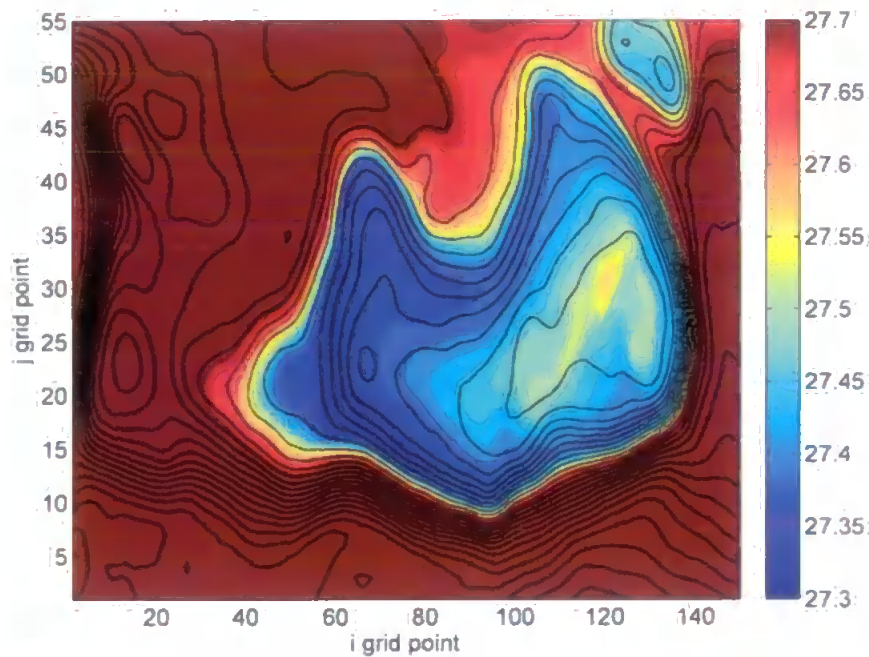


Figure 6.16 *F1950: Potential density σ_θ kgm^{-3} along the bottom s -level on 13 May 1951. Bathymetry contour lines are every 100 m. The colours highlight the range $27.3\text{--}27.7 \text{ kgm}^{-3}$.*

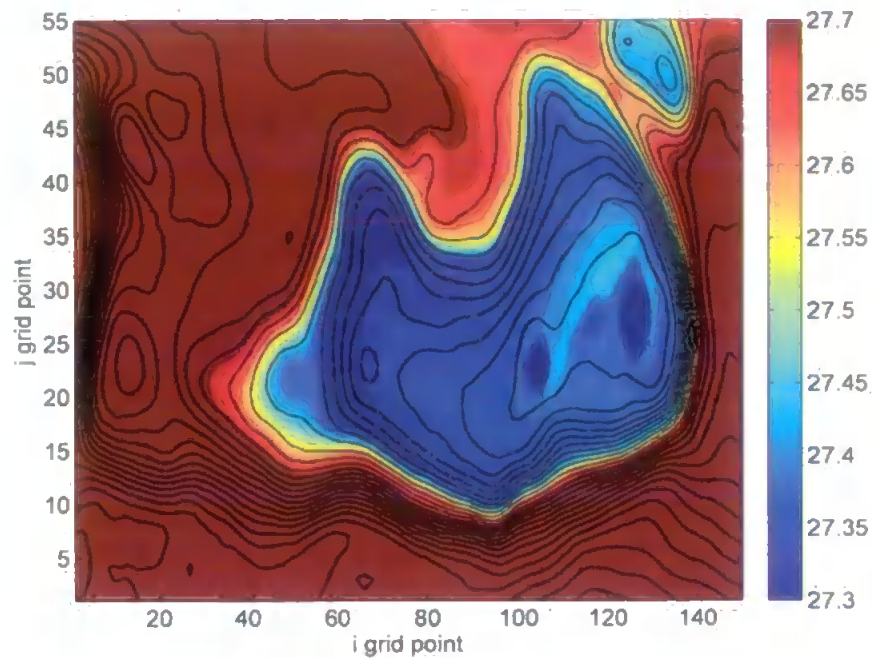


Figure 6.17 *F1950: Potential density σ_0 kg m^{-3} at the end of the run (30 June 1951), on the bottom s -level. Bathymetry contour lines are every 100 m. The colours highlight the range 27.3–27.7 kg m^{-3} .*

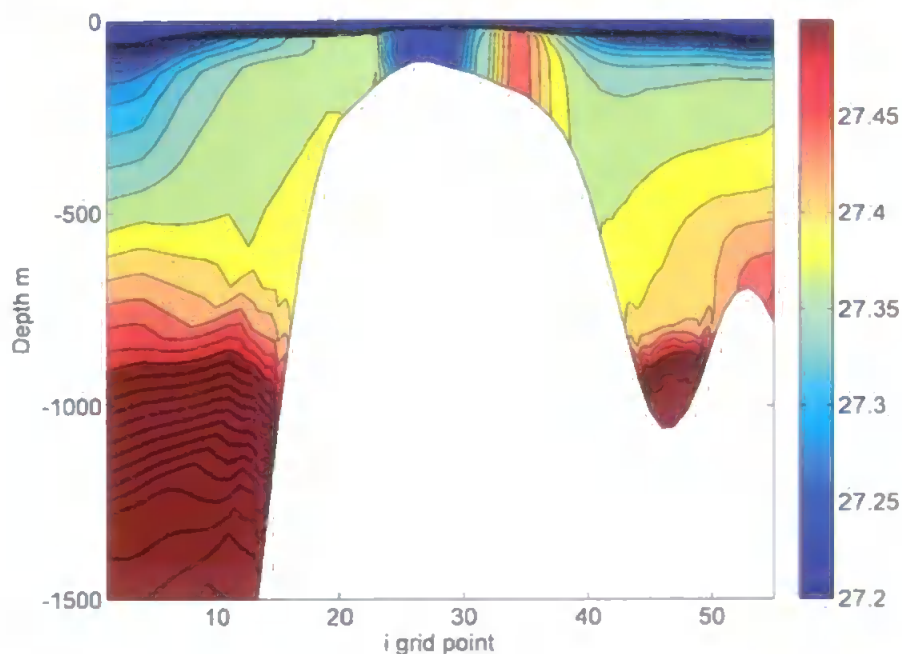


Figure 6.18 *F1950: Cross section of potential density σ_0 kg m^{-3} at the end of the run (30 June 1951), along the section $i=125$. Density contour lines are every 0.02 kg m^{-3} from 27.1 to 27.9. The colours highlight the range 27.2–27.5 kg m^{-3} . (note that this is a different colour scale to the other F1950 figures)*

6.4 F1978

Run F1978 tells a similar story to F1950. The dense water over the Bank forms slightly later, around mid to late December and is at its strongest from mid February–mid April which is similar to F1950. Again the typical density difference between the Bank and surrounding ocean is around $0.2\text{--}0.3\text{ kg m}^{-3}$ but F1978 eventually reaches a higher density than F1950. Figures 6.19 and 6.20 show examples of the density distribution during March, which may be compared to Figures 6.13 and 6.14 for F1950. We see that overall the density structure is similar, but by this stage the maximum density over the Bank is F1978 is somewhat higher than in F1950. In addition the s-level section shows that the horizontal extent of this densest water is greater at this stage than it was in F1950.

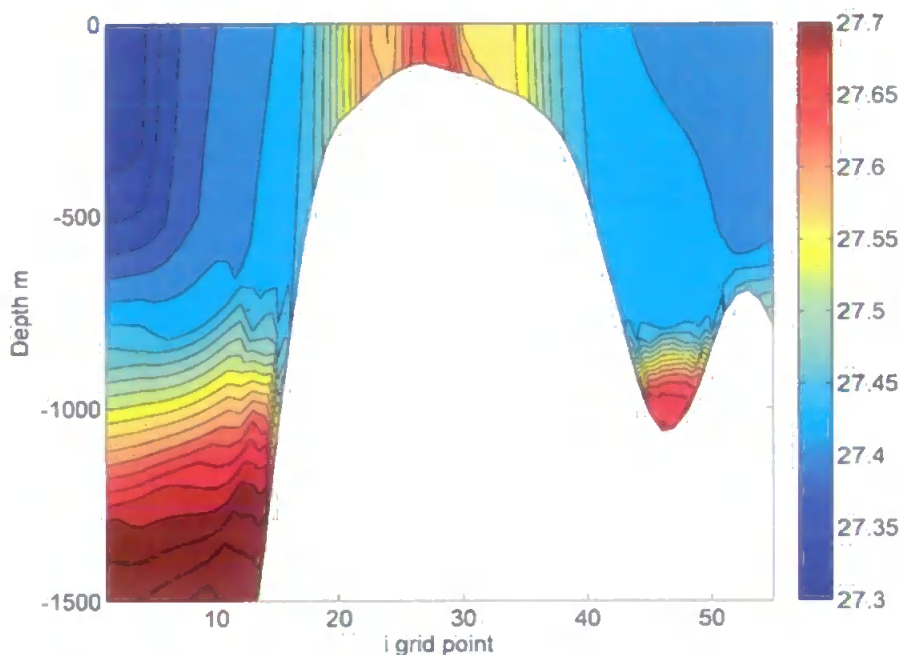


Figure 6.19 *F1978: Cross section of potential density σ_0 kg m^{-3} on 15 March 1979, along the section $i=125$. Density contour lines are every 0.02 kg m^{-3} from 27.1 to 27.9. The colours highlight the range $27.3\text{--}27.7\text{ kg m}^{-3}$.*

As we saw in F1950 the dense water remains present throughout the entire run. Figures 6.21 and 6.22 show the density distribution in May and we see very similar results to those of F1950. By comparing these Figures to Figures 6.15 and 6.16 we see that the density magnitude is now the same as it was in F1950. However, there is less surface strati-

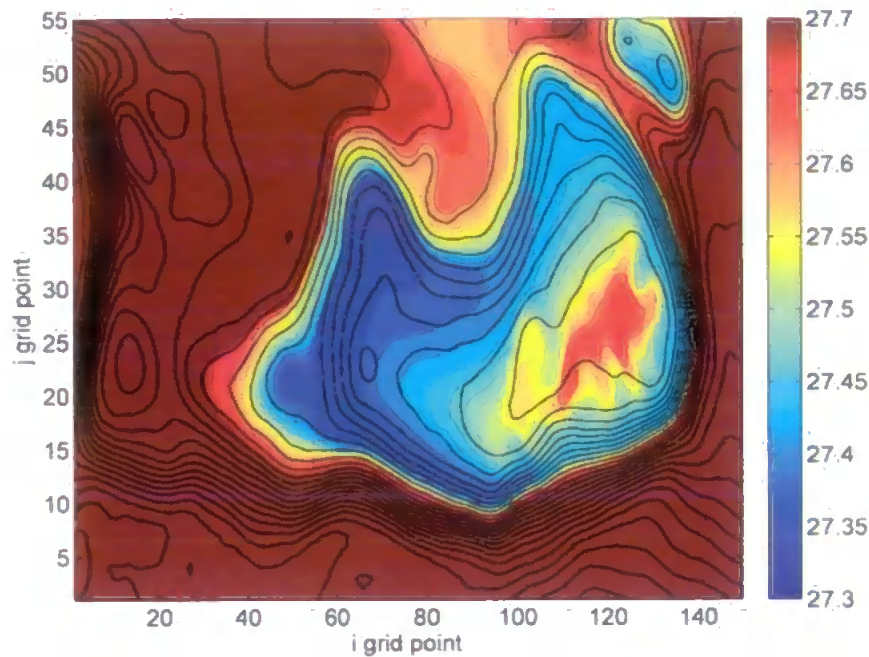


Figure 6.20 *F1978: Potential density σ_θ kgm^{-3} along the bottom s -level on 15 March 1979. Bathymetry contour lines are every 100 m. The colours highlight the range 27.3–27.7 kgm^{-3} .*

fication evident in F1978. The water column over the top of the Bank in particular is slightly more well mixed in this run.

Finally, the pattern of both high and low density areas over the Bank in the latter part of the run that we saw in F1950 is also present here. Figures 6.24 and 6.23 show that the final density distribution is similar to F1950. In particular we see the remaining area of dense water in the same location as it was in run F1950, but in this run the density has remained slightly higher. Additionally, the water column over the Bank in F1978 is slightly more well mixed than in F1950. Although it is generally highly stratified over the Bank, Figure 6.24 shows a small area, indicated by the arrow, where the stratification appears to break down.

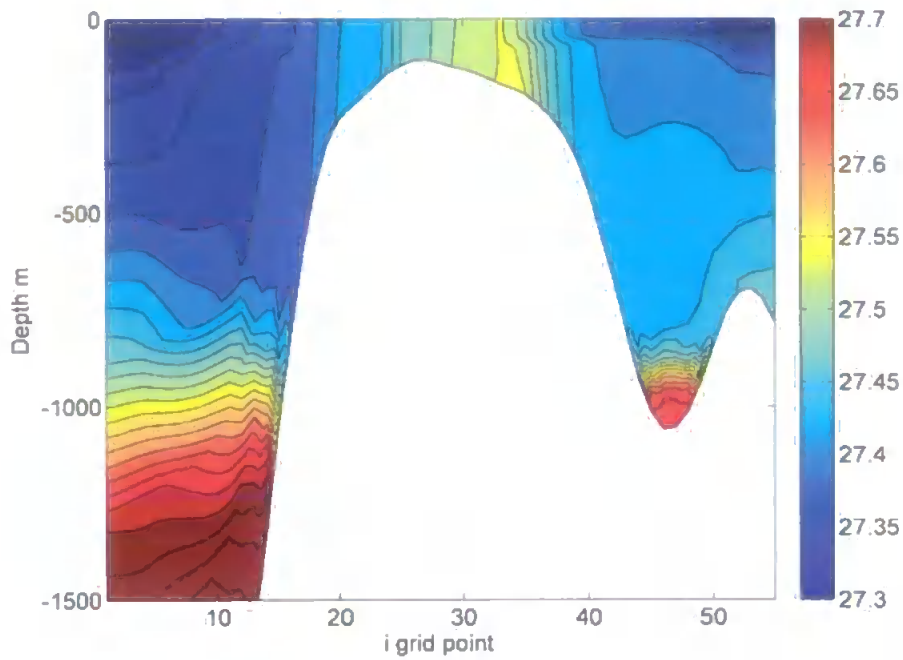


Figure 6.21 F1978: Cross section of potential density $\sigma_0 \text{ kgm}^{-3}$ on 13 May 1979, along the section $i=125$. Density contour lines are every 0.02 kgm^{-3} from 27.1 to 27.9. The colours highlight the range $27.3\text{--}27.7 \text{ kgm}^{-3}$.

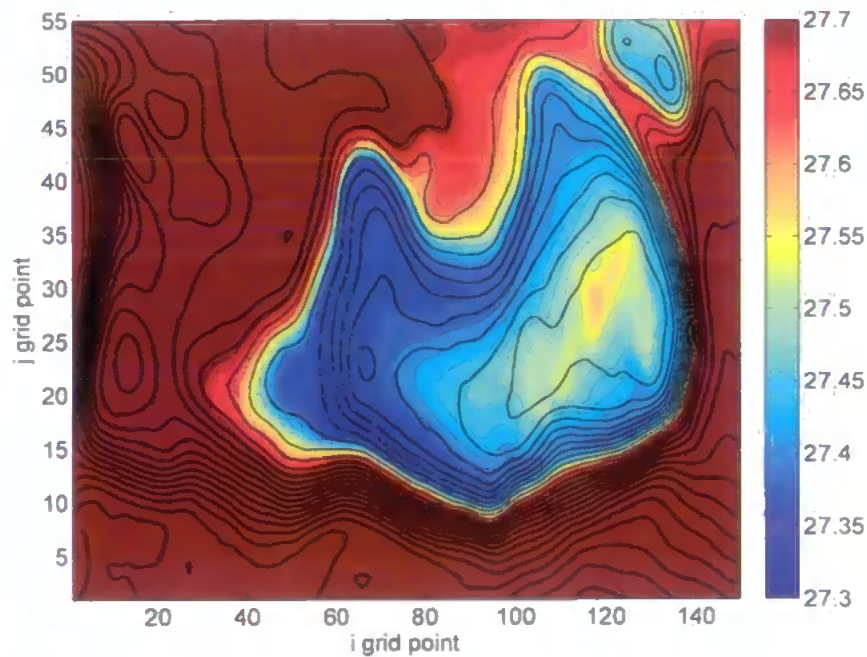


Figure 6.22 F1978: Potential density $\sigma_0 \text{ kgm}^{-3}$ along the bottom s -level on 13 May 1979. Bathymetry contour lines are every 100 m. The colours highlight the range $27.3\text{--}27.7 \text{ kgm}^{-3}$.

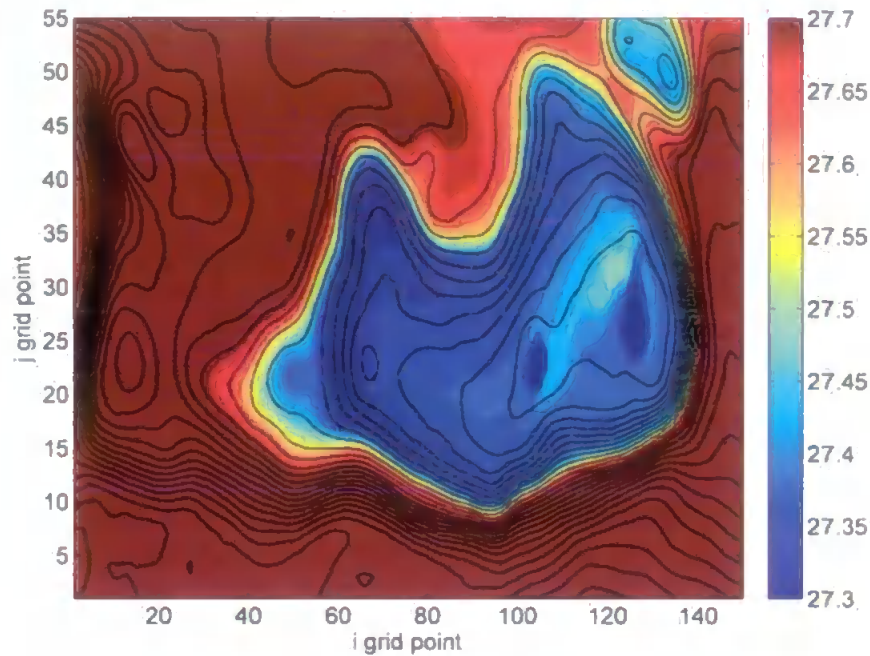


Figure 6.23 *F1978: Potential density σ_0 kg m^{-3} at the end of the run (30 June 1979), on the bottom s -level. Bathymetry contour lines are every 100 m. The colours highlight the range 27.3–27.7 kg m^{-3} .*

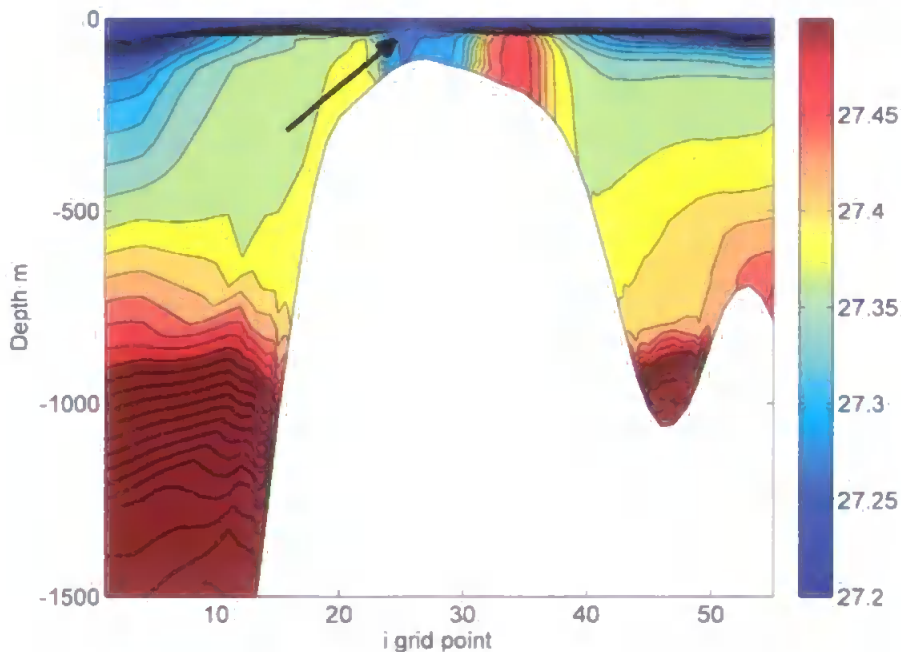


Figure 6.24 *F1978: Cross section of potential density σ_0 kg m^{-3} at the end of the run (30 June 1979), along the section $i=125$. The arrow indicates less highly stratified area. Density contour lines are every 0.02 kg m^{-3} from 27.1 to 27.9. The colours highlight the range 27.2–27.5 kg m^{-3} . (note that this is a different colour scale to the other F1978 figures)*

6.5 Mixed Layer Depth and Stratification

The timing and degree of stratification of the water column also varies between the three modelled years. In order to provide representative data that can be compared, mean density profiles were created for representative 'Bank' and 'Ocean'. The location of these is shown in Figure 6.25.

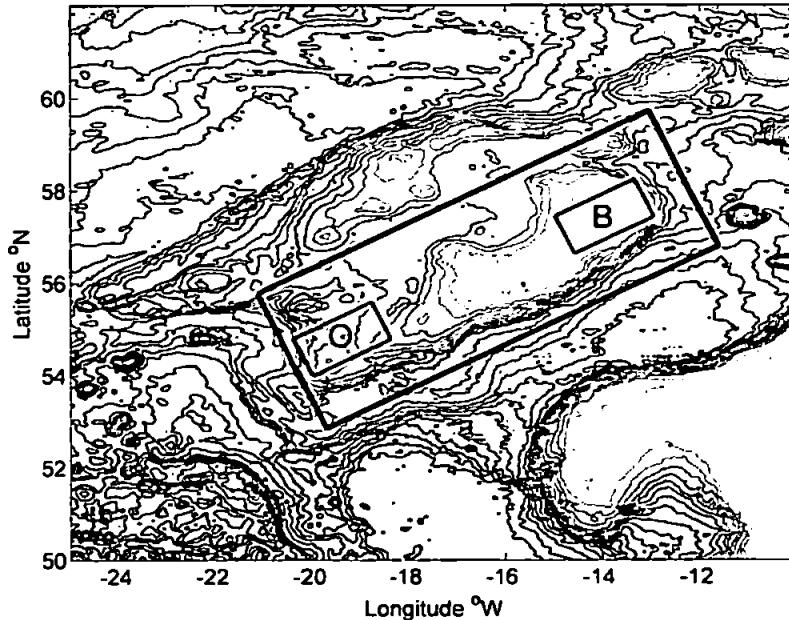


Figure 6.25 *Location of the areas sampled to analyse changes in stratification*

The method used is as follows, and is repeated for both boxes and for each day of the model runs:

1. For each grid point separately, the density is linearly interpolated in the vertical to a single set of depth levels
2. For each new depth level the mean density across all the grid points within the box is calculated. Where the level is deeper than some of the points in the box, the mean value is taken only from those profiles that reach this depth.

Vertical profiles were then plotted for the duration of the runs in order to compare the stratification behaviour in the different model years. Illustrative figures are found together on pages 127 to 135.

We begin by discussing the deeper ocean box. On day one, at the start of November,

all three years show almost identical density profiles (Figure 6.26: 1 November). There is a shallow mixed layer to 50 m and below this the density increases to the bottom at nearly 1400 m. As time progresses the surface density in each year begins to increase, with F1978 and F1950 increasing more quickly than F2001. At the same time the mixed layer depth starts to deepen, again at a faster rate in the two colder years. By the middle of November the mixed layer has already doubled to 100m in F1978 and F1950 (Figure 6.27: 15 November) whereas in F2001 it does not reach 100m until the beginning of December (Figure 6.28: 1 December). The density profile of the deeper water below the mixed layer remains very similar in all three years. This pattern continues as time progresses such that by the middle of February the mixed layer depth in F1950 and F1978 has reached 500m compared to 300m in F2001 (Figure 6.29: 8 February). As the mixed layer depth continues to increase, reaching 700 m by early March in F1978 and F1950 (Figure 6.30: 6 March), the density of the deeper waters begins to show variation between the different years. The mixed layer in F1978 and F1950 is now at its maximum depth and as F2001 catches up, reaching 700 m in early April (Figure 6.32: 9 April), the deep water profiles converge and are again very similar in all three years. This maximum mixing depth of 700 m is consistent with observations (e.g. Meincke, 1986; New and Smythe-Wright, 2001). Meanwhile, before the deep mixed layer had reached 700 m F2001 was starting to show intermittent signs of the surface shallow stratification in late March (Figure 6.31: 27 March). This is much earlier than is the case in F1950 and F1978 where we do not see this until the beginning of May, with F1978 (Figure 6.34: 6 May) following several days after F1950 (Figure 6.33: 1 May). Once the surface warming begins to take effect we see the surface density decrease again, while the water below the shallow stratification remains reasonably well mixed to 700 m. The seasonal pycnocline deepens from this point until the end of the runs at the end of June, at which point it is at approximately 100m (Figure 6.35: 30 June). Although there were differences in the stratification between the warm and cool years, there was not a significant difference in the maximum density reached.

Moving on to the Bank box next we see that all three years again begin with weak stratification, being well mixed down to 40 or 50 m (Figure 6.36: 1 November). Straight

away from the beginning of the runs the surface density starts to increase, and the mixing depth increases. F1950 and F1978 increase in density more quickly than F2001 as we have seen previously in the initial analysis. The upper density quickly becomes equal to the deeper density, leading to the entire water column becoming well mixed by the end of November in runs F1950 and F1978 (Figure 6.37: 30 November). The water column in run F2001 is still weakly stratified around 100 m at this stage, and does not become fully mixed until late December (Figure 6.38: 28 December). From early December until June the upper 150 m in F1978 and F1950 appears to become slightly more dense than the deeper water, leading to an apparently unstable water column (Figures 6.38–6.43). This is likely to be an artefact due to the method of averaging the density profile across the area of the box. Figure 6.44 shows that the grid points which have a water depth greater than 150 m are dominated by areas with relatively lower density. In mid-April the density begins to decrease again as the summer warming begins to take effect, and shortly after this we begin to see restratification starting in F2001 (Figure 6.39: 20 April). As with the ocean box the two colder years do not begin to restratify near the surface until later on, with F1978 again being slightly later (Figure 6.41: 24 May) than F1950 (Figure 6.40: 14 May) in the mid to late May. As the surface density continues to decrease in all three years, the pycnocline deepens until it reaches around 50 m in F2001 and 25 m in F1978 and F1950 at the end of May (Figure 6.42: 30 May). By the end of the run at the end of June the F2001 pycnocline has reduced to around 75 m, and F1950 and F1978 to 30–40 m (Figure 6.43: 30 June). Both F1950 and F1978 show a continual gradient of density down to the pycnocline, but F1978 has a shallow mixed layer from the surface to 20 m. F1950 and F1978 are very similar to each other below 50 m whereas F2001 is less dense.

Mean Density Profiles

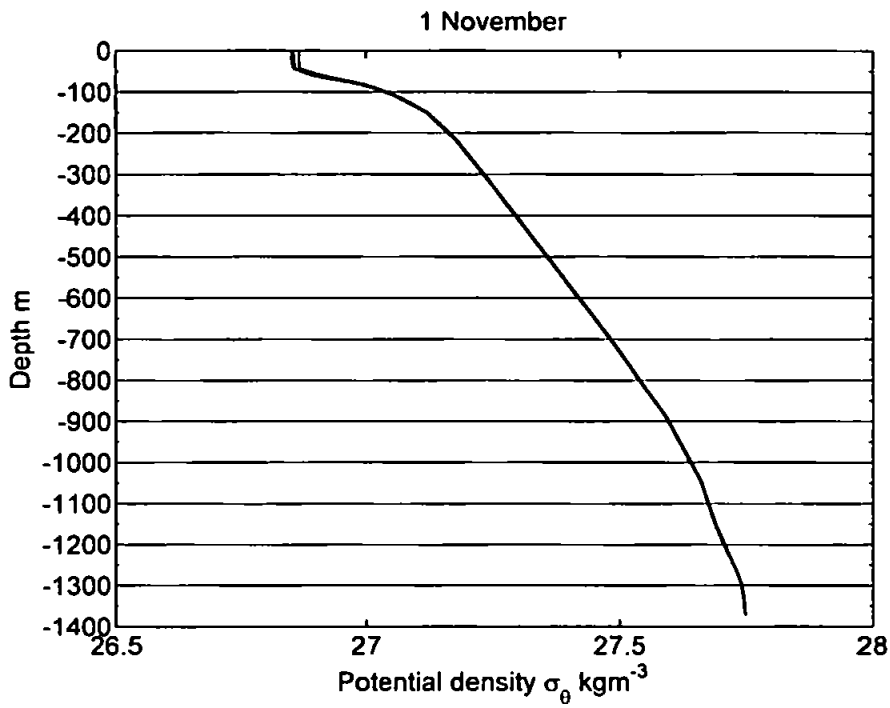


Figure 6.26 Mean density profiles σ_θ kgm^{-3} for the full model runs from the 'ocean box' on 1 November. Black: F2001, Red: F1950, Blue: F1978.

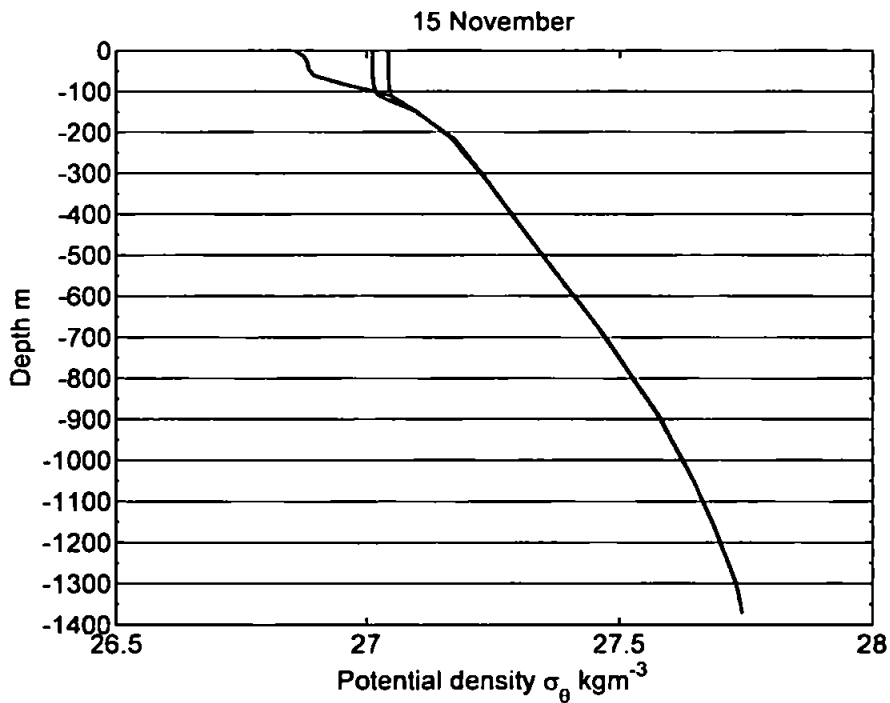


Figure 6.27 Mean density profiles σ_θ kgm^{-3} for the full model runs from the 'ocean box' on 15 November. Black: F2001, Red: F1950, Blue: F1978.

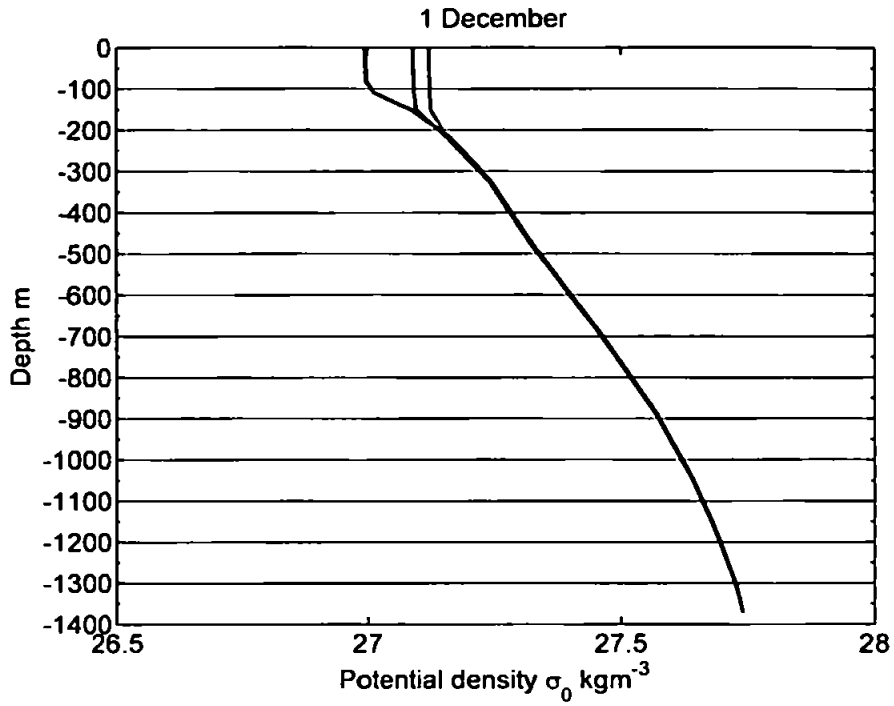


Figure 6.28 Mean density profiles $\sigma_0 \text{ kgm}^{-3}$ for the full model runs from the 'ocean box' on 1 December. Black: F2001, Red: F1950, Blue: F1978.

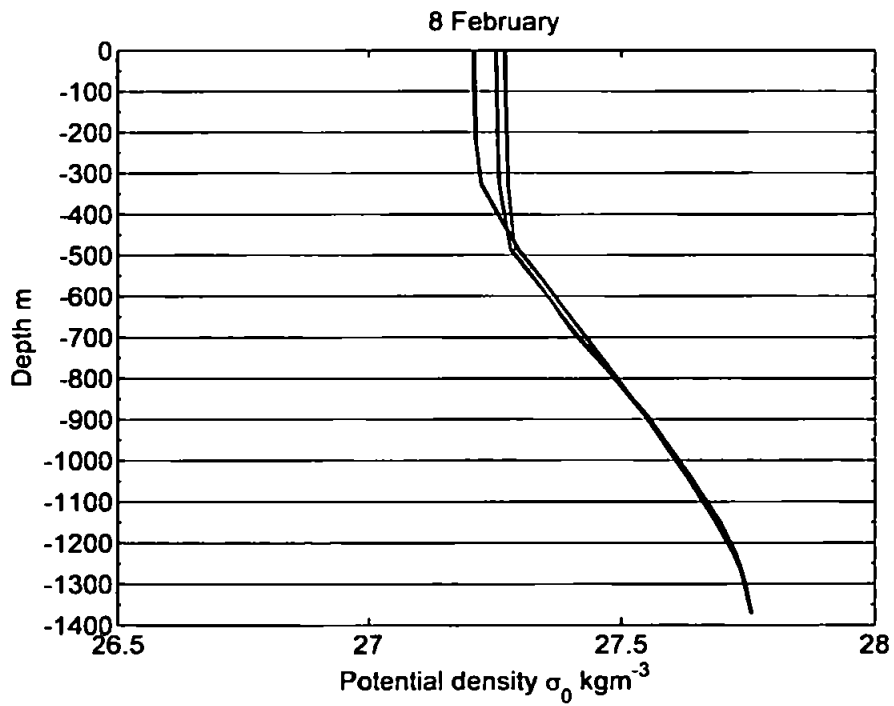


Figure 6.29 Mean density profiles $\sigma_0 \text{ kgm}^{-3}$ for the full model runs from the 'ocean box' on 8 February. Black: F2001, Red: F1950, Blue: F1978.

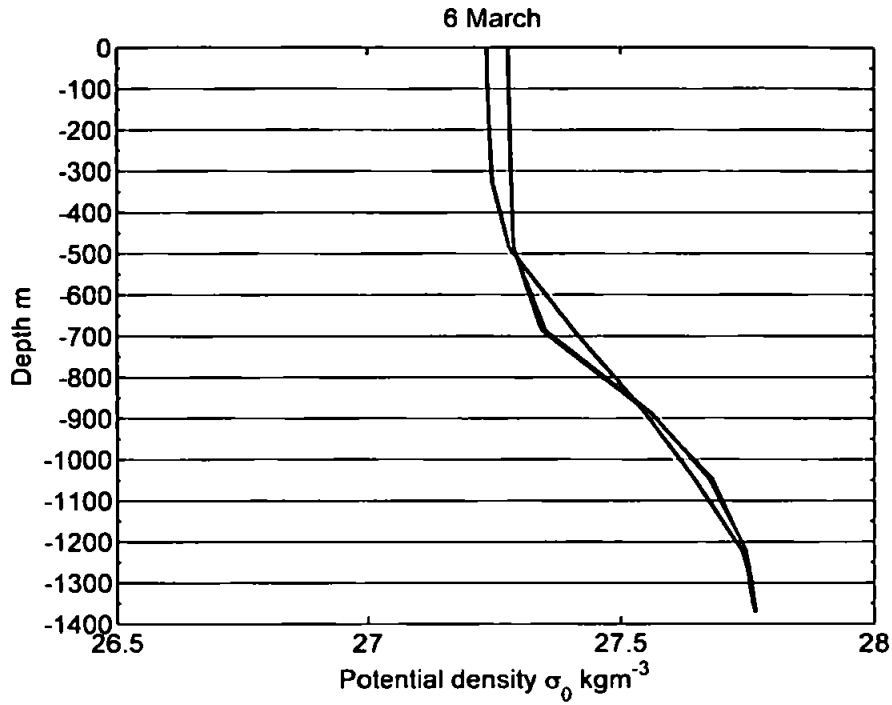


Figure 6.30 Mean density profiles σ_0 kgm⁻³ for the full model runs from the 'ocean box' on 6 March. Black: F2001, Red: F1950, Blue: F1978.

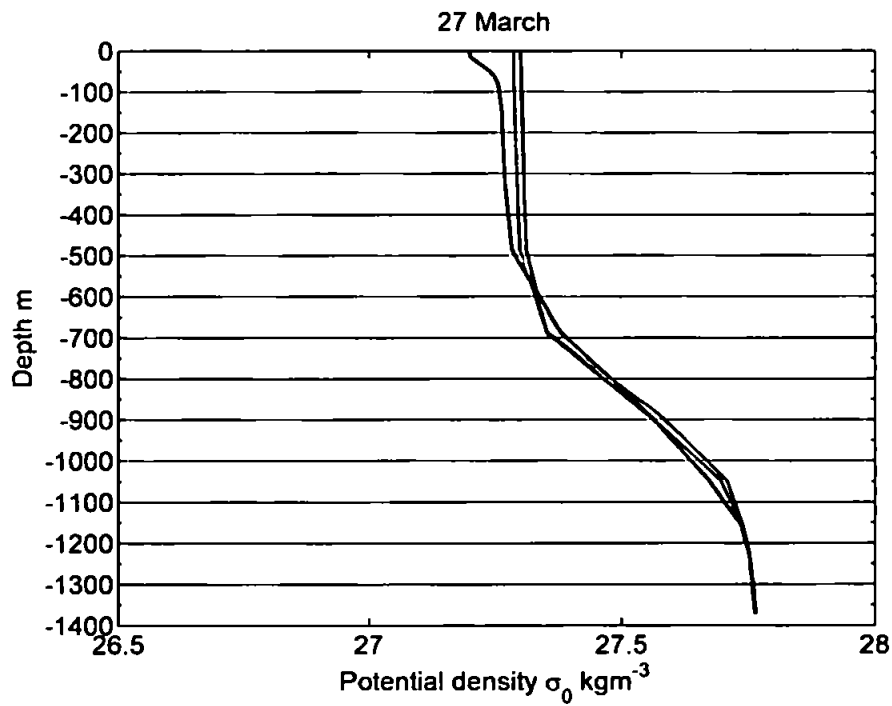


Figure 6.31 Mean density profiles σ_0 kgm⁻³ for the full model runs from the 'ocean box' on 27 March. Black: F2001, Red: F1950, Blue: F1978.

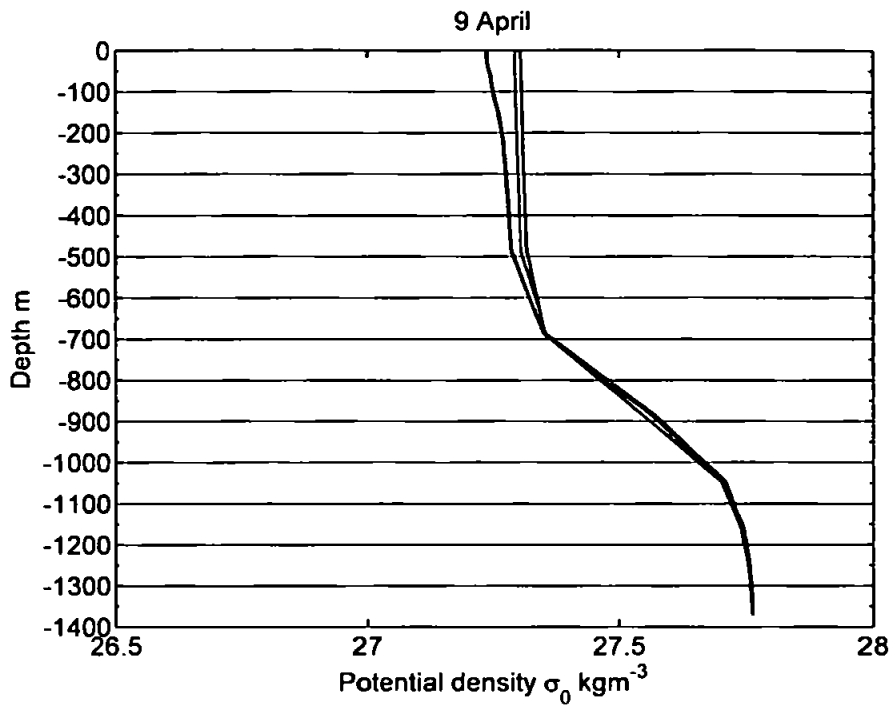


Figure 6.32 Mean density profiles $\sigma_0 \text{ kg m}^{-3}$ for the full model runs from the 'ocean box' on 9 April. Black: F2001, Red: F1950, Blue: F1978.

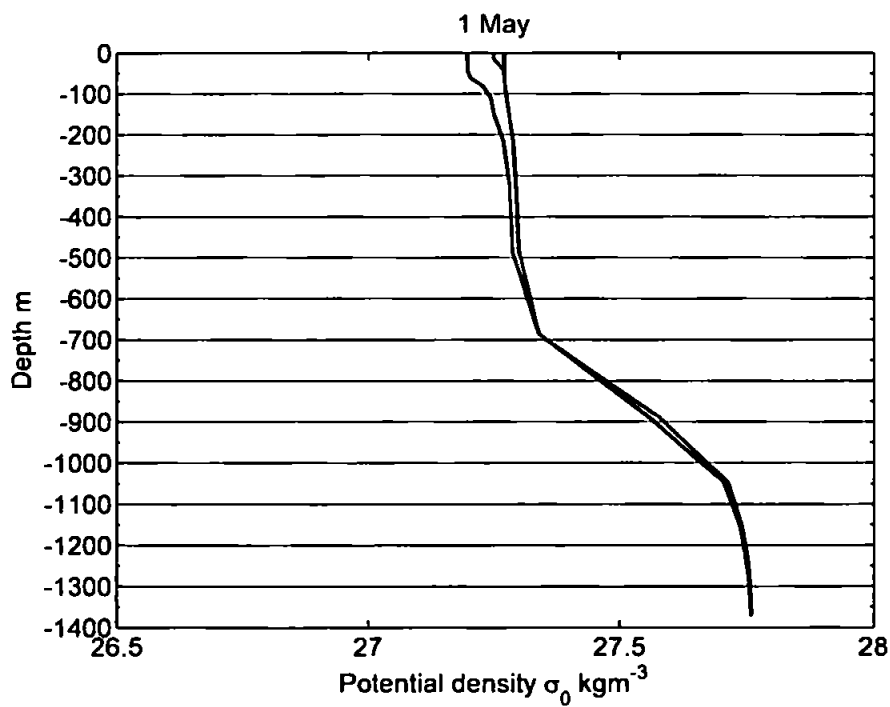


Figure 6.33 Mean density profiles $\sigma_0 \text{ kg m}^{-3}$ for the full model runs from the 'ocean box' on 1 May. Black: F2001, Red: F1950, Blue: F1978.

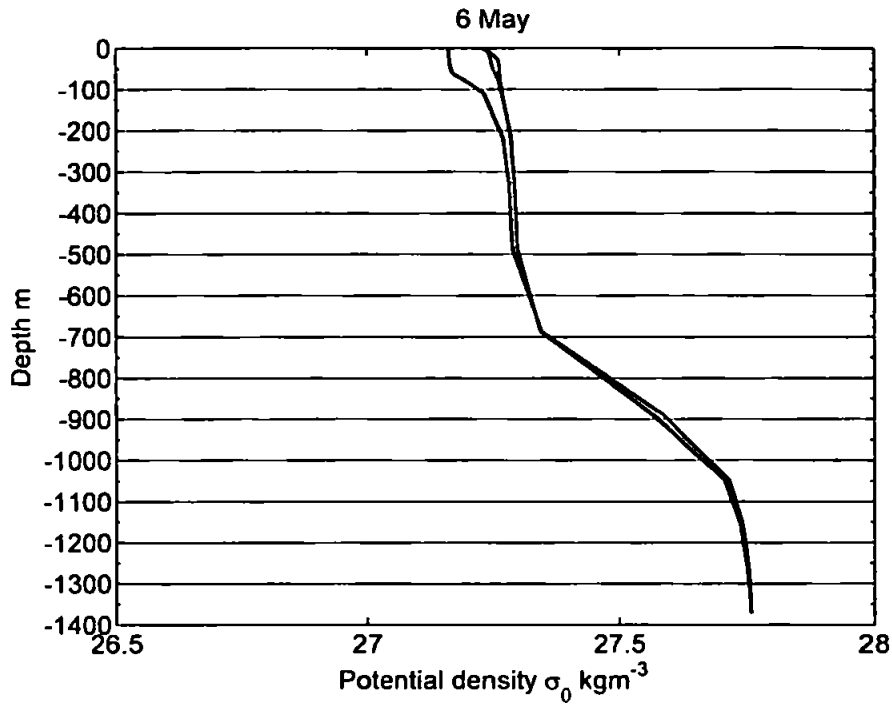


Figure 6.34 Mean density profiles σ_θ kgm⁻³ for the full model runs from the 'ocean box' on 6 May. Black: F2001, Red: F1950, Blue: F1978.

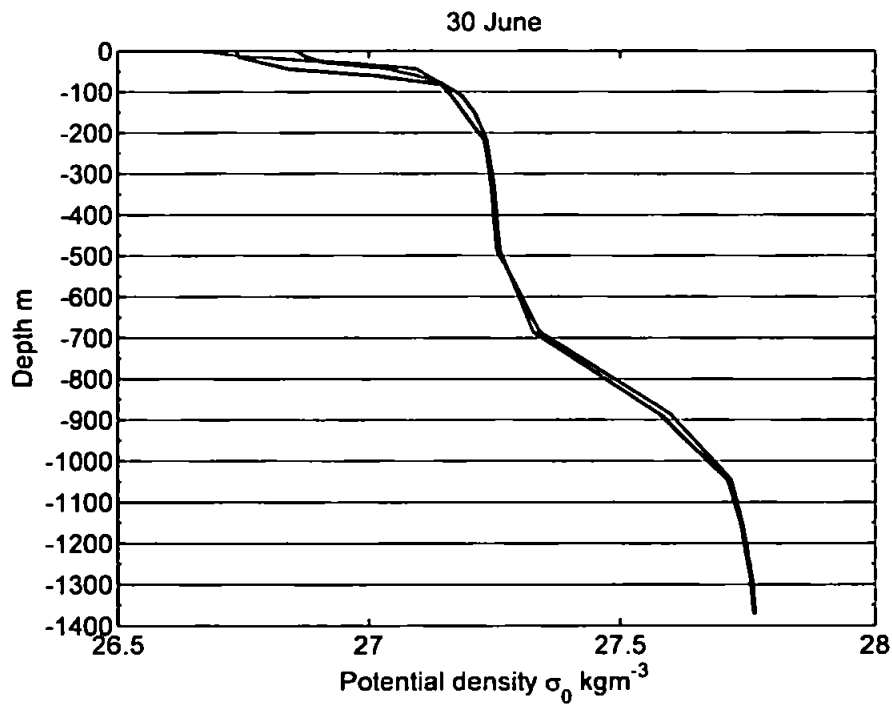


Figure 6.35 Mean density profiles σ_θ kgm⁻³ for the full model runs from the 'ocean box' on 30 June. Black: F2001, Red: F1950, Blue: F1978.

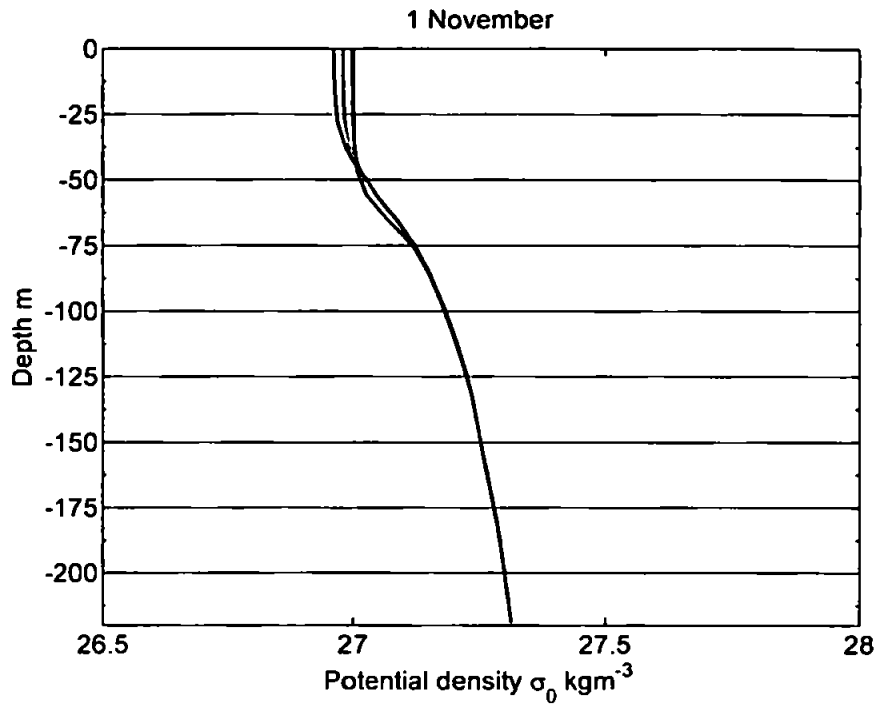


Figure 6.36 Mean density profiles σ_0 kgm⁻³ for the full model runs from the 'bank box' on 1 November. Black: F2001, Red: F1950, Blue: F1978.

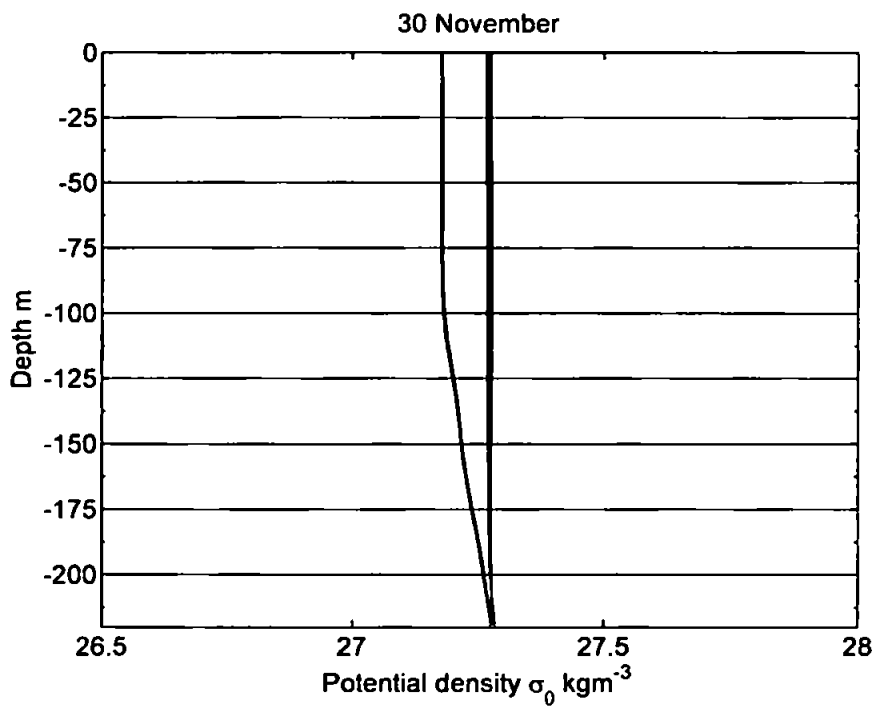


Figure 6.37 Mean density profiles σ_0 kgm⁻³ for the full model runs from the 'bank box' on 30 November. Black: F2001, Red: F1950, Blue: F1978.

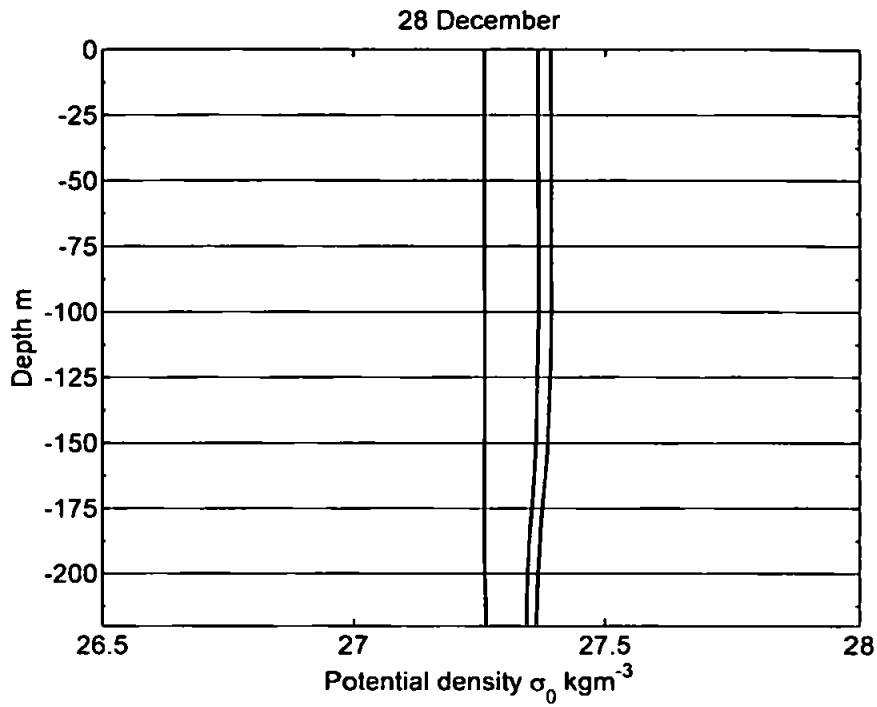


Figure 6.38 Mean density profiles σ_0 kgm^{-3} for the full model runs from the 'bank box' on 28 December. Black: F2001, Red: F1950, Blue: F1978.

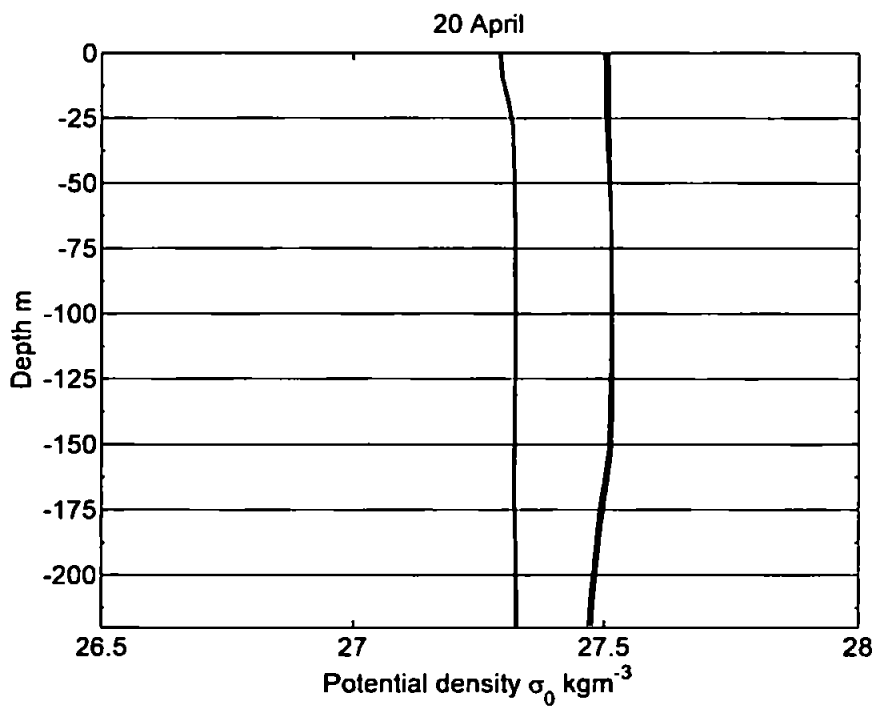


Figure 6.39 Mean density profiles σ_0 kgm^{-3} for the full model runs from the 'bank box' on April. Black: F2001, Red: F1950, Blue: F1978.

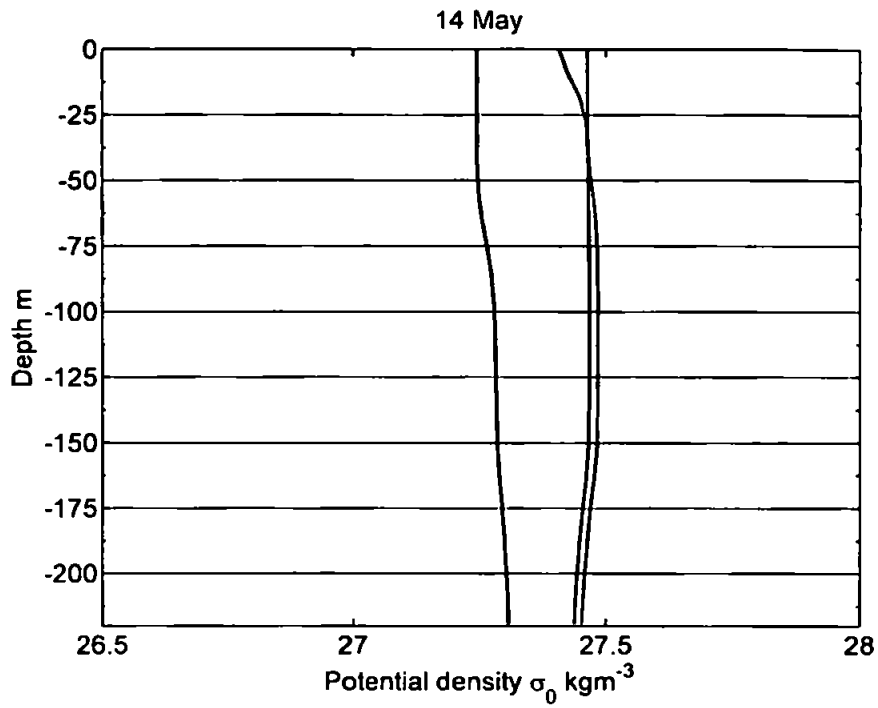


Figure 6.40 Mean density profiles σ_0 kgm^{-3} for the full model runs from the 'bank box' on 14 May. Black: F2001, Red: F1950, Blue: F1978.

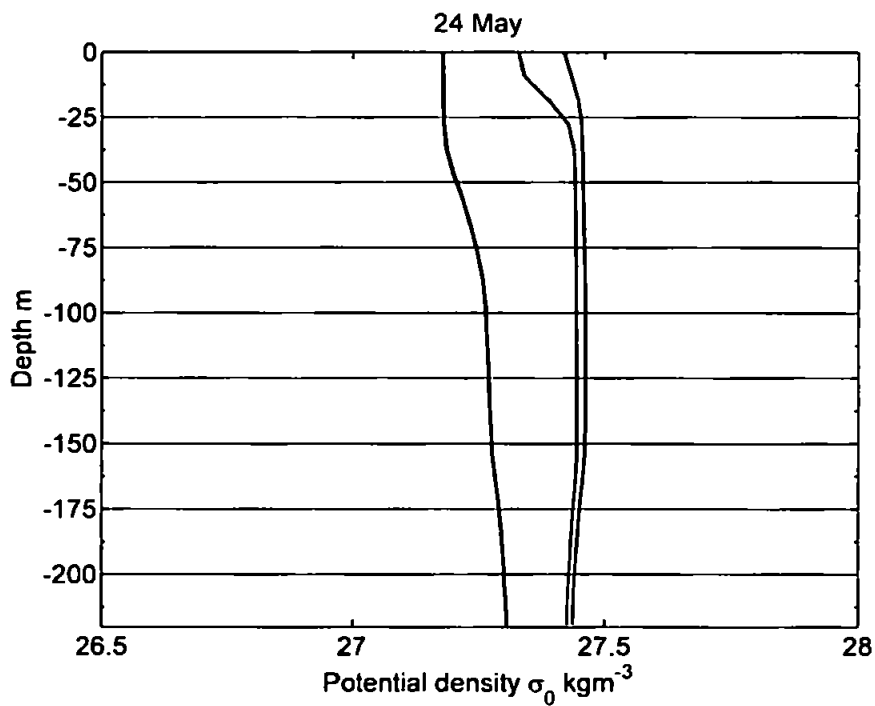


Figure 6.41 Mean density profiles σ_0 kgm^{-3} for the full model runs from the 'bank box' on 24 May. Black: F2001, Red: F1950, Blue: F1978.

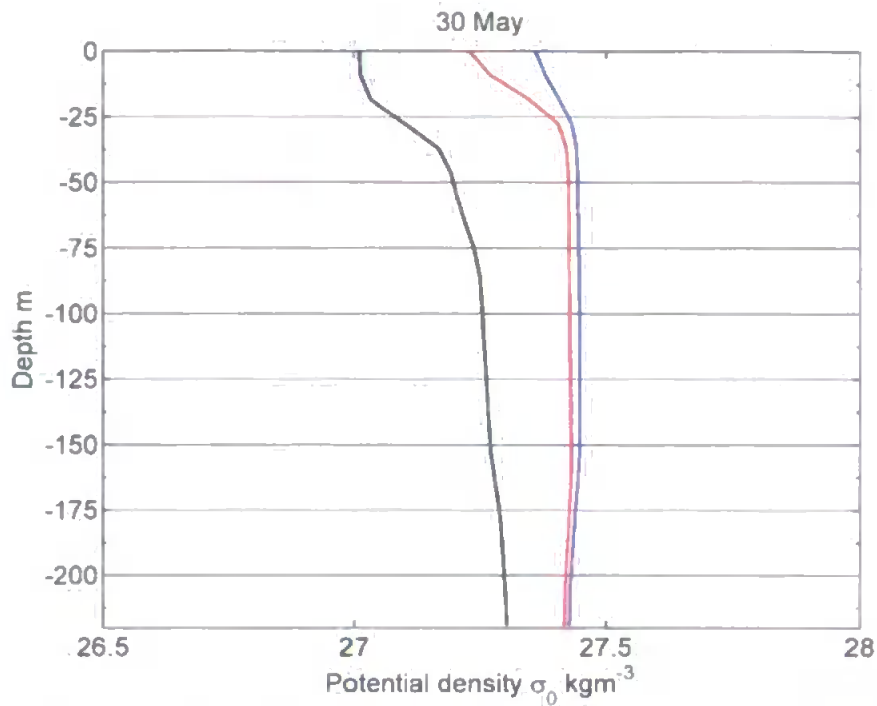


Figure 6.42 Mean density profiles $\sigma_\theta \text{ kgm}^{-3}$ for the full model runs from the 'bank box' on 30 May. Black: F2001, Red: F1950, Blue: F1978.

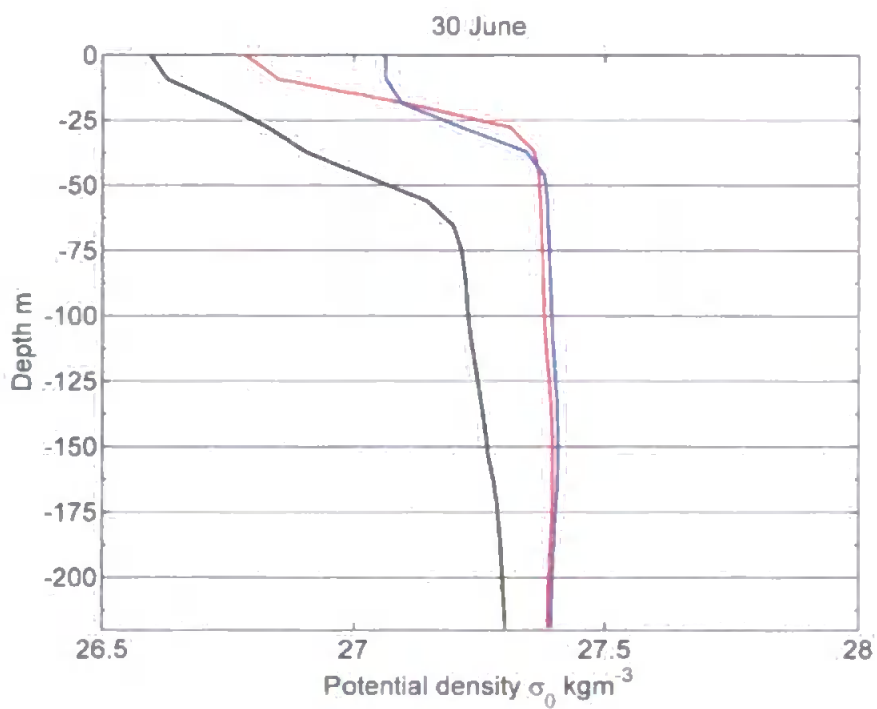


Figure 6.43 Mean density profiles $\sigma_\theta \text{ kgm}^{-3}$ for the full model runs from the 'bank box' on 30 June. Black: F2001, Red: F1950, Blue: F1978.

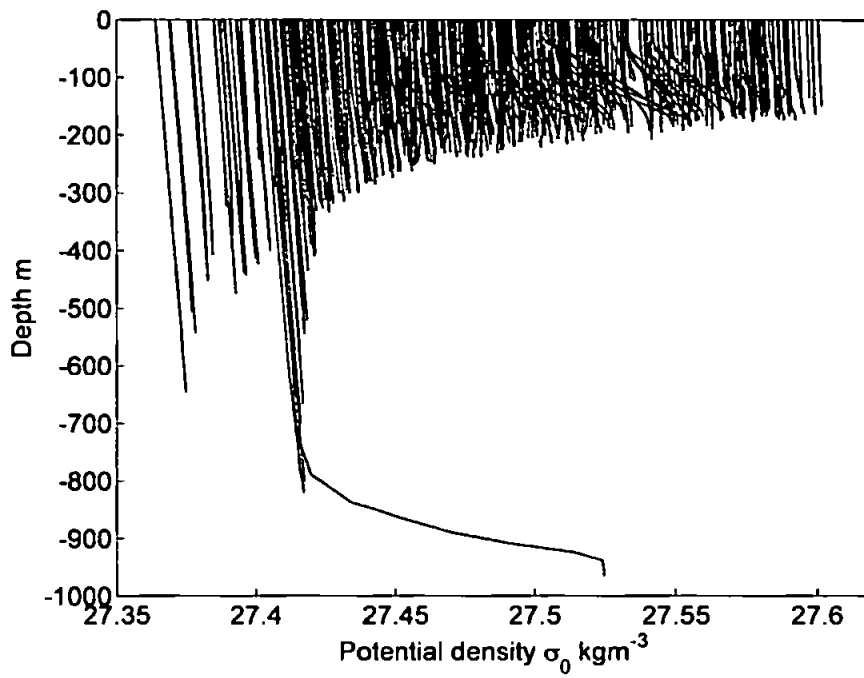


Figure 6.44 Density profiles $\sigma_0 \text{ kgm}^{-3}$ for all points within the 'Bank box' from 2 January 1979.

Chapter 7

Model Validation

7.1 Comparison of model to satellite SST

The surface temperature from run F2001 was compared to the satellite data described in Chapter 4 in order to validate the model results. The model results were averaged over the month for January, February, and March so that they may be compared to the monthly composite AVHRR data. Figures 7.1 to 7.3 show these comparisons, with model temperature on the left and satellite temperature on the right. In general we see a good agreement between the model and observational results. The cold patch is well represented in February and March, although it is less strong in the January model results than the satellite data indicate. The model temperature is slightly underestimated compared to the satellite SST by up to around 0.5°C in the South of the domain. A likely reason for this discrepancy is the use of climatological data to provide the initial and boundary temperature and salinity structure. Figure 7.4 shows the WOA01 March surface temperature as an example. Comparing this to Figure 7.3 we see that the 2001 SST from the satellite data is warmer than the climatic mean from WOA01, and the model results fit well with this mean (with the addition of the cold patch).

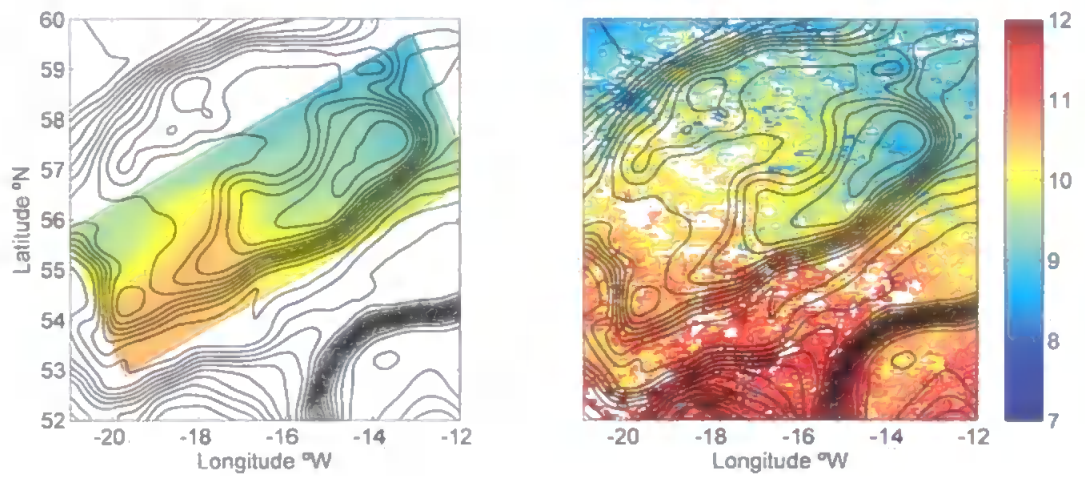


Figure 7.1 F2001: January sea surface temperature °C from the model and from satellite data.

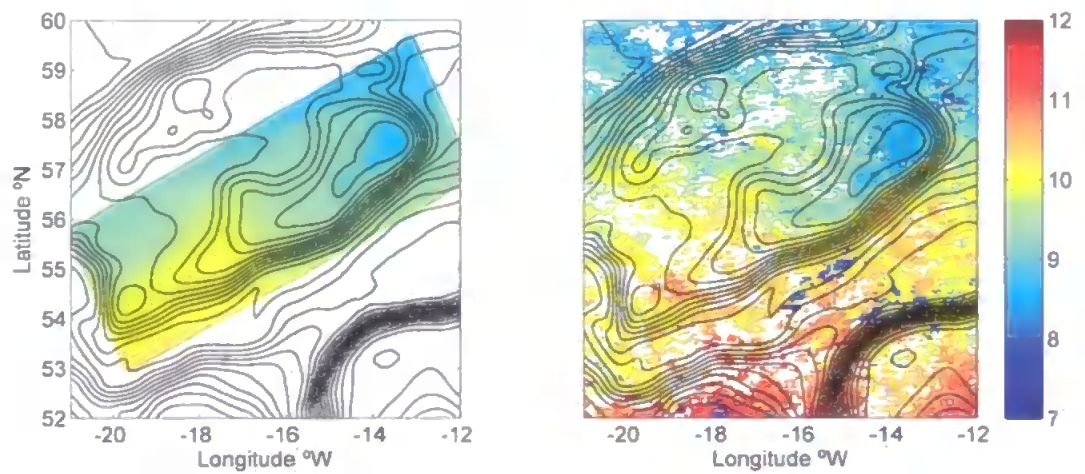


Figure 7.2 F2001: February sea surface temperature °C from the model and from satellite data.

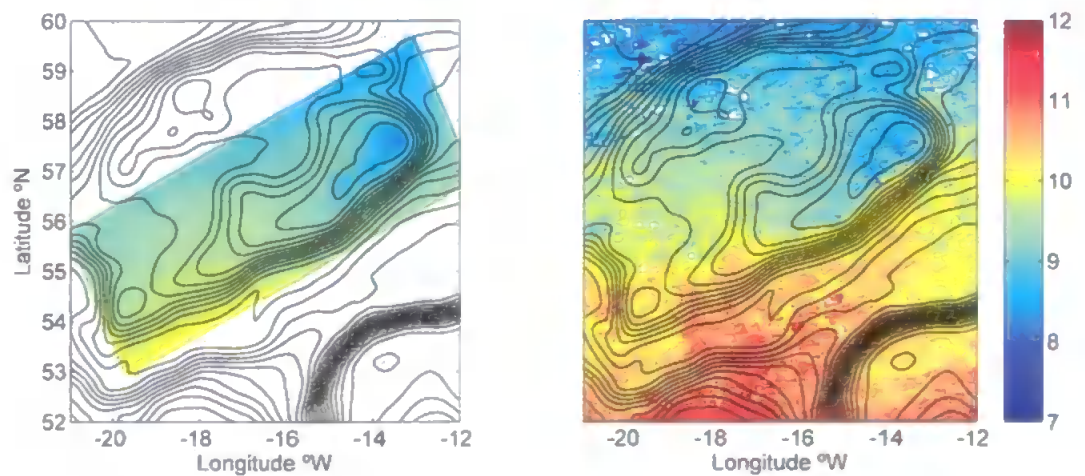


Figure 7.3 F2001: March sea surface temperature °C from the model and from satellite data.

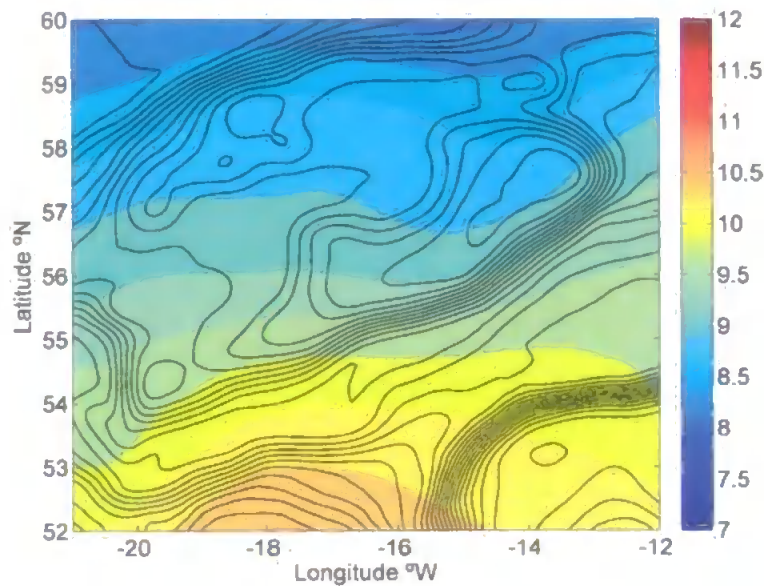


Figure 7.4 March sea surface temperature, °C from the WOA01 data set.

7.2 Geostrophic Currents

Recall from Chapter 5 that the preliminary run T3 included no forcing other than the density variation and the rotation of the Earth. In other words T3 is effectively a geostrophic run and as such we expect the induced currents to be geostrophic. Geostrophic currents were estimated from the density distribution using the method described in §3.5 (page 55) and were then compared to the currents generated by the model. The locations of the sections that were used are shown in Figure 7.7. The model results fit well with the expected velocity distribution, with the pattern and magnitudes of the currents from the model being similar to those calculated from the density fields. There is some deviation from the geostrophic currents in the vicinity of the bank, where the bed is very shallow, and we cannot therefore expect the geostrophic calculation to produce accurate results. This is illustrated by Figures 7.5 and 7.6 where the reference level is only 150 m. The influence of the bank can be seen in the shallowest area from around $i = 105$ to $i = 135$. Nevertheless the currents in the other areas, away from the top of the Bank, fit well with the expected currents.

Figure 7.8 shows the velocity along the same section but at a single time, the end of the run. We see that the model velocity fits well again except in the area over the bank. Similar results are seen along other sections such as those shown in Figures 7.9

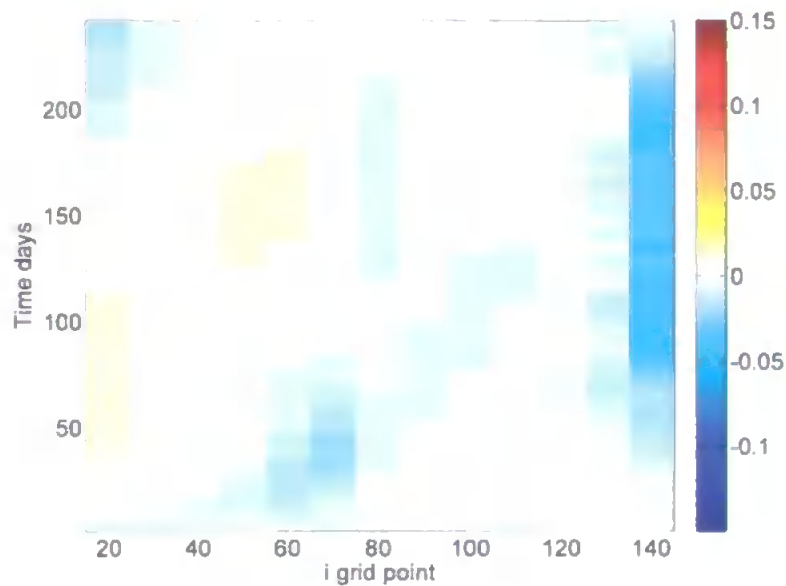


Figure 7.5 Geostrophic surface v component ms^{-1} calculated from the density distribution of run *T3* for the section $j=30$ over the length of the model run. The section runs from $i=10$ to $i=150$, meaning the calculated velocity is equivalent to the v component.

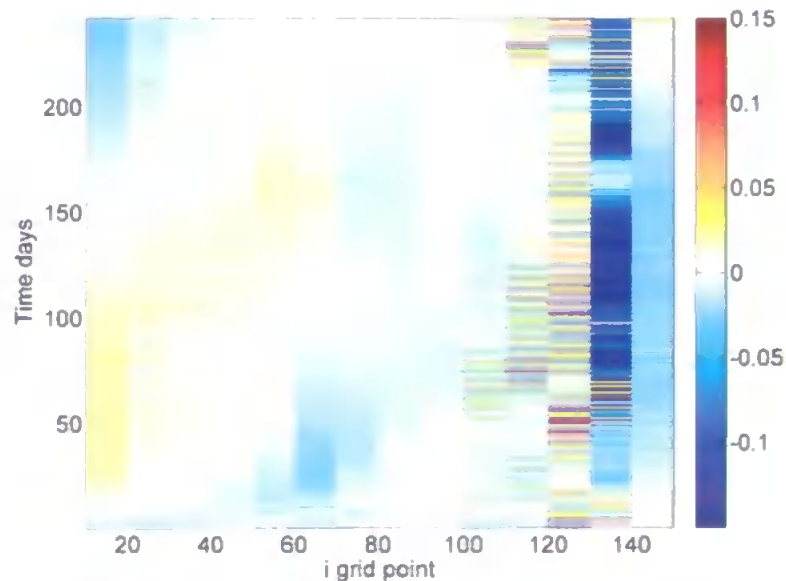


Figure 7.6 V component of surface velocity ms^{-1} from model run *T3* for the section $j=30$ over the length of the model run. Note that the effect of the shallow bank can be seen between $i=105$ and $i=135$.

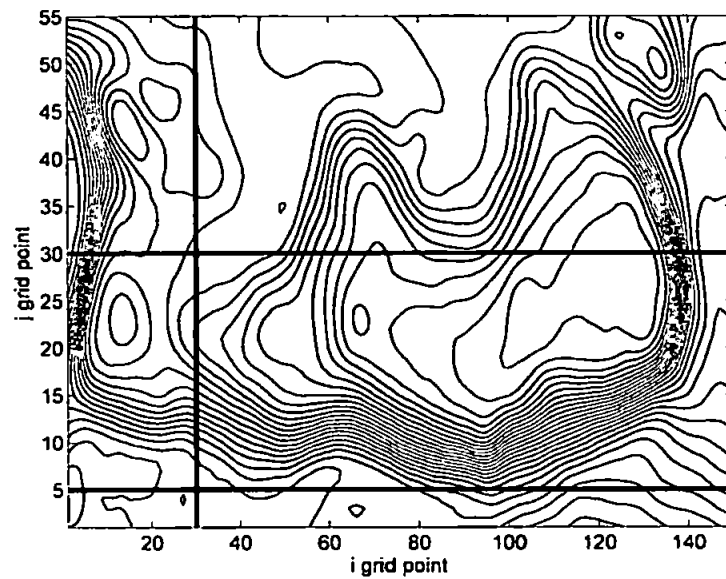


Figure 7.7 Location of the sections used in the calculation of geostrophic currents. The vertical line is section $i=30$ and the horizontal lines are $j=5$ (bottom) and $j=30$ (top). Bathymetry contours are every 100 m.

(section $j=5$) and 7.10 (section $i=30$). The section $j=5$ shows more deviation from the geostrophic currents, although the general structure is clearly related. As Figure 7.7 shows, most of this section is very close to the steep slope. The largest deviations from the geostrophic currents are seen in the vicinity of the Bank

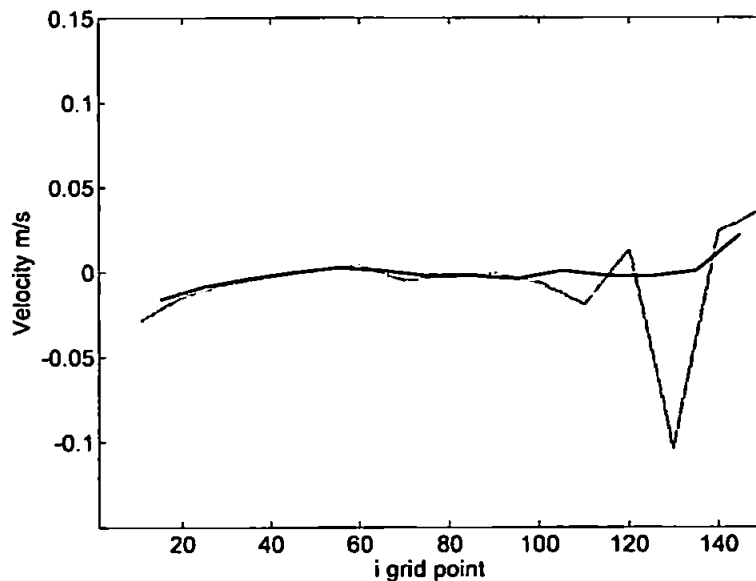


Figure 7.8 Model output v velocity and calculated geostrophic v velocity m.s^{-1} from run T3 for the section $j=30$ at 30 June. The solid line is the velocity calculated from the geostrophic equation, the dashed line is the velocity from the model.

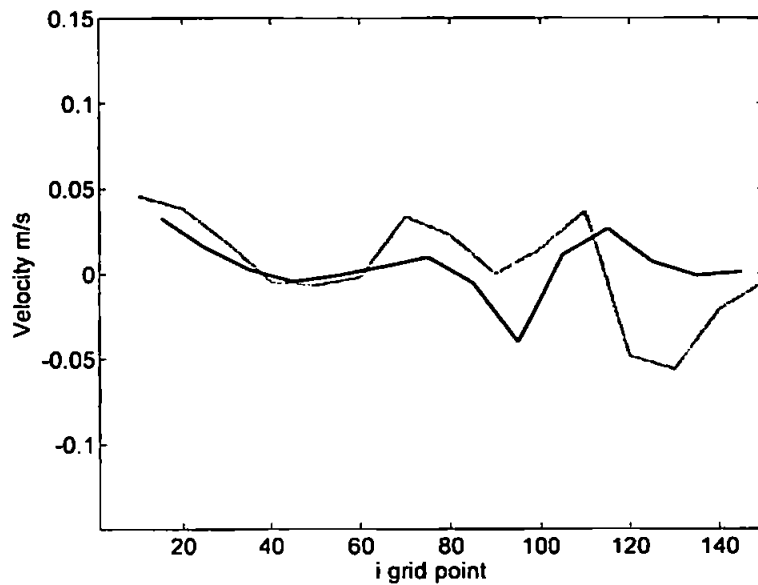


Figure 7.9 Model output v velocity and calculated geostrophic v velocity m.s^{-1} from run T3 for the section $j=5$ at 30 June. The solid line is the velocity calculated from the geostrophic equation, the dashed line is the velocity from the model.

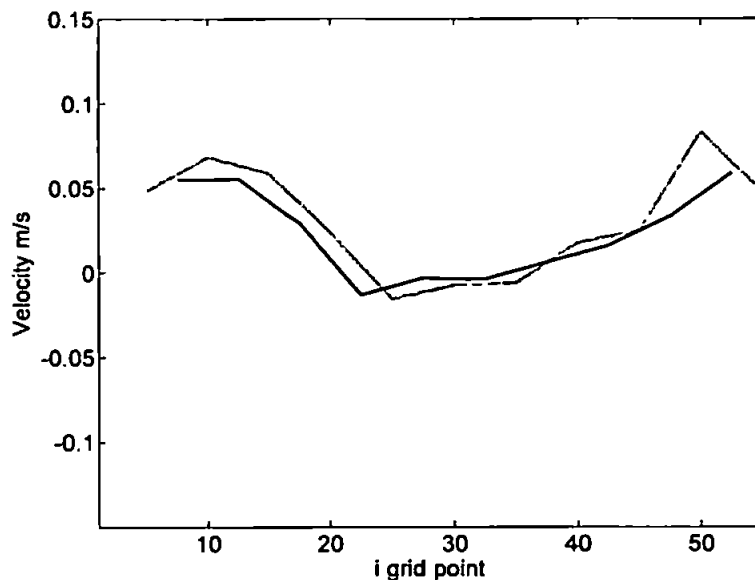


Figure 7.10 Model output v velocity and calculated geostrophic v velocity m.s^{-1} from run T3 for the section $i=30$ at 30 June. The solid line is the velocity calculated from the geostrophic equation, the dashed line is the velocity from the model.

7.3 Time Averaged Currents

Time averaged depth mean (0–500 m) currents for the geostrophic run T3 were calculated over a two month period from late March to late May. This period was chosen as it was after the large kinetic energy peak and corresponds to a relatively settled period (approximately 3500–4900 hours on Figure 5.7). The resulting velocity field is shown

in Figure 7.11. There is a clear anti-cyclonic circulation around the Bank in accordance with previous studies (e.g. Ellett *et al.*, 1986; Huthnance, 1986; Mohn and White, 2007). The typical magnitude of the main current around the Bank is $10\text{--}20\text{ cm s}^{-1}$, again in agreement with the literature (e.g. Mohn and White, 2007). The flow on top of the centre of the Bank, in the shallowest area, is less than 5 cm s^{-1} in magnitude and also does not follow the direction of the main flow. The results of this run, which did not include any tidal forcing, indicate that a Taylor column process alone is enough to set up an anti-cyclonic flow, without requiring the added influence of the tidal rectification noted by Huthnance (1974). Figure 7.11 also shows a persistent clockwise eddy located in the top left corner.

As discussed previously in Chapter 3, sigma-coordinate models are susceptible to errors in the calculation of the horizontal pressure gradient (Haney, 1991; Mellor *et al.*, 1994; Griffies, 2004). The results of the geostrophic run, as well as Run T2 in which the bathymetry was used with no other forcing, show that the approach taken in POLCOMS has reduced this problem and the steep topography has not generated significant spurious currents.

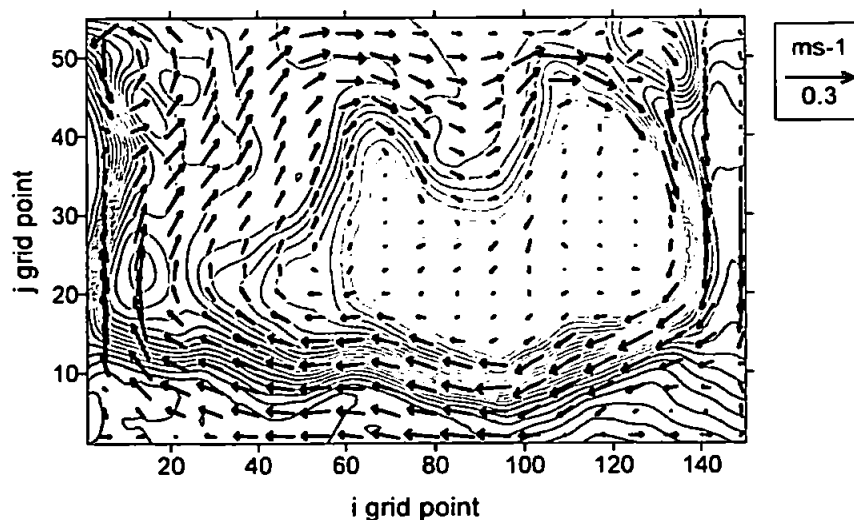


Figure 7.11 Depth mean currents ms^{-1} (top 500m) averaged over a two month period from run T3. Note that not all grid points have been plotted for clarity.

Similar analysis was conducted for the full model runs (Figure 7.12), using a four week period so as to include a whole number of spring/neap tidal cycles.

We see from Figure 7.12 that the main features are similar to those of the geostrophic

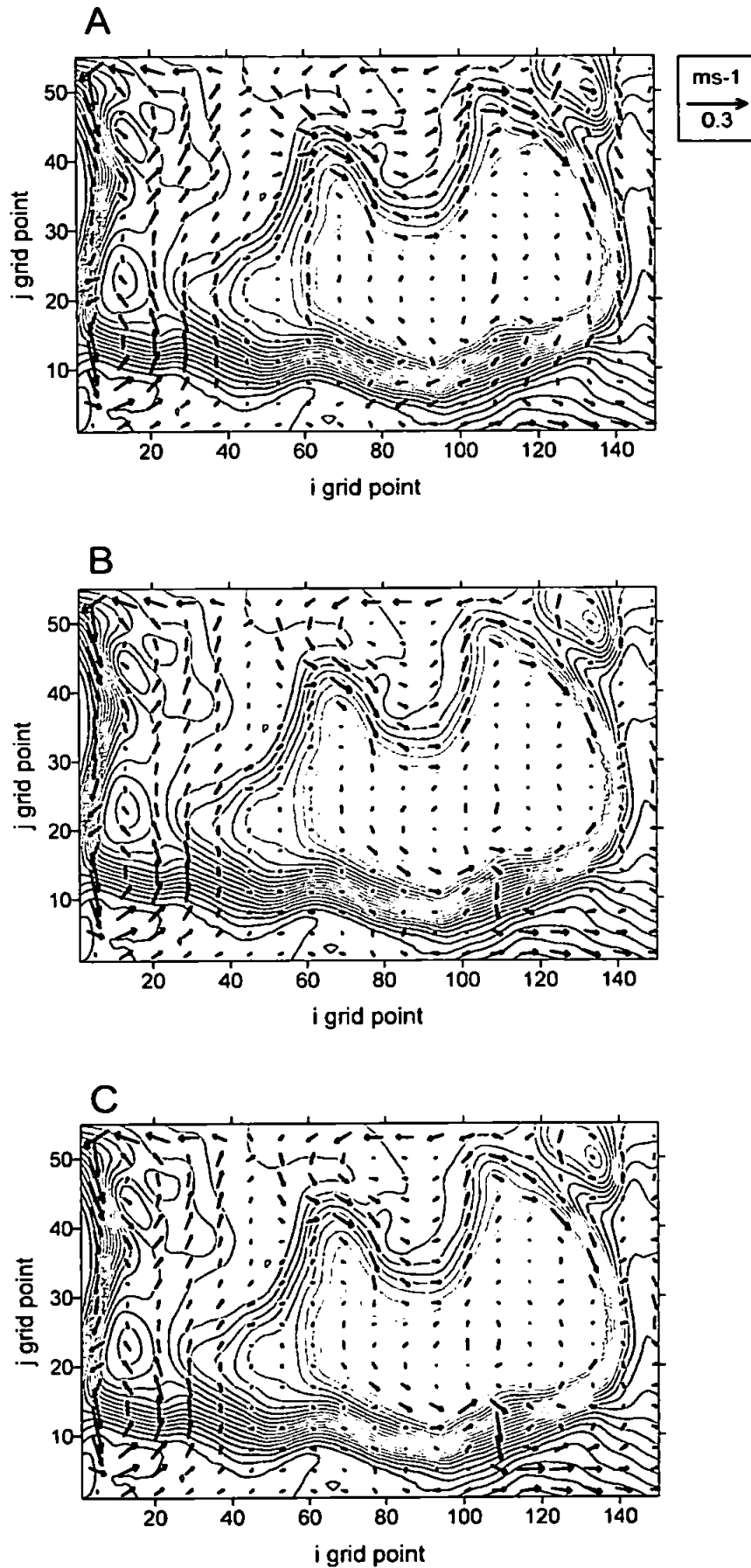


Figure 7.12 Depth mean currents ms^{-1} (top 500m) averaged over a 4 week period from run F2001 (A), F1950 (B), F1978 (C). Note that not all grid points have been plotted for clarity.

run T3. We see a broadly anti-cyclonic circulation around much of the Bank with similar magnitudes of $10\text{--}20\text{ cm s}^{-1}$. This is true particularly of run F2001, whereas F1950 and F1978 show a weaker circulation. In all three cases the anti-cyclonic nature of the flow breaks down along the bottom part of the domain.

The eddy that was seen in the top left corner of Figure 7.11 has, in the full runs, expanded to run down the entire left edge of the domain. At first glance we might assume that the open boundary was not behaving correctly here, causing water to be trapped along a perceived coastline. However, we do see flow going across this boundary in some areas, especially when looking at the instantaneous currents. Figure 7.13 shows an example of the surface velocity from run F2001 at a time within the period that was averaged. This counter current was not seen in the runs that did not include tides, so is presumably due to interaction between the tidal currents and the steep slope. It has previously been noted that there is strong tidal amplification in this area (Huthnance, 1974).

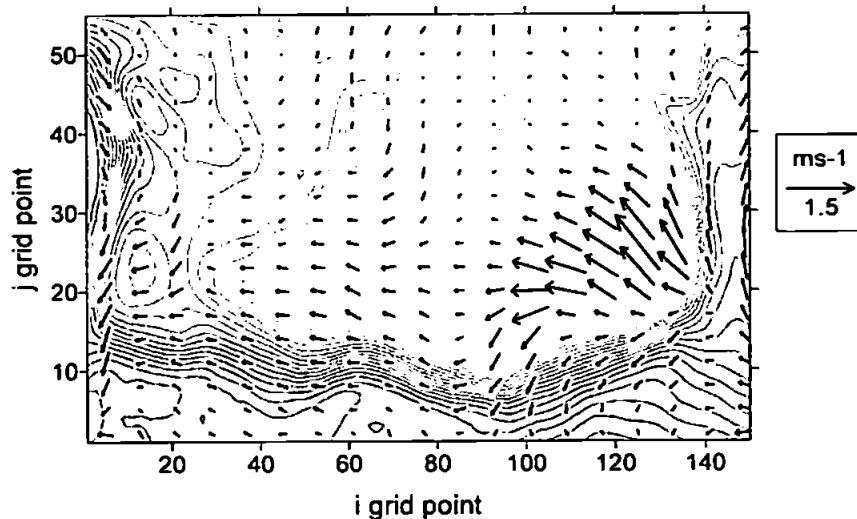


Figure 7.13 *Instantaneous surface currents ms^{-1} from 9 April of run F2001. Note that not all grid points have been plotted for clarity.*

7.4 Summary

In general the model results agree well with existing data and measurements. The sea surface temperature is slightly underestimated for the year 2001, but fits well with the climatological data that were used for initialisation and boundary forcing. This indicates

that for future work it may be desirable to assimilate real data measurements with the climatological field in the boundary forcing.

The circulation is predominantly anti-cyclonic around Rockall Bank, consistent with previous work (e.g. Ellett *et al.*, 1986; Huthnance, 1986; Mohn and White, 2007), and agrees well in geostrophic runs with the currents that would be expected from the density distribution.

The currents along the southern flank of the Bank do not fit so well with observed data.

Chapter 8

Discussion

8.1 Annual Variation in Dense Water Formation

The principal aim of this research was to fill in some gaps in our knowledge of the dense water formation at Rockall Bank by establishing how much it varies when the meteorological conditions change. We saw in Chapter 6 that there were significant differences between the ‘cool’ and ‘warm’ simulated years in the timing and degree of the formation of dense water over Rockall Bank. In order to qualitatively compare these results, two density parameters were calculated: one for a sample area on top of the Bank, and one over the deeper ocean. The location of these sample areas is the same as those used in the stratification analysis in Chapter 6 and they are illustrated by Figure 6.25. The density parameter was produced by taking the maximum density value found within the top 500 m of the water column in each of these two locations. These two parameters, which we label σ_B and σ_O for the Bank and ocean boxes respectively, may then be used to compare the evolution of the dense water in the three different model runs. Figure 8.1 shows a comparison of σ_B and σ_O in two of the runs: F2001 and F1978. We will begin by looking at the difference in the Bank density parameter σ_B in 2001 and 1978, indicated by the lines with markers.

We see from Figure 8.1 that the peak Bank density σ_B in F1978 is much higher than in F2001—reaching 27.45 kgm^{-3} in F2001 and 27.68 kgm^{-3} in F1978. This leads to a typical difference between σ_B and σ_O of $0.2\text{--}0.3 \text{ kgm}^{-3}$ in F1978 compared to only 0.1

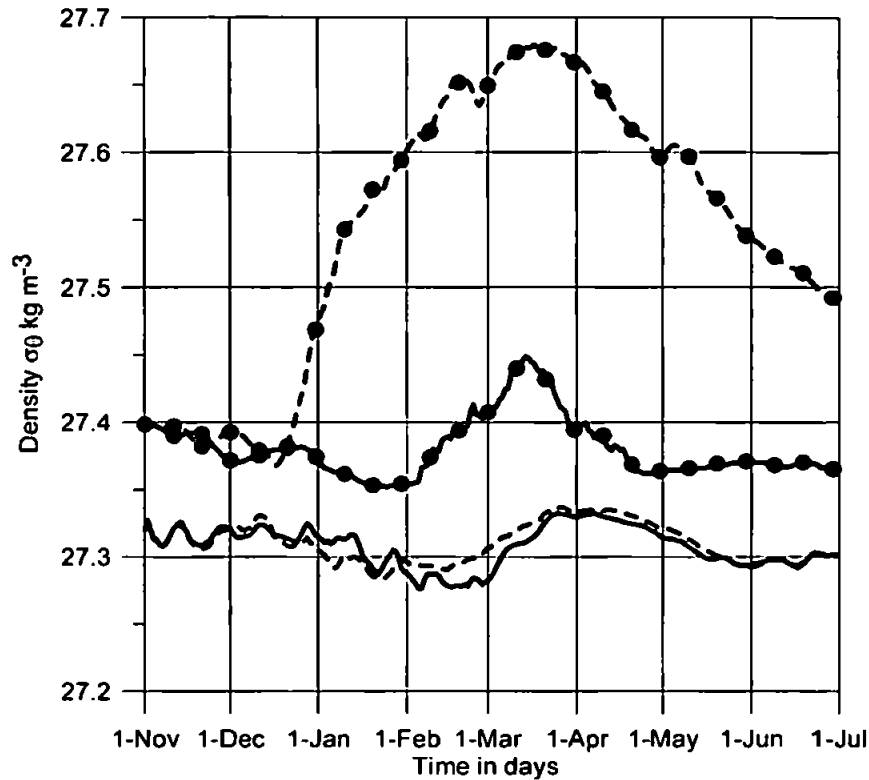


Figure 8.1 Maximum density $\sigma_0 \text{ kg m}^{-3}$ value found in the top 500 m of sample areas over the Bank (lines with markers) and offshore (without markers) in F2001 (solid lines) and F1978 (dashed lines). The areas sampled are shown in Figure 6.25.

kg m^{-3} in F2001 while the maximum difference reached is 0.36 kg m^{-3} in F1978 and only 0.14 kg m^{-3} in F2001. It is not just the strength of the density difference that varies: there is also significant variation in the duration of the densest water between the two years. In F2001 σ_B value begins to increase at the start of February before reaching its maximum value in mid-March. It then immediately begins to decrease again, until it levels off in the second half of April. In F1978, on the other hand, σ_B starts to increase much earlier in mid-December, and the rate of increase is quicker than in F2001. The peak value is reached in mid-March, similarly to F2001. σ_B then decreases at a steady rate which continues until the run finishes at the end of June. At the end of the run the σ_B value in F2001 is lower than it was at the start, whereas in F1978 then final σ_B value is almost 0.1 kg m^{-3} higher than the initial value. These marked differences in the evolution of the density structure may be attributed to the different meteorological conditions as both runs were initialised from the same state, and receive the same boundary temperature forcing.

We can compare the F2001 results with the temperature series for 2001/2002 from the

satellite data analysed earlier. As listed in Table 4.1 a surface cold water patch was observed over the Bank from December–April inclusive during the winter of 2001/2002. This correlates with the decreasing σ_B value in April of the F2001 model run. However, the dense water did not form as early as December in the model. It can be seen beginning to form at the start of January, but only begins to strengthen in February.

Looking now to the model results from the area over the deep ocean (Figure 8.1, lines without markers) the results are very different: there is almost no difference in the behaviour of the density parameter σ_O in the two modelled years. This indicates that meteorological changes are not enough on their own to produce the large variation in the dense water formation seen over Rockall Bank. In other words, the topography of the Bank hugely amplifies the effect of the increased heat flux and is crucial in allowing dense water to form, and therefore cascade, in this area. Another feature that we see in the σ_O data is a strong apparent spring-neap tidal signal from November until around early February. This is likely due to vertical movement of the pycnocline caused by the tides. We saw in Chapter 5 that there is a strong spring-neap tidal signal in this area of the model domain. This modification of the σ_O value disappears after February, which is around the time that the mixed layer depth of this box reaches 500 m (see Figure 6.29 for example). This is the maximum depth that was used in the calculation of σ_O . Therefore, as the mixed layer starts to become deeper than this, the tidal movement is no longer able to modify the density in the upper 500 m, and we see the tidal signal disappear from the σ_O values.

The strong difference in the effect of changing meteorology on the Bank and ocean densities is confirmed by the SST data that were analysed in Chapter 4. Recall that a similar analysis was conducted, in which the median temperature was calculated for two sample boxes. Again there was one box over the Bank, and one over the deeper ocean. Their location is shown in Figure 4.5 and we label the temperature parameters produced T_B and T_O respectively. Figure 8.2 shows T_B and T_O for two example years: 1993/1994 and 1996/1997. We see a similar pattern to that of the density parameters, namely that the temperature over the Bank T_B is more susceptible to change than the temperature over the deep ocean T_O . Therefore we see variability in the temperature

difference between the Bank and ocean areas. The effect here is not as extreme as in the model results, perhaps because there was not such a large difference in meteorological conditions as there was between 1978 and 2001. Alternatively, this could be an effect of using satellite sea surface temperature data which can only measure the very surface of the water, which is susceptible to short time scale solar and wind heating/cooling.

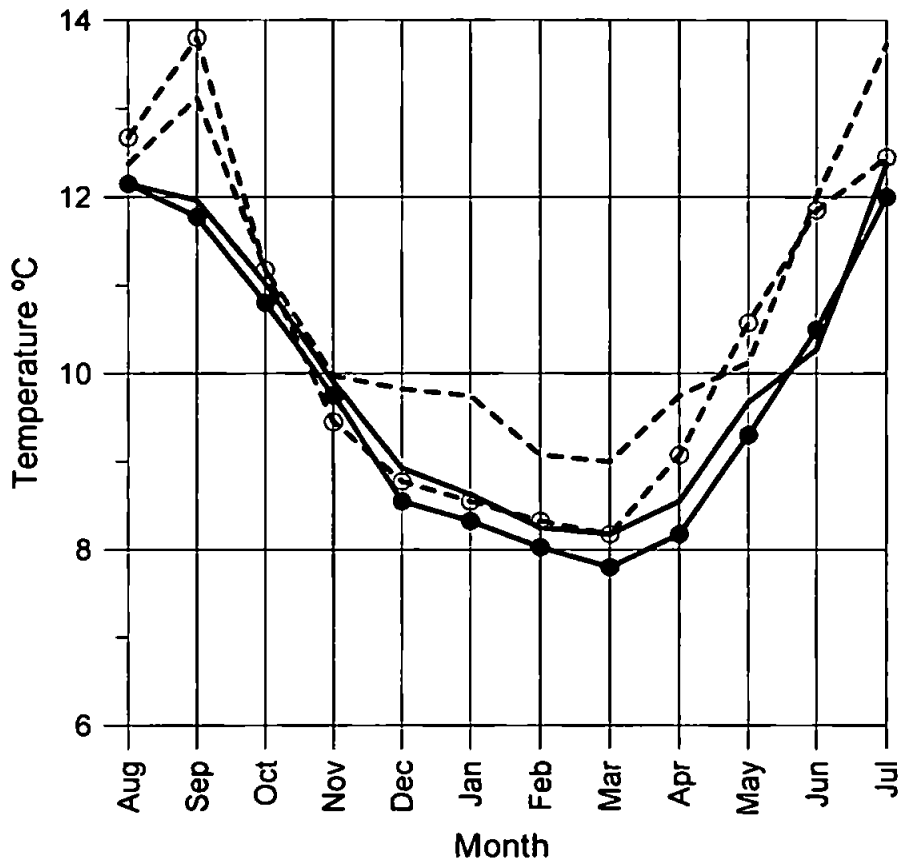


Figure 8.2 Mean SST °C from the AVHRR sample areas over the Bank (lines with markers) and offshore (without markers) in 1993/1994 (solid lines) and 1996/1997 (dashed lines). The areas sampled are shown in Figure 4.5.

The difference in density distribution between the two modelled cold years, F1950 and F1978 is much smaller than it was between F1978 and F2001. Figure 8.3 shows σ_B and σ_O in F1978 and F1950; we see there is much more similarity between these years than there is in Figure 8.1 and both of the cold years have typical density differences of $0.2\text{--}0.3\text{ kgm}^{-3}$. Nevertheless there are some variations. The maximum density difference reached in F1950 is 0.32 kgm^{-3} , slightly lower than F1978's 0.36 kgm^{-3} and there are also some differences in the timing and evolution of the dense water. The density over the Bank, σ_B , in F1950 begins to increase slightly earlier than it does in F1978—the first half of December rather than the second half—but the rate of increase is slower.

This leads to σ_B in F1978 overtaking F1950 at the start of January. Whereas σ_B in F1978 reaches its peak (27.68 kgm^{-3}) in mid-March, F1950 reaches its maximum value (27.63 kgm^{-3}) earlier, in late February. It remains around this level until mid-April when it begins to decrease. Conversely, in F1978 σ_B begins to decrease immediately after reaching the peak value. The rate of decrease is slightly quicker in F1950, such that the final value of σ_B is slightly higher in F1978 (by 0.03 kgm^{-3}). In both simulations σ_B is higher at the end than it was at the start.

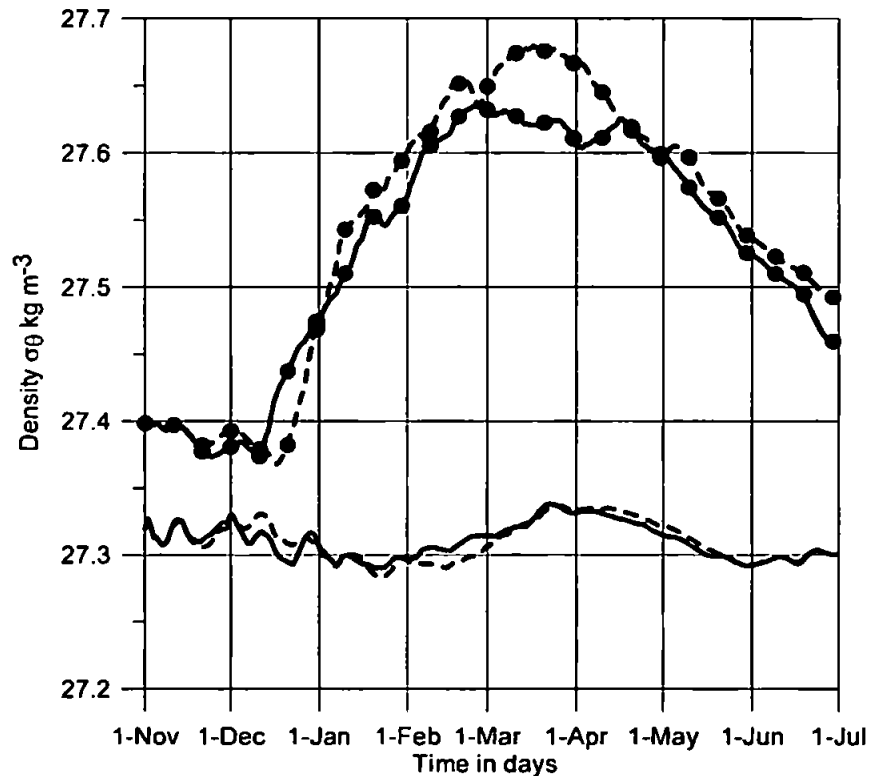


Figure 8.3 Maximum density $\sigma_\theta \text{ kgm}^{-3}$ over the Bank (lines with markers) and offshore (without markers) in F1950 (solid lines) and F1978 (dashed lines). The areas sampled are shown in Figure 6.25.

8.2 Cascading

Although there are clear areas of dense water formed, to varying degrees, in each of the full runs, we do not see the degree of cascading that was present in the preliminary run T6. In F2001 particularly, where the density difference between the Bank and deep sea areas was smaller, there is no evidence at all of the dense water cascading downslope. Instead, the water remains on top of the Bank and circulates anti-cyclonically until it disappears

due to warming in the spring. This is similar to the behaviour of the preliminary run T9, which featured the initial density distribution and the 2001/2002 heat flux but no other forcing, and also showed no cascading. Again this implies that it is the surface heat flux and resulting dense water that is most important, and adding wind and tidal forcing does not increase the water's ability to cascade. This supports the validity of the hypotheses used in the reduced-physics models of Symonds and Gardiner-Garden (1994) and Shapiro and Hill (1997).

F1950 and F1978 on the other hand do show some signs of cascading. However, this is not as frequent as it was in T6. In addition whereas T6 showed water cascading down both the southern and north eastern slopes of the Bank, in F1950 and F1978 water appears only to move down the southern slope. Figure 8.4 shows the density for a selected area along the southern slope of the Bank for selected days from F1978. We see that initially there is no dense water over the Bank; by January dense water has started to accumulate and later in February and March we see a 'tongue' of dense water protruding downslope.

Dense water cascades have been observed at Rockall Bank, so it is perhaps surprising that we do not see clear examples in the simulations conducted in this study. This could be due to the particular years chosen, or limitations of the model parametrization of processes such as internal wave mixing. Nevertheless, the model results here provide a useful comparison between different winter conditions.

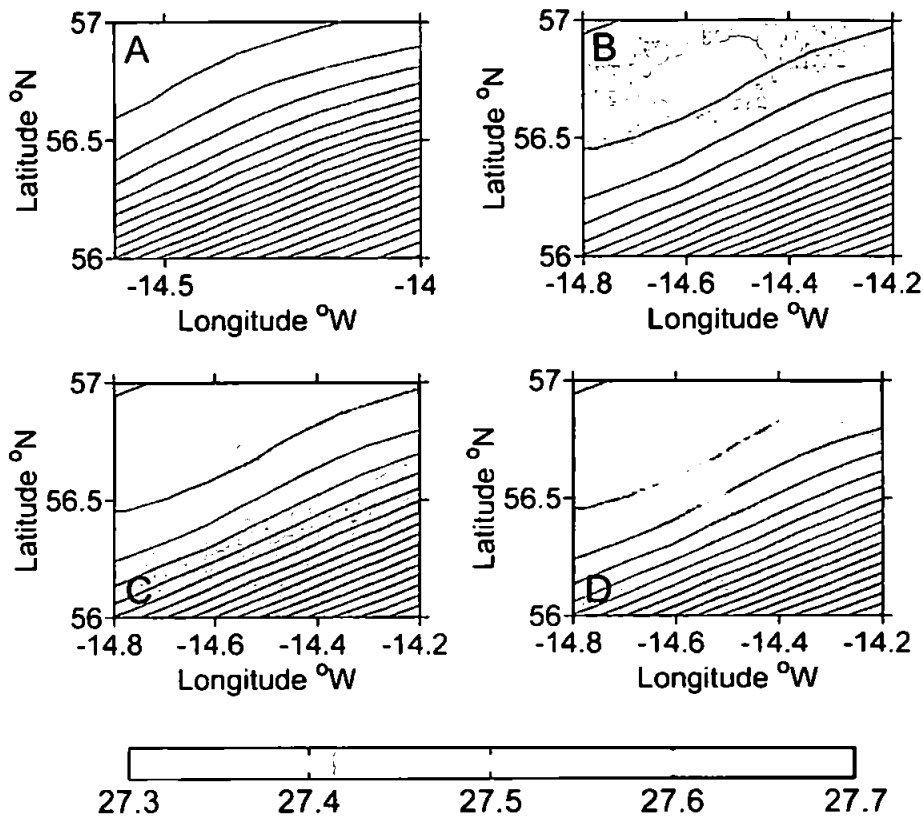


Figure 8.4 Bottom density for selected days of F1978. Shaded contours are potential density σ_θ kgm^{-3} . Bathymetry contours (solid lines) every 100m are also shown. A: 15 November 1978, B: 3 January 1978, C: 14 February 1979, D: 19 March 1979.

8.3 Summary

By comparing the results of the three simulations F2001, F1978 and F1950 we deduce that the dense water formation at Rockall Bank is extremely susceptible to changes in winter air temperature. The topography of the area greatly amplifies the effect of the changing heat flux and with only around a 2°C difference in mean air temperature we saw a three-fold increase in the difference between the two density parameters σ_B and σ_O . It is therefore likely that climate change will have a significant impact on this system. In particular, cascading did not occur at all when the air temperature was high and not much dense water was formed. A reduction in dense water cascading here would have both physical and biological implications. Cascading adds to the ventilation of deeper water, and facilitates shelf-ocean exchange (Shapiro *et al.*, 2003). Further research in this area to establish the relative size of the contribution from cascading to these processes is needed in order to fully understand the potential effects of any future

reduction in dense water formation.

On the other hand, the difference in mean winter wind speed between 1978 (relatively high wind) and 1950 (relatively low wind) does not appear to have a significant influence on the amount or timing of the dense water formation.

Chapter 9

Conclusions

This study has used both numerical modelling and analysis of remotely-sensed sea surface temperature data to investigate the formation of cold, dense water over Rockall Bank. Previous work has found evidence of this water formation (Mohn and White, 2007) and its subsequent cascading (Shapiro *et al.*, 2003; Ivanov *et al.*, 2004), but little is known about the variability of these processes here. The aim of this research was to build upon these previous results and add to our knowledge of the formation and cascading of dense water at Rockall Bank by investigating its variation and sensitivity to changing climatology. Satellite data were used to provide a long time-series of surface temperature so that the annual variation could be studied. Secondly, the POLCOMS model was used to fully simulate dense water formation in a number of sample years, allowing us to determine the contribution from changing air temperature and wind speed.

Simpler initial model runs demonstrated that the model was behaving reasonably. The results of these initial runs showed that the model set up is capable of accurately reproducing the anti-cyclonic circulation around the Bank, as well as allowing the formation and cascading of dense water. When full atmospheric and tidal forcing were later introduced the results were reasonable. There does appear to be some interaction between the bathymetry and the tide along the steep slope close to the left hand edge of the model domain. In all three full simulations the mixed layer depth reached 700m in the deep water area, in agreement with previous findings (e.g. Meincke, 1986).

The years chosen for the full simulations were 1950/1951, 1978/1979, and 2001/2002

(labelled F1950, F1978 and F2001 respectively). The winter of 2001/2002 was 1.0–1.5 °C warmer than the climatological mean and was selected to be modelled as a sample "warm year". By contrast the winter air temperature in both 1950/1951 and 1978/1979 was 0.5–1.0 °C cooler than the climatological mean. Both were chosen to be modelled as "cool years" as they have different wind speed anomalies, so a comparison of these two simulations would highlight the contribution to dense water formation that the wind mixing and cooling has. 1950/1951 had lower than average winds (by 10–15%), and 1978/1979 higher than average (by around 10%).

The results of both the satellite SST data and the model runs showed that there is significant variation in the formation of cold water over Rockall Bank in different years. The SST analysis found that cold water linked with Rockall Bank could be seen every year across the 1992-2004 study period, in accordance with previous work (Mohn and White, 2007). There were two modes identified: a front corresponding to the southern edge of the Bank, and a more distinct cold patch located over the Bank. There was significant annual variation in the length of time that these features could be seen in the data, with the presence of the distinct cold patch varying from 0 to 5 months in duration. Analysis of the temperature difference between two sample areas—one on top of the Bank, one over deeper water—showed a clear correlation between the mean temperature difference during the winter and the duration of the cold water patch. Less intuitively there was also an inverse correlation between the mean temperature difference and the total duration of the front and cold patch combined. We therefore also saw an inverse correlation between the total duration of the front and cold patch, and the duration of the cold patch alone. Currently we do not have an explanation as to why the temperature difference and front duration are linked in this counterintuitive way and further research would be required in order to fully understand these results.

The results of the full model runs showed that a decrease in air temperature has a significantly larger effect on the Bank's density than it does on the deeper ocean. In other words, the topography of Rockall Bank greatly amplifies the effect of the increased surface heat flux, and the Bank-ocean density difference was up to three times greater in runs F1950 and F1978 than in F2001. Additionally the dense water lasted longer in

F1950 and F1978. In F2001 the dense water completely disappears by mid-May and is replaced by water that is less dense than in the surrounding areas. By contrast, in both F1950 and F1978 there is still some trace of dense water remaining at the end of June. The similarity of runs F1978 and F1950 suggests that dense water formation at Rockall Bank is much more sensitive to winter air temperature than wind speed.

A large amount of cascading was seen in a simple run which included surface heat flux, but a homogeneous initial density distribution. When the more realistic density distribution was introduced this cascading was inhibited and the dense water took longer to form. This was also the case in the full run F2001. F1950 and F1978 did show some downslope flow of dense water, although this was far less often than in the initial test run. The significant reduction in dense water formation, and subsequent loss of cascading, in the warmer year suggests that climate change could potentially have a large effect on this system. Dense water cascades are important for the ventilation of intermediate waters, and for shelf-ocean exchange (Shapiro *et al.*, 2003) and therefore the variability of cascading is important. Additionally, the cold water over Rockall Bank is associated with high productivity (Mohn and White, 2007) and therefore any change in the formation of dense water following changing climate could have a significant implications for the local ecosystem.

It should be noted that the model simulations conducted here all started with the same climatic initial density distribution, in order to investigate only the differences caused by the meteorology. Further research would be needed to elucidate the details of what would happen if changing sea temperature were also included.

The **main conclusions** of this study are as follows:

- The POLCOMS model was successfully applied to the Rockall Bank area.
- Dense water is formed (to varying degrees) on top of the Bank each year. The duration of the cold water patch is linked to the magnitude of the temperature difference between the Bank and open ocean over the winter. In addition, where the cold water is not observed for a lengthy period, there tends to be a more long-lived SST front associated with the Bank.
- The topography of Rockall Bank greatly amplifies the effect of changes in meteorology on the formation of dense water. The dense water formation is much more sensitive to air temperature than wind speed, with around a 2°C air temperature difference leading to a three-fold increase in the density difference between Bank and ocean.
- Despite dense water being formed there was no evidence of cascading in the warm year of 2001/2002. There was limited evidence in the two cool years 1950/1951 and 1978/1979.
- The large variability in the formation and cascading of dense water under different meteorological conditions suggests that climate change could have a major impact on the Rockall Bank system, both in terms of the ventilation and shelf-sea exchange, and on the local ecosystem.

References

- Arakawa, A., 1972. Design of the UCLA general circulation model. Technical Report 7, Dept. of Meteorology, University of California
- Boyer, T., Levitus, S., Garcia, H., Locarnini, R., Stephens, C., and Antonov, J., 2005. High resolution (1/4 degree) temperature and salinity analyses of the world's oceans. version 2. *International Journal of Climatology*, 25, 931–945
- Burchard, H., 2001. On the q^2l equation by Mellor and Yamada (18=982). *Journal of Physical Oceanography*, 31, 1377–1387
- Burchard, H., Petersen, O., and Rippeth, T. P., 1998. Comparing the performance of the mellor-yamada and the $k - \epsilon$ two-equation turbulence models. *Journal of Geophysical Research: C*, 103, 10,543–10,554
- Colella, P. and Woodward, P., 1984. The piecewise parabolic method (ppm) for gas-dynamical situations. *Journal of Computational Physics*, 54, 174–201
- Computational Science Education Project, 1995. Ocean models. URL <http://www.phy.ornl.gov/csep/CSEP/OM/OM.html>. [online; accessed 10-September-2008]
- Condie, S., 1995. Descent of dense water masses along continental slopes. *Journal of Marine Research*, 53(6), 897–928
- Cressie, N. A. C., 1993. *Statistics for Spatial Data*. Wiley Series in Probability and Mathematical Statistics. John Wiley & Sons Inc.
- Dickson, R. R., Gould, W. J., Griffiths, C. R., Medler, K. J., and Gmitrowicz, E. M., 1986. Seasonality of currents of the Rockall Channel. *Proceedings of the Royal Society of Edinburgh*, 88B, 103–125
- Dyke, P. P. G., 2001. *Coastal and Shelf Sea Modelling*. Topics in Environmental Fluid Mechanics. Kluwer Academic Publishers
- Ellett, D., Edwards, A., and Bowers, R., 1986. The hydrography of the Rockall Channel—an overview. *Royal Society of Edinburgh. Proceedings. Section B [Biological Sciences]*, 88, 61–81
- Ellett, D. J. and Martin, J. H. A., 1973. The physical and chemical oceanography of the Rockall Channel. *Deep Sea Research*, 20, 585–625
- Elliott, A. J. and Clarke, T., 1991. Seasonal stratification on the northwest European shelf seas. *Continental Shelf Research*, 11(5), 467–492
- Enriquez, C., 2005. *Mesoscale Circulation in the Black Sea: A Study Combining Numerical Modelling and Observations*. Ph.D. thesis, University of Plymouth

- Flather, R. A., 1981. Results from a model of the northeast Atlantic relating to the Norwegian Coastal Current. In R. Saetre and M. Mork (editors), *The Norwegian Coastal Current, Proceedings from the Norwegian Coastal Current Symposium, Geilo, 9-12 September 1980*, volume II, pages 427–458. University of Bergen
- Galperin, B., Kantha, L. H., Hassid, S., and Rosati, A., 1988. A quasi-equilibrium turbulent energy model for geophysical flows. *Journal of the atmospheric sciences*, 45(1), 55–62
- Gill, A. E., 1982. *Atmosphere-Ocean Dynamics*. Academic Press
- GOTM, 2006. General Ocean Turbulence Model [software]. URL <http://www.gotm.net/index.php?go=software>. [online; accessed 10-September-2008]
- Griffies, S., 2004. *Fundamentals of Ocean Climate Models*. Princeton University Press
- Gyory, J., Mariano, A. J., and Ryan, E. H., 2003. The slope/shelf edge current. URL <http://oceancurrents.rsmas.miami.edu/atlantic/slope.html>
- Haney, R. L., 1991. On the pressure gradient force over steep topography in sigma coordinate ocean models. *Journal of Physical Oceanography*, 21, 610–619
- Harris, I., 2003. NCEP/NCAR reanalysis data. URL <http://www.cru.uea.ac.uk/cru/data/ncep/>. [online; accessed 10-September-2008]
- Holliday, N., Pollard, R., Read, J., and Leach, H., 2000. Water mass properties and fluxes in the Rockall Trough, 1975–1998. *Deep-Sea Research. Part 1: Oceanographic Research Papers*, 47(7), 1303–1332
- Holt, J. and James, I., 1999. A simulation of the southern North Sea in comparison with measurements from the North Sea Project. part 1: Temperature. *Continental Shelf Research*, 19(8), 1087–1112
- Holt, J. and James, I., 2001. An s coordinate density evolving model of the northwest European continental shelf: 1, model description and density structure. *Journal of Geophysical Research*, 106(C7), 14,015–14,034
- Holt, J. and James, I., 2006. An assessment of the fine-scale eddies in a high-resolution model of the shelf seas west of Great Britain. *Ocean Modelling*, 13(3-4), 271–291
- Huthnance, J. M., 1974. On the diurnal tidal currents over Rockall Bank. *Deep-Sea Research*, 21, 23–35
- Huthnance, J. M., 1986. The Rockall slope current and shelf-edge processes. *Proceedings of the Royal Society of Edinburgh*, 88B, 83–101
- Huthnance, J. M., 1995. Circulation, exchange and water masses at the ocean margin: the role of physical processes at the shelf edge. *Progress in Oceanography*, 35, 353–431
- Ivanov, V., Shapiro, G., Huthnance, J., Aleynik, D., and Golovin, P., 2004. Cascades of dense water around the world ocean. *Progress in Oceanography*, 60(1), 47–98
- James, I., 1996. Advection schemes for shelf sea models. *Journal of Marine Systems*, 8, 237–254

- James, I. D., 1986. A front-resolving sigma coordinate model with a simple hybrid advection scheme. *Applied Mathematical Modelling*, 10, 87–92
- Kalnay, E., Kanamitsu, M., Kistler, R., Collins, W., Deaven, D., Gandin, L., Iredell, M., Saha, S., White, G., Woollen, J., Zhu, Y., Leetmaa, A., Reynolds, B., Chelliah, M., Ebisuzaki, W., Higgins, W., Janowiak, J., Mo, K., Ropelewski, C., Wang, J., Jenne, R., and Joseph, D., 1996. The NCEP/NCAR 40-year reanalysis project. *Bulletin of the American Meteorological Society*, 77, 437–470
- Kenyon, N. H., Akhmetzhanov, A. M., Wheeler, A. J., van Weering, T. C. E., de Haas, H., and Ivanov, M. K., 2003. Giant carbonate mud mounds in the southern Rockall Trough. *Marine Geology*, 195, 5–30
- Mansbridge, J., McIntosh, P., and O'Connor, R., 1997. The CSIRO netCDF/OPeNDAP interface to matlab. URL <http://www.marine.csiro.au/sw/matlab-netcdf.html>. [Online; accessed 10-September-2008]
- Maul, G. A., 1985. *Introduction to satellite oceanography*. Martinus Nijhoff Publishers
- Meincke, J., 1986. Convection in the oceanic waters west of Britain. *Proceedings of the Royal Society of Edinburgh*, 88B, 127–139
- Mellor, G., 1991. An equation of state for numerical models of oceans and estuaries. *Journal of Atmospheric and Oceanic Technology*, 11, 609–611
- Mellor, G. L., Ezer, T., and Oey, L.-Y., 1994. The pressure gradient conundrum of sigma coordinate ocean models. *Journal of Atmospheric and Oceanic Technology*, 11, 1126–1134
- Mellor, G. L. and Yamada, T., 1974. A hierarchy of turbulence closure models for planetary boundary layers. *Journal of the atmospheric sciences*, 31(7), 1791–1806
- Mohn, C. and White, M., 2007. Remote sensing and modelling of bio-physical distribution patterns at Porcupine and Rockall Bank, northeast Atlantic. *Continental Shelf Research*, 27, 1875–1892
- Morgan, P., 1993. CSIRO seawater toolkit (ver 2.0.1). URL ftp://ftp.marine.csiro.au/pub/morgan/seawater/ver2_0_1/. [Online; accessed 10-September-2008]
- NASA Physical Oceanography Distributed Active Archive, 2003. NOAA/NASA AVHRR Oceans Pathfinder Sea Surface Temperature Data Set. URL <http://podaac.jpl.nasa.gov/PRODUCTS/p216.html>. [Online; accessed 10-September-2008]
- National Centre for Ocean Forecasting, 2008. Coastal seas model description. URL <http://www.ncof.co.uk/Coastal-Seas-Model-Description.html>. [online; accessed 10-September-2008]
- National Geophysical Data Center; NOAA, 2005. Geodas grid translator — design-a-grid. URL http://www.ngdc.noaa.gov/mgg/gdas/gd_designagrid.html. [Online; accessed 10-September-2008]
- New, A., Barnard, S., Herrmann, P., and Molines, J.-M., 2001. On the origin and pathway of the saline inflow to the Nordic Seas: insights from models. *Progress in Oceanography*, 48, 255–287

- New, A. L. and Smythe-Wright, D., 2001. Aspects of circulation in the Rockall Trough. *Continental Shelf Research*, 21, 777–810
- Physical Sciences Division NOAA/ESRL, 2007. NCEP/NCAR reanalysis 1 project. URL <http://www.cdc.noaa.gov/cdc/data.ncep.reanalysis.html>. [Online; accessed 10-September-2008]
- POL, 2005. Polcoms documentation. URL http://cobs.pol.ac.uk/mod1/metfcst/POLCOMS_DOCUMENTATION/polcoms.html. [Online; accessed 25-April-2008]
- Pond, S. and Pickard, G. L., 1983. *Introductory Dynamical Oceanography*. Butterworth-Heinemann
- Pugh, D., 1987. *Tides, Surges and Mean Sea Level*. John Wiley and Sons
- Remote Sensing Systems, 2003. Microwave oi sst data. URL http://www.remss.com/sst/microwave_oi_sst_data_description.html. [Online; accessed 10-September-2008]
- Roberts, J., Long, D., Wilson, J., Mortensen, P., and Gage, J., 2003. The cold-water coral *Lophelia pertusa* (Scleractinia) and enigamtic seabed mounds along the north-east Atlantic margin: are they related? *Marine Pollution Bulletin*, 47, 7–20
- Robinson, I. S., 1997. *Satellite Oceanography*. Wiley-Praxis Series in Remote Sensing. John Wiley & Sons
- Shapiro, G. and Hill, A., 1997. Dynamics of dense water cascades at the shelf edge. *Journal of Physical Oceanography*, 27(11), 2381–2394
- Shapiro, G., Huthnance, J., and Ivanov, V., 2003. Dense water cascading off the continental shelf. *Journal of Geophysical Research: Oceans*, 108(C12), 20–1 – 20–19
- Smith, S. and Banke, E., 1975. Variation of the sea surface drag coefficient with wind speed. *Quarterly Journal of the Royal Meteorological Society*, 101(429), 665–673
- Song, Y. and Haidvogel, D., 1994. A semi-implicit ocean circulation model using a generalized topography-following coordinate system. *Journal of Computational Physics*, 115, 225–244
- Symonds, G. and Gardiner-Garden, R., 1994. Coastal density currents forced by cooling events. *Continental Shelf Research*, 14, 143–157
- Wade, I., Ellett, D., and Heywood, K., 1997. The influence of intermediate waters on the stability of the eastern North Atlantic. *Deep-Sea Research. Part 1: Oceanographic Research Papers*, 44(8), 1405–1426
- White, M. and Bowyer, P., 1997. The shelf-edge current north-west of Ireland. *Annales Geophysicae*, 15, 1076–1083
- Wikipedia, 2008. Equation of time. URL http://en.wikipedia.org/w/index.php?title=Equation_of_time&oldid=230180083#More_details. [Online; accessed 10-September-2008]

Appendix A

Matlab Routines used for data pre- and post-processing

This Appendix contains a list of the Matlab routines, and the associated variables and arrays, used in the data pre-processing and in processing the model output. Those routines which perform the processes in the flow charts in Figures 3.7 to 3.13 are highlighted.

2 files are used in several folders:

dayno2date.m Calculates the day number from the date (d/m/y)

date2dayno.m Calculates the date (in the form of a string, and integers for day/month/year) from the day number (and year - leap years)

Satellite SST Data Processing

Routines

Note: Files with *Night* at the end process night-time data, files without process day-time data. Files with *Combined* in the name use an average of the two—these are the ones used here.

R1_Extract.m Reads in the data for the entire period Oct 1992–Dec 2003. Uses the equation from JPL to convert from their units into °C. Replaces all values less than 2.5 with NaN. Also calculates a mean for each month over the 10 years. Then saves the data, one file per month.

R4_Plot.m Plots normal figures for each month

R4_Plot_anomaly.m Plots difference between mean and actual SST for each month

R4_Plot_colours.m Plot each month but with "stripy" colour scale to try and enhance the contrast.

R5_analyse.m Calculate mean and median SST for boxes over the bank and over ocean for each month. Save in columns to be plotted in Grapher. nb Grapher file needs manual adding of more columns - date format etc.

W1_ExtractSST.m Extracts the weekly files that were downloaded, does same calculations as *R1_Extract* and saves and plots data

Variables

SST The SST for the particular month. 500x1000x10 or 500x1000x11 (Oct/Nov/Dec have an extra year to get the whole of that winter). This is a large area - don't plot the whole lot.

meanSST mean SST for the particular month over the 10/11 years. 500x1000.

weeklySST weekly data 500x1000x4 as only downloaded 4 weeks' worth as trial

lat latitude values: 46.13 to 68.07

lon longitude values: -26.22 to 17.69

Bathymetry

Routines

R1N_Extractbat.m Reads data from GEODAS

R2N_Savebat.m saves **Rbat1N** as a .dat file with 3 columns - lon, lat, and depth.

R4_Redodomain.m Rotates the domain (uses **Rbat1N**) by multiplying the coordinates by a rotation matrix. Changes the origin of the coords to the SW point of the domain [$\min(\mathbf{RlonN})$, $\min(\mathbf{RlatN})$], so that the rotation is about this point. Then uses griddata to interpolate to the new coords. — *this performs step "Fit to rotated grid" in flow chart Figure 3.7.*

R5SaveRotbat.m Saves rotated bathy as an ascii file to be read into Surfer and cropped/interpolated/smoothed

Now open the file in surfer and grid using moving average to smooth the data. — *this performs step "Smooth in Surfer using moving average" in flow chart Figure 3.7.*

R6ExtractRotatedSmoothedBat.m Reads the smoothed rotated bathy from surfer

R7CreateModelFiles.m Creates ascii files of bathy and mask in correct format for model input. — *this performs steps "Write bathymetry file" and "Write mask file" in flow chart Figure 3.7.*

R10CreateLatArray.m Makes a file containing the latitude at each point, as needed for heat flux calculation in model. Order of points as normal (but only 1 level). — *this performs steps "Calculate latitude and longitude of each grid point" and "Write files" in flow chart Figure 3.12.*

Variables

Rbat1N 361 x 451 array. Grid is **RlatN** and **RlonN**

RlatN 361 length vector. 50N to 62N. Steps still 2 mins

RlonN As **Rlon**

RbatRotated Bathy (**Rbat1N**) rotated to new coords **RXcoord** and **RYcoord**

smoothbatRot Bathymetry which was rotated then smoothed in Surfer. 55 x 150. Uses **sX** and **sY**

sX Rotated x coords of **smoothbatRot**. 150 points from 6 to 15

sY Rotated y coords of **smoothbatRot**. 55 points from 0.25 to 3.5

RotMatrix The rotation matrix used in **R4** to rotate the bathymetry

newx Matrix of the x coordinate of each gridpoint of **Rbat1N** in new, rotated, coords

newy As **newx** but y coords

RXcoord New X coordinates to fit the bathymetry to a regular grid. 564 points from min(**newx**) to max(**newx**)

RYcoord 522 points from min(**newy**) to max(**newy**) *nb: The lengths of these chosen so that total area of bathymetry remains at approx 361 x 451 (Pythagoras)*

Initial Temperature and salinity

Original files were read in with the Fortran routine ReadWOA01.exe which saved the outputs as ASCII files (1 per month) to read into Matlab.

Routines

R1_ReadData.m Reads in the data files and saves the temperature and salinity as 4d arrays (lon, lat, level, month)

R3_Rotate.m Rotates and interpolates **temp** and **sal** to the model domain and saves as **rottemp** and **rotsal** — *this performs step "Fit to rotated grid in Matlab" for the monthly files in flow chart Figure 3.8.*

R4_Surfout.m Creates ASCII files for t and s for interpolation into Surfer (in preparation for converting to SCORDS - need all gaps filled). Creates a file per month, with columns: lon, lat, 24 t columns (surface first), 24 s columns (surface first)

Now open the files in Surfer and grid using krigging, 150x55 grid points. — *this performs step "Interpolate in Surfer using krigging" for the monthly files in flow chart Figure 3.8.*

R5_Surfin.m Reads the files interpolated in Surfer back in, and stores as **teminterp** and **salinterp**

R6a_ReadSeasonals.m In order to convert to the SCORDS, we need a few levels deeper than the 1500m of the monthly ts files. So use the seasonal data which go to deeper levels. Open the files and save them in ASCII format for opening in Surfer. — *this performs step "Fit to rotated grid in Matlab" for the seasonal files in flow chart Figure 3.8.*

Now open the files in Surfer and grid using krigging, 120x120 grid points. — *this performs step "Interpolate in Surfer using krigging" for the seasonal files in flow chart Figure 3.8.*

R6b_ReadSeasonals.m .grd files are read back and then rotated as with other data, and the rotated seasonal ts then stored as **seastemp** and **seassal** — *this performs step "Fit to rotated grid in Matlab" for the seasonal files in flow chart Figure 3.8.*

R7_Interscoord1.m This calculates the z depth at each point on each scoord level and stores in array **zzz3** — *this performs step "Calculate position of s levels" in flow chart Figure 3.8.*

R8_Interscoord2.m Uses **teminterp** and **salinterp**, and **seastemp/seassal** for deeper levels. Vertically interpolates the ts data from z coords to scoords (ie interpolates to the depths in **zzz3**). Also reverses the ts array so that now it starts at the bottom level. New scoord T and S arrays have 22 levels only at this stage — *this performs steps "Combine monthly and seasonal data" and "Linearly interpolate data from z to s levels" in flow chart Figure 3.8.*

R9_wts.m Interpolates in time to the start of the model run. Then writes the initial TS file for the model (starting in SW corner, does all t (bottom first) then all sal — *this performs steps "Linearly interpolate in time for desired start points" and "Write TS file" in flow chart Figure 3.8.*

Variables

temp The first temperature array. Size 120x120x24x12 (ie 120 lon and lat points, 24 depth levels, 12 months) Top-bottom

sal As tem but salinity Top-bottom *nb temp and sal are also used as the names of the initial arrays for the seasonal files in R6 (but not saved)*

WOAlon -29.875 to -0.125 120 points

WOAlat 40.125 N to 69.875 120 points

rottem temp rotated to the model bathy (so 150x55, use **sX/sY**). Top-bottom

rotsal Rotated sal. Details as **rottem**

teminterp Interpolated (kriging) **rottem** in surfer to ensure there is something at each point so that we can interpolate to scoords next. Still coords **sX/sY** Top-bottom

salinterp As **teminterp**

seastemp The temp from the SEASONAL files (which go deeper). Only levels 25-28 are saved, as these are the ones we need to add to the monthly data (which have levels 1-24). Is rotated to **sX/sY**. Dimensions: Y,X, level, season. Size 55x150x4x4. Note that seasons go Winter(1), Spring(2), Summer(3), Autumn(4) 'Top'-bottom

zzz3 The depth (in z coords) of each scoord level for each xy point. Uses same code as model. 24 levels. Bottom-Top

seas A vector determining which of the seasonal data to use with which month.

temi2 **teminterp** (and **seastemp** for deeper data) interpolated from z coords to 22 evenly spaced s coords (the z depth in **zzz3**). Has 22 levels, ie 2 fewer than used in the model. Bottom-Top

sali2 As **temi2**

tem3 The final temperature array. **temi2** interpolated to correct time. This is the array written to the file for the model. Bottom-Top

sal3 As **tem3**

Boundary Temperature and Salinity

Routines

BoundaryTS1.m Use the re-written indexing in the model code. This uses the index output **iboindex.mat** to pick out the relevant points in the TS arrays. Clockwise from SE. An additional option for longer runs which use new version of **bost** (**bostlong**) also writes a file containing the times relating to each set of values. — *this performs steps "Use index of boundary points to extract boundary zone data", "Write TS file" and "Write file with time (days since start of run) for each monthly dataset" in flow chart Figure 3.9.*

T1-5boundary.m Create files for specific model runs.

Variables

tempbound The array of boundary temperature values, starting in the SE corner and going clockwise. In **BoundaryTS1.m**, the size is 1576x22x12 for the 1576 points in the relaxation zone, 22 depth levels and 12 months.

salbound As **tempbound** but salinity

ibonew The array of index values within the relaxation zone

Wind

Routines

Note that there are two data sources as the original source (CRU, UEA) does not go back as far as 1950.

R1_ReadData_ascii.m Reads in the CRU u and v files (one per year, with 6 hourly data). Stores each wind component as an array 97x48x1460 — 97 lon points, 48 lat points, 365*4 time steps (=6 hourly)

R1_extractNetCDF.m Reads in the NOAA netcdf u and v files (one per year, with 6 hourly data) using the NetCDF tools from CSIRO. Because directory needs to be changed to where the CSIRO files are, need to have full directory paths for opening and saving heat files - check them!. Stores each wind component as an array 97x48x1460 — 97 lon points, 48 lat points, 365*4 time steps (=6 hourly)

R4a_RotateSpeeds.m Uses same method as the bathy rotation (**R4_RedoDomain.m**) to fit the wind to the same rotated domain. Note that this rotation actually rotates the COORDINATES. We also need to rotate the directions of the wind stress

component, from zonal/meridional to the new X/Y directions. So this requires the wind vectors to be rotated also (as with the boundary tidal data) — *this performs the steps "Fit to rotated grid in Matlab" and "Rotate wind vectors to find components in rotated system" for the data obtained from CRU in flow chart Figure 3.10.*

R4_RotateNetCDFnew.m As above but for the NetCDF files — *this performs the steps "Fit to rotated grid in Matlab" and "Rotate wind vectors to find components in rotated system" for the data obtained from NOAA in flow chart Figure 3.10.*

R5a_CreateModelFileSpeeds.m Writes data file. Everything for the run is one big file - U then V components for each time step in turn — *this performs the step "Write wind file" for the data obtained from CRU in flow chart Figure 3.10.*

F1950windspeednew.m etc Files tailored to specific model runs. — *this performs the step "Write wind file" for the data obtained from NOAA in flow chart Figure 3.10.*

Variables

uwind The u component as read in by **R1_ReadData_ascii.m** or **R1_extractNetCDF.m**. For ascii: 97x48x1460 array coords **NCEPlon/NCEPlat**. For netCDF: 10x14x2920 (2 years per file), coords **LON** and **LAT**

vwind As above but the v component

urot The u component fitted to model grid, and in the new u direction for the grid. 150x55 points. Coordinates sX and sY.

vrot As above but the v component

NCEPmask A land mask read in from the mask file (**R3** takes out points 27:34lon and 35:44lat)

NCEPlon The longitude points of the data. From 90W to 90E, approx every 1.9° (**R4** takes out points 35:44 and names this **NCEPlon**)

NCEPlat The latitude points. From 0.9524S to 88.5N, approx every 1.9° (**R4** takes out points 27:34 and names this **NCEPlat**)

LON netcdf longitude. 14 points, 330E to 354.375E

LAT netcdf latitude. 10 points, 63.8079N to 46.6658N

Heat Flux Variables

Routines

R1_ExtractNetCDFdata.m Reads the NetCDF format heat flux files using the NetCDF tools from CSIRO. Because directory needs to be changed to where the CSIRO files are, need to have full directory paths for opening and saving heat files - check them! Extracts lon, lat, time and data for each variable (**airtemp**, **pressure**, **relh**, **cloud**). The variable names in files are found with ncdump.exe nb there are

two slightly different versions of this routine - only difference is different filename formats for the input files.

R2_Rotate.m Combines the 4 fluxes into the total heat flux, and then rotates and interpolates to the model bathy (coords **sX/sY**). *this performs the step "Fit to rotated grid in Matlab" in flow chart Figure 3.12.*

R3_CreateModelFile.m Writes the file for the model. All timesteps in one file. Arranged same way as bathy etc, starting in SW corner and going along rows *this performs the steps "Convert air temperature from K to C" and "Write Files" in flow chart Figure 3.12.*

findstarttime.m The time in the NetCDF file is "hours since 00:00 1/1/1". This routine finds the date of some timestep

storetimes.m Calculates the date of every timestep (and which of the 4 daily datasets it is) and stores in a structural array **cumulative**. Uses **dayno2date.m**

Variables

airtemp Air temperature array

pressure Surface pressure

relh Relative humidity

cloud Total cloud cover

TIME Time in hours of each data file

LON Original longitude of the data

LAT Original latitude

airtemprot Air temperature rotated to coords **sX** and **sY**

pressrot Surface pressure, rotated

relhrot Relative humidity, rotated

cloudrot Total cloud cover, rotated

Tidal Constituents

Routines

R1_ReadInData.m Reads in the tidal constituent data (hcosg and hsing for zet, u and v) from Sarah. Rotates the current vectors so that the components are along the new xy directions instead of lon/lat directions. Then writes the file for the model — z1,z2,u1,u2,v1,v2 for each of the 15 constituents. In order of the boundaries — SNWE. Note that the sigma values for the 15 constituents must be pasted in at the beginning of the file *This performs the steps "Rotate current vectors to find components in rotated system" and "Write tide data file" in flow chart Figure 3.11. Step "Add phase speeds to start of data file" is performed manually.*

Variables

hcosgz, hsingz The elevations. Size is 410x15 for the 410 boundary points (each boundary done separately, so corners each in both their boundaries) and 15 tidal constituents. The boundary order is SNWE.

hcosgu, hsinqu The u current. As **hcosgz/hsingz**, except that there are 414 points instead of 410 as these values are on the U boundaries, which are each an extra gridpoint long.

hcosgv, hsingv As above but v current

hcosgu1 etc As **hcosgu** etc, but rotated so that the velocity components are along the **sX** and **sY** directions instead on zonal and meridional

Post-processing of Model Results

Routines

Used for all runs:

ExtractKE.m Plots the KE output

R1_read_UVTSbin_Long.m Reads in TSUV binary file, interpolates to z coords (set the levels in *Load_zzz3_mas.batL.m*) and saves s and z level data. Saves in one file per output timestep. It calls *Load_zzz3_mas.batL.m* and *frScoord_toZ_3d.m*.

R3_Plot.m Does horizontal section plots = can do s or z levels. Lots of variables - uncomment the one you want. Saves automatically (but check names)

R3_plotsection plots vertical cross sections. Uncomment the one you want. Saves automatically.

Used for some runs:

R4_density Calculates density using *SEAWATER Toolkit*

R4_plotdensity.m plot density sections and plots. Saves automatically.

R5_geostrophic Calculates geostrophic velocity along a section that you specify and plots against time. Does same for model output

R5_geostrophic_singletime Calculates geostrophic velocity for a particular output timestep and plots against the model velocity

R1_Read_zetabin.m Read elevation from the tidal test runs

R2_frequencies.m plot elevation over time for a particular point

R2_frequencies_v.m plot velocity components over time for a particular point

plotprofiles.m plot velocity profiles with depth

R5_compareKEandWind.m compare KE with wind speed in the wind test run

R6_ekman.m plot velocity with depth for a point to show the Ekman spiral

Read_heatflux.m read in heat flux binary files from runs that output them

R4_plot_plume.m Plot subplots showing movement of plume if one is identified.

Variables

t temperature on s levels

tzet temperature on z levels

s temperature on s levels

szet temperature on z levels

u temperature on s levels

uzet temperature on z levels

v temperature on s levels

vzet temperature on z levels

ptheta_s potential density on s levels

ptheta_z potential density on z levels

sigmas density on s levels from a different toolbox

sigmaz density on z levels from a different toolbox

svans specific volume anomaly on s levels (for geostrophic calculation)

svanz specific volume anomaly on z levels (for geostrophic calculation)

Appendix B

List of All Changes Made to the Model Code

This Appendix details the changes made to the POLCOMS code to enable its use in this study. Many changes are common to all the runs whereas some are unique to particular runs; the run will be named where this is the case. Sections are organised according to the file name. Note that the line numbers refer to their position in the version of the code used for the full runs, except where otherwise noted. In order to use the code files with the Windows system, the file extensions were first changed from .f to .for.

advpbv.for

- line 917: added the *i,j* to write (ludbg,fr) 'ds(k-1)',ds(k-1,i,j) to fix bug
- line 1053: added the *i,j* to write (ludbg,fr) 'sigo(k+1)',sigo(k+1,i,j) to fix bug
- line 1054: added the *i,j* to write (ludbg,fr) 'sigo3(k+1)',sigo3(ka,i,j) to fix bug

bcalc.for

- lines 196–198: commented `real*8 di(n,1-mhalo:iesub+mhalo,1-mhalo:jesub+mhalo)` and replaced with
`real*8, allocatable, dimension(:,:,:) :: di`
`allocate (di(n,1-mhalo:iesub+mhalo,1-mhalo:jesub+mhalo))`

b3d.for

- line 32: added integer `:: avcount`. This was designed to be used in the output routine `tidemeanout` although the final model runs used `data_out` instead for all output.

- line 109: added `real*8, allocatable, dimension(:, :) :: latgrid , longrid`. These new variables store the latitude and longitude of each point, and are used in the heat flux calculations
- line 151: added `& , prh`. This new variable stores the atmospheric pressure so that it is only used in the heat flux calculation.
- **Runs T6/T7/T9 only** line 151: added `, wes, wns` because these runs required the use of new arrays to ensure that the wind data were only used in `heatin` or `saltflux`
- line 155: added `& , ev, sflst, hlstor, skstor, skestor`. These extra variables were used to output heat flux and evaporation data. Used mainly in debugging.
- **Run T3A only** line 178: added `real*8, allocatable, dimension(:, :, :) :: told, sold` as these variables are used to keep the constant temperature/salinity
- lines 189–190: `#ifdef METOFFICE` was commented out and `#ifdef HEATOUT` added. This allows heat fluxes to be outputted by specifying `HEATOUT` as a pre-processor option.
- lines 199–200: added `real*8, allocatable, dimension(:, :, :, :) & :: aaold, akold, qsqold, salold, tmpold, uold, vold, alold`. These were originally used in outputting data, but not used for final runs.

b3dalloc.for

- lines 357–412: added allocation of variables `aaold, akold, qsqold, salold, tmpold, uold, vold, alold`. See above.
- lines 430–431: `#ifdef METOFFICE` was commented out and `#ifdef HEATOUT` added. This allows heat fluxes to be outputted by specifying `HEATOUT` as a pre-processor option.
- lines 756–769: added allocation for variables `latgrid , longrid`. See above.
- lines 1044–1055: added allocation for variables `ev, sflst` which were used when testing precipitation/evaporation routine.
- lines 1075–1105: added allocation for variables `prh, hlstor, skstor, skestor`. See above.
- **Runs T6/T7/T9 only** lines 1080–1092: added allocation for variables `wes, wns` because these runs required the use of new arrays to ensure that the wind data were only used in `heatin` or `saltflux`
- lines 1929–1930: `call abort()` was commented and replaced with `stop` as the former command caused the compiler to stop

b3dgrid.for

- lines 250–256: lines `iucoast(i,j)=1` and `ipexub(i,j)=1` were placed inside a new `#ifdef ROCKALLBC` loop and new lines `iucoast(i,j)=0` and `ipexub(i,j)=0` were used if `ROCKALLBC` was not to be used. Due to problems with the original code when used with a Black Sea domain.

b3dinit.for

- lines 250–256: call `metset` replaced with call `metset_cko` and placed in `#ifdef ROCKALLBC` loop. As this study used a purpose-built file to read in met data.

b3drun.for

- line 4: added `#include "param.h"`
- **Run T3A only** lines 468–469: added `told=tmp` and `sold=sal` to store the temperature and salinity
- **Run T3A only** lines 953–954: added `tmp=told` and `sal=sold` to reset temperature and salinity to previous values

baroc.for

- lines 93–97: commented `if (salflux)` then and corresponding `endif` as there was another logical variable `lsaltflux` and it was not necessary to use both.

barot.for

- lines 62–77: commented


```
real*8 dub(1-mhalo:iesub+mhalo,1-mhalo:jesub+mhalo)
real*8 dvb(1-mhalo:iesub+mhalo,1-mhalo:jesub+mhalo)
real*8 fuc(1-mhalo:iesub+mhalo,1-mhalo:jesub+mhalo)
real*8 fvc(1-mhalo:iesub+mhalo,1-mhalo:jesub+mhalo)
real*8 dz(8,1-mhalo:iesub+mhalo,1-mhalo:jesub+mhalo)
real*8 hsz(1-mhalo:iesub+mhalo,1-mhalo:jesub+mhalo)
integer imask(8,1-mhalo:iesub+mhalo,1-mhalo:jesub+mhalo)
integer ipexb_temp(1-mhalo:iesub+mhalo,1-mhalo:jesub+mhalo)
```

and added

```
real*8, allocatable,dimension (:,:) :: dub,dvb,fuc,fvc,hsz
real*8, allocatable,dimension (:,:,) :: dz
```

```
integer,allocatable,dimension (:,:,) :: imask
integer,allocatable,dimension (:,:) :: ipexb_temp
```

- lines 1194–1195: added missing bracket to end of line 1194 and missing + to beginning of line 1195

bost.for

There were very substantial changes made to this routine as the indexing method did not work correctly, and there is almost no original code left uncommented. For the final runs, a new routine `bostlong` was used instead.

bostlong.for

This was a new routine written for this study. It includes all the changes made to `bost` with the addition of a new algorithm for reading in data which allows longer runs to be conducted. As this does not contain commented old code it is much clearer to follow than `bost`.

boundarycon.h

This file defines which temperature and salinity boundary routine is to be used. The runs in this study used the option `#define TS_boundary_condition bostlong`.

data_out.for

This routine was altered for each run depending on the outputs required.

- line 22: commented call `tidemeanout_cko(36,37,38)` as all outputs were handled by `data_out` for the final runs
- line 30: `navtm=mod(itimt,3600)` is altered depending on how often outputs are required
- lines 30–47: main outputs are listed here
- lines 53–55: call `zKEcount(136)` and call `zTScount(136)` commented and replaced by call `KEout`
- lines 71, 107, 116–118: commented existing output commands as we did not require these

endstep.for

- line 46: added `iheat = iheat -1` so that heat counter (to keep track of when to read in data) is updated correctly
- lines 54–58: call `metset` replaced with call `metset_cko` and placed in `#ifdef ROCKALLBC` loop. As this study used a purpose-built file to read in met data.

filope.for

- lines 60–61: call `abort()` was commented and replaced with `stop` as the former command caused the compiler to stop

heatin.for

- line 66: added `,iitimt,ntimt` to define these variables
- line 70: added `& ,tm1,Barg, hl,sk,ske`. `tm1` and `Barg` are used in the calculation of the local time; `hl,sk,ske` were used in debugging and to output heat flux
- lines 73,79: added `real*8, allocatable, dimension(:,:) :: qqs` and `allocate(qqs(1,m))`. New variable `qqs` was used to store solar radiation data and used in debugging
- lines 92–95: added `read(116,'(5f9.4)') latgrid` and `read(117,'(5f9.4)') longrid` and placed them inside `#ifdef FLAT` loop - due to rotated domain we can't calculate lat/lon from the grid coordinates, so they need to be read from files
- lines 124–126: `rlat = alat1 + (jcg-1)*dbed` placed inside `#ifndef FLAT` loop
- lines 128–139: added
`rlat = latgrid(i,j)`
`!-----Adjust time from GMT to local apparent solar time-----`
`!First longitude diff (1=4 mins)`
`tm1=tm + 4*longrid(i,j)/60.0d0`
`!Then equation of time (approximation) /60 for mins->hrs`
`Barg = (2*pi*(jday-81))/364.0d0`
`tm1=tm1 + (9.87*sin(2*Barg) - 7.83*cos(Barg)-1.5*sin(Barg))/60.0d0`
`!----end----`
 and placed inside `#ifndef FLAT` loop. This adjusts the time to local time for each point.
- **Runs T6/T9 only** lines 141–142: `uw = we(i,j)` and `vw = wn(i,j)` were replaced with `uw = wes(i,j)` and `vw = wns(i,j)` because these runs required the use of new arrays to ensure that the wind data were only used in `heatin`
- line 148: added `p = prh(i,j)` so that pressure is only used here

- line 155–156: commented call `solrad(tm, rlat, qs)` and replaced with call `solrad(tm1, rlat, qs)` so that solar radiation calculation uses the corrected time
- line 159: added `qqq(i,j)=qs` so that solar radiation can be outputted. Used in debugging.
- line 164: commented call `heatls(ts, ta, ww, r, c, p, ql)` and replaced with call `heatls(ts, ta, ww, r, c, p, ql, hl, sk, ske)` used in debugging.

horizdiffuse.for

- lines 114–115: commented `ahcc=0.2d0` and replaced with `ahcc=ahc` so that it is read from the parameters file

hset.for

- lines 172–180: commented
if (nens.gt.1) then
write (filbath, '(bathymetry_', i3.3, '.dat')') myens
else
filbath = 'bathymetry.dat'
endif
close(13)
open(13, file=filbath)
write(13, '(50f8.2)') depth
close(13)
as we did not need to output the bathymetry to a file.

KEout.for

This is a new routine, based on previous ones written for the Black Sea (Enriquez, 2005), which estimates the kinetic energy per unit volume.

metset_cko.for

This is a new routine written specifically for the meteorological data used in this study. It is based on `metset.for` but is simpler as it contains only the options and formats we need.

- **Run T6/T7/T9 only** required the wind data to be read in for the heat fluxes or salt flux, but not be used anywhere else. To achieve this, the code for these runs was changed so that the wind components are read into new arrays `wes` and `wns`.

out.for

- lines 45–46: commented `allocate (workout(L,m,n-2))` and replaced with `allocate (workout(L,m,n))` so that all data are outputted.
- lines 55–56: commented `do k=1,n-2` and replaced with `do k=1,n`
- lines 44–45: commented `workout(i,j,k)=work3d(k+1,i,j)` and replaced with `workout(i,j,k)=work3d(k,i,j)`

param.h

This file contains the main preprocessor settings. The following options were used in all runs:

```
#define NOGUI
#define SERIAL
#define SC00RD
#define SIMPLECASEI
#define PGRAD
#define PGRAD_SPLINE
#define READ_INITIAL_TS
#define MY25CBF
#define HORIZDIF
#define HORIZDIFTS
#define NOTIDE
#define GOTM

#undef UBC_CALC
#undef NO_CONVADJ
#undef MPICH
```

In runs with full forcing, option `#ifdef ROCKALLFULL` was used which has the effect of also defining the following options:

```
#define ROCKALLBC
#define FLAT
#undef NOTIDE
#define READ_TIDECON
#define BULKMET
#undef NOHEAT

#define SALTFLUX
#define HEATOUT
```

The geostrophic runs used the option `#ifdef ROCKALLGA` which causes only `#define FLAT` and `#define ROCKALLBC` to be used. Some runs had particular needs which

required modifications to these two main settings:

- T4/T8** These runs needed tides but no other forcing. Therefore option `#ifdef ROCKALLGA` was enabled, with `#undef NOTIDE` and `#define READ_TIDECON` also added.
- T5** This run contained wind but no other meteorological forcing. Option `#ifdef ROCKALLGA` was enabled, with `#define BULKMET` and `#define NOHEAT` also added. This ensured the wind data were read in, but the heat flux calculations were not done.
- T6/T9** In contrast T6/T9 required the heat flux calculations, for which the wind data must be read in, but the wind must not be used to generate currents. Option `#ifdef ROCKALLGA` was enabled, with `#define BULKMET` and `#undef NOHEAT` also added. Routines `metset_cko`, `heatin` were altered so that the wind data were read into new arrays that were only used for the heat flux calculations.
- T7** This run was similar to T6 in that it required the wind speed and meteorological data in order to calculate the evaporation rate, but it was also necessary to stop the heat flux calculations. Option `#ifdef ROCKALLGA` was enabled, with `#define BULKMET` and `#undef NOHEAT`, and `SALTFLUX` also added. Routines `metset_cko`, `evap_prep` were altered so that the data were read into new arrays that were only used for the salt flux calculations.

param.for

- line 21: added integer `nob`, `nin`. These variables are used by `new bost.for` and `bostlong.for`

parmargs.for

- lines 94–95: commented `elseif(argv(1:10).eq.'-resettm')` then and replaced with `elseif(argv(1:10).eq.'-tmreset')` then as existing code had a bug which did not allow the time to be reset when starting from a warm start — placing `-resettm` in the start options triggered the response for `-reset` which resets the whole system.

partit.for

- lines 312–313: call `abort()` was commented and replaced with `stop` as the former command caused the compiler to stop
- lines 471–472: call `abort()` was commented and replaced with `stop` as the former command caused the compiler to stop

pfinish.for

- lines 109–110: call abort() was commented and replaced with stop as the former command caused the compiler to stop

pgrad.for

- lines 30–35; 458–460; 695–703: commented real*8 di(n,1-mhalo:iesub+mhalo,1-mha and replaced with

```
real*8, allocatable, dimension(:,:,:) :: di
allocate (di(n,1-mhalo:iesub+mhalo,1-mhalo:jesub+mhalo))
```
- lines 700–704: as above but variable bpp

saltflux.for

- line 24: added call evap_prep to do the evaporation calculation
- line 43: added sflst(i,j)=sfl which allows salt flux to be stored for debugging
- lines 123–126: commented

```
QW=(0.62*EW)/(PR(i,j) - 0.38*EW)
QA=(0.62*EA)/(PR(i,j) - 0.38*EA)
```

and replaced with

```
QW=(0.62*EW)/(Prh(i,j) - 0.38*EW)
QA=(0.62*EA)/(Prh(i,j) - 0.38*EA)
```

as we used prh to store atmospheric pressure.
- **Run T7 only** lines 128–131: commented

```
WSP=SQRT(WE(i,j)**2+WN(i,j)**2)
evap=CE*RHO*WSP*(QW - QA)/row
```

and replaced with

```
WSPs=SQRT(Wes(i,j)**2+Wns(i,j)**2)
evap=CE*RHO*WSPs*(QW - QA)/row
```

because this run required the use of new arrays to ensure that the wind data were only used in saltflux
- line 134: added ev(i,j)=evap to store evaporation rate (used in debugging)

setopenbc.for

- lines 60–65: if(icg.eq.1 .and. ipexb(i,j) .ne. 0) incb(i,j)=1
if(icg.eq.L .and. ipexb(i,j) .ne. 0) incb(i,j)=1
if(jcg.eq.1 .and. ipexb(i,j) .ne. 0) incb(i,j)=1
if(jcg.eq.m .and. ipexb(i,j) .ne. 0) incb(i,j)=1
were placed in #ifdef ROCKALLBC loop as they caused problems when used with a Black Sea domain during other work.

tidbndrp2.for

- lines 135–136: added `write(*,*)'read nfac'` and `write(*,*)nfac` for information
- lines 148–149: added `write(*,*)'read iidate'` and `write(*,*)iidate` for information
- lines 153–154: added `write(*,*)'read indx'` and `write(*,*)indx` for information
- lines 174–175: commented `do i=1,15` and replaced with `do i=1,ncond` so that fewer than 15 constituents could be used if necessary
- lines 178–179: commented `mcond=15` and replaced with `mcond=ncond` so that fewer than 15 constituents could be used if necessary

tidemeanout.for

Note that for the final runs this routine was not used.

- lines 23–24: commented `#ifdef METOFFICE` and replaced with `#ifdef HEATOUT`
- lines 91–92: commented `#ifdef METOFFICE` and replaced with `#ifdef HEATOUT`
- lines 128–129: commented `#ifdef METOFFICE` and replaced with `#ifdef HEATOUT`
- lines 255–256: commented `#ifdef METOFFICE` and replaced with `#ifdef HEATOUT`
- line 437: added `#ifdef HEATOUT`
- lines 521–522: commented `#ifdef METOFFICE` and replaced with `#ifdef HEATOUT`

tidemeanout_cko.for

This was a new routine designed to keep a running average of variables before outputting them. In the final runs however, it was not used.

Appendix C

bostlong.for Code

This is the new routine that was used to perform relaxation of temperature and salinity at the open boundary. It was based on the original POLCOMS file `bost.for` but substantial changes were made in order for it to work correctly with the domain used in this study. The underlying process remains the same, but the method of indexing the boundary points was altered, and the way in which files are read in had to be changed to allow longer model runs to be performed.

```

module bostmodlong

real*8, allocatable, dimension(:) :: botime1, botime2 !cko
real*8, allocatable, dimension(:, :) :: botmp1, botmp2 !cko
real*8, allocatable, dimension(:, :) :: bosal1, bosal2 !cko
real*8, allocatable, dimension(:, :) :: botmp, bosal !cko
real*8, allocatable, dimension(:, :) :: work2d !cko
real*8, allocatable, dimension(:) :: sigr(:), dsi(:), dsiu(:) !cko
integer, allocatable, dimension(:), save :: ipoint, jpoint !cko
    integer, allocatable, dimension(:):: boday !cko
    integer, allocatable, dimension(:, :) :: work2di !cko

end

subroutine bostlong

!jth boundary relaxation to climatology
!jth s-coordinates or sigma coordinates
!jth reads in and sets climatological sal and temp at boundaries.
!jth climate values taken to represent values at 15th of month
!jt botime is this time in days from 1st nov (=0)

#include "param.h" !cko
    use param
    use parallel
    use b3d
    use bostmodlong
!
    implicit none

!cko For all open boundary, nob = 2*l + 2*m -4
!cko The no of points in each of the concentric squares

```

```

                                (starting at outer edge) is then
!cko nob = 8*(q-1) (q is from 1:niw)
!cko THE total no of points in the relaxation zone is then
!cko niw*nob = 4*niw*(niw-1)

!cko      integer nob,nin
           integer ic,jc,iq,ib,iq1,iq2,kk,ipq,icg,jcg,      ipq1
           integer i,j,k,kb,ip
           integer ipstor(niw),ntimt !cko
           real*8 days,pnt,r,bt,bs      ,pt
           logical first
           save first
           data first /.true./

100  format(22f8.4) !cko Format for the boundary file inputs
!+++++
!cko Set up the allocations and indexing
!+++++
      if(first) then
         first=.false.
         nob = 2*1 + 2*m - 4
         nin = n

         allocate (botmp1(nob*niw - (4*niw*(niw-1)),n-2))
         allocate (botmp2(nob*niw - (4*niw*(niw-1)),n-2))
         allocate (bosall(nob*niw - (4*niw*(niw-1)),n-2))
         allocate (bosall2(nob*niw - (4*niw*(niw-1)),n-2))
         allocate (botime1(1))
         allocate (botime2(1))
         allocate (work2d(L,m))
         allocate (work2di(L,m))
         allocate(ipoint(nob*niw - (4*niw*(niw-1))))
         allocate(jpoint(nob*niw - (4*niw*(niw-1))))
         allocate(boday(1))
         boday=0
         allocate(sigr(nin),dsi(nin),dsiu(nin))

         do k=1,nin-2 !cko
            do ipq=1,nob*niw - (4*niw*(niw-1)) !cko
               botmp1(ipq,k)=0. !cko
               botmp2(ipq,k)=0. !cko
               bosall(ipq,k)=0. !cko
               bosall2(ipq,k)=0. !cko
            enddo !cko
         enddo

         if(master) then

!*****

!jth      set up indices and parameters
!jth      iboindex(lm) holds index of niw*1..nob, clockwise round boundary

```

```

!jth      relfac(lm) hold relaxation factor
!jth      ipoint holds i index of boundary point
!jth      jpoint holds j index of boundary point

      do j=1,m
        do i=1,l
          work2d(i,j)=0.0d0
          work2di(i,j)=0
        enddo
      enddo

!cko Changed the indexing
      do iq=1,niw
        ipstor(iq)=0
      enddo
      do iq=1,niw
!----- Southern Boundary -----
        jc=1
        ip=ipstor(iq)
        do ic=1-(iq-1),1+(iq-1),-1
          ip=ip+1
          ib=ic+(jc-1+(iq-1))*1
          work2di(ic,jc+iq-1)=ip+(nob*(iq-1)-4*(iq-2)*(iq-1))
          work2d (ic,jc+iq-1)=dble(niw+1-iq)/dble(niw)
        enddo
        ipstor(iq)=ip

!----- Western Boundary -----
        ic=1
        ip=ipstor(iq)
        do jc=2+(iq-1),m-1 -(iq-1)
          ip=ip+1
          ib=ic+(iq-1)+(jc-1)*1
          work2di(ic+iq-1,jc)=ip+(nob*(iq-1)-4*(iq-2)*(iq-1))
          work2d (ic+iq-1,jc)=dble(niw+1-iq)/dble(niw)
        enddo
        ipstor(iq)=ip

!----- Northern Boundary -----
        jc=m
        ip=ipstor(iq)
        do ic=1+(iq-1),l-(iq-1)
          ip=ip+1
          ib=ic+(jc-1+(1-iq))*1
          work2di(ic,jc+1-iq)=ip+(nob*(iq-1)-4*(iq-2)*(iq-1))
          work2d (ic,jc+1-iq)=dble(niw+1-iq)/dble(niw)
        enddo
        ipstor(iq)=ip

!----- Eastern Boundary -----
        ic=1
        ip=ipstor(iq)

```

```

      do jc=m-1 -(iq-1),2+(iq-1),-1
        ip=ip+1
        ib=ic+(1-iq)+(jc-1)*1
        work2di(ic+1-iq,jc)=ip+(nob*(iq-1)-4*(iq-2)*(iq-1))
        work2d (ic+1-iq,jc)=db1e(niw+1-iq)/db1e(niw)
      enddo
      ipstor(iq)=ip

    enddo !iq=1:niw

!jth      special treatment for corners

!jth      southwest

      do iq1=1,niw
        do iq2=1,niw
          work2d(iq1,iq2)=max(db1e(niw+1-iq1)/
                                &
                                db1e(niw),db1e(niw+1-iq2)/db1e(niw))
        enddo
      enddo

!jth      north west

      do iq1=1,niw
        do iq2=1,niw
          ib=1+(m-1)*1+(iq1-1)-(iq2-1)*1
          work2d(iq1,m-(iq2-1))=max(db1e(niw+1-iq1)/
                                    &
                                    db1e(niw),db1e(niw+1-iq2)/db1e(niw))
        enddo
      enddo

!cko-----
!      North East
      do iq1=1,niw
        do iq2=1,niw
          work2d(1-(iq1-1),m-(iq2-1))=max(db1e(niw+1-iq1)/
                                             &
                                             db1e(niw),db1e(niw+1-iq2)/db1e(niw))
        enddo
      enddo

!      South East
      do iq1=1,niw
        do iq2=1,niw
          work2d(1-(iq1-1),iq2)=max(db1e(niw+1-iq1)/
                                     &
                                     db1e(niw),db1e(niw+1-iq2)/db1e(niw))
        enddo
      enddo

!cko-----

    endif !if master

    call dist (leadid,work2d,relfac,1) !cko v6.2 version
    call dist (leadid,work2di,iboindex,1) !cko v6.2 version

```



```

        deallocate (work2d) !cko
        deallocate (work2di) !cko

!cko=====
!   Set up array of ib locations
    ipq=0
    do iq=1,niw
        do ipq1=1-(iq-1),1+(iq-1),-1 !South
            ipq=ipq+1
            ipoint(ipq)=ipq1
            jpoint(ipq)=1+(iq-1)
        enddo
        do ipq1=2+(iq-1),m-1 - (iq-1) !West
            ipq=ipq+1
            ipoint(ipq)=1+(iq-1)
            jpoint(ipq)=ipq1
        enddo
        do ipq1=1+(iq-1),1-(iq-1) !North
            ipq=ipq+1
            ipoint(ipq)=ipq1
            jpoint(ipq)=m-(iq-1)
        enddo
        do ipq1=m-1 -(iq-1),2+(iq-1),-1 !East
            ipq=ipq+1
            ipoint(ipq)=1 - (iq-1)
            jpoint(ipq)=ipq1
        enddo
    enddo
!cko=====
!Read in data for first 2 months ('last month' and 'this month')
    do ipq=1,niw*nob - 4*niw*(niw-1) !The total no of points in
                                     the relaxation zone
        read(81,100) (botmp1(ipq,k),k=1,nin-2)
    enddo
    do ipq=1,niw*nob - 4*niw*(niw-1) !The total no of points in
                                     the relaxation zone
        read(81,100) (bos11(ipq,k),k=1,nin-2)
    enddo

    do ipq=1,niw*nob - 4*niw*(niw-1) !The total no of points in
                                     the relaxation zone
        read(81,100) (botmp2(ipq,k),k=1,nin-2)
    enddo
    do ipq=1,niw*nob - 4*niw*(niw-1) !The total no of points in
                                     the relaxation zone
        read(81,100) (bos12(ipq,k),k=1,nin-2)
    enddo

    read(82,*) botime1
    read(82,*) botime2

endif !if first

```

```

!+++++
!Is it time to read in more data?
!+++++
!Add 1 to day counter every 24 hours
  if (mod(timt,86400.00).eq.0) then
    boday=boday+1
  endif
  if (boday(1).eq.botime2(1)) then !If we're at the end of the second
                                   interpolation time
    write(*,*)'Reading more boundary data'
    !Swap arrays
      botmp1=botmp2
      bosall=bosal2
      botime1=botime2

!Read next data
      do ipq=1,niw*nob - 4*niw*(niw-1) !The total no of points in
                                   the relaxation zone
        read(81,100) (botmp2(ipq,k),k=1,nin-2)
      enddo
      do ipq=1,niw*nob - 4*niw*(niw-1) !The total no of points in
                                   the relaxation zone
        read(81,100) (bosall(ipq,k),k=1,nin-2)
      enddo
      read(82,*) botime2
    endif

    allocate (botmp(niw*nob - 4*niw*(niw-1),n-2)) !cko
    allocate (bosall(niw*nob - 4*niw*(niw-1),n-2)) !cko

!+++++
!jth interpolate in time
!+++++

    if (mod(timt,3600.00).eq.0) then !cko

      days=mod(timt/86400.,365.)
      pnt=(days-botime1(1))/(botime2(1)-botime1(1))

      do ipq=1,niw*nob - 4*niw*(niw-1) !cko
        icg = ipoint(ipq) !cko
        jcg = jpoint(ipq) !cko

        do k=1,n-2

          botmp(ipq,k) = botmp1(ipq,k)*(1.-pnt) & !cko
                        + botmp2(ipq,k)*pnt      !cko
          bosall(ipq,k) = bosall1(ipq,k)*(1.-pnt) & !cko
                        + bosall2(ipq,k)*pnt      !cko

        enddo
      enddo
    endif

```

```

!+++++
!jth relaxation
!+++++
      do j=1,jesub
        do i=1,iesub

          if ((ipexb(i,j).ne.0).and.(iboindex(i,j).ne.0)) then
            r=relfac(i,j)

            do k=2,n-1

              bt=botmp(iboindex(i,j),k-1)
              bs=bosal(iboindex(i,j),k-1)

              tmp(k,i,j)=bt*r+(1.-r)*tmp(k,i,j)
              sal(k,i,j)=bs*r+(1.-r)*sal(k,i,j)

            enddo

          endif
        enddo
      enddo !cko

      deallocate(botmp) !cko
      deallocate(bosal) !cko
      return

end

```